Reshaping Oncology Research Through Imaging Flow Cytometry

Article Collection

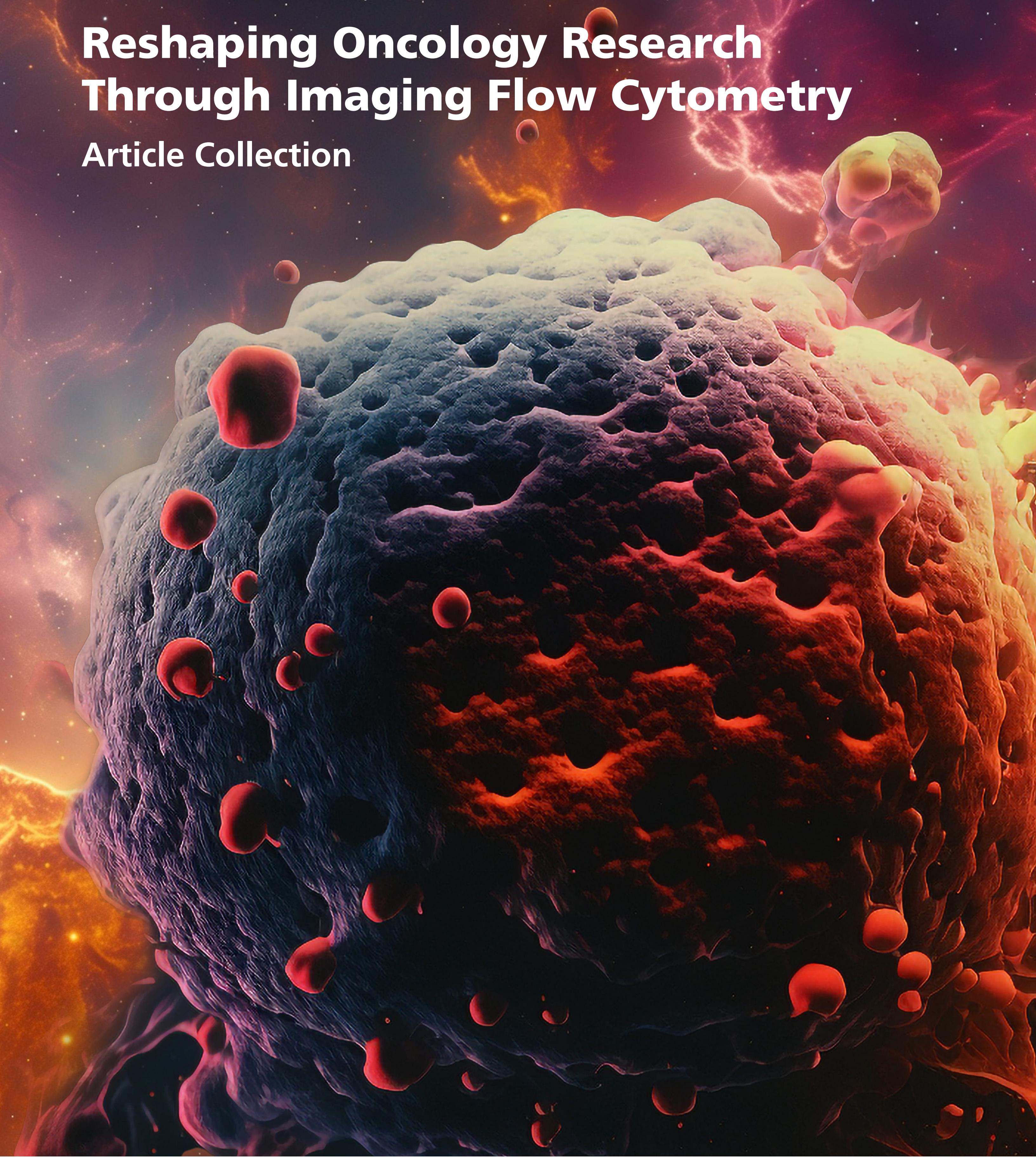

Sponsored by:

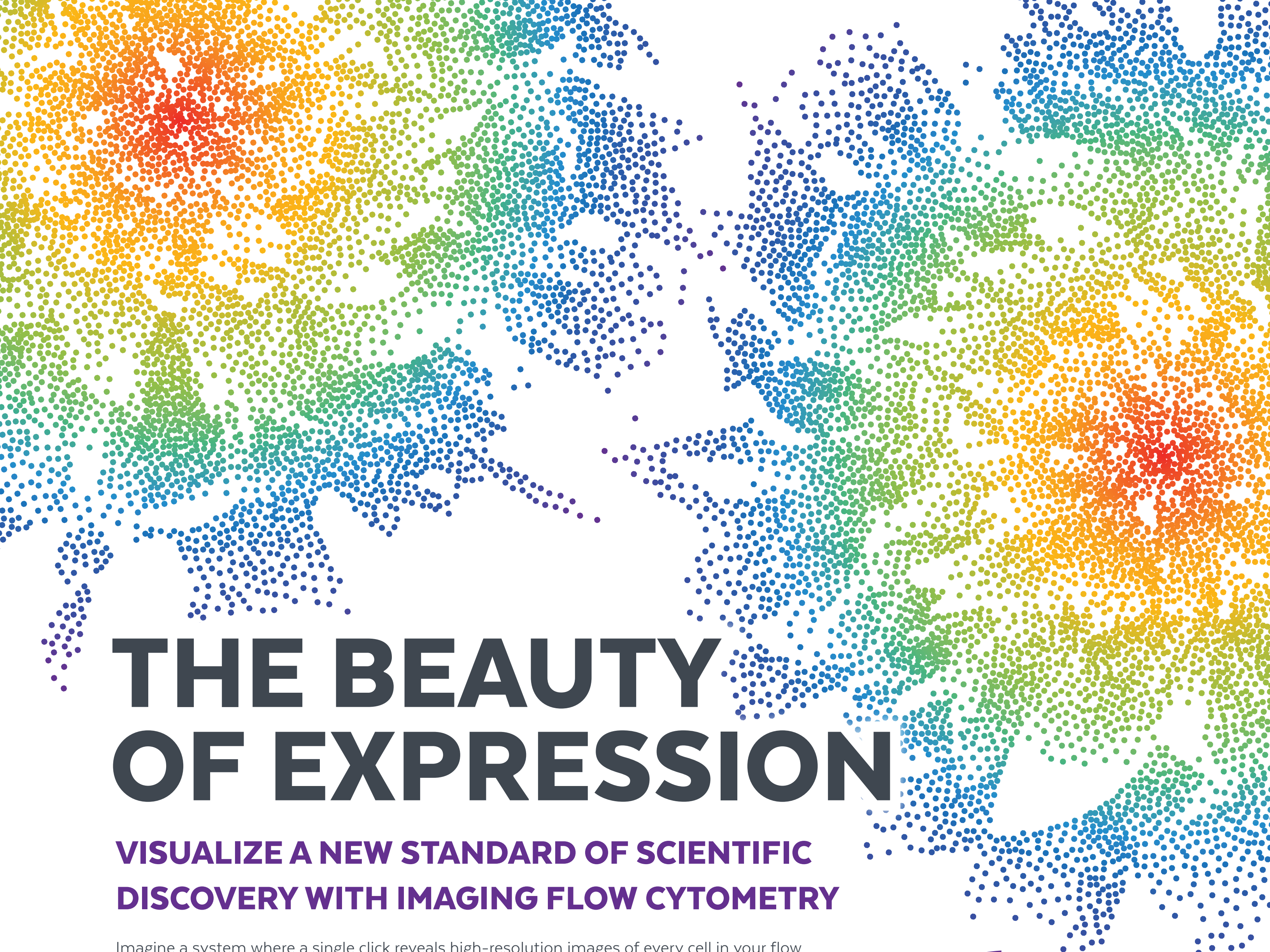

THE BEAUTY OF EXPRESSION

VISUALIZE A NEW STANDARD OF SCIENTIFIC DISCOVERY WITH IMAGING FLOW CYTOMETRY

Imagine a system where a single click reveals high-resolution images of every cell in your flow cytometry data while automatically generating key microscopy statistics. The Cytek® Amnis® ImageStream®X Mk II imaging flow cytometer offers exactly that. The instrument captures detailed images of each cell, applies pixel-by-pixel spectral compensation, and extracts hundreds of fluorescent and morphological features. This depth of per cell information is unmatched by any other system. Explore how imaging flow cytometry can elevate your research and shape the future of your discoveries.

- **Visualize** intricate cell structures and subcellular components for important insights with fine detail high-resolution cell imagery up to 0.3 µm per pixel resolution
- **Capture** large image data sets at rates of 5,000 cells per second for high-throughput analysis and faster results
- **Ensure** accuracy of fluorescent measurements with fully compensated images to reliably determine that the signal is located where expected
- **Gain** significant and incisive conclusions with a comprehensive sophisticated image analysis software suite that includes machine learning and AI tools

Cytek is committed to providing powerful solutions through scientific innovation. See what the Cytek Amnis ImageStream®X imaging flow cytometer can do for you. **Reveal the beauty of cellular expression.**

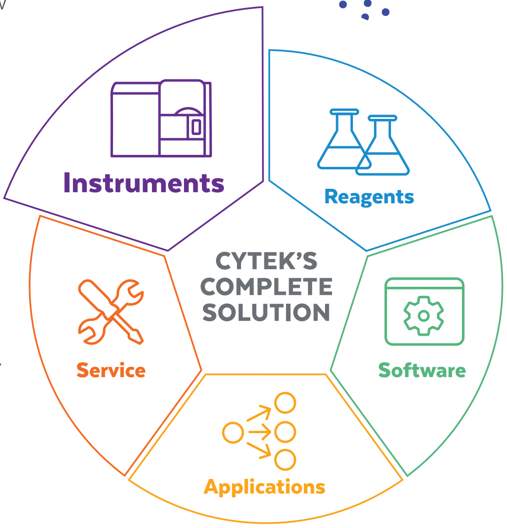

Cytek® Amnis® ImageStream®X Mk II Imaging Flow Cytometer

CYTEK®
TRANSCEND THE CONVENTIONAL
WWW.CYTEKBIO.COM

Contents

Further Reading and Resources:

Imprint

© Wiley-VCH GmbH,
Boschstr. 12,
69469 Weinheim, Germany

Senior Account Manager:
Joseph Tomaszewski

Editor:
Róisín Murtagh

Cover image: ©2024 Adobe Stock

Introduction

The relentless pursuit of innovation in medical science has given rise to a transformative approach in oncology research: imaging flow cytometry (IFC). This advanced technique represents the next generation of cancer investigation, merging the quantitative power of flow cytometry with the detailed spatial resolution of microscopy. In the intricate battlefield of oncology, where cellular anomalies give rise to complex diseases, the ability to scrutinize the inner workings of individual cells is paramount. IFC stands at the forefront of this effort, offering unprecedented insights that are propelling cancer research into a new era.

Why does resolution matter in this context? The answer lies in the heterogeneity of cancer cells. Traditional flow cytometry has been instrumental in analyzing millions of cells, providing valuable data regarding cell size, granularity, and protein expression. However, it lacks the capacity to capture the nuanced spatial information of cellular components, which can be critical in understanding the morphological changes that accompany malignant transformation. IFC fills this gap by delivering high-resolution images of each cell, allowing researchers to observe intricate details such as the organization of the cytoskeleton, nuclear shape, and the distribution of biomarkers across the cell surface. This level of detail is crucial for identifying subtle phenotypic changes that could signal the onset of cancer or the efficacy of a therapeutic intervention.

Furthermore, the synergy of image capture and flow cytometric analysis enables the examination of cell populations with a precision that was previously unattainable. It allows for the identification and characterization of rare cell types, such as circulating tumor cells (CTCs), which play a significant role in metastasis and are often present in extremely low numbers. The high-resolution imagery of these cells can uncover characteristics that might predict disease progression or response to treatment, thereby enhancing the personalization of cancer therapy.

The next generation of oncology research, empowered by imaging flow cytometry, is not just about observing cells, but about seeing them with clarity and understanding the complex language of their morphology. As we continue to unravel the molecular intricacies of cancer, the importance of resolution becomes ever more apparent. The detailed imagery provided by this technology is not just a window into the cell; it is a lens focusing on the future of oncology, where the minutiae of cellular structure could hold the key to groundbreaking discoveries and innovative treatments. Imaging flow cytometry, with its high-resolution capabilities, is thus an indispensable tool in the arsenal against cancer, transforming how we research, diagnose, and ultimately, combat this multifaceted disease.

This article collection begins with a study by Stanley *et al*. [1] that explored IFC as a novel approach for chromosomal analysis. Traditional methods such as karyotyping and fluorescent *in situ* hybridization (FISH) face analytical challenges, limiting their use in cytogenetics. IFC enhances these techniques by providing digital images alongside fluorescence intensity data, allowing direct visualization of chromosomes and FISH signals. This advancement has led to new methods for assessing chromosome number and structure in cells, with the added benefit of immunophenotyping to identify specific cells and chromosomal abnormalities. The high sensitivity and specificity of IFC particularly demonstrated in blood cancers, suggest significant potential for cytogenomic applications in diagnosis and disease monitoring.

Next, Durdik *et al*. [2] assessed cellular DNA damage with γH2AX pan-staining after ionizing radiation and compared IFC results with fluorescence microscopy (FM). IFC demonstrated superior detection capabilities, revealing dose-dependent pan-staining that FM could not fully detect. The researchers found that therapeutic doses of γ-rays, but not low doses, induced γH2AX pan-staining, and correlated well with the percentage of apoptic cells as measured by Annexin-V/7-AAD assay. The pan-staining occurred early in apoptosis and persisted through later stages. This study also found a correlation between apoptotic DNA fragmentation with cell viability. The efficacy of IFC was further validated in lymphocytes from breast cancer patients post-radiotherapy, indicating the potential for personalized radiosensitivity assessment.

A study by Yazdi *et al*. [3] focused on improving the delivery of small-interfering RNAs (siRNAs) for gene silencing in disease treatment. Novel lipid nanoparticles (LNPs) with pH-responsive lipoamino xenopeptide (XP) carriers were developed and demonstrated high efficiency in cellular uptake and gene silencing at low siRNA doses. These XPs, with unique topologies, enhanced endosomal escape, leading to successful *in vitro* and *in vivo* gene silencing. Notably, LNPs with LAF4-Stp1 XPs achieved targeted gene knockdown in liver endothelial cells and moderate gene silencing in hepatocytes in mice. Further optimization with click-modified ligands effectively silenced VEGFR-2 in tumor endothelial cells, indicating potential for targeted therapeutic applications.

Jesperson *et al*. [4] introduced a high-throughput IFC method for screening factors that influence cortical cell polarity (CCP) in melanoma cells, a key element in metastasis, which was supported by artificial intelligence analysis. This method is significantly faster, more accurate, and more reproducible than traditional manual quantification and can be adapted to assess additional cellular parameters. A pilot experiment with various drugs demonstrated the efficiency of the method in identifying how these drugs affect CCP. This new workflow paves the way for large-scale studies to uncover novel factors, both intrinsic and systemic, that regulate CCP and thereby control metastasis.

Finally, Rosenberg *et al*. [5] explored the use of IFC as an objective and standardized method for diagnosing myelodysplastic syndrome (MDS), which is often difficult due to the variable presentation of bone marrow dysplasia. Through analysis of a substantial number of erythroblasts from MDS patients, healthy donors, and controls, the study confirmed normal erythroid maturation patterns and identified aberrations in MDS, such as enlarged cell size and increased macronormoblasts. Machine learning algorithms helped identify a higher frequency of binucleated erythroblasts in MDS. The results suggest that IFC could significantly reduce inter-observer variability in MDS diagnostics, offering a promising tool for evaluating dysplasia.

We hope to educate researchers on advancements in imaging flow cytometry through the methods and applications presented in this article collection. To gain a deeper understanding of available options for advancing your research, we encourage you to visit Cytek Biosciences.

Róisín Murtagh
Senior Content Strategist at Wiley

References

[1] Stanley, J. *et al.* (2021). Analysis of human chromosomes by imaging flow cytometry. *Cytometry Part B - Clinical Cytometry.* https://doi.org/10.1002/cyto.b.22023.

[2] Durdik, M. *et al.* (2021). Imaging flow cytometry and fluorescence microscopy in assessing radiation response in lymphocytes from umbilical cord blood and cancer patients. *Cytometry Part A.* https://doi.org/10.1002/cyto.a.24468.

[3] Yazdi, M. *et al.* (2024). In Vivo Endothelial Cell Gene Silencing by siRNA-LNPs Tuned with Lipoamino Bundle Chemical and Ligand Targeting. *Small.* https://doi.org/10.1002/smll.202400643.

[4] Jespersen, J.H. *et al.* (2023). Analysis of cortical cell polarity by imaging flow cytometry. *Journal of Cellular Biochemistry.* https://doi.org/10.1002/jcb.30476.

[5] Rosenberg, C.A. *et al.* (2021). Exploring dyserythropoiesis in patients with myelodysplastic syndrome by imaging flow cytometry and machine-learning assisted morphometrics. *Cytometry Part B - Clinical Cytometry.* https://doi.org/10.1002/cyto.b.21975.

BACK TO CONTENTS

Received: 29 December 2020 | Revised: 18 April 2021 | Accepted: 14 May 2021
DOI: 10.1002/cyto.b.22023

REVIEW ARTICLE

CLINICAL CYTOMETRY WILEY

Analysis of human chromosomes by imaging flow cytometry

Jason Stanley[1] | Henry Hui[1] | Wendy Erber[1,2] | Britt Clynick[3] | Kathy Fuller[1]

[1]Translational Cancer Pathology Laboratory, School of Biomedical Sciences, The University of Western Australia, Crawley, Western Australia, Australia

[2]PathWest Laboratory Medicine, Nedlands, Western Australia, Australia

[3]Institute for Respiratory Health, Harry Perkins Institute of Medical Research, Nedlands, Western Australia, Australia

Correspondence
Kathy Fuller, School of Biomedical Sciences (M504), The University of Western Australia, 35 Stirling Highway, Crawley, WA, 6009, Australia.
Email: kathy.fuller@uwa.edu.au

Abstract

Chromosomal analysis is traditionally performed by karyotyping on metaphase spreads, or by fluorescent in situ hybridization (FISH) on interphase cells or metaphase spreads. Flow cytometry was introduced as a new method to analyze chromosomes number (ploidy) and structure (telomere length) in the 1970s with data interpretation largely based on fluorescence intensity. This technology has had little uptake for human cytogenetic applications primarily due to analytical challenges. The introduction of imaging flow cytometry, with the addition of digital images to standard multi-parametric flow cytometry quantitative tools, has added a new dimension. The ability to visualize the chromosomes and FISH signals overcomes the inherent difficulties when the data is restricted to fluorescence intensity. This field is now moving forward with methods being developed to assess chromosome number and structure in whole cells (normal and malignant) in suspension. A recent advance has been the inclusion of immunophenotyping such that antigen expression can be used to identify specific cells of interest for specific chromosomes and their abnormalities. This capability has been illustrated in blood cancers, such as chronic lymphocytic leukemia and plasma cell myeloma. The high sensitivity and specificity achievable highlights the potential imaging flow cytometry has for cytogenomic applications (i.e., diagnosis and disease monitoring). This review introduces and describes the development, current status, and applications of imaging flow cytometry for chromosomal analysis of human chromosomes.

KEYWORDS
chromosome, chronic lymphocytic leukemia, del(17p), FISH, fluorescence in situ hybridization, imaging flow cytometry, immunophenotyping

1 | INTRODUCTION

Chromosomal analysis plays a pivotal role in the assessment and understanding of cellular biology in health and disease. Since first introduced in the 1950s, a range of methods has been utilized to assess chromosomes in the life sciences and human disease (Ferguson-Smith, 2015; Hsu, 1952; Tjio & Levan, 1956). This includes using cell cultures and colchicine followed by chromosome banding methods. Chromosome size, type and shape can be determined and defects in constitutional disorders and malignancies (i.e., leukemia, lymphoma) identified (Martin & Warburton, 2015; O'Connor, 2008). These include changes in chromosome number (aneuploidy) such as whole chromosome loss (e.g., monosomy) or gain (e.g., trisomy) (Ferguson-Smith, 2015). Structural alterations, such as translocations between chromosomes, inversions, insertions, rings, deletions, isochromosomes, and duplications, can also be identified. Other methods were subsequently introduced including fluorescent in situ hybridization (FISH), chromosome painting and comparative genomic hybridization. FISH is a molecular-based method that utilizes hybridization of fluorescent-labeled probes to complementary DNA sequences to detect a specific region on a chromosome (Carter, 1994; Guo et al., 2014; Sinclair, 2002; Weiss et al., 1999). FISH is typically performed on metaphase spreads and interphase cells, including on tissue sections, on a slide, to detect numerical or structural alterations, and assessed by fluorescent microscopy (Cui et al., 2016; Van Der Logt et al., 2015). Flow cytometry was first applied to analyze chromosomes in the mid-1970s (Gray, Carrano, Moore, et al., 1975; Gray, Carrano, Steinmetz, et al., 1975; Stubblefield et al., 1975). Although not widely applied in human disease, it did offer rapid and high-throughput analysis as well as the ability to flow sort chromosomes. Subsequent developments in flow cytometric instrumentation, in particular the addition of digital cameras and visual imagery, is now leading to a reawakening of flow cytometry for the analysis of chromosomes (Figure 1). The new instrumentation is now being applied to assess ploidy and structural chromosome changes using FISH probes. Such is the capability of this new technology that it has been described as an "unexplored frontier" in cytogenomics and the molecular testing of cytological samples (Weissleder & Lee, 2020). In this review, the development and current status of imaging flow cytometry for chromosomal analysis in human disease are presented.

2 | FLOW CYTOMETRY FOR CHROMOSOME ANALYSIS

Flow cytometry of chromosomes in suspension is a high-throughput, rapid and accurate method to assess chromosome number and structure (Gray, Carrano, Moore, et al., 1975; Gray, Carrano, Steinmetz, et al., 1975; Stubblefield et al., 1975). It has been applied for karyotyping, FISH analysis of telomeres and centromeres, as well as chromosome sorting for downstream analysis. Although neither flow karyotype nor flow FISH has been widely adopted for analysis of human chromosomes, an overview of each technique is presented to give some background to the field (Stepanov et al., 1996).

2.1 | Karyotyping

Flow karyotyping, pioneered by Gray et al. was the first chromosomal analytical technique developed for flow cytometry (Gray, Carrano, Moore, et al., 1975; Gray, Carrano, Steinmetz, et al., 1975). This technique enabled the detection of metaphase chromosomes in suspension by utilizing two DNA stains: Hoechst 33342 (HO) and Chromomycin A3 (CA3), which bind to the A-T rich and G-C rich regions of the DNA respectively (Chazotte, 2011; Zihlif et al., 2010). Subsequent improvements in instrumentation and DNA dyes allowed better discrimination between chromosomes (e.g., 4′,6-diamidino-2-phenylindole [DAPI], HO, CA3, and propidium iodide) resulting in the ability to separate chromosome 9 from the chromosome 9–12 cluster (Ng et al., 2019). However, it is still not possible to clearly

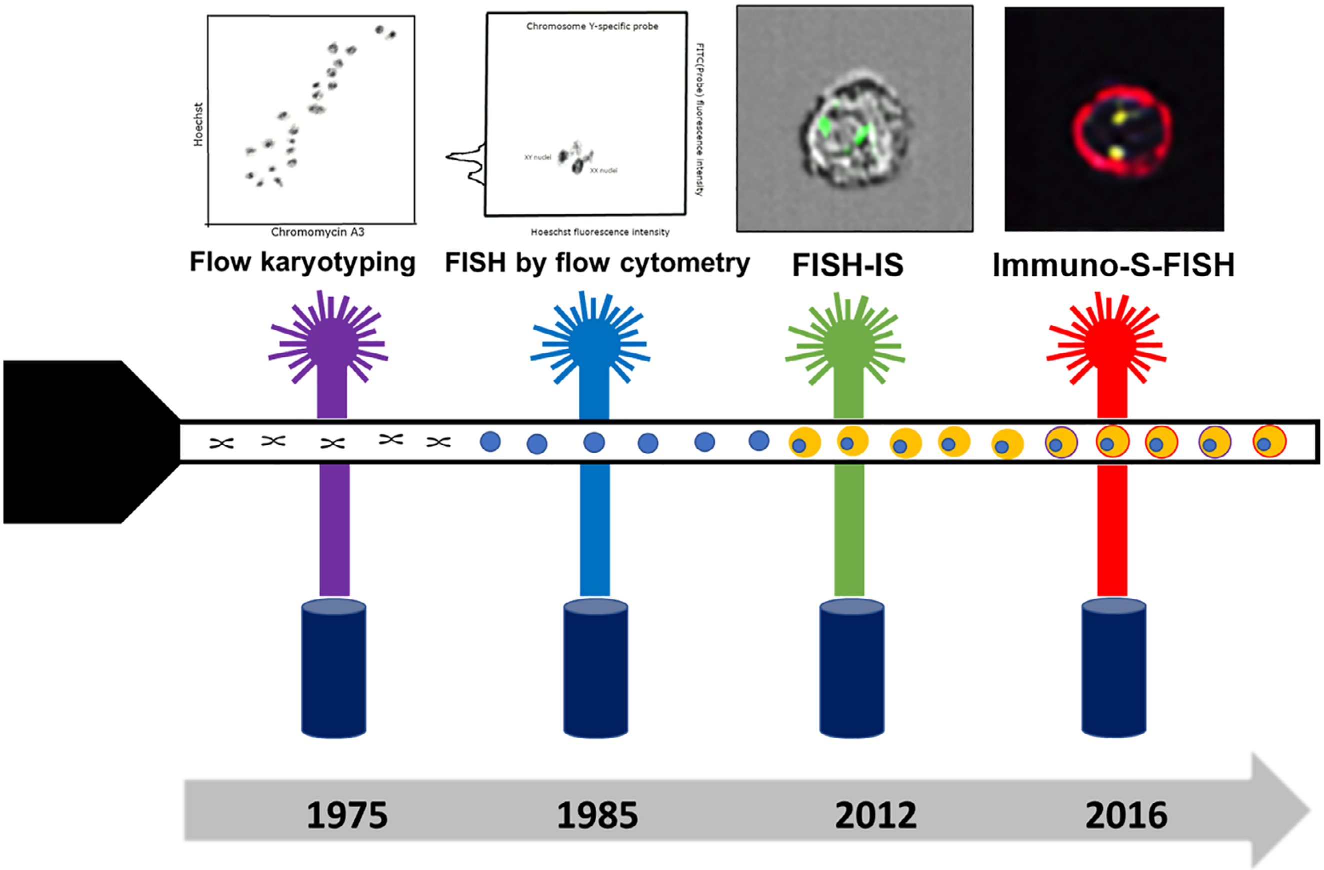

FIGURE 1 Major milestones in the development of chromosomal analysis by flow cytometry

separate all chromosomes with chromosomes 10–12 forming a cluster, due to their similarity in size and base pair composition (Langlois et al., 1982; Ng et al., 2019). Chromosomes are assessed for the fluorescence profile and abnormalities detected by deviations compared to normal (Gray et al., 1988). Numerical changes are seen as changes in the volume or bivariate mean of each peak, whereas translocations cause changes in the DNA composition of chromosomes resulting in the presence of a new peak (Gray et al., 1988; Lebo et al., 1986). Flow karyotyping can be performed on standard high throughput flow cytometers (e.g., BD LSRFortessa and Beckman Coulter MoFlo Legacy) (Ng et al., 2019). It is not widely utilized to study human disease but is applied to animal and plant cells (Frohlich et al., 2017; Popescu et al., 1993; Schmitz et al., 1998; Stanyon & Stone, 2008).

2.2 | FISH

Flow cytometers have also been used to analyze specific chromosomes and regions, including centromeres and telomeres, using FISH probes. Flow FISH is primarily performed on isolated chromosomes or nuclei of cells in interphase, but can also be achieved on preserved intact cells (Keyvanfar et al., 2012). The FISH probes used generally bind to the centromeres by hybridizing to specific alpha satellite sequences of individual chromosomes (Arkesteijn et al., 1995; Trask et al., 1985; Trask et al., 1988; van Dekken et al., 1990). Changes in the fluorescence intensity emitted by the probe can identify abnormalities in the number of chromosomes (Brind'Amour & Lansdorp, 2011; Keyvanfar et al., 2012). For example, a chromosome gain (e.g., trisomy) increases the fluorescence intensity compared to normal due to the presence of an extra chromosome; whereas with a chromosome loss (monosomy) there is a decrease. Examples of the clinical applicability have been demonstrated for the analysis of chromosomes 1, 8, and Y in leukemia (Arkesteijn et al., 1995).

Telomeres and their length have also been studied by flow cytometry by measuring the fluorescence of the labeled peptic nucleic acid (PNA) probe (Alder et al., 2018; Aubert et al., 2012; Baerlocher et al., 2006). PNA probes differ from conventional DNA FISH probes, by having different underlying chemistry, allowing them to bind more readily to complementary nucleic acid sequence and with higher affinity (Genet et al., 2013). Telomere flow FISH also generates an intensity value which represents relative but not absolute telomere length. Using reference samples of known telomere length and calibration controls allows this data to be used to calculate approximate telomere length. (Rufer et al., 1998; Wand et al., 2016). Telomere flow FISH has been applied clinically to detect shortened telomeres. These can be due to inherited mutations resulting in decreased telomere length and causing accelerated aging (Armando et al., 2019; Mangaonkar & Patnaik, 2018; Stanley & Armanios, 2015).

2.3 | Chromosome sorting

Fluorescence-activated cell sorting, introduced in the mid-1970s, can be used to isolate chromosomes with high yield and purity (Gray, Carrano, Moore, et al., 1975; Gray, Carrano, Steinmetz, et al., 1975). The ability to generate a large number of chromosomes has led to the widespread use of this technique in understanding DNA. The principle relies on the ability to generate droplets containing the chromosomes of interest. The instrument adds a charge to the droplets containing the desired chromosomes, which are then deflected in a static electric field into a collection vessel. The collected chromosomes can then be processed with other downstream techniques for further investigation (Doležel et al., 2011; Ibrahim & Van Den Engh, 2004). Flow sorting of chromosomes has been utilized in the preparation of genomic libraries, chromosome paints, mapping of genetic markers and was crucial in the early stages of the “Human Genome Project” (Ibrahim & Van Den Engh, 2004; Monard, 2016; Van Dilla et al., 1986; Van Dilla & Deaven, 1990). In addition to application in human disease research, flow karyotyping and sorting has been crucial to isolate and understand the chromosomes of plants and animal (Doležel et al., 2021; Yao et al., 2020). Yao et al., 2020 have shown the effectiveness of flow karyotyping and sorting in isolating complex chromosomes of sheep prior to sequencing. This approach has then been applied to study chromatin conformation, BAC library construction, optical mapping and sequencing amplified chromosomal DNA of plants (Doležel et al., 2021).

3 | IMAGING FLOW CYTOMETRY: PRINCIPLES

Imaging flow cytometers were first reported in the late 1970s. These used slit scanning flow cytometry, strobed illumination techniques, and flying spot scanning (Cambier et al., 1979; Kachel et al., 1979; Kay et al., 1979). Further developments in instrumentation have led to the incorporation of digital image capture combined with standard high-throughput flow cytometry capability (Barteneva et al., 2012; Basiji et al., 2007). The inclusion of imagery brings a new dimension to the analysis of chromosomes, as will be described. There are a number of imaging flow cytometry instruments available or in development, such as the Amnis ImageStream^{X} markII, Amnis FlowSight, Sysmex MI-1000, spectral resonance modulator (SRM) flow cytometer, and virtual-freezing fluorescence imaging flow cytometer (Basiji et al., 2007; Huang et al., 2016; Mikami et al., 2020). Instrument configuration varies in the number of lasers (presently up to 6), fluorescence channels and the method of image and fluorescence capture. The types of imaging technologies include:

1. Camera based imaging device which utilizes either charged couple device (CCD) or complementary metal-oxide semiconductor, for example, ImageStreamX (Basiji et al., 2007) and virtual freezing imaging flow cytometry (Mikami et al., 2020).
2. Photomultiplier (PMT) tube-based imaging device which utilizes PMT combined with a technique named spatial–temporal transformation, for example, 3D imaging flow cytometry (Han & Lo, 2015).

This review will focus on imaging flow cytometry utilizing CCD, specifically the Amnis ImageStream^X, as this has been most commonly reported for the analysis of human chromosomes.

Key components of the Amnis ImageStream^X are image magnification, extended depth of field and digital cameras. The microscope objectives in the device, commonly ×20, ×40, and ×60, give the operator the option to determine the degree of magnification required to identify the cell and chromosome of interest. Reports indicate for chromosome applications, both the ×40 and ×60 objectives enable high resolution analysis of the probe signal (Hui et al., 2019; Minderman et al., 2012; Sanderson & Simon, 2017). The "extended depth of field" (EDF) functionality is another key feature required for chromosome analysis. EDF incorporates a specialized element in the standard optical system that causes light from widely different focal positions in the object to be imaged and in focus on the detector plane simultaneously, a process called Wavefront Coding™ (Ortyn et al., 2007). Wavefront coding uses a special optical element near the aperture stop which makes the imaging system insensitive to a range of mis-focus related aberrations thereby extending the depth of field of the system. Images acquired using EDF have an effective depth of field of approximately 15 μm with all cellular components, even as small as 2 μm, in precise focus. This results in a high-resolution image of the cell as well as all cellular features simultaneously in focus (Basiji et al., 2007). This is especially important when analyzing large cells as the standard image focal plane is set to the center of the core stream however the part of the cell that is of interest (e.g., nucleus) may be at the front or back of the stream therefore appearing out of focus.

The digital cameras in the imaging flow cytometer capture images of all cells. There are different camera types, including CCD with time delay integration (TDI) and beam scanners with a scientific complementary metal-oxide semiconductor camera (Basiji & O'Gorman, 2015; Mikami et al., 2020). TDI works by accumulating multiple continuous exposures of a moving object at a rate that is synchronized with the motion of the object. By combining it with a CCD camera it produces an effect that is akin to panning the camera to track the object. The outcome is that CCD-TDI cameras allow cell images to be collected while in motion and without streaking (Basiji, 2016). The need to achieve synchrony and alignment between the motion of the object and the read-out rate of the camera does however hinder the capacity to integrate sorting capabilities (Han et al., 2016).

A number of software tools can be used to facilitate analysis of the digital images. First, "masks", or specified regions within the cell of interest, can be selected and digitally "isolated" (Figure 2) (Dominical et al., 2017). These masks are akin to "gates" which are applied to interrogate a specific part of an object of interest on the digital images. For chromosomal analysis, masks have been used to target the cell nucleus or FISH probe signals and further evaluation is restricted to this selected cellular region. This makes the creation of accurate masks the cornerstone for image-based analysis; suboptimal masks can lead to other parts of the cells, that are not of interest, being evaluated (Dominical et al., 2017). Once a mask is determined, parameters within that area of interest can be assessed. For example, the localization, enumeration, size, shape, and fluorescence intensity of an object such as a chromosomal signal can be interrogated. It is this combination of in-focus digital images and ability to isolate a specific cell region of interest, that makes chromosomal analysis by imaging flow cytometry possible (Figure 2) (Hui et al., 2018).

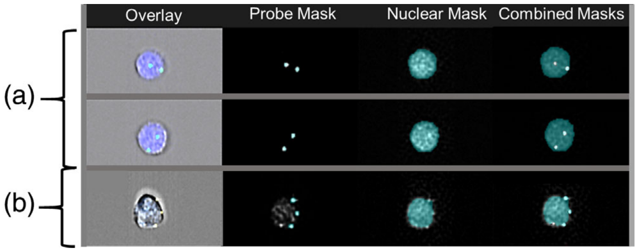

FIGURE 2 Imaging flow cytometry galleries showing image analysis of cells, their nuclei and FISH probe hybridization (×60 magnification). (a) Two cells with specific hybridization with the probe colocalised to the nucleus, as shown with the "Combined Masks". (b) A cell with nonspecific hybridization. The FISH probe signal is outside and not overlying the nucleus

4 | CHROMOSOME ANALYSIS BY IMAGING FLOW CYTOMETRY

The application of imaging flow cytometry to study chromosomes on cells in suspension was pioneered by Minderman et al. (2012). Termed "FISH in solution" (FISH-IS), they showed that the number of copies of chromosomes X, Y and 8 in normal leucocytes and leukemic cells could be determined using centromeric FISH probes. The method they used required initial cell fixation, exposure to high temperature to denature double stranded DNA, followed by hybridization of the FISH probes to the complementary DNA sequence. DAPI stain was applied to highlight cell nuclei and a minimum of 20,000 cells acquired in the imaging flow cytometer. IDEAS software was used for evaluation of single cells in focus with bound FISH probe based on brightfield image analysis and probe fluorescence intensity. Masking of FISH signals ("spots") was achieved by utilizing the software image analysis features to identify the centromeric FISH probe fluorescence signals. Accuracy of the masks applied was confirmed by manually visualizing the generated images from the digital cameras. The software was then able to enumerate the number of probes in each cell providing the overall spot count profiles (Figure 3). The capacity to interrogate FISH probe spots based on combined morphology and fluorescence features on tens of thousands of cells improved the sensitivity and utility of this technique.

Minderman et al. then used fluorescence intensity measurements to take into account heterogeneity of FISH hybridization (e.g., due to incomplete saturation or asynchronous replication of sequences) and the possibility of overlapping FISH spots. This was to distinguish between the possibility of two aligned FISH signals being misinterpreted as monosomy due to the presence of a single spot on the imagery. This verification method was shown to be important as it

BACK TO CONTENTS

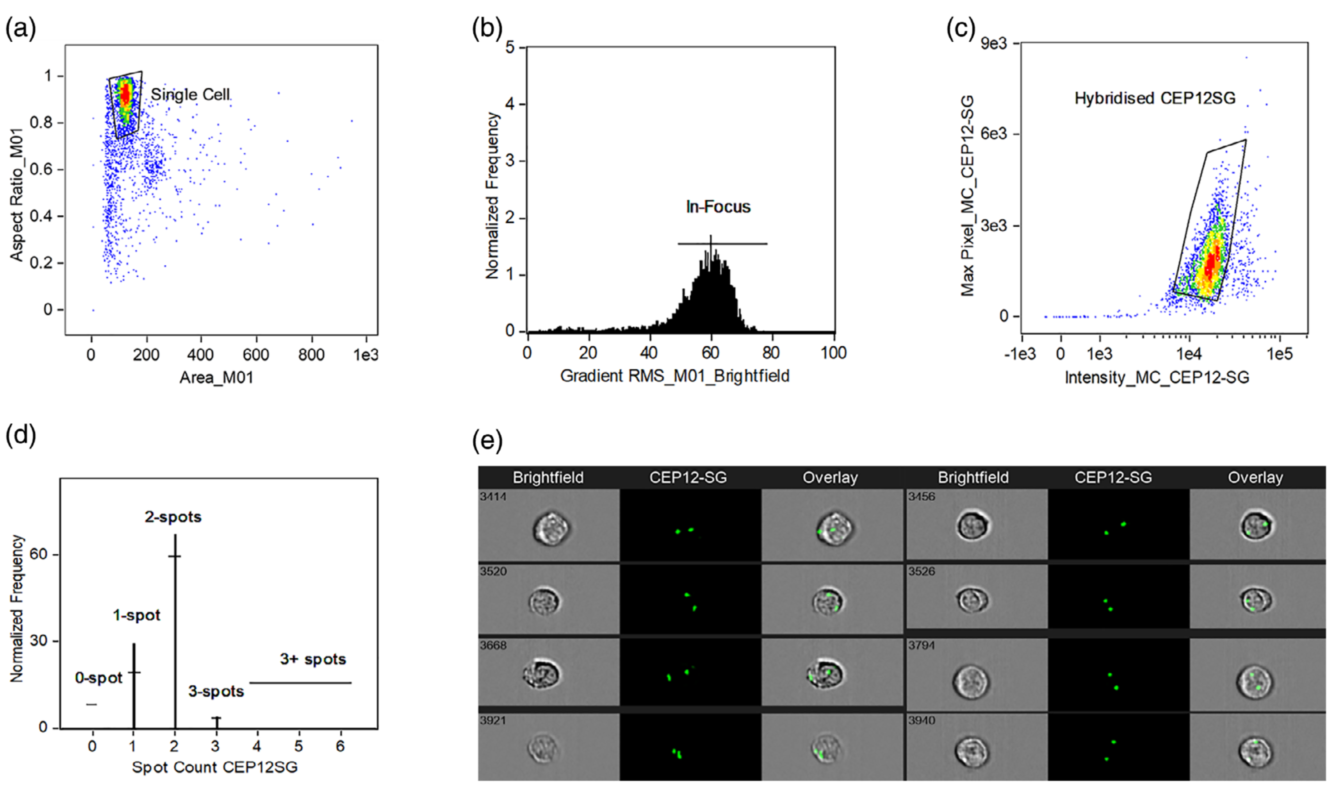

FIGURE 3 Analysis of chromosome 12 in a normal blood. (a–c) The sequential gating strategy used to generate FISH data (d, e) using IDEAS software. (a) Single cells are identified using area and aspect ratio. (b) In focus events are selected based on high gradient root mean square (RMS) value of the brightfield image. (c) Intensity versus max pixel of the probe channel identifies cells with signals from hybridized CEP12 probe. (d) Spot count profile for the selected cells. (e) Cells with dual CEP12 probe signals (×60 magnification).
Source: Adapted from Minderman et al., 2012

was estimated there is at least 12.4% chance of overlapping signals for each FISH probe; further, this would increase with additional probes used (Minderman et al., 2012). Two overlapping spots gave twice the mean fluorescence intensity of a "real" single FISH signal (Figure 4). Cases of trisomy with a true third FISH signal would have 1.5× the fluorescence of true disomy (2n). By assessing the mean fluorescence intensity of FISH "spots", the authors were able to detect monosomy, disomy, and trisomy for the chromosomes studied. This was accurate in detecting genetic aberrations with a sensitivity of 1% based on 20,000 cells analyzed and had high correlation ($R^2 = 0.99$) with standard FISH (Minderman et al., 2012). However, at levels below 1% there was an increase in false positive rates requiring for the manual inspection of the selected population.

5 | CHROMOSOME ANALYSIS IN IMMUNOPHENOTYPED CELLS

The next development was the incorporation of immunophenotyping to identify the cell of interest. This technique, developed by Fuller et al., was shown to increase precision by ensuring chromosomes were only assessed in cells with a specific antigenic profile (Fuller et al., 2016). Termed "Immuno-S-FISH" this method required no prior cell separation or isolation and could detect FISH probe signals in specific cell types identified by the phenotypic profile. Evaluated on normal lymphocytes, this method could detect chromosome 1, using a centromeric probe, in >90% of normal T and B lymphocytes identified with CD3 and CD19 antibodies (Figure 5).

In this seminal work, Fuller et al. demonstrated the importance of preserving cellular integrity, including the surface membrane antigens, while ensuring FISH probes could access nuclear material and hybridize to denatured DNA. This posed several challenges as optimal FISH conditions are damaging to cell structure, antigens and the antibody fluorescent signal. They highlighted the importance of cell phenotyping with fluorescent-conjugated antibodies being performed prior to FISH; reversing the order resulted in increased nonspecific antibody binding to the cells. To preserve the antibody-fluorochrome conjugate, an amine cross-linker was required to stabilize the antibody–antigen complex on the cell membrane prior to commencing the FISH process. The amine cross-linker *bis*(sulfosuccinimidyl)suberate (BS3) is a noncleavable, membrane-impermeable and water-soluble cross-linking agent. BS3 is commonly used to cross-link cell surface proteins in order to identify near-neighbor protein relationship and ligand-receptor interaction by stabilizing the protein-to-protein complexes (Suchanek et al., 2005). Fuller et al. found that when used after antibody staining BS3 can preserve immunophenotyping throughout acid incubation and the high temperatures required for FISH (Fuller et al., 2016). A post-phenotyping fixation step (4% formaldehyde) was then used to preserve cellular integrity while

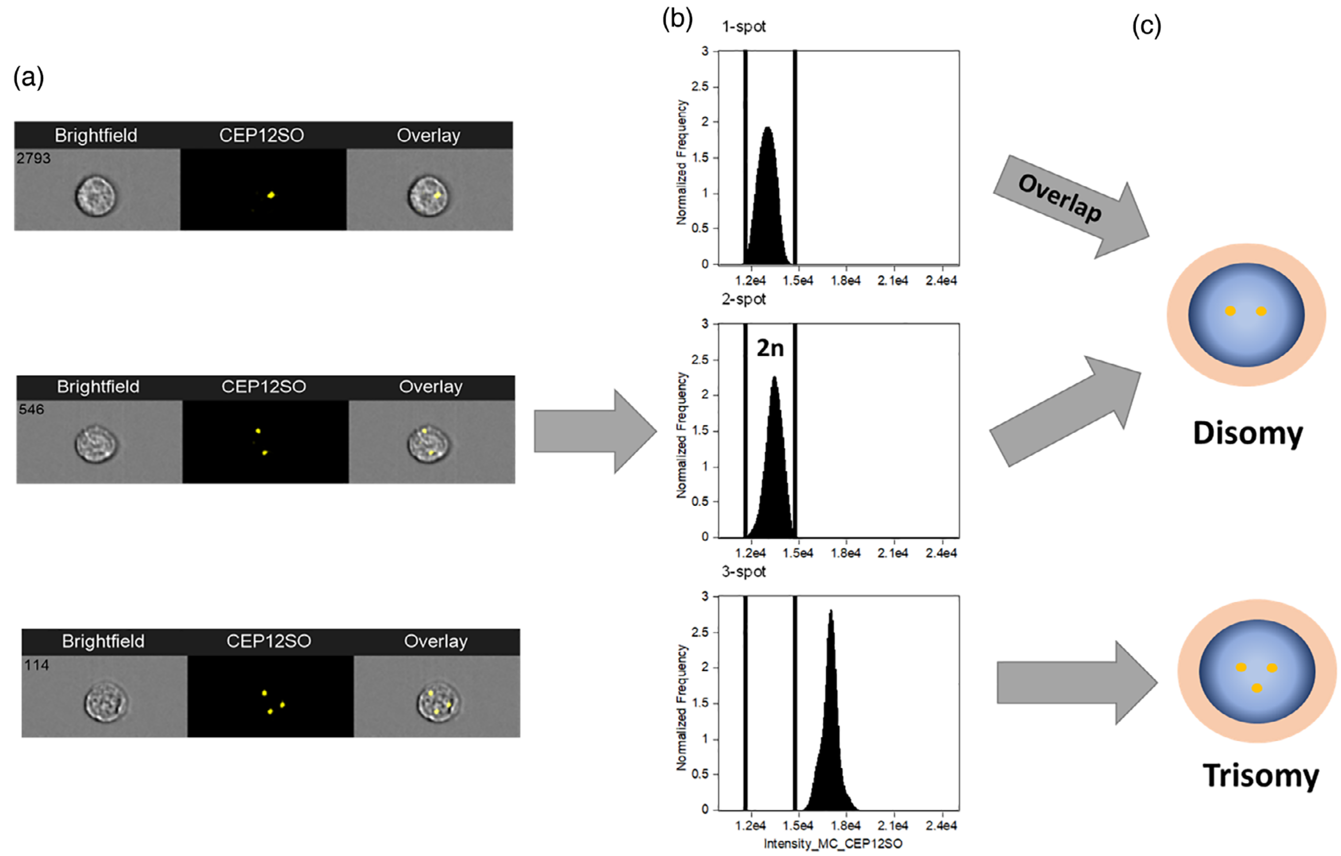

FIGURE 4 Fluorescence verification of probe spot counts for CEP12. (a) Cells hybridized with CEP12 categorized as having one spot (cell 2793), two spots (cell 546), or three spots (cell 114). (b) Histograms showing CEP12 fluorescence Intensity. The intensity of cells with two CEP12 spots are gated (2n) and this gate was applied to the one-spot and three-spot populations. (c) Fluorescence adjustment verification shows most of the 1-spot population have two overlapping probe signals. Cells with additional chromosomal material (e.g., trisomy) have higher fluorescence intensity than 2n of disomic cells (×60 magnification)

retaining sufficient immunophenotyping fluorescent signal for detection. Alternate fixatives, such as Carnoy's solution, were found to be less suitable as they caused shedding of some antibodies and/or quenching of the fluorophore signal.

FISH probe hybridization was performed after antibody labeling, cross-linking and fixation; the method used bore similarities to those developed by others. However, Fuller et al. found that an additional acid incubation step was necessary to promote denaturation of double-stranded DNA and allow probe hybridization to the complementary DNA sequence. Their protocol also included a cell membrane permeabilisation step with a nonionic detergent to allow probes to enter the DNA with minimal cellular structure disruption. FISH probes were then added and after overnight hybridization, samples were stained with a nuclear marker prior to analysis.

To evaluate the chromosomes, Fuller et al. gated in focus, single and nondividing cells (based on nuclear marker intensity) and used the "Spot Count" feature to count the number of probe "spots" per cell using the FISH probe fluorescence mask. This calculation analyses the pixel intensity of the probe spots to cell background ratio, the radius of the spots and the intensity of the probe fluorescence (Figure 5). The spot count profile was then verified and, by fluorescence intensity adjustment accounting for overlapping spots (as described by Minderman) and nonspecifically hybridized probes, an adjusted spot count result was generated. The data was presented as the number and percent of all cells, and those with the phenotype of interest, with the specific chromosomal change.

This principle of simultaneous assessment of chromosomes and phenotype had already been established in tissue pathology. "FICTION" ("fluorescence immunophenotyping and interphase cytogenetics as a tool for the investigation of neoplasms") and immunoFISH are both methods used on sections of fixed tissue to assess FISH in immunophenotyped cells (Mattsson et al., 2007; Weber-Matthiesen et al., 1992, 1993, 1995). Immuno-S-FISH also assesses chromosomes by FISH in immunophenotyped cells. The differences are the starting material is fresh (i.e., blood samples), many thousand intact whole cells are evaluated, the analysis is automated on an imaging flow cytometer and numerical data as well as imagery is generated.

5.1 | Applications to blood cancers

The first demonstration of the use of FISH on immunophenotyped human cancer cells using imaging flow cytometry was published in

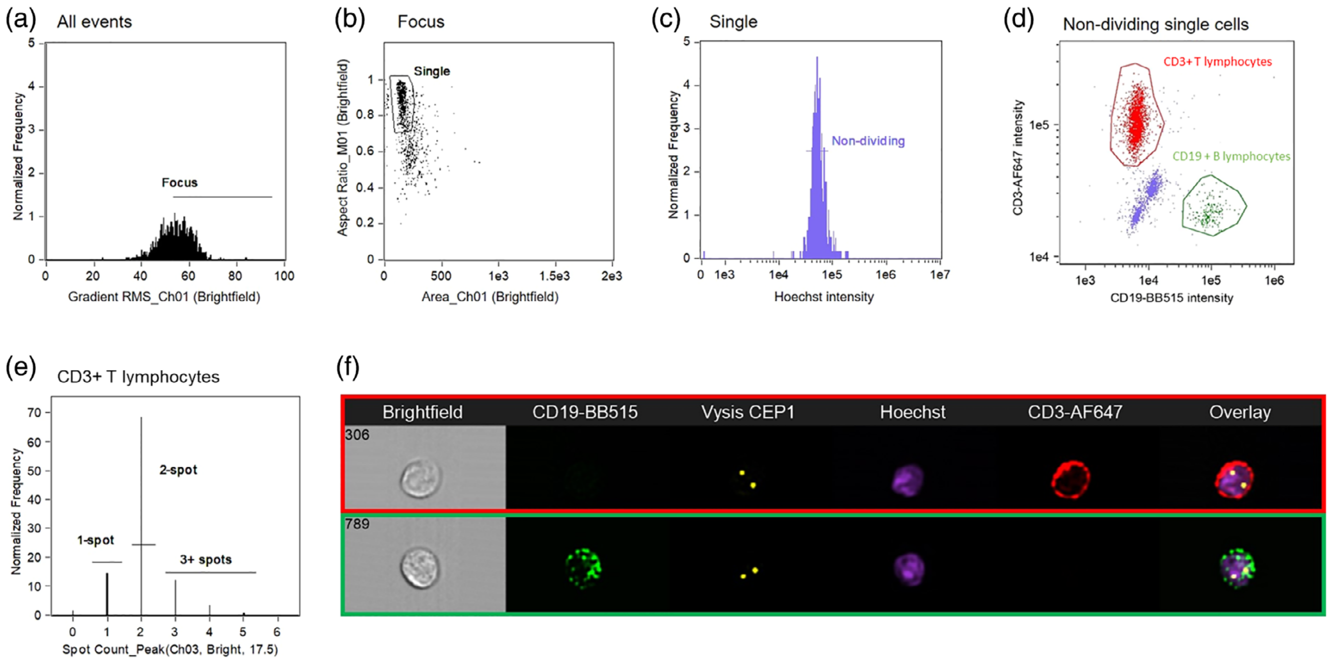

FIGURE 5 Immuno-S-FISH analysis of normal blood demonstrating CEP1 probe hybridization. (a) Cells were gated for those in focus based on high root mean square (RMS) gradient value of the brightfield image. (b) Single cells were selected based on a scatter plot of Aspect Ratio versus Area. (c) A fluorescence histogram of Hoechst 33342 used to select for nondividing cells. (d) Surface antigen expression of CD19-BB515 and CD3-AF647 was used to identify T and B lymphocytes. (e) Spot count histogram of the T lymphocytes generated using the "peak" mask. (f) Galleries of a T (cell 306) and B lymphocyte (cell 789) with two FISH spots for the centromere of chromosome 1. Overlay images are a merge of cell surface immunophenotype, CEP12 probe and Hoechst (×60 magnification).
Source: Data was based on 20,000 cells analyzed. Adapted from Fuller et al., 2016

2018 (Hui et al., 2018). Both numerical and structural chromosomal changes have now been reported for the blood cancers, chronic lymphocytic leukemia (CLL) and plasma cell myeloma (Erber et al., 2020; Hui et al., 2018; Hui et al., 2019). Immuno-S-FISH was refined to improve the percent analyzable cells, range of detectable antigens, suitable FISH probes (e.g., locus specific) and an expanded fluorophore repertoire. The resulting protocol, called "immuno-flowFISH", has been studied for trisomy 12 and micro-deletions of 17p (del(17p)), two prognostically significant abnormalities, in CLL. Utilizing a phenotypic panel to identify CLL cells in blood samples, and the CEP12 centromeric probe, Hui et al. were able to identify trisomy 12 in CLL cells and distinguish these from T and B lymphocytes (Figure 6). Up to 20,000 cells were acquired and the number of cells with trisomy 12 ranged from as few as 26 to 9000 (0.1–46% of CLL cells). In the digital images, three CEP12 FISH spots could be seen in the CLL population, and two spots in the normal T and B lymphocytes. The ratio of spot counts comparing the CLL with normal lymphocytes was shown to be a useful mathematical tool to screen for trisomy 12. Called a "spot count ratio", this utilized the quantitative data from the software and calculated as follows:

$$\text{Spot count ratio} = \frac{\text{Mean spot count CLL cells}}{\text{Mean spot count normal T lymphocyte}}$$

A chromosomal gain in the CLL cells, gave a ratio that exceeded one, whereas with a normal result the ratio was one (Figure 6). An abnormal ratio could then be verified by assessing the imagery of individual cells. Since 20,000 cells were captured, the data for this ratio was found to be robust and a useful indicator for the presence of an abnormality within the CLL cells.

The 17p locus, a critical region of study because of *TP53*, has also been assessed by immuno-flowFISH in both CLL (blood) and plasma cell myeloma (bone marrow) (Erber et al., 2020; Hui et al., 2019). Deletion of 17p is predictive of poor prognosis in both malignancies, and treatment decisions are based on the presence of this chromosomal defects (Avet-Loiseau et al., 2007; Döhner et al., 2000). For CLL, analysis was with a 3-antibody panel and 2 FISH probes (17p12 and chromosome 17 centromeric probe [CEP17]) (Figure 7). The FISH probe fluorophores used were SpectrumGreen and OrangeRed, with emission spectra of 524 and 565 nm, respectively. Careful choice of antibody fluorophores was required as the standard channels were utilized by the FISH probes, leaving only channels suitable to tandem dyes available. Most protein-based tandem dyes (e.g., PECy5, PECy7, and APCCy7) were found to be unsuitable for Immuno-S-FISH and Immuno-flowFISH analysis. In contrast, synthetic polymer-based tandem dyes (e.g., BV480, BV605) were able to withstand the low pH and high temperature conditions required for optimal FISH hybridization (Fuller et al., 2016; Hui et al., 2018). For plasma cell myeloma, two antibodies (CD38 and CD138) were used to identify plasma cells (Figure 7). CEP17 was included as an internal numeric control to ensure diploid chromosome 17 signals. This would mean that if there

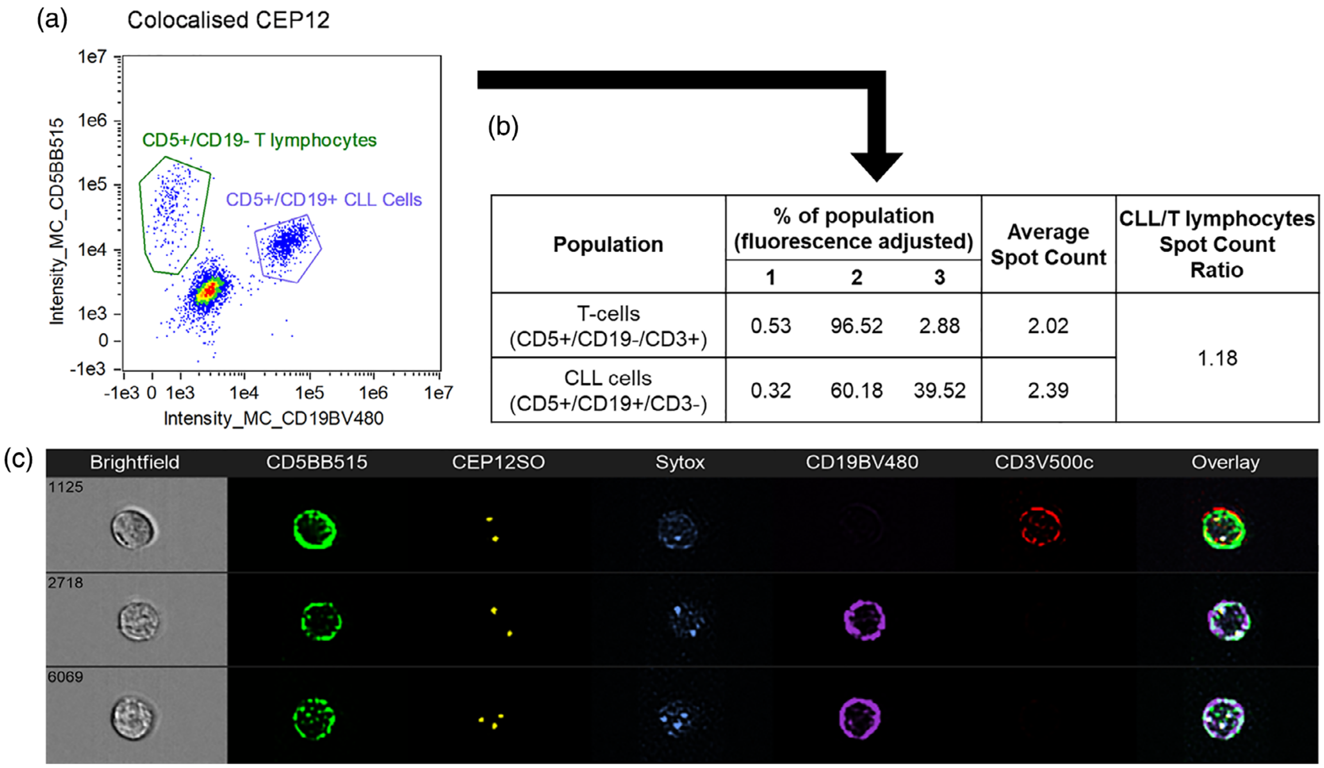

Population	% of population (fluorescence adjusted)			Average Spot Count	CLL/T lymphocytes Spot Count Ratio
	1	2	3		
T-cells (CD5+/CD19-/CD3+)	0.53	96.52	2.88	2.02	1.18
CLL cells (CD5+/CD19+/CD3-)	0.32	60.18	39.52	2.39	

FIGURE 6 Immuno-flowFISH for CEP12 in CLL. (a) Gating of CLL cells by CD19+/CD5+ and T lymphocytes by CD19−/CD5+. (b) Spot count ratio comparing CLL with the T lymphocytes. The ratio of 1.18 indicates additional copies of chromosome 12 in the CLL cells. (c) Digital images confirmed the presence of trisomy 12 (+12) as shown in cell 6069 with three CEP12 signals. Trisomy 12 was seen in 40% of the CLL cells. Another CLL cell (cell 2718) and a normal T lymphocyte (cell 1125) with normal CEP12 two-spot pattern are shown (×60 magnification).
Source: Data was based on 20,000 cells analyzed. Adapted from Hui et al., 2019

was only one spot for the "test" probe (17p12), that it was due to loss of this region of the chromosome and not monosomy.

Del(17p) could be detected in both CLL and myeloma plasma cells, as identified by their phenotype (Figure 7). The number and percent CLL cells with del(17p) ranged from 270–35,441 cells (2–35% of CLL cells) with a limit of detection of 0.4% of all cells in the sample. For myeloma, del(17p) was detected in 2340–2964 plasma cells (13–19%), giving a limit of detection of 1% of cells (Erber et al., 2020). These impressive data suggest that with further validation, immuno-flowFISH may prove to be more sensitive than traditional FISH-on-a-slide which has a reportable positive cut-off of 5–7%. If confirmed, immuno-flowFISH could potentially be used to monitor residual disease following therapy (e.g., autologous transplantation for myeloma).

5.2 | Application to telomeres

Telomere length has also been assessed by imaging flow cytometry by integrating FISH with antibody-based immunophenotyping for a range of other cell types such as HeLa cells and normal blood mononuclear cells (Figure 8) (Sanderson & Simon, 2017). These authors used a number of fluorophore-conjugated antibodies (including CD27, CD19, CD45RA, IgM, CD38, and CD8). Telomere detection was carried out by hybridizing unfixed cells with PNA-FITC probe and a total of 30,000 events were collected on ImageStream 100 or ImageStream^X markII flow cytometers. Similar to the previously described analyses, specific cell types identified by their phenotype were analyzed for telomere expression. The study by Sanderson et al. emphasized that image-based analysis of telomere length can provide a better correlation of telomeric length with age than fluorescence intensity measurements alone. The addition of immunophenotyping now also enables telomere length to be determined by using a spot count per cell rather than traditional intensity only.

6 | ATTRIBUTES OF IMAGING FLOW CYTOMETRY FOR CHROMOSOMAL ANALYSIS

Imaging flow cytometry, particularly incorporating immunophenotyping, has already shown to have potential for the assessment of chromosomes in human disease. Attributes of imaging flow cytometry for chromosomal analysis are:

1. the high number of cells that can be analyzed increasing sensitivity
2. there is no need for any pre-analytical cell isolation or sorting
3. high-throughput and high quantity analysis of whole cells in suspension

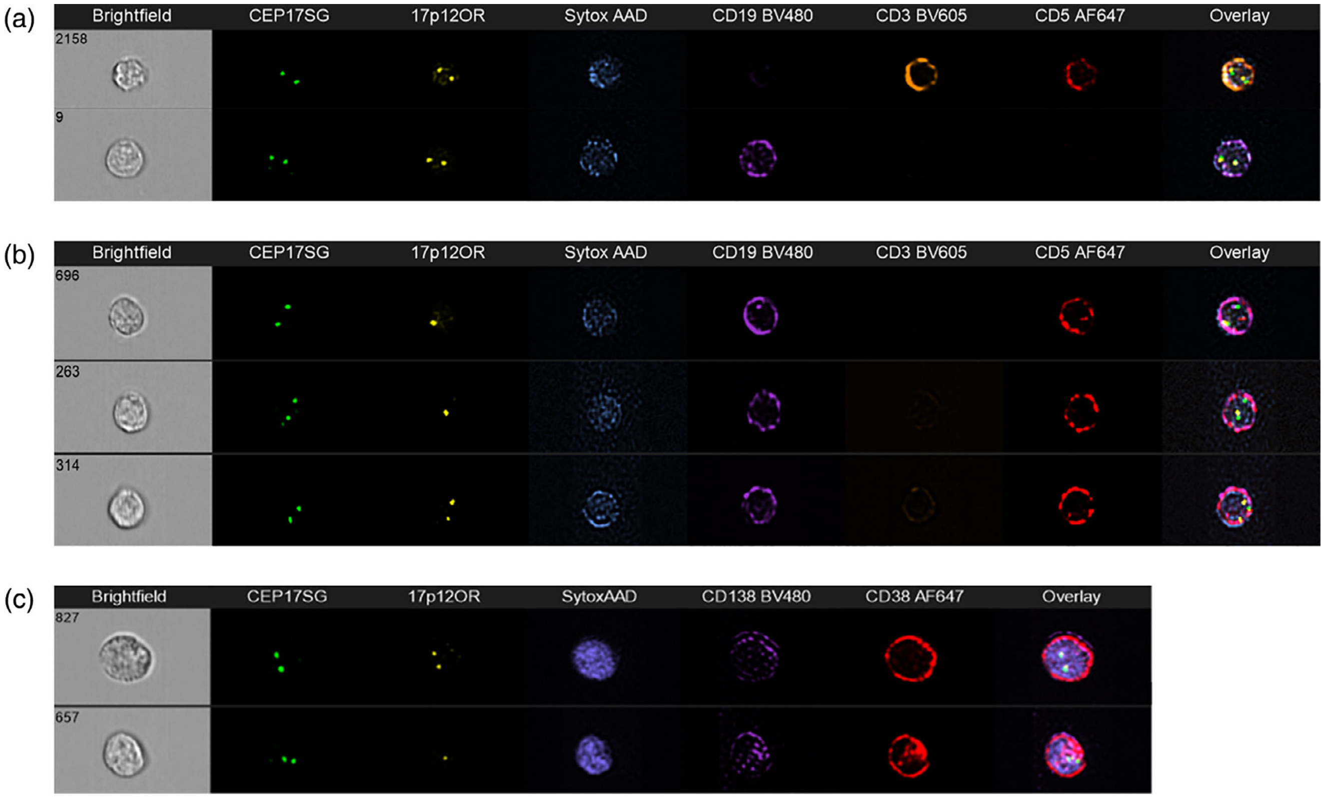

FIGURE 7 Analysis of chromosome 17 using 17p and CEP17 probes by immuno-flowFISH. (a) Normal T and B lymphocytes with 2-spot pattern for chromosome 17 and 17p. (b) Two CLL cells (696 and 263) with one spot for 17p indicating deletion 17p. Cell 657 has two spots for 17p. (c) Two plasma cells in myeloma assessed for 17p. Cell 327 has the normal two spots whereas cell 657 has one spot for 17p indicating deletion of 17p. All cells had normal 2-spot pattern for CEP17 (×60 magnification)

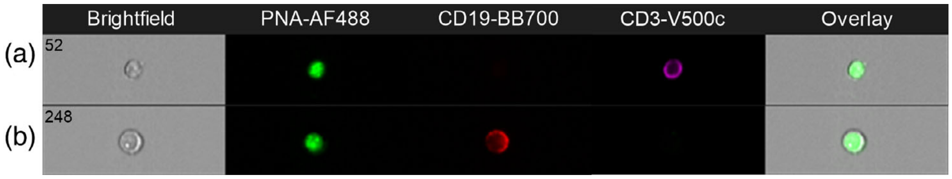

FIGURE 8 Telomere immuno-flow FISH of normal blood. (a) Normal T lymphocyte (CD3+/CD19−), (b) Normal B lymphocyte (CD3−/CD19+) (×40 magnification).
Source: Clynick et al., unpublished data

4. the power of digital images which allows simultaneous visualization of cells, their nucleus, phenotype and chromosomal signal at high throughput with single cell resolution
5. depth of field enabling the cell and FISH spot count images to be in focus
6. improved specificity through the positive identification of cells of interest based on immunophenotype

The digital images and ability to detect FISH signals are a major advance over standard flow cytometry for analyzing chromosomes. Specifically moving from fluorescence intensity measures to being able to see the cells and their chromosomal signal. Further, when combined with a nuclear stain, provides direct confirmation of the localization of the FISH signal. This has three main advantages: first, the ability to see the FISH spot over the nuclear stain provides evidence of specific chromosome labeling and reduces false positive results. Second, the visual images provide objective data and overcome the limitations of using mean fluorescence intensity or other indirect subjective data interpretation. Third, the incorporation of immunophenotypic analysis of cytological samples ensures that the FISH signal is only interpreted in the positively identified cell with the antigen expression pattern of interest.

FISH analysis by imaging flow cytometry does not require pre-analytical cell isolation as cell identification comes from standard immunophenotypic gating. This increases the specificity over traditional FISH which only assesses cell nuclei, and not specific cell populations. This has limitations when the cell of interest (e.g., neoplastic cell) makes up only a sub-population of the sample. Hence the chromosomal analysis could be of any cell type in the sample. This is addressed with some FISH applications, such as plasma cell myeloma where CD138-positive cell isolation is commonly performed.

Test sensitivity is also greatly increased as tens of thousands of cells are analyzed in a single test; this is in comparison with standard FISH which typically only assesses nuclei of 200 cells. To date, the limit of detection of immuno-flowFISH has been reported as being able to detect a chromosomal defect when present in less than 1% of cells in the sample (Erber et al., 2020; Hui et al., 2019). Acquiring data for thousands of cells and restricting analysis of cytogenetic features to cells with a specific phenotype, shows potential of this approach for chromosomal analysis for detecting rare events.

7 | THE FUTURE OF IMAGING FLOW CYTOMETRY FOR CHROMOSOMAL ANALYSIS

Imaging flow cytometry for chromosomal analysis is still in its infancy and its precise place in the repertoire of cytogenomic testing for human disease requires further work. There are technical and analytical issues that are still to be assessed prior to the method being ready for clinical applications. These include the need for beta testing in multiple sites and clearing regulatory requirement for in vitro diagnostic products from the relevant governing body such as the U.S Food and Drug Administration. Testing to date has been restricted to blood and bone marrow which require minimal treatment for single cell analysis. Further work is required to evaluate the applicability of the technique to other cytological specimens (e.g., fine needle aspirate) and cells extracted from fresh solid tumor samples. Other aspects in relation to the sample that remain to be validated include the optimal anticoagulant and time from collection to analysis. Published literature has suggested that different anticoagulants and the length of time blood was in the anticoagulant may have a detrimental effect on the expression of some surface markers (Diks et al., 2019; Dorwal et al., 2014; Stetler-Stevenson et al., 2016). Lastly evaluation of the technique on larger patient cohorts and across multiple laboratories is required to confirm the clinical utility of this approach (Hui et al., 2019; Minderman et al., 2012).

Other antibodies and fluorophores need to be studied, specifically to determine whether they can withstand the low pH environment and high heat necessary for an immunophenotyping FISH technique. The effect of permeabilisation of cells for intracellular staining (e.g., TdT or myeloperoxidase, or cell cycle Ki67) prior to stabilization and fixation is unknown and will require additional investigation. Commonly used bright immunophenotyping fluorophores such as PE, APC and their tandem conjugates lose their fluorescence after incubation in acid and hybridization at high temperature (Fuller et al., 2016). FISH probes have been designed for fluorescent microscopy and are generally produced with a limited rage of fluorophores such as FITC and TexasRed. Use of these fluorophores for the FISH component has placed restrictions on the fluorophores that can be used for the immunophenotyping. New synthetic-based polymer fluorophores provide a promising avenue to expand the number of parameters with this technique providing a more stable base structure and tandem conjugation chemistry in low pH and high temperature protocols (Panchuk-Voloshina et al., 1999; Roura et al., 2016; Skotheim & Reynolds, 2007).

Imaging flow cytometry devices have significantly lower throughput than standard flow cytometers. The Amnis ImageStream^{X} markII, for example, has a throughput speed of up to 6000 cells/s, but with chromosomal analysis requires acquisition speeds of <1000 cells/s for highest sensitivity image analysis. This is ten times slower than that of standard flow cytometers such as the BD FACSCantoII or Beckman Coulter Aquios CL. However for an imaging flow cytometer which utilizes a CCD camera, there is a limitation in its maximum speed due to the manner in which fluorescence photons are collected and transferred without electron multiplication (Han et al., 2016). Although acknowledged, to date, this lower acquisition speed has not been recognized as a problem.

Advances in instrumentation are likely to occur over the coming years as the technology becomes more widely adopted. This could include auto-sampling and image-based sorting of specific chromosomal populations for further analysis. Prototype instruments such as the ENMA by CYBO, enable real-time cell sorting based on morphological features at a throughput of 100 cells/s (Isozaki et al., 2020; Nitta et al., 2018).

Advances in data analysis software are ongoing with the release of IDEAS v6.3 and Amnis Artificial Intelligence (AI) Image Analysis Software packages (Probst et al., 2020; Pugsley & Kong, 2020). These should enhance the sensitivity for detection of dim FISH spots, as seen with small probes, and reduce operator input into the analysis. The future could see machine learning software providing automated analysis of cytogenetic aberrations. This would increase automation, provide objective analysis and standardize interpretation. Machine learning could also add a new dimension to data handling and reveal FISH images as well as morphological profiles currently undetectable by eye or the software (Doan et al., 2018). This is exemplified in telomeric FISH where image-based analysis is already capable of achieving better separation of cells with different telomere lengths compared to operator selected fluorescence intensity measurement.

In summary, chromosomal analysis by imaging flow cytometry is showing enormous promise and has already been described as a “new frontier” in cytogenomics of cytological specimen (Weissleder & Lee, 2020). The ability to identify chromosomes and abnormalities in specific cell types in human disease has been a significant breakthrough. The techniques developed using imaging flow cytometry are likely to become a valuable addition to chromosome analysis in a range of disorders at diagnosis, for assessing low level circulating cells with a chromosomal defect and detecting residual disease following therapy. The technology may also open avenues for the detection of emergent and drug-resistant new clones following therapy.

REFERENCES

Alder, J. K., Hanumanthu, V. S., Strong, M. A., DeZern, A. E., Stanley, S. E., Takemoto, C. M., Danilova, L., Applegate, C. D., Bolton, S. G., Mohr, D. W., Brodsky, R. A., Casella, J. F., Greider, C. W., Jackson, J. B., & Armanios, M. (2018). Diagnostic utility of telomere length testing in a hospital-based setting. *Proceedings of the National Academy of Sciences of the United States of America*, *115*(10), E2358–E2365.

Arkesteijn, G. J. A., Erpelinck, S. L. A., Martens, A. C. M., & Hagenbeek, A. (1995). Chromosome specific DNA hybridization in suspension for flow cytometric detection of chimerism in bone marrow transplantation and leukemia. *Cytometry*, *19*(4), 353–360.

Armando, R. G., Mengual Gomez, D. L., Maggio, J., Sanmartin, M. C., & Gomez, D. E. (2019). Telomeropathies: Etiology, diagnosis, treatment and follow-up. Ethical and legal considerations. *Clinical Genetics*, *96*(1), 3–16.

Aubert, G., Hills, M., & Lansdorp, P. M. (2012). Telomere length measurement-caveats and a critical assessment of the available technologies and tools. *Mutation Research - Fundamental and Molecular Mechanisms of Mutagenesis*, *730*(1–2), 59–67.

Avet-Loiseau, H., Attal, M., Moreau, P., Charbonnel, C., Garban, F., Hulin, C., Leyvraz, S., Michallet, M., Yakoub-Agha, I., Garderet, L., Marit, G., Michaux, L., Voillat, L., Renaud, M., Grosbois, B., Guillerm, G., Benboubker, L., Monconduit, M., Thieblemont, C., … Mathiot, C. (2007). Genetic abnormalities and survival in multiple myeloma: The experience of the Intergroupe francophone du Myélome. *Blood*, *109*(8), 3489–3495.

Baerlocher, G. M., Vulto, I., de Jong, G., & Lansdorp, P. M. (2006). Flow cytometry and FISH to measure the average length of telomeres (flow FISH). *Nature Protocols*, *1*(5), 2365–2376.

Barteneva, N. S., Fasler-Kan, E., & Vorobjev, I. A. (2012). Imaging flow cytometry: Coping with heterogeneity in biological systems. *Journal of Histochemistry and Cytochemistry*, *60*(10), 723–733.

Basiji, D. (2016). Principle of Amnis imaging flow cytometry. In N. Barteneva & I. Vorobjev (Eds.), *Imaging flow cytometry methods and protocols* (pp. 28–36). Springer.

Basiji, D., & O'Gorman, M. R. G. (2015). Imaging flow cytometry. *Journal of Immunological Methods*, *423*, 1–2.

Basiji, D. A., Ortyn, W. E., Liang, L., Venkatachalam, V., & Morrissey, P. (2007). Cellular image analysis and imaging by flow cytometry. *Clinics in Laboratory Medicine*, *27*(3), 653–670.

Brind'Amour, J., & Lansdorp, P. M. (2011). Analysis of repetitive DNA in chromosomes by flow cytometry. *Nature Methods*, *8*(6), 484–486.

Cambier, J. L., Kay, D. B., & Wheeless, L. L. (1979). A multidimensional slit-scan flow system. *Journal of Histochemistry and Cytochemistry*, *27*(1), 321–324.

Carter, N. P. (1994). Cytogenetic analysis by chromosome painting. *Cytometry*, *18*(1), 2–10.

Chazotte, B. (2011). Labeling nuclear DNA with Hoechst 33342. *Cold Spring Harbor Protocols*, *1*, pdb.prot5556.

Cui, C., Shu, W., & Li, P. (2016). Fluorescence in situ hybridization: Cell-based genetic diagnostic and research applications. *Frontiers in Cell and Developmental Biology*, *4*(89), 1–11.

Diks, A. M., Bonroy, C., Teodosio, C., Groenland, R. J., de Mooij, B., de Maertelaere, E., Neirynck, J., Philippé, J., Orfao, A., van Dongen, J. J. M., & Berkowska, M. A. (2019). Impact of blood storage and sample handling on quality of high dimensional flow cytometric data in multicenter clinical research. *Journal of Immunological Methods*, *475*, 112616.

Doan, M., Vorobjev, I., Rees, P., Filby, A., Wolkenhauer, O., Goldfeld, A. E., Lieberman, J., Barteneva, N., Carpenter, A. E., & Hennig, H. (2018). Diagnostic potential of imaging flow cytometry. *Trends in Biotechnology*, *36*(7), 649–652.

Döhner, H., Stilgenbauer, S., Benner, A., Leupolt, E., Kröber, A., Bullinger, L., Döhner, K., Bentz, M., & Lichter, P. (2000). Genomic aberrations and survival in chronic lymphocytic leukemia. *New England Journal of Medicine*, *343*(26), 1910–1916.

Doležel, J., Kubaláková, M., Cíhalíková, J., Suchánková, P., & Simková, H. (2011). Chromosome analysis and sorting using flow cytometry. *Methods in Molecular Biology (Clifton, N.J.)*, *701*, 221–238.

Doležel, J., Lucretti, S., Molnár, I., Cápal, P., & Giorgi, D. (2021). Chromosome analysis and sorting. *Cytometry Part A*, *99*(4), 328–342.

Dominical, V., Samsel, L., & McCoy, J. P. (2017). Masks in imaging flow cytometry. *Methods*, *112*, 9–17.

Dorwal, P., Thakur, R., & Rawat, S. (2014). CD138 expression in plasma cells is volatile and time-lag dependent. *The Egyptian Journal of Haematology*, *39*(4), 258–259.

Erber, W. N., Hui, H., Stanley, J., Mincherton, T., Clarke, K., Augustson, B., Ng, T. F., Cheah, C. Y., McQuillan, A. D., & Fuller, K. (2020). Detection of Del(17p) in hematological malignancies by imaging flow cytometry. *Blood*, *136*(Supplement 1), 9–10.

Ferguson-Smith, M. A. (2015). History and evolution of cytogenetics. *Molecular Cytogenetics*, *8*(19), 1–8.

Frohlich, J., Kubickova, S., Musilova, P., Cernohorska, H., Muskova, H., Vodicka, R., & Rubes, J. (2017). Karyotype relationships among selected deer species and cattle revealed by bovine FISH probes. *PLoS One*, *12*(11), e0187559.

Fuller, K. A., Bennett, S., Hui, H., Chakera, A., & Erber, W. N. (2016). Development of a robust immuno-S-FISH protocol using imaging flow cytometry. *Cytometry Part A*, *89*(8), 720–730.

Genet, M. D., Cartwright, I. M., & Kato, T. A. (2013). Direct DNA and PNA probe binding to telomeric regions without classical in situ hybridization. *Molecular Cytogenetics*, *6*(42), 1–5.

Gray, J. W., Carrano, A. V., Moore, D. H., Steinmetz, L. L., Minkler, J., Mayall, B. H., Mendelsohn, M. L., & Van Dilla, M. A. (1975). High speed quantitative karyotyping by flow microfluorometry. *Clinical Chemistry*, *21*(9), 1258–1262.

Gray, J. W., Carrano, A. V., Steinmetz, L. L., Van Dilla, M. A., Moore, D. H., Mayall, B. H., & Mendelsohn, M. L. (1975). Chromosome measurement and sorting by flow systems. *Proceedings of the National Academy of Sciences of the United States of America*, *72*(4), 1231–1234.

Gray, J. W., Trask, B., Van Den Engh, G., Silva, A., Lozes, C., Grell, S., Schonberg, S., Yu, L. C., & Golbus, M. S. (1988). Application of flow karyotyping in prenatal detection of chromosome aberrations. *American Journal of Human Genetics*, *42*(1), 49–59.

Guo, B., Han, X., Wu, Z., Da, W., & Zhu, H. (2014). Spectral karyotyping: An unique technique for the detection of complex genomic rearrangements in leukemia. *Translational Pediatrics*, *3*(2), 135–139.

Han, Y., Gu, Y., Zhang, A. C., & Lo, Y. H. (2016). Review: Imaging technologies for flow cytometry. *Lab on a Chip*, *16*(24), 4639–4647.

Han, Y., & Lo, Y.-H. (2015). Imaging cells in flow cytometer using spatial-temporal transformation. *Scientific Reports*, *5*, 13267.

Hsu, T. C. (1952). Mammalian chromosomes in vitro: I. the karyotype of man. *Journal of Heredity*, *43*(1), 167–172.

Huang, E., Ma, Q., & Liu, Z. (2016). Ultrafast imaging using spectral resonance modulation. *Scientific Reports*, *6*, 25240.

Hui, H., Fuller, K. A., Chuah, H., Liang, J., Sidiqi, H., Radeski, D., & Erber, W. N. (2018). Imaging flow cytometry to assess chromosomal abnormalities in chronic lymphocytic leukaemia. *Methods*, *134–135*, 32–40.

Hui, H. Y. L., Clarke, K. M., Fuller, K. A., Stanley, J., Chuah, H. H., Ng, T. F., Cheah, C., McQuillan, A., & Erber, W. N. (2019). "Immuno-flowFISH" for the assessment of cytogenetic abnormalities in chronic lymphocytic leukemia. *Cytometry Part A*, *95*(5), 521–533.

Ibrahim, S. F., & Van Den Engh, G. (2004). High-speed chromosome sorting. *Chromosome Research*, *12*, 5–14.

Isozaki, A., Mikami, H., Tezuka, H., Matsumura, H., Huang, K., Akamine, M., Hiramatsu, K., Iino, T., Ito, T., Karakawa, H., Kasai, Y., Li, Y., Nakagawa, Y., Ohnuki, S., Ota, T., Qian, Y., Sakuma, S., Sekiya, T., Shirasaki, Y., … Goda, K. (2020). Intelligent image-activated cell sorting 2.0. *Lab on a Chip*, *20*(13), 2263–2273.

Kachel, V., Benker, G., Lichtnau, K., Valet, G., & Glossner, E. (1979). Fast imaging in flow: A means of combining flow-cytometry and image analysis. *Journal of Histochemistry and Cytochemistry*, *27*(1), 335–341.

Kay, D. B., Cambier, J. L., & Wheeless, L. L. J. (1979). Imaging in flow. *Journal of Histochemistry and Cytochemistry*, *27*(1), 329–334.

Keyvanfar, K., Weed, J., Swamy, P., Kajigaya, S., Calado, R. T., & Young, N. S. (2012). Interphase chromosome flow-FISH. *Blood*, *120*(15), e54–e59.

Langlois, R. G., Yu, L. C., Gray, J. W., & Carrano, A. V. (1982). Quantitative karyotyping of human chromosomes by dual beam flow cytometry. *Proceedings of the National Academy of Sciences of the United States of America*, *79*(24), 7876–7880.

Lebo, R. V., Golbus, M. S., & Cheung, M. C. (1986). Detecting abnormal human chromosome constitutions by dual laser flow cytogenetics. *American Journal of Medical Genetics*, *25*(3), 519–529.

Mangaonkar, A. A., & Patnaik, M. M. (2018). Short telomere syndromes in clinical practice: Bridging bench and bedside. *Mayo Clinic Proceedings*, *93*(7), 904–916.

Martin, C. L., & Warburton, D. (2015). Detection of chromosomal aberrations in clinical practice: From karyotype to genome sequence. *Annual Review of Genomics and Human Genetics*, *16*(1), 309–326.

Mattsson, G., Tan, S. Y., Ferguson, D. J. P., Erber, W., Turner, S. H., Marafioti, T., & Mason, D. Y. (2007). Detection of genetic alterations by immunoFISH analysis of whole cells extracted from routine biopsy material. *Journal of Molecular Diagnostics*, *9*(4), 479–489.

Mikami, H., Kawaguchi, M., Huang, C. J., Matsumura, H., Sugimura, T., Huang, K., Lei, C., Ueno, S., Miura, T., Ito, T., Nagasawa, K., Maeno, T., Watarai, H., Yamagishi, M., Uemura, S., Ohnuki, S., Ohya, Y., Kurokawa, H., Matsusaka, S., … Goda, K. (2020). Virtual-freezing fluorescence imaging flow cytometry. *Nature Communications*, *11*(1), 1162.

Minderman, H., Humphrey, K., Arcadi, J. K., Wierzbicki, A., Maguire, O., Wang, E. S., Block, A. W., Sait, S. N., George, T. C., & Wallace, P. K. (2012). Image cytometry-based detection of aneuploidy by fluorescence in situ hybridization in suspension. *Cytometry Part A*, *81*(9), 776–784.

Monard, S. (2016). Chromosome sorting for the masses? *Cytometry Part A*, *89*(9), 797–798.

Ng, B. L., Fu, B., Graham, J., Hall, C., & Thompson, S. (2019). Chromosome analysis using benchtop flow analysers and high speed cell sorters. *Cytometry Part A*, *95*(3), 323–331.

Nitta, N., Sugimura, T., Isozaki, A., Mikami, H., Hiraki, K., Sakuma, S., Iino, T., Arai, F., Endo, T., Fujiwaki, Y., & Fukuzawa, H. (2018). Intelligent image-activated cell sorting. *Cell*, *175*(1), 266–276.e13.

O'Connor, C. (2008). Karyotyping for chromosomal abnormalities. *Nature Education*, *1*(1), 27.

Ortyn, W. E., Perry, D. J., Venkatachalam, V., Liang, L., Hall, B. E., Frost, K., & Basiji, D. A. (2007). Extended depth of field imaging for high speed cell analysis. *Cytometry Part A*, *71*(4), 215–231.

Panchuk-Voloshina, N., Haugland, R. P., Bishop-Stewart, J., Bhalgat, M. K., Millard, P. J., Mao, F., Leung, W. Y., & Haugland, R. P. (1999). Alexa dyes, a series of new fluorescent dyes that yield exceptionally bright, Photostable conjugates. *Journal of Histochemistry and Cytochemistry*, *47*(9), 1179–1188.

Popescu, C. P., Boscher, J., Popescu, D., Hausmann, M., Kerboœf, D., Dölle, J., & Cremer, C. (1993). Identification and cytogenetic analysis of an abnormal pig chromosome for flow cytometry and sorting. *Zeitschrift Fur Naturforschung—Section C Journal of Biosciences*, *48*(7–8), 645–653.

Probst, C., Zayats, A., Venkatachalam, V., & Davidson, B. (2020). Advanced characterization of silicone oil droplets in protein therapeutics using artificial intelligence analysis of imaging flow cytometry data. *Journal of Pharmaceutical Sciences*, *109*(10), 2996–3005.

Pugsley, H. R., & Kong, R. K. (2020). Demonstration of high gain mode in combination with imaging flow cytometry for improved EV analysis. *Journal of Immunology*, *204*(1 Supplement), 159.15 LP-159.15.

Roura, S., Fernández, M. A., Elchinova, E., Teubel, I., Requena, G., Cabanes, R., Lupón, J., & Bayes-Genis, A. (2016). Brilliant violet fluorochromes in simultaneous multicolor flow cytometry-fluorescence in situ hybridization measurement of monocyte subsets and telomere length in heart failure. *Laboratory Investigation: A Journal of Technical Methods and Pathology*, *96*(11), 1223–1230.

Rufer, N., Dragowska, W., Thornbury, G., Roosnek, E., & Lansdorp, P. M. (1998). Telomere length dynamics in human lymphocyte subpopulations measured by flow cytometry. *Nature Biotechnology*, *16*(8), 743–747.

Sanderson, S. L., & Simon, A. K. (2017). In aged primary T cells, mitochondrial stress contributes to telomere attrition measured by a novel imaging flow cytometry assay. *Aging Cell*, *16*(6), 1234–1243.

Schmitz, A., Oustry, A., Vaiman, D., Chaput, B., Frelat, G., & Cribiu, E. P. (1998). Comparative karyotype of pig and cattle using whole chromosome painting probes. *Hereditas*, *128*(3), 257–263.

Sinclair, A. (2002). Genetics 101: Cytogenetics and FISH. *Canadian Medical Association Journal*, *167*(4), 373–374.

Skotheim, T. A., & Reynolds, J. R. (2007). Electrochemistry of conducting Poymers. In T. A. Skotheim & J. R. Reynolds (Eds.), *Conjugated polymers: Theory, synthesis, properties, and characterization* (3rd ed., pp. 40–81). CRC press.

Stanley, S. E., & Armanios, M. (2015). The short and long telomere syndromes: Paired paradigms for molecular medicine. *Current Opinion in Genetics and Development*, *33*, 1–9.

Stanyon, R., & Stone, G. (2008). Phylogenomic analysis by chromosome sorting and painting. *Methods in Molecular Biology (Clifton, N.J.)*, *422*, 13–29.

Stepanov, S. I., Konyshev, V. N., Kotlovanova, L. V., & Roganov, A. P. (1996). Karyotyping of individual cells with flow cytometry. *Cytometry*, *23*(4), 279–283.

Stetler-Stevenson, M., Paiva, B., Stoolman, L., Lin, P., Jorgensen, J. L., Orfao, A., van Dongen, J., & Rawstron, A. C. (2016). Consensus guidelines for myeloma minimal residual disease sample staining and data acquisition. *Cytometry Part B, Clinical Cytometry*, *90*(1), 26–30.

Stubblefield, E., Cram, S., & Deaven, L. (1975). Flow microfluorometric analysis of isolated Chinese hamster chromosomes. *Experimental Cell Research*, *94*(2), 464–468.

Suchanek, M., Radzikowska, A., & Thiele, C. (2005). Photo-leucine and photo-methionine allow identification of protein-protein interactions in living cells. *Nature Methods*, *2*(4), 261–268.

Tjio, J., & Levan, A. (1956). The chromosome number of man. *Hereditas*, *42*(1–2), 1–6.

Trask, B., van den Engh, G., Landegent, J., de Wal, N. J., & van der Ploeg, M. (1985). Detection of DNA sequences in nuclei in suspension by in situ hybridization and dual beam flow cytometry. *Science*, *230*(4732), 1401–1403.

Trask, B., van den Engh, G., Pinkel, D., Mullikin, J., Waldman, F., van Dekken, H., & Gray, J. (1988). Fluorescence in situ hybridization to interphase cell nuclei in suspension allows flow cytometric analysis of chromosome content and microscopic analysis of nuclear organization. *Human Genetics*, *78*(3), 251–259.

van der Logt, E. M., Kuperus, D. A., van Setten, J. W., van den Heuvel, M. C., Boers, J. E., Schuuring, E., & Kibbelaar, R. E. (2015). Fully automated fluorescent in situ hybridization (FISH) staining and digital analysis of HER2 in breast cancer: a validation study. *PloS ONE*, *10*(4), e0123201.

van Dekken, H., Arkesteijn, G. J. A., Visser, J. W. M., & Bauman, J. G. J. (1990). Flow cytometric quantification of human chromosome specific repetitive DNA sequences by single and bicolor fluorescent in situ hybridization to lymphocyte interphase nuclei. *Cytometry*, *11*(1), 153–164.

Van Dilla, M. A., & Deaven, L. L. (1990). Construction of gene libraries for each human chromosome. *Cytometry*, *11*(1), 208–218.

Van Dilla, M. A., Deaven, L. L., Albright, K. L., Allen, N. A., Aubuchon, M. R., Bartholdi, M. F., Brown, N. C., Campbell, E. W., Carrano, A. V., Clark, L. M., & Cram, L. S. (1986). Human chromosome–specific DNA libraries: Construction and availability. *Bio/Technology*, *4*(6), 537–552.

Wand, T., Fang, M., Chen, C., Hardy, N., McCoy, J. P., Jr., Dumitriu, B., Young, N. S., & Biancotto, A. (2016). Telomere content measurement in human hematopoietic cells: Comparative analysis of qPCR and flow-FISH techniques. *Cytometry Part A*, *89*(10), 914–921.

Weber-Matthiesen, K., Deerberg, J., Poetsch, M., Grote, W., & Schlegelberger, B. (1995). Numerical chromosome aberrations are present within the CD30+ Hodgkin and reed-Sternberg cells in 100% of analyzed cases of Hodgkin's disease. *Blood*, *86*(4), 1464–1468.

Weber-Matthiesen, K., Muller-Hermelink, A., Deerberg, J., Scherthan, H., Schlegelberger, B., & Grote, W. (1993). Discrimination of distinct subpopulations within a tumor with a double immunophenotyping and interphase cytogenetics. *Journal of Histochemistry and Cytochemistry*, *41*(11), 1641–1644.

Weber-Matthiesen, K., Winkemann, M., Muller-Hermelink, A., Schlegelberger, B., & Grote, W. (1992). Simultaneous fluorescence immunophenotyping and interphase cytogenetics: A contribution to the characterization of tumor cells. *Journal of Histochemistry and Cytochemistry*, *40*(2), 171–175.

Weiss, M. M., Hermsen, M. A., Meijer, G. A., van Grieken, N. C., Baak, J. P., Kuipers, E. J., & van Diest, P. J. (1999). Comparative genomic hybridisation. *Molecular Pathology*, *52*(5), 243–251.

Weissleder, R., & Lee, H. (2020). Automated molecular-image cytometry and analysis in modern oncology. *Nature Reviews Materials*, *5*, 409–422.

Yao, Y., Zhang, Y., Liu, W., & Deng, X. (2020). Highly efficient synchronization of sheep skin fibroblasts at G2/M phase and isolation of sheep Y chromosomes by flow cytometric sorting. *Scientific Reports*, *1*, 9933.

Zihlif, M., Catchpoole, D. R., Stewart, B. W., & Wakelin, L. P. G. (2010). Effects of DNA minor groove binding agents on global gene expression. *Cancer Genomics and Proteomics*, *7*(6), 323–330.

Received: 11 February 2021 | Revised: 31 May 2021 | Accepted: 1 June 2021
DOI: 10.1002/cyto.a.24468

ORIGINAL ARTICLE

MIFlowCyt MIFlowCyt
ISAC INTERNATIONAL SOCIETY FOR ADVANCEMENT OF CYTOMETRY
CYTOMETRY Journal of Quantitative Cell Science PART A

Imaging flow cytometry and fluorescence microscopy in assessing radiation response in lymphocytes from umbilical cord blood and cancer patients

Matus Durdik[1] | Pavol Kosik[1] | Lukas Jakl[1] | Maria Kozackova[1] | Eva Markova[1] | Katarina Vigasova[1] | Katarina Beresova[1] | Jana Jakubikova[2] | Eva Horvathova[3] | Lucian Zastko[1] | Marta Fekete[4] | Ingrid Zavacka[4] | Margita Pobijakova[4] | Igor Belyaev[1]

[1] Department of Radiobiology, Cancer Research Institute, Biomedical Research Center, University Science Park for Biomedicine, Slovak Academy of Sciences, Bratislava, Slovakia

[2] Department of Tumor Immunology, Cancer Research Institute, Biomedical Research Center, University Science Park for Biomedicine, Slovak Academy of Sciences, Bratislava, Slovakia

[3] Department of Genetics, Cancer Research Institute, Biomedical Research Center, University Science Park for Biomedicine, Slovak Academy of Sciences, Bratislava, Slovakia

[4] Department of Radiation Oncology, National Cancer Institute, Bratislava, Slovakia

Correspondence
Matus Durdik, Cancer Research Institute, Biomedical Research Center, Dubravska cesta 9, 845 05 Bratislava, Slovakia.
Email: matus.durdik@savba.sk

Funding information
Agentúra Ministerstva školstva, vedy, výskumu a športu SR, Grant/Award Number: 26220220200; Agentúra na Podporu Výskumu a Vývoja, Grant/Award Number: APVV-15-0250; European Regional Development Fund TRANSMED 2, Grant/Award Number: ITMS: 26240120030; International Atomic Energy Agency, Grant/Award Number: 22259/R0; Vedecká Grantová Agentúra MŠVVaŠ SR a SAV, Grant/Award Numbers: 2/0089/18, 2/0147/17

Abstract

DNA double strand breaks (DSB) induced by ionizing radiation (IR) are usually measured using γH2AX/53BP1 DNA repair foci, that is considered to be the most sensitive assay for DSB analysis. While fluorescence microscopy (FM) is the gold standard for this analysis, imaging flow cytometry (IFC) may offer number of advantages such as lack of the fluorescence background, higher number of cells analyzed, and higher sensitivity in detection of DNA damage induced by IR at low doses. Along with appearance of γH2AX foci, the variable fraction of the cells exhibits homogeneously stained γH2AX signal resulting in so-called γH2AX pan-staining, which is believed to appear at early stages of apoptosis. Here, we investigated incidence of γH2AX pan-staining at different time points after irradiation with γ-rays using IFC and compared the obtained data with the data from FM. Appearance of γH2AX pan-staining during the apoptotic process was further analyzed by fluorescence-activated cell sorting (FACS) of cells at different stages of apoptosis and subsequent immunofluorescence analysis. Our results show that IFC was able to reveal dose dependence of pan-staining, while FM failed to detect all pan-staining cells. Moreover, we found that γH2AX pan-staining could be induced by therapeutic, but not low doses of γ-rays and correlate well with percentage of apoptotic cells was analyzed using flow cytometric Annexin-V/7-AAD assay. Further investigations showed that γH2AX pan-staining is formed in the early phases of apoptosis and remains until later stages of apoptotic process. Apoptotic DNA fragmentation as detected with comet assay using FM correlated with the percentage of live and late apoptotic/necrotic cells as analyzed by flow cytometry. Lastly, we successfully tested IFC for detection of γH2AX pan-staining and γH2AX/53BP1 DNA repair foci in lymphocyte of breast cancer patients after radiotherapy, which may be useful for assessing individual radiosensitivity in a clinically relevant cohort of patients.

KEYWORDS
53BP1, apoptosis, breast cancer, human lymphocytes, imaging flow cytometry, ionizing radiation, Metafer, radiotherapy, γH2AX foci and pan-staining

wileyonlinelibrary.com/journal/cytoa
Cytometry. 2021;99:1198–1208.

1 | INTRODUCTION

DNA repair foci assay is considered as the most sensitive among the methods used for analysis of DNA double strand breaks (DSB) [1–4]. After DSB induction, histone H2AX is phosphorylated across affected 2 Mb-sized chromatin domain (γH2AX when phosphorylated). This phosphorylation is recognized by other downstream factors such as Mediator of DNA damage checkpoint protein 1 (MDC1), Nijmegen breakage syndrome protein 1 (NBS1), and tumor suppressor p53 binding protein 1 (53BP1), which create so-called DNA repair foci at the location of DSB. γH2AX [5] and 53BP1 are the most commonly used biomarkers for the DSB assessment [6]. In particular, DNA repair foci are used for assessing DSB induced by ionizing radiation (IR) at low and therapeutic doses [1,2,7–9] . Peripheral blood lymphocytes (PBL) are often used for such assessment in radiobiological studies due to: (a) PBL are easy to obtain, (b) nearly all PBL are in the same cell cycle phase, and (c) ability of PBL to be used for clinical applications While 53BP1/γH2AX biomarkers were already used to predict the adverse effect of radiotherapy in PBL of breast cancer (BC) patients using fluorescence microscopy (FM) [10–12], the method was not shown to be appropriately sensitive and specific. Along with γH2AX foci, some cells undergoing apoptosis display whole nuclei γH2AX pan-staining, [2,8,13–16]. Imaging flow cytometry (IFC) is a method that combines the imaging features of FM with speed and quantitative analysis of flow cytometry. It is able to analyze more cells faster and directly from the tube what could prevent cell loss, it could be more useful and powerful in assessing γH2AX pan-staining compare to FM, which tends to be more subjective and less quantitative than IFC due to its laborious nature.

Ding et al. showed that γH2AX pan-staining was induced by 0.5 Gy of X-rays and co-localized with the total phosphorylation of ATM and DNA-PKcs kinases in fresh adult human PBL [17]. Anglada et al. sorted live, early, and late apoptotic lymphoblasts 24 h post-irradiation and found γH2AX pan-staining in both fractions of apoptotic cells [18]. Turesson et al. had used γH2AX pan-staining for assessment of apoptosis in skin biopsies from cancer patients undergoing local radiotherapy for evaluation of individual radiosensitivity [19]. During apoptosis of human lymphocytes, 2 Mb DNA loops are cleaved from chromosomal DNA followed by subsequent cleavage to 50 kb fragments and further fragmentations to oligonucleosomes [20,21]. Fragmentation of DNA present in different stages of apoptosis has been studied previously by Czene and colleagues using the comet assay [22]. In this work we aimed to study induction of γH2AX pan-staining by low and high doses of γ-rays by IFC in lymphocytes from umbilical cord blood (UCB) and compare obtained data with FM results. We also aimed to study the exact stage of the apoptotic process when γH2AX pan-staining is present. Next, we studied apoptotic DNA fragmentation by comet assay and compared the results with standard cytometric Annexin-V/7-AAD assay and IFC analysis of γH2AX pan-staining. Lastly, we aimed to test IFC-based γH2AX foci and pan-staining analysis in the BC PBL.

2 | MATERIALS AND METHODS

2.1 | Chemicals

Reagent grade chemicals were obtained from Millipore Sigma (Burlington) and Thermo Fisher Scientific (Waltham).

2.2 | Cells

This study has been approved by the Ethics Committee of Children's Hospital in Bratislava and the Institutional Review Board of the National Cancer Institute, Bratislava. Written informed consent was obtained for each participant. Mononuclear cells (MNC) were extracted from umbilical cord blood (UCB) as previously described [8] and were provided by Dr. M. Kubes, Eurocord-Slovakia, Bratislava, Slovak Republic. After separation, the cells were frozen and thawed on the day of experiment as previously described [23]. Fresh blood samples collected from five breast cancer (BC) patients were also used. Patient's MNC were isolated from fresh blood by centrifugation on lymphocyte separation medium (LSM) as described previously [10]. Adherent monocytes were removed from the sample by an incubation of mononuclear cells for 2 h in RPMI medium supplemented with 10% FBS and 100 IU/ml penicillin, 100 μg/ml streptomycin, at 37°C in a 5% CO_2-incubator. Viability of remaining lymphocytes was at least 95% as defined by the trypan blue exclusion assay.

2.3 | Irradiation

The MNC were irradiated in water bath on ice by γrays at the dose rate of 0.35 Gy/min using a *THERATRON® Elite 80* (MDS Nordion). The irradiated cells were quickly warmed up to 37°C in a water bath and then incubated at 37°C in a CO_2-incubator till time of analysis.

2.4 | Imaging flow cytometry

IFC was performed as described previously [2,24]. Briefly, after incubation, 3 million cells were washed with cold PBS, and fixed in cold 3% paraformaldehyde. The cells were resuspended in 70% ethanol at −20°C and stored overnight. The next day, the cells were rehydrated in buffer containing PBS, 1% bovine serum albumin, and 0.1% Triton X-100, centrifuged and incubated for 2 h at room temperature with the primary antibodies: 53BP1polyclonal/rabbit (Novus biologicals, Cambridge, United Kingdom) and γH2AX monoclonal/mouse (Novus biologicals), at 1:800 and 1:500 dilution, respectively (Novus biologicals). After washing in PBS, the secondary antibody mix: FITC IgG (H + L) anti-mouse, 1:100 (Beckmann Coulter, Brea) and Alexa Fluor 488 antirabbit, 1:200 (Thermo Fisher Scientific), was added and incubated for 1 h at room temperature in the dark. Finally, the cells were stained with 3 μM DAPI (Thermo Fisher Scientific). From each sample, at least 1000 cells were captured using the ImageStreamX (Luminex) at 60× objective with the extension depth of field 1 (EDF1) turned on. Three lasers, 405, 488, and 785 nm, and CCD camera were used to analyze DNA, γH2AX/53BP1, granularity, and cell morphology, respectively, in four channels. Images of cells were acquired at the rate of 10–50 cell/sec.

Image compensation was performed on cells fixed 30 min after irradiation with 2 Gy. The cells stained with anti γH2AX-FITC/53BP1-AF488 only and DAPI only were used for generating the compensation matrix. The compensation matrix was calculated automatically by the IDEAS 5.0 compensation wizard.

Using the IDEAS software, DNA repair foci and percentage of γH2AX pan-staining cells were quantified in appropriate cells, which were selected as described earlier [2]. Briefly, single round-shaped, well focused, DAPI positive lymphocytes were gated. Next, the selected cells were divided according to their γH2AX signal into γH2AX pan-stained and non-pan-stained cells (Figure S1). Threshold between the γH2AX pan-stained and non-pan-stained cells was set manually after visual inspection of cells. DNA repair foci were counted in non-pan-stained cells using the custom made masks for analysis of γH2AX, 53BP1 or γH2AX/53BP1 co-localizing foci, using *Spot*, *Peak* and *Intensity* features as previously described [2]. First, *Spot* feature was used for the selection of spots with size at least 1 pixel and spot-to-background ratio of 3. Second, *Peak* feature was used to select spots with the spot-to-background ratio 1. Third, by *Intensity* feature and based on inspection of cell images a threshold was set for discrimination of foci with the lowest intensity from background fluorescence (for masking example see Figure 6A). IFC data were not uploaded to the flow repository, due to their big size, so they are available upon request.

2.5 | Fluorescence-activated cell sorting and standard flow cytometry

Cells at different stages of apoptosis were analyzed using Annexin/7-AAD assay as previously described. Briefly, cells in complete RPMI medium were centrifuged and the pellet was resuspended in 200 μl of Annexin-V staining buffer (Roche). Annexin-V-FIT-C conjugate (1:60) (Roche), CD45-V450 conjugate (1:100) (BD biosciences), and 7-AAD (1:70) (BD biosciences) were added to the suspension and incubated for 30 min at RT in dark. After washing with PBS, the cells were diluted in 200 μl of Annexin-V staining buffer and analyzed using BD fluorescence-activated cell sorting (FACS) Canto II (BD biosciences). In experiments with cell sorting, cells were diluted in 300 μl of Annexin-V staining buffer, and cells were sorted using the BD FACS Aria special order research product cell sorter (BD biosciences). We have sorted/analyzed three populations according to the staining with Annexin-V and 7-AAD: live cells (Annexin−/7-AAD-), early apoptotic (Annexin+/7-AAD-), and late apoptotic/necrotic (LAN) cells (Annexin+/7-AAD+) (Figures 2B and S2).

2.6 | Fluorescence microscopy

Sorted cells were cytospun on microscopic cytoslides (ThermoShandon) before being fixed with 3% paraformaldehyde solution and immunostained as previously described [8]. A primary antibody mix consisting of 53BP1 polyclonal/rabbit antibody at 1:800 dilution and γH2AX monoclonal/mouse antibody (both antibodies from Novus biologicals) at 1:400 dilution was used. The secondary antibody mix consisted of Alexa Fluor 488 IgG (H + L) anti-mouse, 1:200, and Alexa Fluor 555 IgG (H + L) anti-rabbit, 1:200 (Life technologies, Molecular probes). Upon immunostaining, coverslips (Menzel-Gläser) were mounted on microscopic cytoslides with a VECTASHIELD mounting medium (Vector Laboratories) and sealed using a translucent nail polish. Two slides were prepared per treatment condition.

The slides were scanned by a Metafer Slide Scanning System Version 3.6 (MetaSystems) with a Zeiss Axio Imager Z1 microscope (Zeiss Microscopy) using 63× objective. DNA repair foci were enumerated and visual inspection of cell galleries. γH2AX, 53BP1, and co-localizing γH2AX/53BP1 foci were enumerated in at least 150 cells from each slide. Percentage of cells displaying γH2AX pan-staining was assessed and foci were also counted in those cells. Results from two fields per treatment condition were pooled together.

2.7 | Comet assay

Comet assay was performed as previously described [25]. Briefly, cells were mixed with 0.75% agarose 24 h after irradiation and 50 μl of cell suspension (3×10^4 cells) were put onto slides. Afterwards, cells were lysed for 1 h in a fridge. Then slides were put into electrophoretic buffer and incubated in a fridge for 40 min. After incubation, electrophoresis was run for 30 min at 25 V/0.3 A. After electrophoresis, cells were washed with neutralizing buffer 3 times for 5 min. Next, slides were washed with distilled water and dried overnight. Then the slides were stored in cold and dark place and just before the analysis, they were stained by ethidium bromide. At least 400 cells were scanned by Metafer. Subsequently, cell galleries were inspected manually and cells were divided into different categories of apoptotic DNA fragmentation, namely non-defined fragments without fragmented DNA (NDF), cells with High-molecular weight fragments (HMWF), and cells with Intermediate and low-molecular weight fragments (IMWF + LMWF) [22].

2.8 | Statistics

Analysis of variance (ANOVA) and subsequent Fischer LSD test for determining the difference between exact sample pairs was carried out using Statistica 8.0 (Statsoft, Dell). Paired comparison between the treatment conditions was performed using the two tailed *t* test in Microsoft Excel. The results were considered significantly different at

$p < 0.05$. Correlation between percentage of pan-staining cells and cells in different stages of apoptosis was done using Spearman rank order correlation test using Statistica 8.0. A coefficient of determination (R^2) was calculated, which shows how well the data correlate.

3 | RESULTS

3.1 | Time kinetics of γH2AX pan-staining induced by low and high doses of γ-rays

We analyzed percentage of γH2AX pan-stained cells 0, 4, 18, and 42 h after irradiation with 0.1 and 2 Gy of γ-rays using IFC. Two patterns of γH2AX pan-staining were observed as has previously been described: (a) so called "apoptotic ring" [13], and (b) whole nuclei staining [8]. The nuclei of cells with γH2AX pan-staining were of smaller size displaying morphological markers of early apoptotic cells with shrunk nuclei and condensed chromatin. Of note, cells with apoptotic rings represented a very small fraction of the γH2AX pan-stained cells. These findings are in line with our previous study [2], where we have also observed these two types of pan-staining. The level of endogenous γH2AX pan-stained cells rose after 42 h incubation of unirradiated control cells (*t* test, $p = 0.02$). Analysis of the obtained data by univariate ANOVA revealed that γH2AX pan-staining was induced by ionizing radiation in dose ($p = 0.005$) and time ($p = 0.00002$) dependent manner (Figure 1). In-depth inspection of the data by Fisher LSD test showed that significant induction of pan-staining was present only 18 and 42 h after irradiation with 2 Gy ($p = 0.002$ and 0.006, respectively). The dose of 0.1 Gy was not sufficient to induce pan-staining. Thus, we can conclude that γH2AX pan-staining is induced with high but not low dose of γ-rays in UCB lymphocytes.

3.2 | Time kinetics of apoptosis induced by low and high doses of γ-rays

To validate pan-staining data obtained by IFC, we analyzed radiation—induced apoptosis using Annexin —V/PI assay by FC at the same time points as γH2AX pan-staining. In line with the γH2AX pan-staining data we observed decreased survival of cells after irradiation with γ-rays (ANOVA, time and dose $p < 0.0000001$) (Figure 2A) as well as increased level of the radiation induced apoptosis measured by means of Annexin -V positive (ANOVA, time $p = 0.002$; dose $p = 0.003$) (Figure 2A) and LAN cells (ANOVA, time and dose $p < 0.0000001$) (Figure 2A). Detailed analysis of data at each time point showed that only the 2 Gy dose, but not the 0.1 Gy dose, was sufficient to induce a significant decrease in cell survival 18 and 42 h post-irradiation (*t* test, $p = 0.005$, 0.0001, respectively). Neither 0.10 Gy nor 2 Gy were able to induce detectable amounts of apoptosis 4 h post-irradiation. Endogenous apoptosis observed in control samples increased with incubation time (Figure 2A). However significant decrease of cell survival was not present until 42 h incubation (*t* test, $p = 0.49$, 0.055, 0.002, for 4, 18, and 42 h post-irradiation, respectively). Finally, significant increase of γH2AX pan-stained cells was present at the same time points as a decreased cell survival using standard Annexin-V/PI assay (18 and 42 h post 2 Gy and 42 h of incubation in control samples). Thus, the data obtained by the IFC were confirmed using standard FC.

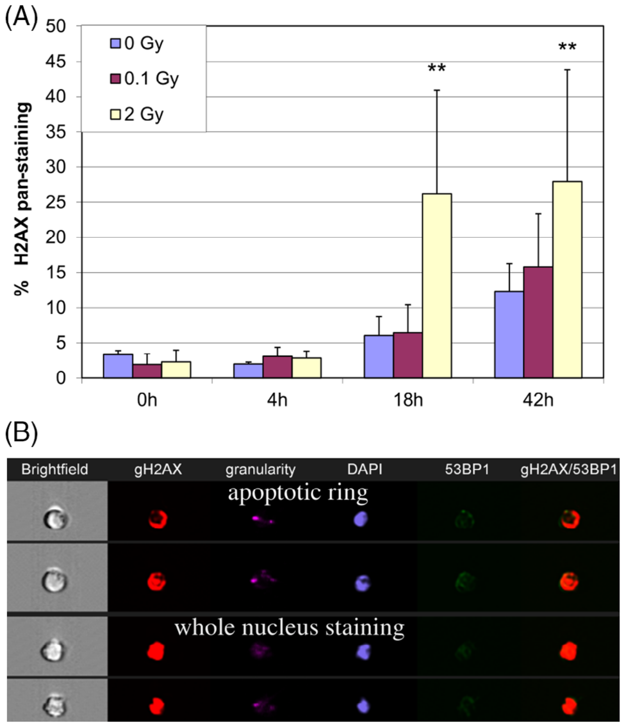

FIGURE 1 Induction of γH2AX pan-staining by IR. Figure shows (a) level of γH2AX pan-staining at different time points after irradiation with 0, 0.1 and 2 Gy of γ-rays as analyzed by imaging flow cytometry. Data from three independent experiments along with *SD* are shown. (B) Representative images of cells displaying whole nucleus γH2AX pan-staining and apoptotic ring. * $p < 0.05$; ** $p < 0.01$; *** $p < 0.0001$ [Color figure can be viewed at wileyonlinelibrary.com]

3.3 | Correlation between γH2AX pan-staining and apoptosis

Next, we correlated the dataset from all irradiation doses and time-points for γH2AX pan-staining with the data from Annexin-V/PI assay. We have found negative correlation of γH2AX pan-staining with the percentage of live cells (Spearman $R = -0{,}739$; $p < 0.0000001$) (Figure 3A), and positive correlations between γH2AX pan-staining and percentage of early apoptotic (Spearman $R = 0.48$; $p < 0.005$) (Figure 3B) as well as LAN cells (Spearman $R = 0{,}76$; $p < 0.0000001$) (Figure 3C). These results provide the experimental evidence that the samples with higher percentage of apoptosis exhibit also higher level of γH2AX pan-staining and that γH2AX pan-staining can be used as a marker of apoptosis. Percentage of early apoptotic cells was about 2-fold lower than the total amount of γH2AX

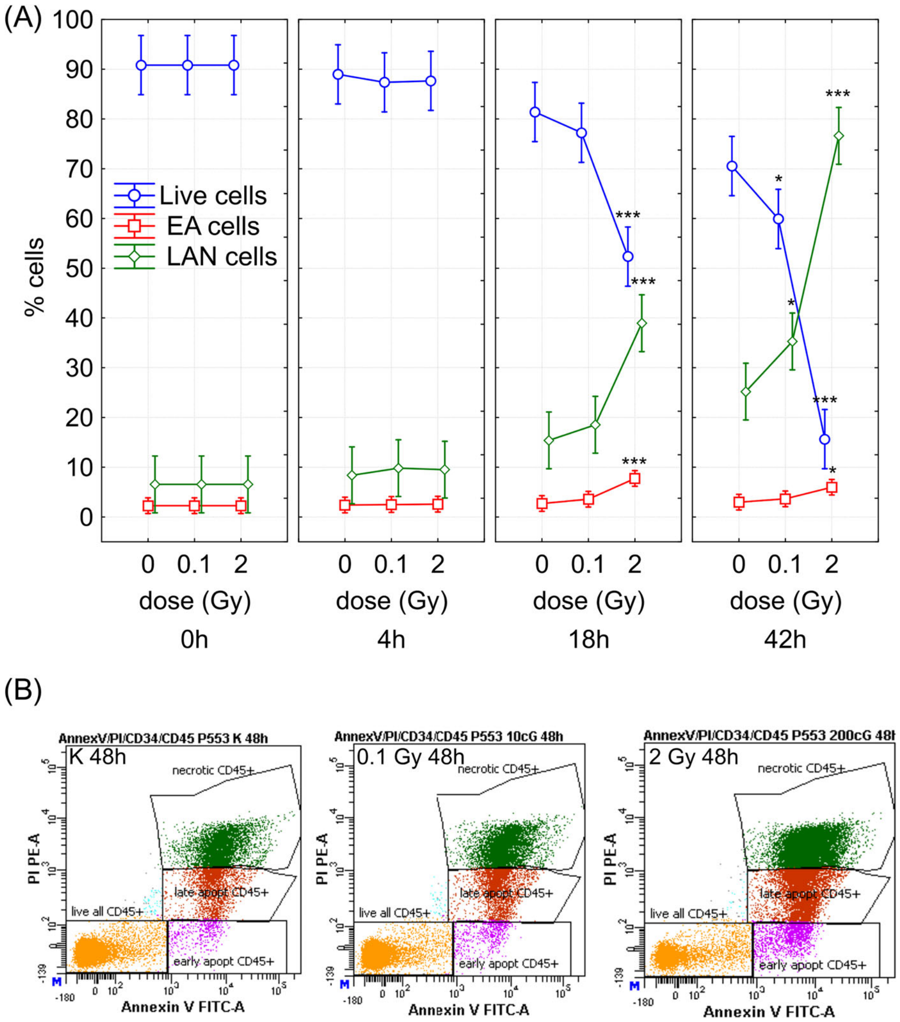

FIGURE 2 Apoptosis after IR. Figure shows (a) percentage of live cells, early apoptotis (EA) cells and late apoptotic/necrotic (LAN) cells at various time points post-irradiation with 0, 0.1 and 2 Gy of γ-rays as analyzed by Annexin/PI assay using flow cytometry. Data from three independent experiments with 95% confidence interval are shown.
(B) Representative gating of cells in BD FACS Diva software. Cells were gated as live, EA, late apoptotic, and necrotic. Percentage of LAN cells was obtained after counting late apoptotic and necrotic cells together. * $p < 0.05$; ** $p < 0.01$; *** $p < 0.0001$ [Color figure can be viewed at wileyonlinelibrary.com]

pan-stained cells 18 and 42 h post-irradiation indicating that γH2AX pan-staining arises in early apoptosis and further develops at the later apoptotic stages. In conclusion, the revealed by us correlation between γH2AX pan-staining and apoptosis indicated that γH2AX pan-staining can be considered as a marker of apoptosis.

3.4 | γH2AX pan-staining and 53BP1 DNA repair foci in cells sorted according to stage of apoptosis by FACS

To directly investigate specific stage of apoptosis, in which γH2AX pan-staining occur, we sorted live, early apoptotic, and LAN cells 24 h post-irradiation with 2 Gy of γ-rays and subsequently analyzed them for γH2AX pan-staining using the Metafer automated FM system. Analysis of the obtained data by multivariate ANOVA has revealed differences between sorted populations in their level of pan-staining ($p = 0.03$). We found that the most enriched population for γH2AX pan-staining cells were early-apoptotic cells (10.4 and 12.2% after 0 and 2 Gy, respectively) (Figure 4). However, γH2AX pan-staining cells were also present in the LAN cell fraction (4.2 and 3.5% after 0 and 2 Gy, respectively) (Figure S3). Clearly, not all early apoptotic/LAN cells displayed γH2AX pan-staining. Further analysis by Fisher LSD test showed that statistically significant difference was present only between early apoptotic cells and live cells ($p = 0.048$), in which practically no pan-staining (< 1%) was seen (Figure 4A). Despite significantly increased apoptosis in irradiated cells, the distribution of γH2AX pan-stained cells between apoptotic fractions was similar in irradiated and unirradiated cells suggesting similar kinetics of γH2AX pan-staining during endogenous and radiation-induced apoptosis (Figure 4A). The absolute value of pan-stained cells per 100,000 cells did not differ significantly in the early apoptotic and LAN cells, showing similar distribution of the pan-stained cells between these two populations in both irradiated and unirradiated cells (Figure S4). Importantly, percentage of γH2AX pan-staining obtained using FM was much lower compared with results obtained with IFC (Table 1). This finding suggests that some pan-stained cells are lost during standard fixation to the microscopic slides after cell sorting and indicates that IFC is the best choice method for analysis of pan-staining. From overall results we conclude that γH2AX pan-staining appears in early apoptotic cells, but remain and even continue to form in some cells until late stages of apoptotic transformation.

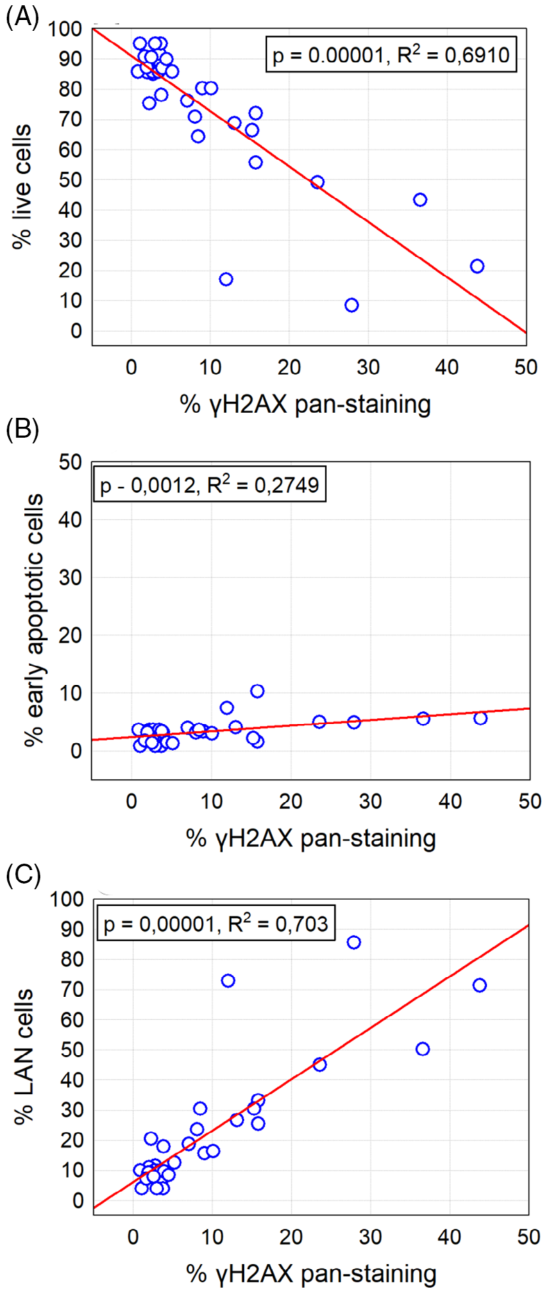

FIGURE 3 Correlation of γH2AX pan-staining with different stages of apoptosis. Percentage of γH2AX pan-staining is correlated with live (A), early apoptotic (B), and LAN (C) cells. Linear regression is indicated as solid line along with the coefficient of determination (R^2) and spearman test *p*-value. Data from three independent experiments were correlated [Color figure can be viewed at wileyonlinelibrary.com]

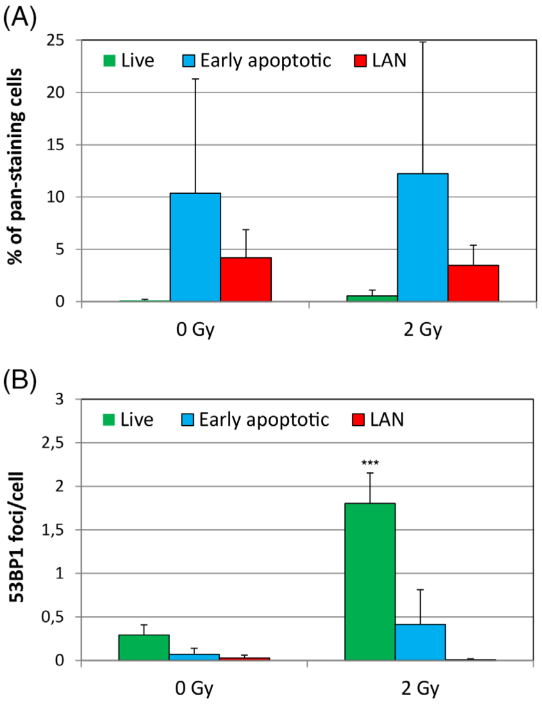

FIGURE 4 γH2AX pan-staining and 53 BP1 foci in different stages of apoptosis. Figure shows percentage of γH2AX pan-staining cells in sorted live, early apoptotic and LAN cells 24 h after irradiation with 0 and 2 Gy as analyzed by fluorescent microscopy (A) and number of 53BP1 foci/ in sorted live, early apoptotic, and LAN cells after irradiation with 0 and 2 Gy as analyzed by fluorescent microscopy (B). The data from three independent experiments along with *SD* are shown. * $p < 0.05$; ** $p < 0.01$; *** $p < 0.0001$ [Color figure can be viewed at wileyonlinelibrary.com]

In this study, we also analyzed correlation between onset of apoptosis, γH2AX pan-staining and 53BP1 DNA repair foci in cells sorted according to the stage of apoptosis. No 53BP1 foci were found in the γH2AX pan-stained cells, what is in line with the previously published data [8]. Statistically significant effect of IR on the level of 53BP1 foci was observed only in live cells ($p = 0.000037$) (Figures 4B and S3). At the same time, there were some 53BP1 foci in the sorted early apoptotic cells after irradiation, what may be due to the fact that those cells have not already developed apoptotic transformation and DNA damage response has not been completed. Formation of radiation-induced 53BP1 foci in live cells was significantly higher than in early apoptotic cells ($p = 0.00000$) and LAN cells ($p = 0.000000$). There was lack of 53BP1 foci in sorted early endogenously apoptotic and LAN cells (Figure 4B). Thus, we can conclude that while 53BP1 foci are induced in live cells, they remain in cells till the onset of early apoptosis and completely disappear at the latter apoptotic stages.

3.5 | Kinetics of γH2AX pan-staining in relationship to apoptotic DNA fragmentation

We analyzed different stages of endogenous and IR-induced apoptotic DNA fragmentation using comet assay. Samples were analyzed immediately and 24 h after irradiation with 2 Gy. Non-defined fragments (NDF), high molecular weight fragments (HMWF) and intermediate molecular weight fragments/low molecular weight fragments (IMWF/LMWF) were assigned to live, early apoptotic and LAN cells (Figure S5), respectively, as previously described [22].

Analysis of results by multifactorial ANOVA showed that the level of DNA fragmentation is induced 24 h post-irradiation ($p = 0.002$) and also increases with the time of incubation ($p = 0.01$). Percentage

TABLE 1 Table compare percentage of γH2AX pan-staining cells obtained by ImageStream and fluorescence microscopy (Metafer) after sorting that were subsequently fixed on the microscopic slides

Time	Dose	Pan-staining ImageStream (%)	h pan-staining fluorescence microscopy (%)
18 h	0 Gy	6.02	1.39
	2 Gy	26.2	3

Note: All populations, namely live, early apoptotic, and LAN cells were taken together.

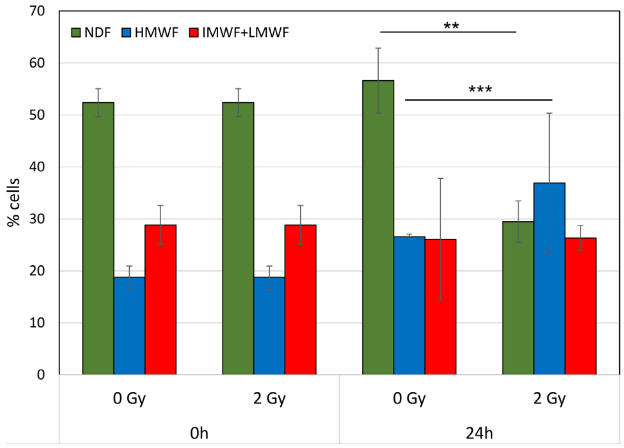

FIGURE 5 Apoptotic DNA fragmentation after IR. Percentage of cells displaying non-defined fragments (NDF), intermediate and high molecular weight fragments (IMWF and HMWF) and low molecular weight fragments (LMWF) in control cells and cells irradiated with 2 Gy of γ-rays is shown. Data from four experiments along with *SD* are shown. * $p < 0.05$; ** $p < 0.01$; *** $p < 0.0001$ [Color figure can be viewed at wileyonlinelibrary.com]

of cells exhibiting NDF were significantly reduced after irradiation with 2 Gy ($p = 0.002$) while HMWF cells were induced by irradiation ($p = 0.001$) (Figure 5A,C). Only percentage of IMWF/LMWF cells was not significantly changed after irradiation (Figure 5B). On the other hand, complementary analysis of apoptosis using Annexin-V/7-AAD assay showed changes in percentage of all fractions, namely live, early apoptotic, and LAN cells (Figure S6). Percentage of NDF significantly correlated with the level of live cells ($p = 0.000161$). HMWF fragments were also induced in time ($p = 0.000011$) and dose-dependent ($p = 0.000866$) manner. Neither HMWF correlated significantly with the level of early apoptotic cells, nor IMWF+LMWF group correlated with the percentage of LAN cells.

In conclusion, while analysis of apoptotic DNA fragmentation by comet assay could be used as a marker of apoptosis it is not that sensitive as the cytometric Annexin-V/7-AAD assay.

3.6 | Pan-staining and DNA repair foci in PBL of breast cancer patients

To the aim of applying IFC for analysis of γH2AX/53BP1 foci along with γH2AX pan-staining we analyzed lymphocytes isolated from peripheral blood of BC patients. We observed low level of endogenous γH2AX foci (0.14 ± 0.12 foci/cell) with very low fluorescence background, what is significant advantage for future applications of this method. On the other hand, relatively high level of 53BP1 foci (1.72 ± 0.63) was present (Figure 6A). Based on morphology characteristics, all these foci could be classified as residual foci, which remain long time after induction and may represent unrepaired DNA damage or alternations in chromatin structure [26]. Thus, revealed differences between γH2AX and 53BP1 foci may indicate longer persistence of 53BP1 protein as compared to persistence of phosphorylated H2AX at the locations of DSB in lymphocytes of BC patients. Different kinetics of these processes at the location of radiation induced DNA damage has already been described [27]. In addition, we found significantly lower number of γH2AX foci in UCB (0.025 ± 0.013) compare to the BC samples (*t* test, $p = 0.014$), but not in 53BP1 foci (*t* test, $p = 0.5$) (Figure 6A). Very low number of γH2AX pan-stained cells was observed (0.8 ± 0.2) in the BC samples, since the number of apoptotic cells in fresh blood samples is usually very low. When compared to the BC samples, percentage of γH2AX pan-stained cells was significantly higher in the UCB samples (6.9 +/− 2.6) (*t* test, $p = 0.002$) (Figure 6B). Most likely reason is the freezing–thawing cycle, which induced apoptosis in a number of the UCB cells. In conclusion, we successfully tested the ImageStream IFC technique for analysis of DNA repair foci and γH2AX pan-staining in BC patients, which might be feasible for evaluation of individual radiosensitivity.

4 | DISCUSSION

In the presented study, we analyzed γH2AX pan-staining that was previously described as a marker of apoptosis [13,14,19] [2,8]. Along with usually applied fluorescent microscopy we have also used imaging flow cytometry. Moreover, using cell sorting and Annexin V/PI assay, we investigated kinetics of γH2AX pan-staining through stages of apoptotic process. Percentage of γH2AX pan-staining cells observed in each of the sorted fractions by FM was much lower compare to pan-staining detected by IFC. In line with our previous studies [8,9], we did not observe dose response of γH2AX pan-staining using FM. However, clear dose response was present when IFC was used. These data are in line with our previous study where we observed increased level of γH2AX fluorescence 18 h after 2 Gy of IR using standard flow cytometry. This increase could be accounted for the increased level of γH2AX pan-staining since standard flow cytometry lacks sensitivity to detect low amount of residual γH2AX foci remaining 18 h after irradiation [28]. The most probable reason for this inter-methodological difference is the fact that not all γH2AX pan-staining cells are able to attach onto the microscopic slides during routine cytotospin centrifugation or/and are washed away during immunostaining procedures. Poly-l-lysine microscope slides are coated placing a permanent positive charge on the microscope slide what ensures a firm electrostatic attraction of cells and tissue sections to the slide binding them to the glass surface. Cell loss during cytospin and immunostaining procedures could be accounted for a change in surface charge on the membrane of the apoptotic cells. The membranes of apoptotic cells are known to have greater fluidity [29]. Their protein organization is changed and their membrane asymmetry is partially lost what could generate changes in the surface charge of these cells [30]. Massive phosphorylation of proteins, such as γH2AX, ATM and DNA-PK, during apoptosis, which changes the total charge of the cell nucleus, could also play a role in the differences in membrane potential that could also account for poor attachment of the γH2AX pan-stained cells to the microscopic slides.

We used IFC for analyzing both time and dose-dependent induction of γH2AX pan-staining in UCB cells and BC patients' PBL. In addition, comet assay was used for analysis of apoptotic DNA fragmentation. Our experiments with cell sorting have shown that the γH2AX pan-staining appear in early apoptotic and remain in LAN cells. These results are in line with the results of Anglada et al. who also observed γH2AX pan-staining in both early and late apoptotic cells [18]. However, only small amount of early apoptotic and LAN cells displayed γH2AX pan-staining pattern, independently on the γ-ray irradiation. The question whether this fraction represents a specific cell population (e.g., B- or CD8+ T- lymphocytes) is warranted to be addressed by further research.

Importantly, a significant increase of γH2AX pan-staining cells was revealed at the same time points (18 and 42 h) where similar decrease/increase in live/LAN cells was detected using Annexin-V/7-AAD assay. Percentage of γH2AX pan-staining obtained by IFC correlated positively with both early apoptotic and LAN cells as analyzed using flow cytometry, but correlation with LAN cells was more significant than with early apoptotic cells (Figure 3). Indeed, the total number of γH2AX pan-stained cells was highest in the sorted LAN cells (Figure S4). In combination, our data indicate that the LAN cells contain majority of γH2AX pan-stained cells. Higher number of pan-stained cells among LAN cells could be accounted for the fact that cells spend longer time in the later stages of apoptosis in comparison to earlier stages. This hypothesis is supported by the data showing no time dependence in accumulation of early apoptotic cells contrary to LAN cells (Figure 2). In fact, the percentage of early apoptotic cells tends to remain the same at different time-points post-irradiation and also after incubation of unirradiated cells suggesting that subset of early apoptotic cells moving into later stages of apoptosis is replaced by the cells that have just started apoptotic process.

Results of Solier and Pommier and also Ding's et al. study have shown that γH2AX pan-staining co-localize with apoptotic DNA fragmentation analyzed by TUNEL assay [13,14,17]. Ding observed more than 94% co-localization between TUNEL assay staining and γH2AX pan-staining. Since the TUNEL staining visualizes DSB occurring in both early and late phases of apoptosis, while at higher intensity of signal in late apoptosis, these results confirmed prevalence of γH2AX pan-staining in both stages of the apoptotic process. Our data are in line with results by other research groups [17,18] and strongly suggest that γH2AX pan-staining appears in the earlier stages of apoptosis and preserves in the latter stages of apoptotic transformation.

Next, we analyzed apoptotic DNA fragmentation using comet assay. During apoptosis of human lymphocytes, 2 Mb DNA loops are cleaved from chromosomal DNA followed by subsequent cleavage to 50 kb fragments and further fragmentations to oligonucleosomes [20,21]. We assigned various degrees of DNA fragmentation to live, early apoptotic and LAN cells as previously described [22]. Percentage of NDF correlated well with the live cells. No correlations of HMWF

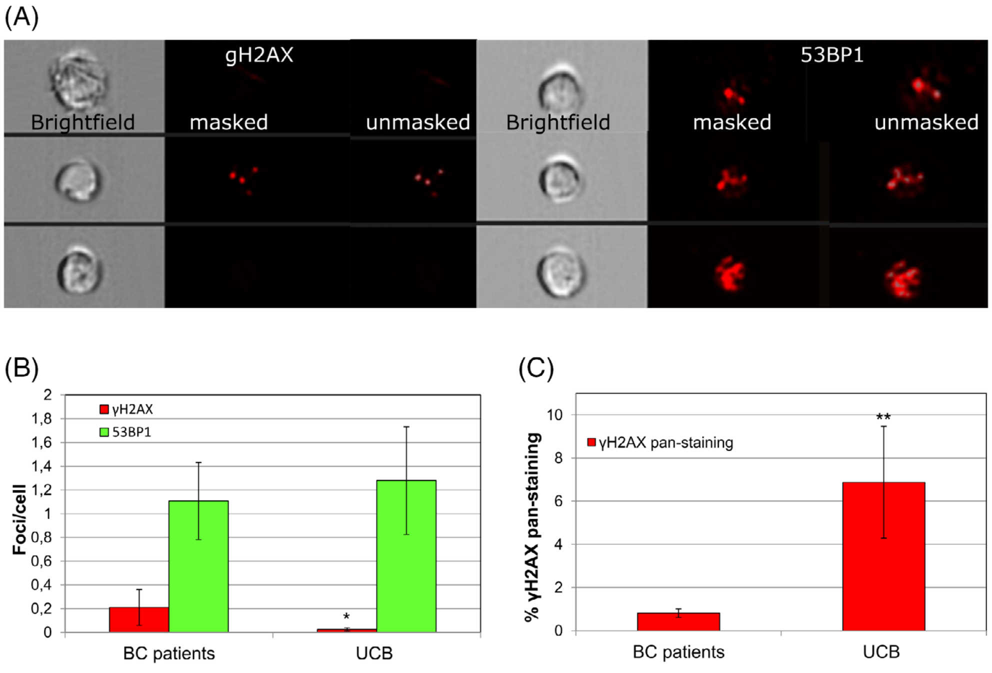

FIGURE 6 DNA damage and γH2AX pan-staining in BC and UCB lymphocytes. Figure shows (A) representative images of γH2AX/53BP1 DNA repair foci in cells from BC patients. Cells in brightfield and fluorescence in channel 2 (505–560 nm) are shown before and also after the application of custom-made mask (B) number of γH2AX/53BP1 DNA repair foci per cell in BC patients 1 year after radiotherapy and thawed UCB lymphocytes and (C) percentage of γH2AX pan-stained cells in BC and UCB lymphocytes. Data from 5 BC patients and 6 UCB samples are shown along with *SD*. * $p < 0.05$; ** $p < 0.01$; *** $p < 0.0001$ [Color figure can be viewed at wileyonlinelibrary.com]

and IMWF/LMWF fragments were observed with early apoptotic and LAN cells, respectively. While we did not observe correlation of HMWF with percentage of early apoptotic cells, significant induction of HMWF 24 h post-irradiation was seen. We hypothesize that cleavage of DNA into 2 Mb relaxed loops takes place even before flipping of phosphatidylserines that are a substrate for Annexin proteins. This hypothesis is supported by comparison of changes in the levels of NDF/HMWF obtained with comet assay and live/early apoptotic cells as analyzed using flow cytometry. Namely, 18 h after irradiation percentage of HMWF was about 20% higher compared to early apoptotic cells as analyzed using Annexin assay (45% vs. 25%, respectively). Approximately the same difference was observed between percentages of NDF compared with cytometry-analyzed live cells (30% vs. 50%, respectively). Similarly, higher percentage of HMWF and lower percentage of NDF could mean that some cells detected 18 h after irradiation as live using Annexin/7-AAD assay are in the very early stage of apoptosis since they have already started DNA fragmentation.

Kinetics of DNA fragmentation and γH2AX pan-staining obtained by IFC were in somewhat different. In particular, γH2AX pan-staining obtained by IFC rose from 5% to 25% 0–18 h after 2 Gy of IR while HMWF and IMWF/LMWF increased from 25% to 45% and from 20% to 25%, respectively. While DNA fragmentation is an irreversible process. Total phosphorylation of γH2AX occurs only for a short time during the course of apoptosis. These data also supported our FM data, which showed that not all of the apoptotic cells display pan nuclear γH2AX staining.

Using IFC analysis, but not FM, we found that γH2AX pan-staining could be induced in the dose and time dependent manner. These data provide further evidence for advantage of IFC analysis over FM. We observed induction of γH2AX pan-staining 18 and 42 h after 2 Gy of γ – rays what supported and broaden the results of Ding et al. that showed induction of γH2AX pan-staining 24 h after irradiation with 0.5 Gy of X-rays in fresh adult PBL [17]. Our current study along with previously published data [24] showed that the low dose of 0.1 Gy was not sufficient to induce either γH2AX pan-staining or decrease live cell percentage as detected using Annexin/7-AAD. In combination, our and Ding's results show that the threshold dose for detection of apoptosis, as analyzed both by γH2AX pan-staining and Annexin-V/7-AAD assays using IFC and FM, respectively, is between 0.1 and 0.5 Gy. We conclude that sensitivity of pan-staining assay if analyzed by IFC but not FM is the same as sensitivity of Annexin-V/7-AAD assay in detection of IR-induced apoptosis in human lymphocytes.

We did not observe any 53BP1 foci either in the γH2AX pan-stained cells or in the LAN cells, what suggest that DNA repair processes do not take place in the cells that are already in the process of the apoptotic transformation. Some 53BP1 foci were present in the subset of early apoptotic cells, but those cells did not display γH2AX pan-staining pattern. Ding et al. showed that other proteins like ATM and DNA-PKcs, co-localized with the γH2AX pan-staining in the apoptotic cells [17], what may suggest binding of these proteins to the ends of apoptotically fragmented DNA. Whole nucleus hyperphosphorylation of abovementioned DNA repair proteins, that probably takes place on the ends of apoptotically fragmented DNA. This hyperphosphorylation could possibly mechanistically eliminate binding of 53BP1 to the DNA breaks as was supported by our results showing no 53BP1 foci in the pan-stained cells. In conclusion our results showed that 53BP1 foci are present only in live cells and not in the apoptotic cells with fragmented DNA. Thus, we conclude that 53BP1 does not bind to the broken ends of apoptotically fragmented DNA and could not be used as a marker of DNA breaks present during DNA fragmentation that occurs during apoptosis.

FM based γH2AX/53BP1 assay has already been tested to predict the individual response of cancer patients to radiotherapy [1,10,31]. So far, this technique was not sensitive and specific enough to distinguish patients with adverse outcome of the therapy from normal responders to the degree that the method could be used in clinics. One limitation is relatively high background restraining efficiency of γH2AX/53BP1 focus assessment. Here, we tested γH2AX/53BP1 foci assay based on the imaging flow cytometry, which is characterized by the lack of fluorescence background, that may be responsible for the insufficient sensitivity and specificity of the FM based γH2AX assay. Indeed, the results of IFC analysis showed very low level of fluorescence background, which will facilitate distinguishing relatively small changes in foci level that is suspected in radiosensitive patients [10].

Comparison of the level of γH2AX foci in the BC patients' samples and UCB showed that BC patients had significantly higher level of γH2AX but not 53BP1 foci. This could be accounted to the fact that mean age of BC patients was 55.8 ± 13 years and UCB samples are derived from blood taken during the birth. Indeed, Rube et al. found that level of γH2AX foci in elderly people were higher than in newborns UCB [32]. The detected between UCB and BC PBL difference might be also due to higher level of DNA damage present in cancer patients compare to healthy subjects, what is in line with our previously published data [10]. On the other hand, the level of γH2AX pan-staining representing fraction of apoptotic cells was significantly higher in UCB samples compare to patients' samples. The reason behind this result may be the fact that UCB cells were frozen in liquid nitrogen and then thawed while fresh samples from BC patients were analyzed. Thus, the difference in the level of γH2AX pan-staining could be accounted to induction of apoptosis by the freezing–thawing cycle. Based on our results we concluded that application of IFC for testing γH2AX foci/pan-staining in the BC samples could be potentially useful in assessing the level of individual radiosensitivity in a clinically relevant cohort of patients.

ACKNOWLEDGMENTS

We are thankful to Dr. G. Kralik and Dr. K. Kontrisova, St. Elisabeth Cancer Institute, Bratislava, Slovak Republic for the irradiation of cells by γ-rays. This work was supported by the Structural Funds of EU (Protonbeam, ITMS: 26220220200), the Slovak Research and Development Agency (APVV 15-0250); the project TRANSMED 2, ITMS: 26240120030, supported by the Research & Development Operational Program funded by the ERDF, International Atomic Energy Agency, IAEA RA No: 22259/R0, and the Vedecká grantová agentúra

BACK TO CONTENTS

(VEGA) Grant Agency (2/0089/18, 2/0147/17) of the Slovak Republic.

AUTHOR CONTRIBUTIONS

Matus Durdik: Conceptualization; data curation; formal analysis; investigation; methodology; visualization; writing-original draft; writing-review & editing. **Pavol Kosik:** Data curation; investigation; methodology. **Lukas Jakl:** Data curation; formal analysis; investigation; methodology. **Maria Kozackova:** Investigation; methodology. **Eva Markova:** Funding acquisition; investigation; methodology; project administration. **Katarina Vigasova:** Investigation; methodology; visualization. **Katarina Beresova:** Investigation; methodology; visualization. **Jana Jakubikova:** Methodology. **Eva Horvathova:** Methodology. **Lucian Zastko:** Investigation. **Marta Fekete:** Investigation. **Ingrid Zavacka:** Investigation. **Margita Pobijakova:** Investigation; resources. **Igor Belyaev:** Conceptualization; formal analysis; funding acquisition; project administration; supervision.

CONFLICT OF INTEREST

The authors report no conflicts of interest.

REFERENCES

1. Roch-Lefèvre S, Voisin P, Gaëtan G, Mesa JEG, Valente M, Bonnesoeur P, et al. Quantification of gamma-H2AX foci in human lymphocytes: a method for biological dosimetry after ionizing radiation exposure. Radiat Res. 2010;174:185–94.
2. Durdik M, Kosik P, Gursky J, Vokalova L, Markova E, Belyaev I. Imaging flow cytometry as a sensitive tool to detect low-dose-induced DNA damage by analyzing 53BP1 and gammaH2AX foci in human lymphocytes. Cytometry A. 2015;87:1070–8.
3. Lobrich M, Rief N, Kuhne M, Heckmann M, Fleckenstein J, Rube C, et al. In vivo formation and repair of DNA double-strand breaks after computed tomography examinations. Proc Natl Acad Sci U S A. 2005;102:8984–9.
4. Jakl L, Lobachevsky P, Vokálová L, Durdík M, Marková E, Belyaev I. Validation of JCountPro software for efficient assessment of ionizing radiation-induced foci in human lymphocytes. Int J Radiat Biol. 2016;92:766–73.
5. Rogakou EP, Boon C, Redon C, Bonner WM. Megabase chromatin domains involved in DNA double-strand breaks in vivo. J Cell Biol. 1999;146:905–16.
6. Schultz LB, Chehab NH, Malikzay A, Halazonetis TD. p53 binding protein 1 (53BP1) is an early participant in the cellular response to DNA double-strand breaks. J Cell Biol. 2000;151:1381–90.
7. Vandevoorde C, Vral A, Vandekerckhove B, Philippé J, Thierens H. Radiation sensitivity of human CD34(+) cells versus peripheral blood T lymphocytes of newborns and adults: DNA repair and mutagenic effects. Radiat Res. 2016;185:580–90.
8. Vasilyev SA, Kubes M, Markova E, Belyaev I. DNA damage response in CD133 + stem/progenitor cells from umbilical cord blood: low level of endogenous foci and high recruitment of 53BP1. Int J Radiat Biol. 2013;89:301–9.
9. Jakl L, Markova E, Kolarikova L, Belyaev I. Biodosimetry of low dose ionizing radiation using dna repair foci in human lymphocytes. Genes (Basel). 2020;11(1):58.
10. Marková E, Somsedíková A, Vasilyev S, Pobijaková M, Lacková A, Lukačko P, et al. DNA repair foci and late apoptosis/necrosis in peripheral blood lymphocytes of breast cancer patients undergoing radiotherapy. Int J Radiat Biol. 2015;91:934–45.
11. Lobachevsky P, Leong T, Daly P, Smith J, Best N, Tomaszewski J, et al. Compromized DNA repair as a basis for identification of cancer radiotherapy patients with extreme radiosensitivity. Cancer Lett. 2016;383:212–9.
12. Djuzenova CS, Elsner I, Katzer A, Worschech E, Distel LV, Flentje M, et al. Radiosensitivity in breast cancer assessed by the histone gamma-H2AX and 53BP1 foci. Radiat Oncol. 2013;8:98.
13. Solier S, Pommier Y. The apoptotic ring: a novel entity with phosphorylated histones H2AX and H2B and activated DNA damage response kinases. Cell Cycle. 2009;8:1853–9.
14. Solier S, Pommier Y. The nuclear gamma-H2AX apoptotic ring: implications for cancers and autoimmune diseases. Cell Mol Life Sci. 2014;71:2289–97.
15. Zastko L, Petrovičová P, Račková A, Jakl L, Jakušová V, Marková E, et al. DNA damage response and apoptosis induced by hyperthermia in human umbilical cord blood lymphocytes. Toxicol In Vitro. 2021;73:105127.
16. Zastko L, Račková A, Petrovičová P, Durdík M, Míšek J, Marková E, Belyaev I. Evaluation of Calyculin A Effect on γH2AX/53BP1 Focus Formation and Apoptosis in Human Umbilical Cord Blood Lymphocytes. Int J Mol Sci. 2021;22:5470.
17. Ding D, Zhang Y, Wang J, Zhang X, Gao Y, Yin L, et al. Induction and inhibition of the pan-nuclear gamma-H2AX response in resting human peripheral blood lymphocytes after X-ray irradiation. Cell Death Dis. 2016;2:16011.
18. Anglada T, Terradas M, Hernandez L, Genesca A, Martin M. Analysis of residual DSBs in ataxia-telangiectasia lymphoblast cells initiating apoptosis. Biomed Res Int. 2016;2016:8279560.
19. Turesson I, Nyman J, Qvarnström F, Simonsson M, Book M, Hermansson I, et al. A low-dose hypersensitive keratinocyte loss in response to fractionated radiotherapy is associated with growth arrest and apoptosis. Radiother Oncol. 2010;94:90–101.
20. Torudd J, Protopopova M, Sarimov R, Nygren J, Eriksson S, Marková E, et al. Dose-response for radiation-induced apoptosis, residual 53BP1 foci and DNA-loop relaxation in human lymphocytes. Int J Radiat Biol. 2005;81:125–38.
21. Belyaev IY. DNA loop organization and DNA fragmentation during radiation-induced apoptosis in human lymphocytes. Radiats Biol Radioecol. 2005;45:541–8.
22. Czene S, Testa E, Nygren J, Belyaev I, Harms-Ringdahl M. DNA fragmentation and morphological changes in apoptotic human lymphocytes. Biochem Biophys Res Commun. 2002;294:872–8.
23. Sorokina S, Markova E, Gursky J, Dobrovodsky J, Belyaev I. Relative biological efficiency of protons at low and therapeutic doses in induction of 53BP1/gammaH2AX foci in lymphocytes from umbilical cord blood. Int J Radiat Biol. 2013;89:716–23.
24. Durdik M, Kosik P, Kruzliakova J, Jakl L, Markova E, Belyaev I. Hematopoietic stem/progenitor cells are less prone to undergo apoptosis than lymphocytes despite similar DNA damage response. Oncotarget. 2017;8:48846–53.
25. Durdik M, Kosik P, Markova E, Somsedikova A, Gajdosechova B, Nikitina E, et al. Microwaves from mobile phone induce reactive oxygen species but not DNA damage, preleukemic fusion genes and apoptosis in hematopoietic stem/progenitor cells. Sci Rep. 2019;9:16182.
26. Markova E, Schultz N, Belyaev IY. Kinetics and dose-response of residual 53BP1/gamma-H2AX foci: Co-localization, relationship with DSB repair and clonogenic survival. Int J Radiat Biol. 2007;83:319-329.
27. Belyaev IY, Markova E, Hillert L, Malmgren LO, Persson BR. Microwaves from UMTS/GSM mobile phones induce long-lasting inhibition of 53BP1/gamma-H2AX DNA repair foci in human lymphocytes. Bioelectromagnetics. 2009;30:129-41.
28. Kosik P, Durdik M, Jakl L, Skorvaga M, Markova E, Vesela G, et al. DNA damage response and preleukemic fusion genes induced by

ionizing radiation in umbilical cord blood hematopoietic stem cells. Sci Rep. 2020;10:13722.

29. Ma Y, Poole K, Goyette J, Gaus K. Introducing membrane charge and membrane potential to T cell signaling. Front Immunol. 2017;8:1513.
30. Weihua Z, Tsan R, Schroit AJ, Fidler IJ. Apoptotic cells initiate endothelial cell sprouting via electrostatic signaling. Cancer Res. 2005;65:11529–35.
31. Horn S, Barnard S, Brady D, Prise KM, Rothkamm K. Combined analysis of gamma-H2AX/53BP1 foci and caspase activation in lymphocyte subsets detects recent and more remote radiation exposures. Radiat Res. 2013;180:603–9.
32. Rube CE, Fricke A, Widmann TA, Furst T, Madry H, Pfreundschuh M, Rube C. Accumulation of DNA damage in hematopoietic stem and progenitor cells during human aging. PLoS One. 2011;6:e17487.

SUPPORTING INFORMATION

Additional supporting information may be found online in the Supporting Information section at the end of this article.

RESEARCH ARTICLE

NANO · MICRO small
www.small-journal.com

In Vivo Endothelial Cell Gene Silencing by siRNA-LNPs Tuned with Lipoamino Bundle Chemical and Ligand Targeting

Mina Yazdi, Jana Pöhmerer, Morteza Hasanzadeh Kafshgari, Johanna Seidl, Melina Grau, Miriam Höhn, Victoria Vetter, Cosima C. Hoch, Barbara Wollenberg, Gabriele Multhoff, Ali Bashiri Dezfouli,* and Ernst Wagner**

Although small-interfering RNAs (siRNAs) are specific silencers for numerous disease-related genes, their clinical applications still require safe and effective means of delivery into target cells. Highly efficient lipid nanoparticles (LNPs) are developed for siRNA delivery, showcasing the advantages of novel pH-responsive lipoamino xenopeptide (XP) carriers. These sequence-defined XPs are assembled by branched lysine linkages between cationizable polar succinoyl tetraethylene pentamine (Stp) units and apolar lipoamino fatty acids (LAFs) at various ratios into bundle or U-shape topologies. Formulation of siRNA-LNPs using LAF$_4$-Stp$_1$ XPs as ionizable compounds led to robust cellular uptake, high endosomal escape, and successful in vitro gene silencing activity at an extremely low (150 picogram) siRNA dose. Of significance is the functional in vivo endothelium tropism of siRNA-LNPs with bundle LAF$_4$-Stp$_1$ XP after intravenous injection into mice, demonstrated by superior knockdown of liver sinusoidal endothelial cell (LSEC)-derived factor VIII (FVIII) and moderate silencing of hepatocyte-derived FVII compared to DLin-MC3-DMA-based LNPs. Optimizing lipid composition following click-modification of siRNA-LNPs with ligand c(RGDfK) efficiently silenced vascular endothelial growth factor receptor-2 (VEGFR-2) in tumor endothelial cells (TECs). The findings shed light on the role of ionizable XPs in the LNP in vivo cell-type functional targeting, laying the groundwork for future therapeutic applications.

1. Introduction

Nucleic acid therapy is a pioneering approach in gene-based medicine, allowing highly selective and potent therapeutic effects toward various life-threatening diseases. Within this concept, the synthetic small-interfering RNA (siRNA) has emerged as a powerful tool to reversibly silence the expression of target genes in a sequence-specific manner by RNA interference (RNAi) phenomenon.[1] Chemically stabilized siRNA conjugated with tri-GalNAc for potent receptor-targeted gene silencing in hepatocytes has been the basis for Inclisiran (Leqvio) and several other approved siRNA drugs.[2–4] Despite this impressive success in liver cell targeting, the clinical use of siRNA to target other tissues is still hampered due to the shortage of safe and efficient delivery systems. As potential alternatives to siRNA conjugates, theoretically ideal nanocarrier systems ensure optimal encapsulation of exogenous synthetic siRNAs and thereby facilitate their systemic circulation for efficacious uptake as well as

---

M. Yazdi, J. Pöhmerer, J. Seidl, M. Grau, M. Höhn, V. Vetter, E. Wagner
Pharmaceutical Biotechnology
Department of Pharmacy
Ludwig-Maximilians-Universität (LMU)
81377 Munich, Germany
E-mail: mina.yazdi@cup.uni-muenchen.de; ernst.wagner@lmu.de

M. Yazdi, E. Wagner
CNATM – Cluster for Nucleic Acid Therapeutics
81377 Munich, Germany

The ORCID identification number(s) for the author(s) of this article can be found under https://doi.org/10.1002/smll.202400643

DOI: 10.1002/smll.202400643

M. Hasanzadeh Kafshgari, G. Multhoff, A. Bashiri Dezfouli
Central Institute for Translational Cancer Research (TranslaTUM), TUM School of Medicine and Health
Technical University of Munich (TUM)
81675 Munich, Germany
E-mail: ali.bashiri@tum.de

M. Hasanzadeh Kafshgari, G. Multhoff, A. Bashiri Dezfouli
Department of Radiation Oncology, TUM School of Medicine and Health
Technical University of Munich (TUM)
81675 Munich, Germany

C. C. Hoch, B. Wollenberg, A. Bashiri Dezfouli
Department of Otorhinolaryngology, TUM School of Medicine and Health
Technical University of Munich (TUM)
81675 Munich, Germany

E. Wagner
Center for Nanoscience (CeNS)
Ludwig-Maximilians-Universität (LMU)
80539 Munich, Germany

cytosolic translocation into the intended target cell type.[4–8] Considerable efforts have been recently expended on the development of efficient nanocarrier platforms, of which lipid nanoparticles (LNPs) are at the forefront of advances, as exemplified by the first siRNA drug Patisiran (Onpattro).[9–11] This siRNA-LNP was approved in 2018 to trigger the transthyretin (TTR) gene in hepatocytes for the treatment of polyneuropathy in people with hereditary TTR-mediated amyloidosis (hATTR).[12] Moreover, the recent approval of anti-COVID-19 mRNA vaccines, Comirnaty (Pfizer/BionTech) and Spikevax (Moderna), has placed LNPs at the center of attention in nanomedicine.[13]

The successful outcomes of LNP-based nucleic acid therapies in numerous preclinical and clinical studies are attributed to the important LNP characteristics such as optimal size and zeta potential range, excellent stability in biological fluids, superior biocompatibility, and high effectiveness in the cellular transfection process.[14] RNA-loaded LNPs are typically composed of four lipid components, including an ionizable cationic lipid, cholesterol, a helper phospholipid, and a polyethylene glycol (PEG)-modified lipid, each of which plays a key role in terms of the structural and functional aspects.[15] Of particular importance is the role of the cationizable lipid in stably packaging anionic nucleic acid payload within LNPs and in promoting endosomal escape, originating from their pH-sensitive protonation property.[16] DLin-MC3-DMA (used in Onpattro), ALC-0315 (used in Pfizer/BionTech), and SM-102 (used in Moderna) are the only examples of clinically approved ionizable lipids that serve as gold standards for RNA therapies.[13] These lipids acquire a positive charge at acidic pH to enable electrostatic interactions with nucleic acids, whereas they become neutral at physiological pH, improving systemic pharmacokinetics and safety profiles.[16] In acidic endosomal milieu ($pH < pK_a$), ionizable lipids become positively charged and fuse with anionic endosomal membranes, leading to destabilization of both LNPs and the phospholipid bilayer of the endosome, all of which facilitate RNA release into the cytosol.[17–19] However, in a realistic scenario, the endosomal escape is still low, with a release rate of 1–2% of the endocytosed RNAs, which can limit their satisfactory effects in target cells.[20] Hence, developing LNP systems for intracellular gene delivery with efficient endosomal escape is an area of active research, kept motivated by designing novel ionizable lipids.[17,21,22] Considering the structure-activity relationship, many researchers have been trying to chemically design new ionizable lipids with an optimal pK_a range to fulfill the efficiency requirements of LNPs for delivery applications. Modifying the structural motifs of ionizable lipids, including the hydrophilic head and lipophilic tail groups, can affect the endosomal escape, transfection efficacy, and in vivo fate of LNPs.[23–27]

Systemic administration of RNA-LNPs ensures the widespread distribution of the cargo throughout the body, providing versatility in targeting different tissues and cell types. Nevertheless, selective delivery is highly demanded from LNP formulations to overcome biological barriers, maximize efficiency, and minimize off-target effects.[28] An excellent example of success in developing tissue/cell-targeted delivery systems is Onpattro, designed to selectively silence TTR expression in hepatocytes following systemic administration. Once injected, sheddable PEG-lipids dissociate from the formulations, which enable the adsorption of serum apolipoproteins (apoE) on the LNP surface, acting as an endogenous ligand for low-density lipoprotein receptor (LDLR)-mediated uptake.[29] Since LNP pharmacokinetics can be affected by their physicochemical properties (e.g., pK_a, size, and surface charge), numerous approaches have been put forth to rationally modify the lipid composition profiles, including the type and amount of each component in the formulations, with the aim of specific tissue/cell delivery of LNPs.[28,30] Replacement of the zwitterionic phospholipid in Onpattro with an anionic alternative shifts the surface charge and leads to the selective targeting of mRNA-LNPs to hepatic reticuloendothelial system instead of hepatocytes.[31] Modifying the charge of LNPs by incorporating/changing the anionic and cationic lipids in four- or five-component formulations can shift their organ-specificity from the liver to lung and spleen. Conversely, including ionizable lipids enhances liver targeting, driven by variations in pKa and the formation of the serum protein corona induced by LNP surface chemistry.[32–35] Furthermore, the specific type of ionizable lipid in the LNP formulation can dictate tissue-specific gene editing.[36,37] Interestingly, a cell-fate conversion in the liver from hepatocytes to endothelial cells is achievable using a mixture of two distinct pH-sensitive cationic lipids to change the ionization status of LNPs.[38] Although PEG-lipids can regulate the tissue/cell selectivity of LNPs, their structure and quantity in LNPs must be carefully adjusted due to their simultaneous impacts on LNP size, blood circulation time, and transfection efficiency.[39–43] As an alternative to chemical targeting, the surface of LNPs can be decorated with exogenous targeting ligands. This modification serves to augment the interaction between LNPs and their corresponding specific receptors on target cells, facilitating ligand-receptor-mediated uptake.[32,43]

We herein aimed to improve LNP platforms for siRNA delivery with a special focus on novel ionizable lipids. Inspired by recently developed double pH-responsive lipo-xenopeptide carriers, we explored their potential as cationizable components within siRNA-LNP formulations, building on the successful application demonstrated in mRNA polyplexes and mRNA LNPs.[44,45] The results reveal the high potency of the novel siRNA-LNP systems, and the best performer (named 1621-LNP) exhibits optimal gene silencing in endothelial cells of both hepatic and non-hepatic tissues via chemical and ligand targeting approaches, respectively.

2. Results and Discussion

2.1. Construction of siRNA-LNPs with Novel Cationizable Lipoamino Xenopeptide (XP) Carriers

A library of novel sequence-defined XP carriers has been recently generated by combining polar cationizable succinoyl tetraethylene pentamine (Stp) and apolar cationizable lipoamino fatty acid (LAF) motifs in different sequences and topologies[44] (**Scheme 1A**). The synthesis of LAFs was achieved through the reductive amination of various amino fatty acids with fatty aldehydes of different chain lengths. The number of carbon atoms in the terminal alkyl chains and the amino fatty acid type are denoted by digits (8, 12, 14, 16) and two-letter abbreviations (Oc, Bu, He), respectively (Scheme 1A-I). XPs were assembled by solid-phase assisted peptide synthesis (SPPS), with branching lysines

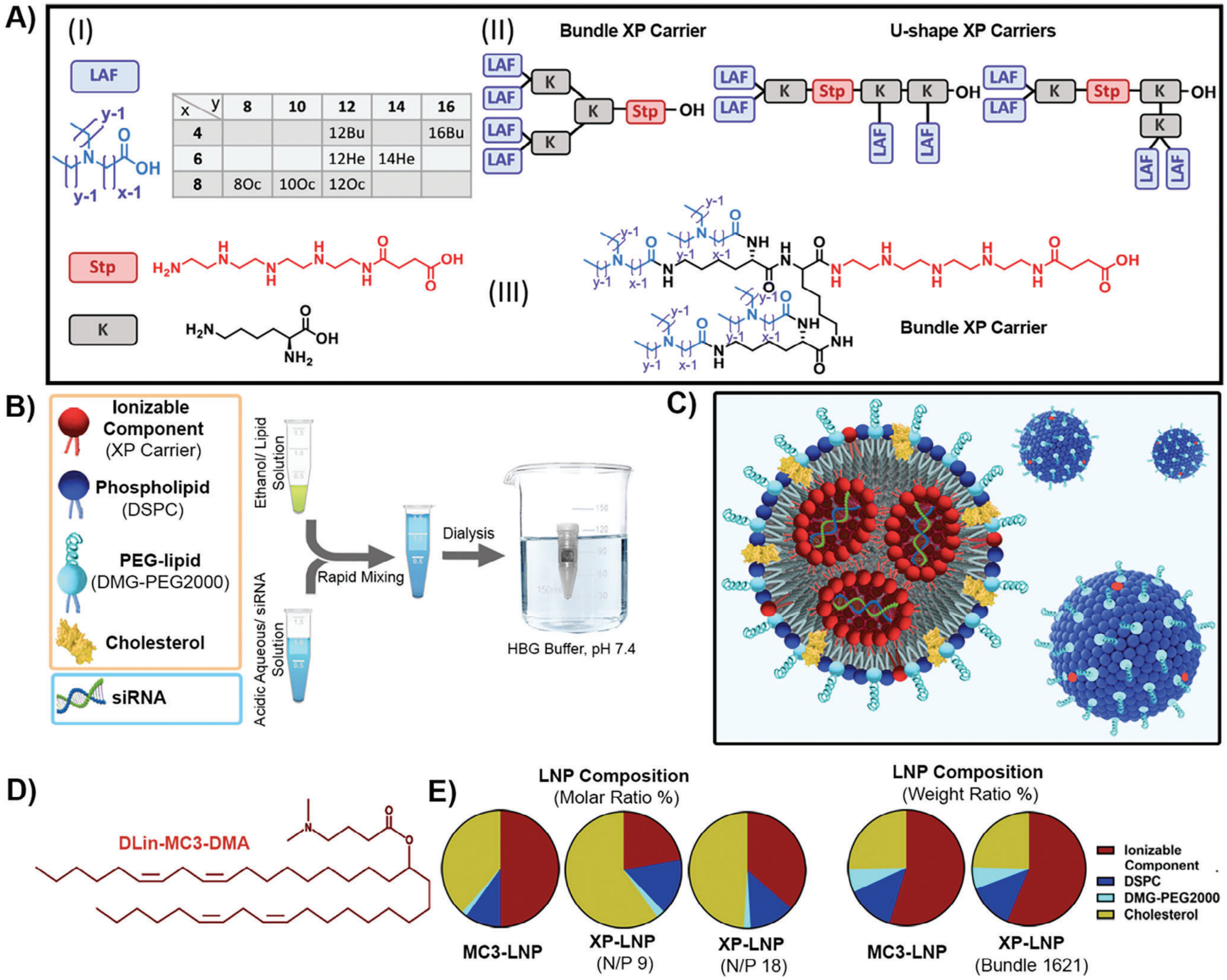

Scheme 1. LNP preparation with lipoamino xenopeptide (XP) carriers. A) Design-based principles for synthesis of XPs. The succinoyl tetraethylene pentamine (Stp) and lipo amino fatty acid (LAF) building blocks (I) at a ratio of 1:4 were connected via lysines (K) into bundle and U-shape topologies (II). A chemical structure is shown exemplarily for bundle XP carriers (III). The digits (8, 10, 12, 14, 16) and two letters (Oc, He, Bu) represent C-atom number of terminal alkyl chains and amino fatty acid type, respectively. Oc, 8-aminooctanoic acid; He, 6-aminohexanoic acid; Bu, 4-aminobutanoic acid. B) Simplistic illustration of components used in siRNA-LNP assembly including an ionizable component, a phospholipid (1,2-distearoyl-sn-glycero-3-phosphocholine, DSPC), a PEG-lipid (1,2-Dimyristoyl-rac-glycero-3-methoxypolyethylene glycol-2000, DMG-PEG2000), and cholesterol as well as the LNP preparation process. An ethanol solution (containing ionizable component, DSPC, DMG-PEG, and cholesterol) was rapidly mixed with an acidic aqueous solution (10 mM citrate buffer, pH 4) containing siRNA at a ratio of 1:3 (v/v) followed by a 10-min incubation at room temperature (RT). The resultant mixture was then dialyzed against HBG buffer (20 mM of HEPES with 5% (w/v) glucose; pH 7.4). C) Schematic drawing of a typical siRNA-LNP formulation. D) DLin-MC3-DMA (MC3) lipid served as a gold standard for siRNA-LNP formulation. E) The siRNA-loaded LNPs were assembled with ionizable component/DSPC/DMG-PEG/cholesterol at molar ratios (%) of 50/10/1.5/38.5 for MC3-LNPs (N/P 3) and 22.2/15.6/2.3/59.9 (N/P 9) or 36.4/12.7/1.9/49 (N/P 18) for XP-LNPs. The N/P ratio corresponds to the mole ratio of the amine groups in ionizable components to siRNA phosphate ones. Our well-optimized molar ratio leads to an almost similar weight ratio (%) between MC3-LNP and XP-LNPs (Bundle XP carrier 1621). The final siRNA concentration in the LNP solution was 0.012 mg mL^{-1} for in vitro applications.

covalently connecting Stp and LAF building blocks at various ratios to configure different topologies (e.g., bundle, and U-shape), as graphically shown in Scheme 1(A-II, III). The introduction of a tertiary amine into LAF, centered between three lipophilic hydrocarbon tails, in combination with secondary aminoethylenes of Stp endow carriers with a double pH-responsive endosomolytic behavior. This tunable property renders XPs into a dynamic delivery platform for various nucleic acid cargos. An alteration in the length of hydrocarbon chains within the used LAF changes the tertiary amine position, diversifying the carriers and their functions.

Considering the influential parameters (i.e., LAF types, LAF/Stp ratio, and carrier topology) on the cargo delivery outcome, top candidates were identified for highly efficient mRNA, pDNA, and siRNA transfer into the cells via polyplexes.[44] Equally remarkable is that the more lipophilic LAF$_4$-Stp$_1$ XPs with bundle (hydrophilic/lipophilic blocks) and U-shape (lipophilic ends) topologies were also suitable for mRNA-LNP

Table 1. Selected LAF$_4$-Stp$_1$ XPs with bundle and U-shape topologies for siRNA-LNP formulation.

Topologies	ID	sequence (N→C)
Bundle	1621	K[K(8Oc)$_2$]$_2$-Stp
	1752	K[K(12Bu)$_2$]$_2$-Stp
	1753	K[K(16Bu)$_2$]$_2$-Stp
	1754	K[K(12He)$_2$]$_2$-Stp
	1755	K[K(14He)$_2$]$_2$-Stp
	1762	K[K(10Oc)$_2$]$_2$-Stp
U-shape	1612	K(12Oc)$_2$-Stp-K(12Oc)-K(12Oc)
	1716	K(12Oc)$_2$-Stp-K[K(12Oc)$_2$]

formulations. These LNPs mediated rapid uptake and functional delivery of mRNA to various types of tumor cells as well as immune cells such as macrophages (MACs) and dendritic cells (DCs). After systemic mRNA-LNP administration in vivo, analysis of different organs revealed a high selectivity of mRNA expression in the spleen over liver with considerable transfection of splenic cells such as MACs, DCs, and B-lymphocyes.[45] That unique finding led us to screen the potent LAF$_4$-Stp$_1$ XPs with bundle and U-shape topologies in the context of LNP formulations for siRNA delivery. Building upon previously established mRNA-LNP formulations, a subset of LAF$_4$-Stp$_1$ XPs was selected for siRNA-LNP formulations. The chemical information of the selected XPs with their respective ID numbers is detailed in **Table 1**. They include bundle 1621 and its analogs, and U-shapes 1612 and 1716. For head-to-head comparison, all siRNA-LNPs were fabricated with cholesterol, 1,2-distearoyl-sn-glycero-3-phosphocholine (DSPC), 1,2-dimyristoyl-rac-glycero-3-methoxypolyethylene glycol-2000 (DMG-PEG2000), and an ionizable XP carrier. The LNP composition and preparation process are schematically illustrated in Scheme 1B. Herein, siRNA-LNPs were assembled by rapidly mixing lipids in ethanol and siRNA in acidic aqueous media (10 mᴍ citrate buffer, pH 4) at a 1:3 (v/v) ratio. After 10 min incubation at room temperature (RT), the LNP solution was dialyzed against HBG buffer (20 mᴍ of HEPES with 5% (w/v) glucose, pH 7.4) for 2 h to remove ethanol and neutralize the ionizable components, resulting in stable and physiologically compatible nanoparticles. According to publications,[46] LNP compositions are commonly depicted in a core-shell architecture (Scheme 1C). Typically, the outer monolayer shell, rich in helper phospholipids, cholesterol, and lipid–PEG conjugates, surrounds a core containing reverse nonlamellar micelles, which have a hydrophobic shell of low-ionized lipid around an ionized core encapsulating the payload such as siRNA.

In this research study, the ionizable lipid DLin-MC3-DMA (MC3) serves as a benchmark for performance comparison (Scheme 1D). LNPs containing LAF$_4$-Stp$_1$ XPs or MC3 lipid are termed as XP-LNP (or ID number-LNP) and MC3-LNP, respectively. Since the structure and the ratio of the ionizable component, in combination with other lipids, are critical for optimizing formulations,[47] the following considerations were made to enhance the overall similarity of the component mixture between our XP-LNPs and the gold standard MC3-LNP. Applying identical carrier amine/siRNA phosphate (N/P) would lead to a reduced total lipid/siRNA mass ratio for XP-LNPs compared to MC3-LNP and also would not be feasible due to the large differences in their ionization potentials. The selected amphiphilic LAF$_4$-Stp$_1$ XP carriers contain seven amine nitrogens, whereas MC3 contain only one tertiary amine per molecule. However, the actual charge of these double pH-responsive XPs at neutral physiological pH strongly differs from their ionizable nitrogen content. Similar as for MC3, the tertiary lipidic LAF amines are expected to be non-protonated, and out of three secondary Stp amines on the polar XP domain only one is expected to be protonated. Furthermore, the C-terminal XP carboxylate is negatively charged. In sum, XPs have a low zwitterionic charge and a high lipidic preference at neutral pH (high logD values, see Thalmayr et al[44]). To address this discrepancy, we generated the XP-LNPs at a higher formal N/P ratio while preserving a similar weight ratio of components to MC3-LNP, resulting in their different molar ratios (%) (Scheme 1E). Therefore, the LNPs were composed with ionizable component/DSPC/DMG-PEG/cholesterol in XP-LNPs either at a molar ratio of 22.2/15.6/2.3/59.9% (for N/P 9) or 36.4/12.7/1.9/49% (for N/P 18), which were then compared with MC3-LNP at the typical molar ratio of 50/10/1.5/38.5% (N/P 3) (Scheme 1E).

2.2. Physicochemical Properties of XP-LNPs Formulated with siRNA

In this work, LNPs were formed by LAF$_4$-Stp$_1$ XPs, as described in Section 2.1. After formulation, the first step was to gain insight into the physicochemical properties of XP-LNPs compared to the standard reference MC3-LNP. To do so, dynamic and electrophoretic light scattering measurements (DLS and ELS) were used to validate the size, polydispersity index (PDI), and the zeta potential of the formulations. The average hydrodynamic diameters of XP-LNPs were between 100 and 200 nm (**Figure 1**A), with corresponding PDI values ranging from 0.2 to less than 0.3, indicating uniform dispersion (Figure 1B). The zeta potential of XP-LNPs indicated a range from near-neutral to slightly negative or positive in charge (with values between −4 and 5 mV) (Figure 1C). In addition to intensity, the number-averaged diameters of LNPs were also presented, which is more comparable with the data of transmission electron microscopy (TEM) (Figure 1D). To get a direct visualization and detailed information on morphology and actual physical dimensions, the XP-LNPs with 8Oc bundle 1621 and 12Oc U-shapes of 1612 and 1716 were analyzed by TEM, whereby their spherical shapes with diameter sizes of < 100 nm were found in good agreement with number-averaged size data (Figure 1E). Empty 1621-LNP (generated without siRNA payload) showed a larger size than 1621-LNP/siRNA (Figure 1E). It has been demonstrated that a portion of cholesterol and DSPC is localized in the core of LNPs after siRNA loading, leading to a smaller LNP size as well as stable siRNA encapsulation efficiency (siRNA-EE).[47] According to the results of the RiboGreen assay, the percentage values of siRNA-EE in XP-LNPs were in a satisfactory range of 89–99.5%, except for 16Bu 1753 (74.1%) and 12He 1754 (83.5%) (Figure 1F). As part of the LNP preparation process, ionizable components are protonated in an acidic environment to form cationic molecules with high binding affinity for negatively charged nucleic acids. Thus, the N/P ratio can influence the RNA loading capacity into LNPs. By comparing

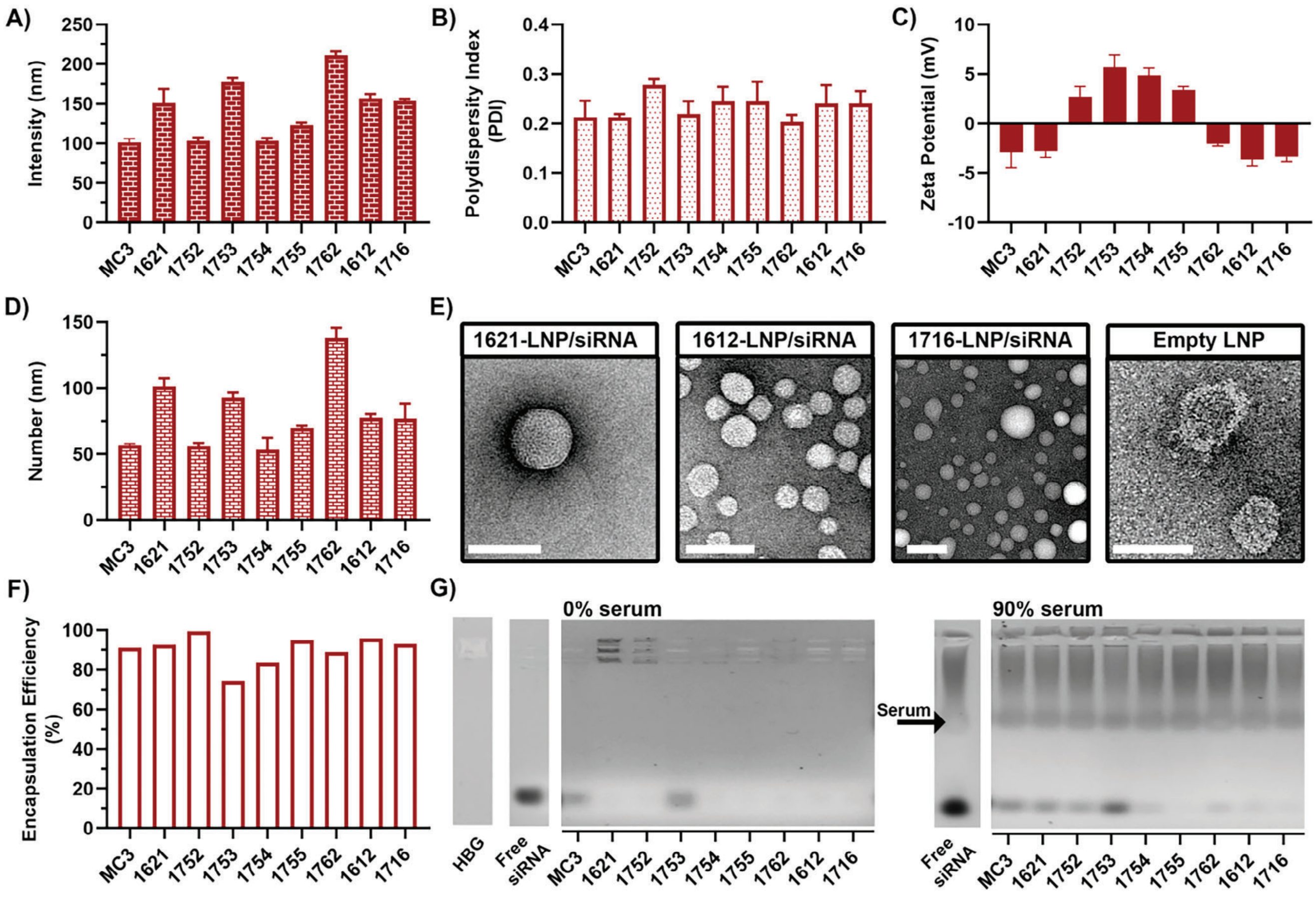

Figure 1. Physicochemical property characterization of XP-LNPs. The XP-LNPs were assembled with siRNA at N/P 9, as described in Scheme 1B and the experimental section. The standard MC3-LNP served as control for comparison. A) The intensity-averaged diameter (nm), B) polydispersity index (PDI), C) zeta potential (mV), and D) number-averaged diameter (nm) of siRNA-LNPs detected by dynamic and electrophoretic light scattering (DLS and ELS) (mean ± SD, $n = 3$). E) Representative TEM images of LNPs formulated with bundle 1621 (8Oc), and U-shapes 1612 (12Oc) and 1716 (12Oc) compared to empty LNPs. The scale bar is 100 nm. F) siRNA encapsulation efficiency (siRNA-EE%) in LNPs measured by RiboGreen assay. G) Stability of LNPs determined by agarose gel electrophoresis. Before gel run, LNPs were incubated in HBG in the absence or presence of fetal bovine serum (FBS, 90% v/v) for 2 h at 37 °C. Free siRNA at the similar concentration to that used in the LNPs and HBG buffer were considered as positive and negative controls, respectively.

the siRNA-EE of several LNPs formulated with 1621, 1612, and 1716 at N/P 9 with N/P 18, little or no significant changes in RNA content were observed, indicating that N/P 9 was already sufficient to effectively condense siRNA in these formulations (Table S1, Supporting Information). The aqueous and serum stability of LNPs were investigated by agarose gel electrophoresis (Figure 1G). For this, LNPs were incubated in HBG buffer in the absence or presence of 90% (v/v) fetal bovine serum (FBS) for 2 h. Compared to free siRNA that easily migrated through the agarose gel during the assay, the slight siRNA release from XP-LNPs implies good siRNA entrapment in most of the XP-LNPs after 2 h incubation in HBG buffer. In the presence of a high percentage of serum, a significant amount of siRNA was still trapped inside the formulations, showing favorable stability of XP-LNPs with the exception of 1753 (Figure 1G). The lower stability of 1753-LNP under both serum-free and high-serum conditions, along with its relatively low siRNA-EE, may limit its utility for delivery. Furthermore, the storage stability of XP-LNPs was analyzed in terms of their size and zeta potential for 142 days at 4 °C (Table S2, Supporting Information). Formulations with LAF 14He bundle 1755 as well as U-shape 1612 showed excellent stability over long-term storage at 4 °C, as reflected by no considerable changes in their sizes and zeta potentials. The analysis of nanoparticle properties led to the conclusion that our LNPs could efficiently and stably encapsulate siRNA in their core and therefore we looked forward to evaluating these XP-LNPs for functional siRNA delivery in vitro. Since the interactions of LNPs with cells are influenced by their physicochemical characteristics, the almost similar properties (in terms of size, surface charge, and serum stability) of XP-LNPs with MC3-LNP ensure a fair comparison. Since the LNP interactions with biological environments affect their in vitro behavior as well as in vivo fate,[48] the stability of two candidate formulations (including 1621 and 1716-LNPs) was also screened by DLS after incubating them in cell culture medium (supplemented with 10% FBS) at 37 °C for various time points (1, 2, and 4 h) (Figure S1, Supporting Information). We first measured the particle diameter of a blank sample (cell culture medium + 10% FBS) and XP-LNPs at 0 h (immediately

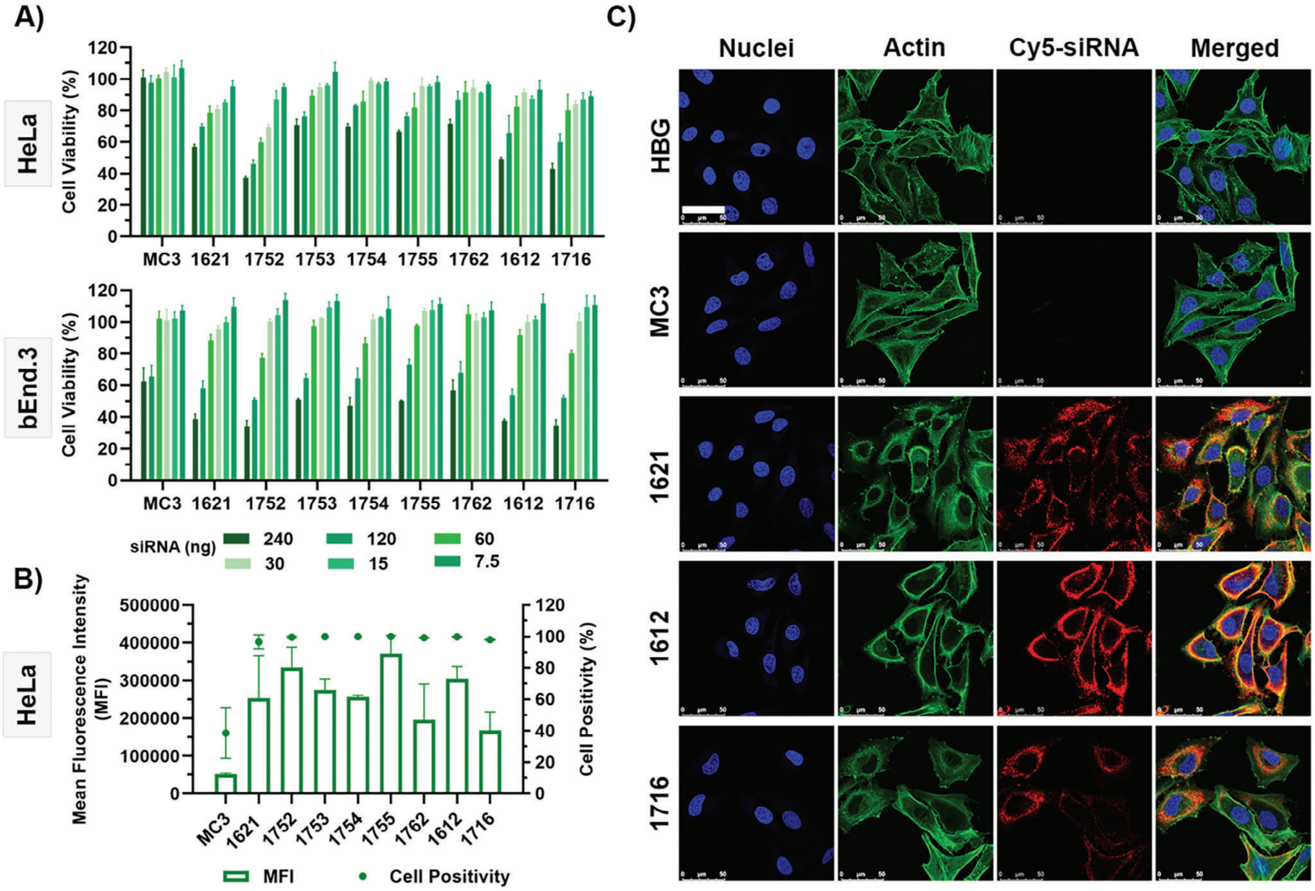

Figure 2. Cellular compatibility and uptake of XP-LNPs. The XP-LNPs were assembled with siRNA at N/P 9, as described in Scheme 1B and the experimental section. The standard MC3-LNP served as control for comparison. A) Viability of human cervical adenocarcinoma (HeLa) and murine brain endothelial (bEnd.3) cells examined after a 48-h exposure to each LNP formulation at various siRNA doses (240, 120, 60, 30, 15, 7.5 ng/5000 cells per well) by MTT assay. The cell viability was calculated as percentage of HBG-treated cells (mean ± SD, $n = 3$). B) Cellular uptake quantified by flow cytometry after 1 h incubation with siRNA-LNPs at an siRNA dose of 30 ng (per 5000 cells) containing 20% Cy5-labeled siRNA (Cy5. The data are presented as percentage of Cy5-positive cells (green dots) and the mean fluorescence intensity (MFI) of Cy5 signal per cell (green bars) (mean ± SD, $n = 3$). C) Cellular uptake and intracellular distribution of siRNA-LNPs imaged by confocal laser scanning microscopy (CLSM) after 1 h incubation. A dose of 30 ng (per 5000 cells) siRNA containing 20% Cy5-siRNA (red) was used. HBG-treated cells were considered as a negative control. The actin skeletons were stained with rhodamine-phalloidin (green) and nuclei with DAPI (blue). The scale bar is 50 µm.

after formulation in HBG), showing distinct peaks in intensity-size distribution plots (Figure S1A,B, Supporting Information). The plots of LNPs incubated in cell culture medium displayed two peaks corresponding to XP-LNPs and 10% FBS. As observed in the overlaid size distribution plots, the diameter of XP-LNPs did not significantly change over the incubation time in cell culture medium compared to time 0 h, suggesting the colloidal stability of the tested XP-LNPs and their ability to maintain their size in the presence of 10% serum (Figure S1C, Supporting Information).

2.3. In Vitro Studies of Cellular Interaction with XP-LNP/siRNA Formulations

As recently reported by Ndeupen et al., LNPs may induce inflammatory responses in mice, depending on the ionizable lipid component. Therefore, high biocompatibility of LNPs is an essential parameter for their successful pre-clinical and clinical performances.[49] In order to determine the optimal cytocompatible dose/s in vitro, HeLa cells were exposed to various doses of siRNA-LNPs formulated with XPs for 48 h (**Figure** 2A). Over 80% cell viability was recorded at siRNA doses lower than 30 ng in all XP-LNP treated cells, except for 12Bu 1752, for which the maximum-tolerated dose was 15 ng. The induced toxicity at high doses (especially 240 ng) was observed in the case of 12Oc U-shapes (1612 and 1716) and 12Bu bundle 1752, while MC3-LNP was well-tolerated at all tested doses. Since host endothelial cells are the first targets encountering nanoparticles after systemic administration, XP-LNP cytotoxicity was also examined in murine brain endothelial cells (bEnd.3 cell line) (Figure 2A). By analyzing the obtained data from both cell lines, the cytotoxic effects of XP-LNPs are not only dose- and XP-dependent but also cell-line specific. Although the cell viability of bEnd.3 was lower than that of HeLa cells at high siRNA doses of 240 and 120 ng, no apparent cytotoxicity was seen in any of the tested cell lines at doses below 30 ng. These findings indicate the importance of the biocompatibility profile, which must be determined to select the appropriate dose for further in vitro studies. Consequently, the siRNA concentration of 30 ng for 5000 cells per well containing 100 µL media (0.3 µg mL^{-1}) was chosen as the tolerated dose for all XP-LNPs, allowing for a better comparison in terms of efficiency. In addition to the siRNA concentration, the cell-line dependency of nanoparticle-induced toxicity should also be considered before transfection.

Given that efficient cellular uptake is a prerequisite for gene transfection, we quantified the uptake of XP-LNPs containing 20% fluorescently labeled siRNA (Cy5-siRNA) by HeLa cells using flow cytometry. The labeled cargo did not significantly change the size, surface charge, or siRNA-EE (data not shown). After a timeframe of 1 h, the Cy5 fluorescence signal was measured within the transfected cells (30 ng siRNA/5000 cells) (Figure 2B). The percentage of Cy5-positive cells was more than 90% after an incubation time of only 1 h with XP-LNPs, and the mean fluorescence intensities (MFIs) of treated cells were much greater than those treated with MC3-LNP. The results of uptake experiments led us to speculate that the marked decrease in cell viability at high doses (such as 240 and 120 ng) was likely due to the excessive amount of LNPs inside the cells, causing cellular stress. The internalization of XP-LNPs in HeLa cells was visualized by confocal laser scanning microscopy (CLSM). Three XP carriers of different topologies, including 8Oc bundle 1621, and 12Oc U-shapes 1612 and 1716, were selected to form LNPs using 20% Cy5-siRNA. HeLa cells were transfected with a single siRNA dose of 30 ng (per 5000 cells) for 1 h, and then subjected to imaging studies. As depicted in Figure 2C, XP-LNPs were internalized by HeLa cells efficiently, albeit with different kinetics and localizations depending on their LAF type and topologies. 1621-LNP mostly showed well-distributed fluorescence dots in the cytosol, which may be in an endocytosed or released form. 1716-LNP followed an almost similar distribution pattern to 1621-LNP but with less Cy5 fluorescence intensity. In contrast, 1612-LNP was concentrated in the regions close to the cell membrane along with a diffuse punctate pattern in the cytosol. Looking at the cellular uptake of MC3-LNP, a small quantity of Cy5-siRNA was detected in the cells, which can be attributed to the low applied dose and short incubation time of this formulation.[50] To conclude, the flow cytometry and confocal microscopy data clearly illustrated a rapid and robust uptake of XP-LNPs. The good biocompatibility and excellent cellular uptake render XP-LNP applications potential for siRNA-mediated gene silencing.

2.4. In Vitro Screening of siRNA-Loaded XP-LNPs for Gene Silencing

Although the efficient cellular internalization of XP-LNPs was rapidly achieved in more than 90% of the transfected cells, allowing favorable siRNA performances, the transfection efficacy does not always correlate with the cellular uptake profile. To illustrate a potential correlation in our study, the gene silencing activity of siGFP targeting enhanced green fluorescence protein (eGFP) was tested in various cancer cell lines that stably express eGFP-luciferase (eGFPLuc) reporter gene. A negative siRNA control (siCtrl) was employed to detect non-specific knockdown effects. As previously well demonstrated, siRNA polyplexes formed with different 12Oc U-shape carriers mediated highly-effective gene silencing at a low dose of ≈15 ng siRNA (per 5000 cells) in various tumor cell types.[44] Thus, a similar dose of siRNA (15 ng) was applied for the screening purposes of XP-LNPs. The obtained biocompatible dose of LNP-loaded siRNA (30 ng) in this study was also exposed to the cells, and the luciferase activity of the eGFPLuc fusion protein in the cells was determined at 48 h after transfection (**Figure 3**). For better comparison, a table was also provided including the differences between the effects of specific and non-specific siRNA for each XP-LNP formulation, defined as gene silencing efficiency (%), which were statistically significance at both tested siRNA doses (30 and 15 ng) (Table S3, Supporting Information).

The formulations were first screened on the hepatocellular carcinoma Huh7 cell line, expressing eGFPLuc reporter (Figure 3A). Expectedly, MC3 achieved a high gene silencing efficiency of over 70% at both tested siRNA doses (30 and 15 ng). When compared, 14He 1755, with different LAF motifs to 8Oc 1621, yielded a similar potency to MC3 under the same transfection condition. The difference in luciferase activity between siCtrl and siGFP-treated cells at the lower dose (15 ng) puts bundle 1621 as well as U-shapes 1612 and 1716 at lower levels of effectiveness than 1755 in Huh7 hepatic cell line (1755> 1621> 1612> 1716), but still with favorable knockdown efficiencies (Table S3, Supporting Information). The gene silencing effects of 1621 analogs, including 1752, 1753, 1754, and 1762-LNPs, were also found in the range of 43–52% on Huh7/eGFPLuc cells (Table S3, Supporting Information). The luciferase activities below 100% observed in siCtrl-treated cells represent non-specific effects on the marker gene expression and metabolic activity of the cells and thus indirectly indicate a slight cytotoxic effect of the formulations (Figure 3). The siRNA-LNPs incorporating U-shapes showed higher non-specific effects than bundles (especially at 30 ng siRNA dose), even though this could be addressed by lowering the siRNA dose to 15 ng while maintaining the carrier performance (Figure 3). These results re-emphasize the importance of finding a suitable formulation dose for in vitro cell transfection by considering a fine balance between efficacy and cytotoxicity in a cell-line dependent manner. After transfection of KB/eGFPLuc cells, all XP-LNPs outperformed MC3-LNP without any appreciable non-specific effects (Figure 3B). The formulations with 14He 1755, 8Oc 1621, and 12Oc 1716 induced respective efficiencies of 88%, 80%, and 75% at a low siRNA dose of 15 ng, whereas control MC3 only 19% (Table S3, Supporting Information). The knockdown efficiencies of 1621 analogs and 12Oc 1612 were more than 50% in KB/eGFPLuc cells at 15 ng siRNA (Table S3, Supporting Information). In N2A/eGFPLuc cells, XP-LNPs gave almost comparable gene silencing activities to MC3-LNP at 30 ng siRNA dose. Surprisingly, at a twofold lower dose (15 ng per well), 1621 and 1612-LNPs could overtake MC3 in efficiency with knockdown rates above 70% (Figure 3C; Table S3, Supporting Information). Although an explicit cell line dependency in the gene knowdown activity of formulations was apparent, the results sufficiently support the promising potential of XPs in the LNP formulation compared to the benchmark MC3. The LNPs formulated with bundles 1621 and 1755 besides U-shapes 1612 and 1716 were ranked as top performers in terms of transfection score in this screening study.

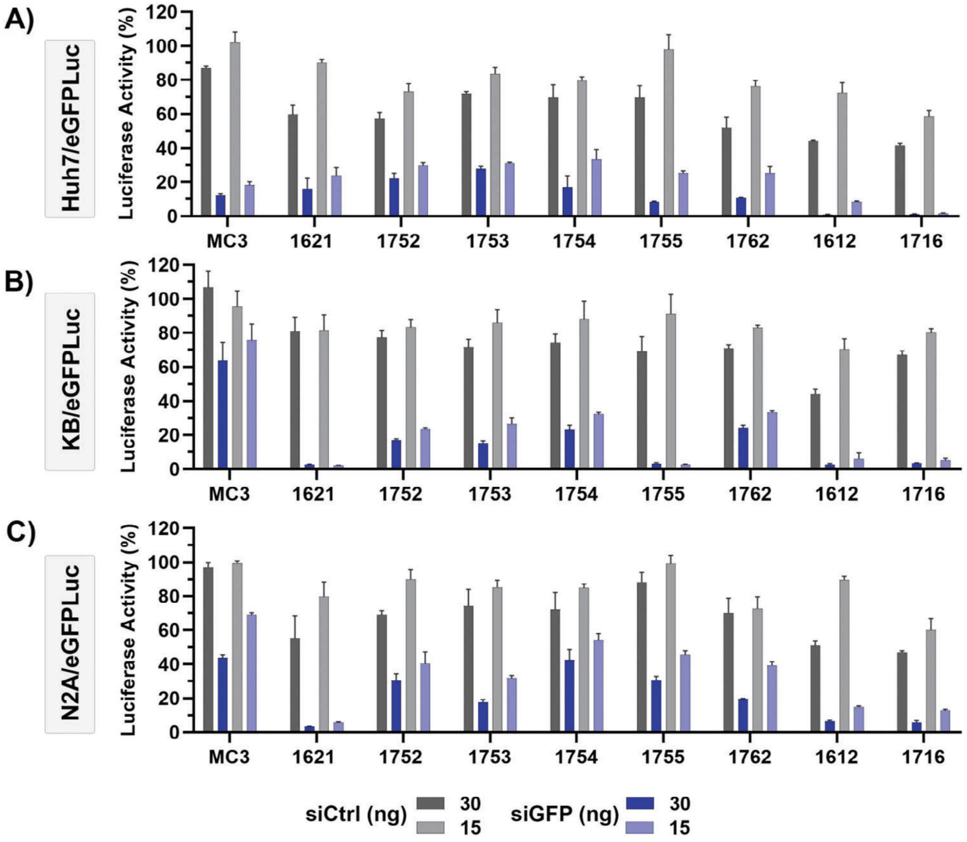

Figure 3. Gene silencing activities of XP-LNP/siRNA formulations in different cancer cell lines. The XP-LNPs were assembled with siRNA at N/P 9, as described in Scheme 1B and the experimental section. The XP-LNPs were loaded with siGFP against enhanced green fluorescent protein (eGFP) or control siRNA (siCtrl) to transfect the cells (5000 cells per well) at two different doses (30 and 15 ng). The standard MC3-LNP served as control for comparison. At 48 h after transfection, the luciferase activity of eGFP-luciferase (eGFPLuc) fusion protein was evaluated in cell lines with stable expression of eGFPLuc reporter gene including A) human hepatocellular Huh7 (Huh7/eGFPLuc), B) human cervix carcinoma KB (KB/eGFPLuc), and C) murine neuroblastoma N2A (N2A/eGFPLuc) cells. The luciferase activity is expressed as percentage relative to that of HBG-treated cells (mean ± SD, $n = 3$).

The siRNA transfection doses were even more reduced to 7.5 ng to distinguish the efficiency differences among the top-performing formulations (1621, 1755, 1612, and 1716). Indeed, dose dilution of LNPs was undertaken in buffer (HBG, pH 7.4) to reach very low doses of 1.5 and 0.15 ng of siRNA per well. As **Figure** 4(A–C) shows, the translation levels of eGFPLuc were altered dose-dependently after siRNA-LNP transfection. The cell type and XP-specific differences were also evident in the outcomes of gene silencing. By comparing the gene silencing efficiency of formulations (Tables S4–S7, Supporting Information) upon the dose reduction assay on various cell lines led us to find an order of potency as 1621 > 1755 > 1612 > 1716. However, the higher non-specific effects of U-shapes limit a more straightforward conclusion, but still, their potencies at very low doses, besides their acceptable physicochemical properties, fulfill our expectation from a suitable carrier. An important finding was the superior gene silencing activity of 1621-LNP at an extremely low siRNA dose of 150 pg when the N/P ratio was increased to 18, remarkably in KB/eGFPLuc and CT26/eGFPLuc cells (Figure 4D; Table S4, Supporting Information). Since the siRNA-EE did not significantly change by increasing the N/P ratio from 9 to 18 in LNP formulations (as found in Section 2.2), the extra XPs may improve the endosomal escaping rate of siRNA, leading to a better gene silencing activity like what was observed in case of 1621-LNP. Altogether, 1621-LNP was scored as the most potent carrier for in vitro siRNA delivery in our study.

The potency ranking of different XP library members in functional delivery strongly depends on the nucleic acid cargo (siRNA, mRNA, pDNA) and the type of formulation (LNP versus polyplex). For small siRNA cargo, the electrostatic stability of polyplexes is far more critical[51] than, for example, siRNA-LNPs. It is worth discussing here the ability of the novel XP carriers for siRNA complexation and delivery in the form of siRNA polyplex in comparison to siRNA-LNP formulation. We recently reported that the U-shape (12Oc) polyplexes exhibit potent gene silencing with the most significant efficacy for 1716, even at a dose of 3 ng siRNA/well in N2A/eGFPLuc cells. Nevertheless, finding an optimal ratio of U-shape carriers (1716 and 1612) with Stp$_1$ to siRNA (N/P), at which polyplex stability and potency could be guaranteed, was challenging for polyplex formation. To mention, the ability of 1716 was better than 1612 to make stable siRNA polyplexes.[44] From a comparative point of view, a similar in vitro transfection efficiency was obtained with 1716-LNP in KB/eGFPLuc cells. The difference can be attributed to the distinct

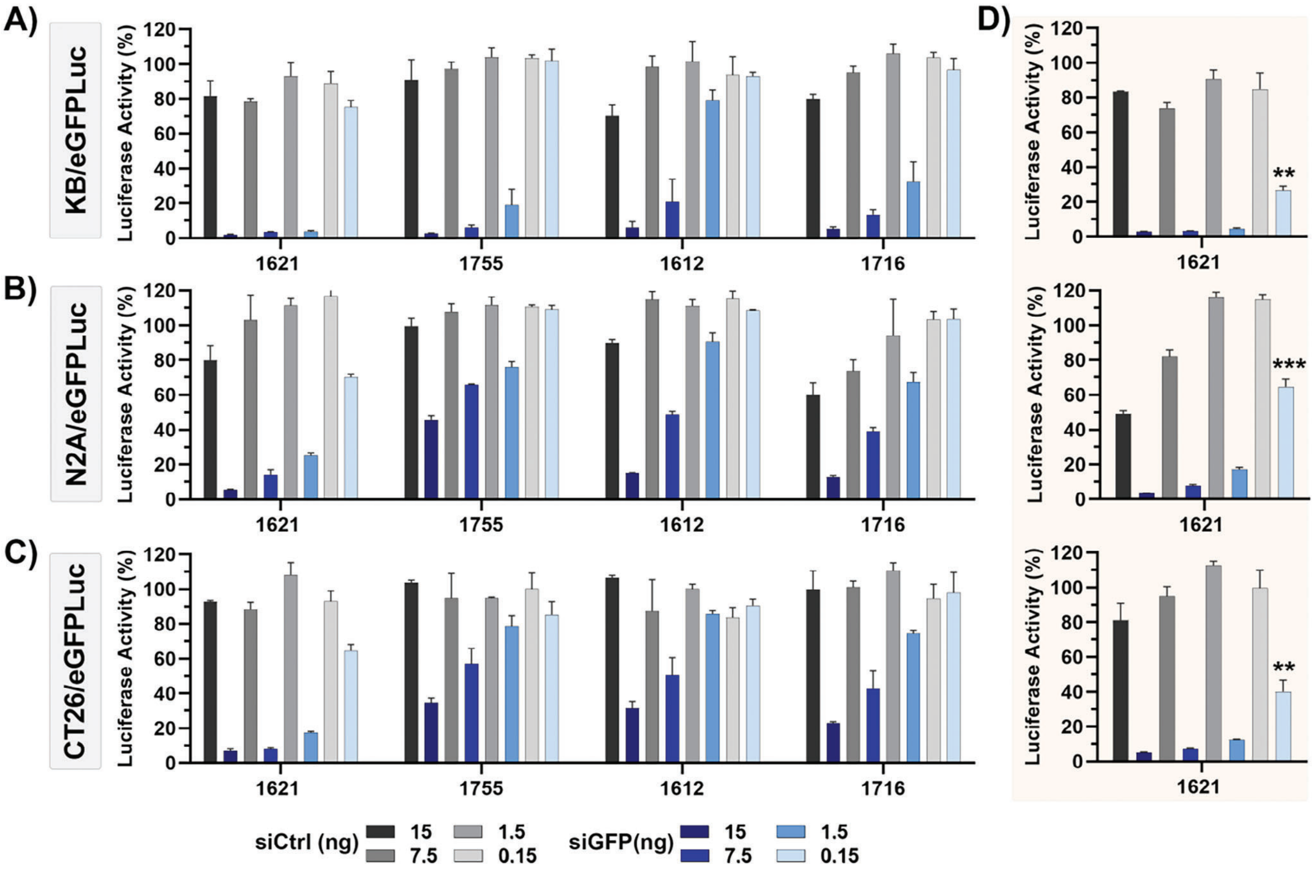

Figure 4. Comparison of siRNA-mediated gene silencing activities among the best-performing XP-LNPs in different cancer cell lines. The XP-LNPs were assembled with siRNA at either N/P 9 (A-C) or N/P 18 (D), as described in Scheme 1B and the experimental section. The XP-LNPs were loaded with siGFP or siCtrl to transfect the cells (5000 cells per well) at different doses (15, 7.5, 1.5, and 0.15 ng). The two low doses (1.5 and 0.15 ng) were obtained by dilution of LNPs in HBG buffer. At 48 h after transfection, the luciferase activity of eGFPLuc fusion protein was evaluated in A) KB/eGFPLuc, B) N2A/eGFPLuc, and C) murine colon carcinoma CT26 (CT26/eGFPLuc) cells. D) The gene silencing activity of 1621-LNP at N/P 18 evaluated in three cell lines of KB/eGFPLuc, N2A/eGFPLuc, and CT26/eGFPLuc after 48 h. The luciferase activity is expressed as percentage relative to that of HBG-treated cells (mean ± SD, $n = 3$). Statistical analysis is shown for the low dose of siRNA (0.15 ng) in Figure 4D and significance was determined as $^{**}p \leq 0.01$ and $^{***}p \leq 0.001$.

structural and functional properties of LNP versus polyplexes in their interaction with cells. In cases of mRNA and pDNA, the XP carriers at Stp/LAF ratio of 1:4 could hardly form polyplexes, with a higher tendency toward aggregation in U-shape than bundle topologies. At an optimized N/P ratio, bundles 8Oc 1621 and Bu 1752 could complex mRNA into positively charged polyplexes with great potential for mRNA delivery.[44] In the case of siRNA polyplexes (Figure S2, Supporting Information), bundle 16Bu 1753 could not form siRNA polyplexes of satisfactory stability. Bundle XPs such as 1754 (12He), 1755 (14He), and 1762 (10Oc) were capable of forming polyplexes at a proper N/P ratio but with moderate gene silencing at a high siRNA dose of 500 ng (per 5000 cells), which is likely due to their low stability in 10% serum-containing culture medium. The siRNA polyplexes with 12Bu 1752 were more stable in size than the other 1621 analogs, even though their surface charge depended on the N/P ratio, suggesting caution in their formulation and application. Although bundle 1621 with shorter LAF (8Oc) can complex siRNA into polyplexes at N/P 18 with acceptable size and PDI, moderate gene silencing efficiency of ≈40% was achieved by delivering a high dose of 500 ng siRNA, a gene silencing value that is even lower than 1621-LNP's potency at 30 ng siRNA in the same cell line (N2A/eGFPLuc). When it comes to a conclusion, the full potential of bundle XPs with one Stp should be utilized in LNP formulations for maximal efficacy. The superior efficiency of siRNA XP-LNPs over XP-polyplexes is well-documented by efficacy at a 20-fold reduced very low dose (0.15 ng versus 3 ng siRNA per well).

2.5. In Vitro Assessment of Endosomal Disruption Mediated by XP-LNP/siRNA Formulations

Having confirmed the potential of XP-LNPs for siRNA delivery, we were interested in evaluating their endosomal disruption capability as one of the underlying reasons for their outstanding functional efficiency. To do this, HeLa cells stably expressing Galectin8-mRuby3 fusion protein (HeLa-Gal8-mRuby3) were applied to visualize the endosomal escape capability of the XP-LNPs. Upon rupture of the endosomal membrane, punctate

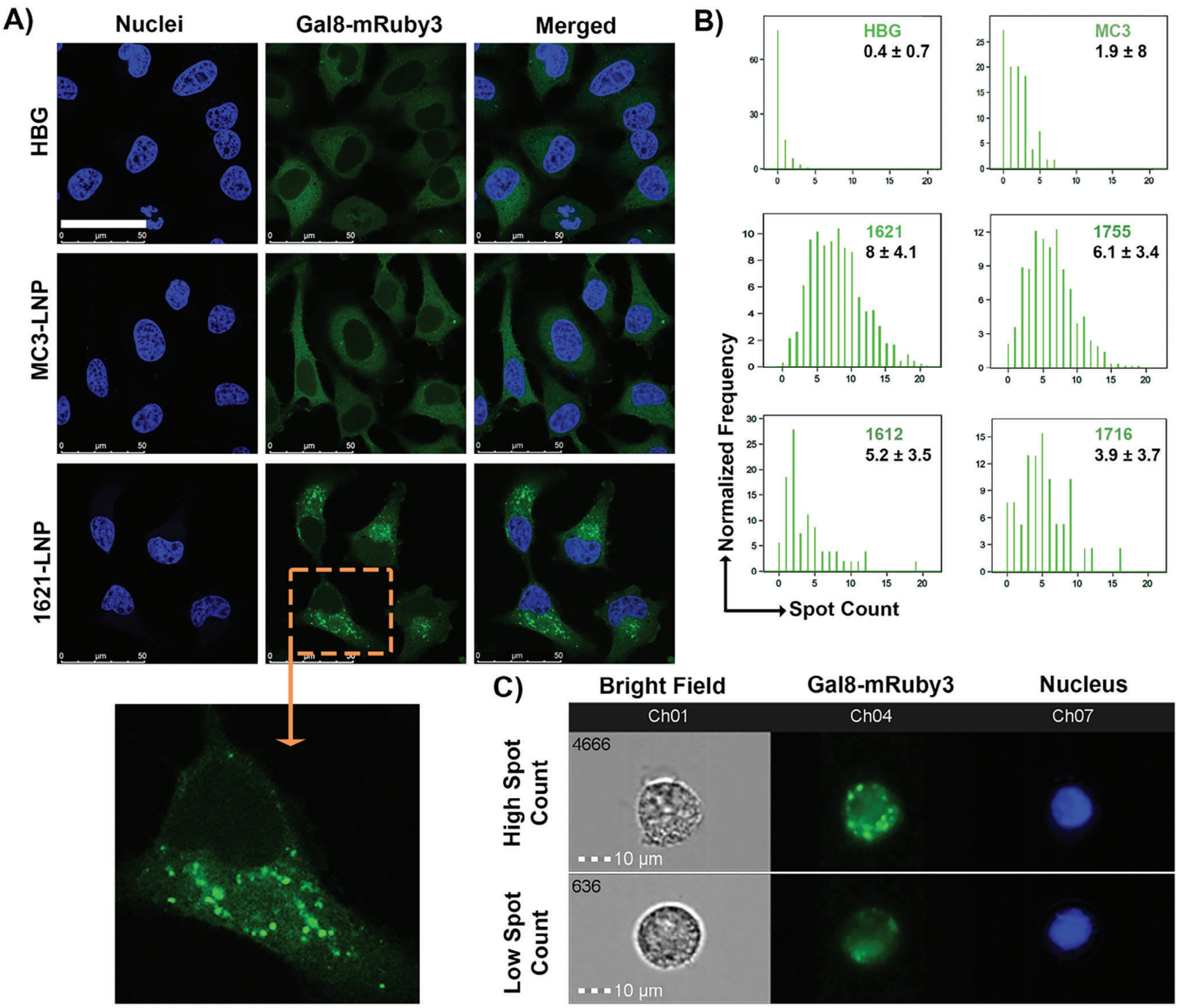

Figure 5. Image-based analysis of endosomal disruption capabilities of XP-LNPs. The XP-LNPs were assembled with siRNA at N/P 9, as described in Scheme 1B and the experimental section. The standard MC3-LNP served as control for comparison. The endosomal disruption was assessed by galectin (Gal8) recruitment assay using HeLa cells expressing Gal8-mRuby3 fusion protein (HeLa-Gal8-mRuby3). In this cell line, the binding of cytosolic Gal8-mRuby3 to intra-endosomal glycans in damaged endosomes leads to punctate fluorescent spots. The reporter cell line was transfected either with XP-LNPs or MC3-LNPs for 4 h at an siRNA dose of 30 ng (per 5000 cells). Then, the cells were prepared for CLSM or the ImageStream imaging flow cytometry according to their respective protocols. HBG-treated cells were considered as a negative control. A) The fluorescent Gal8-mRuby3 puncta (green) tracked by confocal microscopy. The scale bar is 50 µm. B) The Gal8-mRuby3 puncta count per cell quantified by the ImageStream analyzer using the spot count feature of IDEAS software (version 6.2). Histograms were generated by plotting the spot count against the normalized frequency. The mean spot count for each sample was provided in their plots. C) Representative images of transfected cells with 1621-LNP with high and low spot counts. The cells were analyzed in three different channels of bright field (Ch01), Gal8-mRuby3 (Ch04; green), and Hoechst (Ch07; blue). The scale bar is 10 µm.

fluorescent spots appear due to the cytosolic Gal8-mRuby3 binding to the exposed glycosylation moieties on the inner face of the disrupted endosomes. The fluorescent puncta resulting from Gal8-mRuby3 clustering on damaged endosomal membranes can be easily detected via confocal microscopy. Each spot reflects the incidence of endosomal disruption and the subsequent cargo release, thus predicting the intracellular siRNA bioactivity.[52]

The 1621-LNP was initially selected for the Gal8-mRuby3 recruitment assay. As endosomal rupture occurs in a time and dose-dependent manner,[53] the cells were treated with a single siRNA dose of 30 ng for 4 h and then imaged by CLSM (**Figure** 5A). In HBG-treated cells, the Gal8-mRuby3 pattern was dispersed throughout the cytosol due to the presence of intact endosomes. The bright fluorescent punctate pattern showed the high endosomal disruptive activity of 1621-LNP, while no significant Gal8 recruitment was observed in the MC3-treated cells in comparison to HBG-treated cells. These striking differences in the spot patterns between 1621 and MC3 suggest the highly efficient endosomal escape in cells treated with 1621-LNP at a low siRNA dose of 30 ng, thereby leading to its high-efficiency transfection.

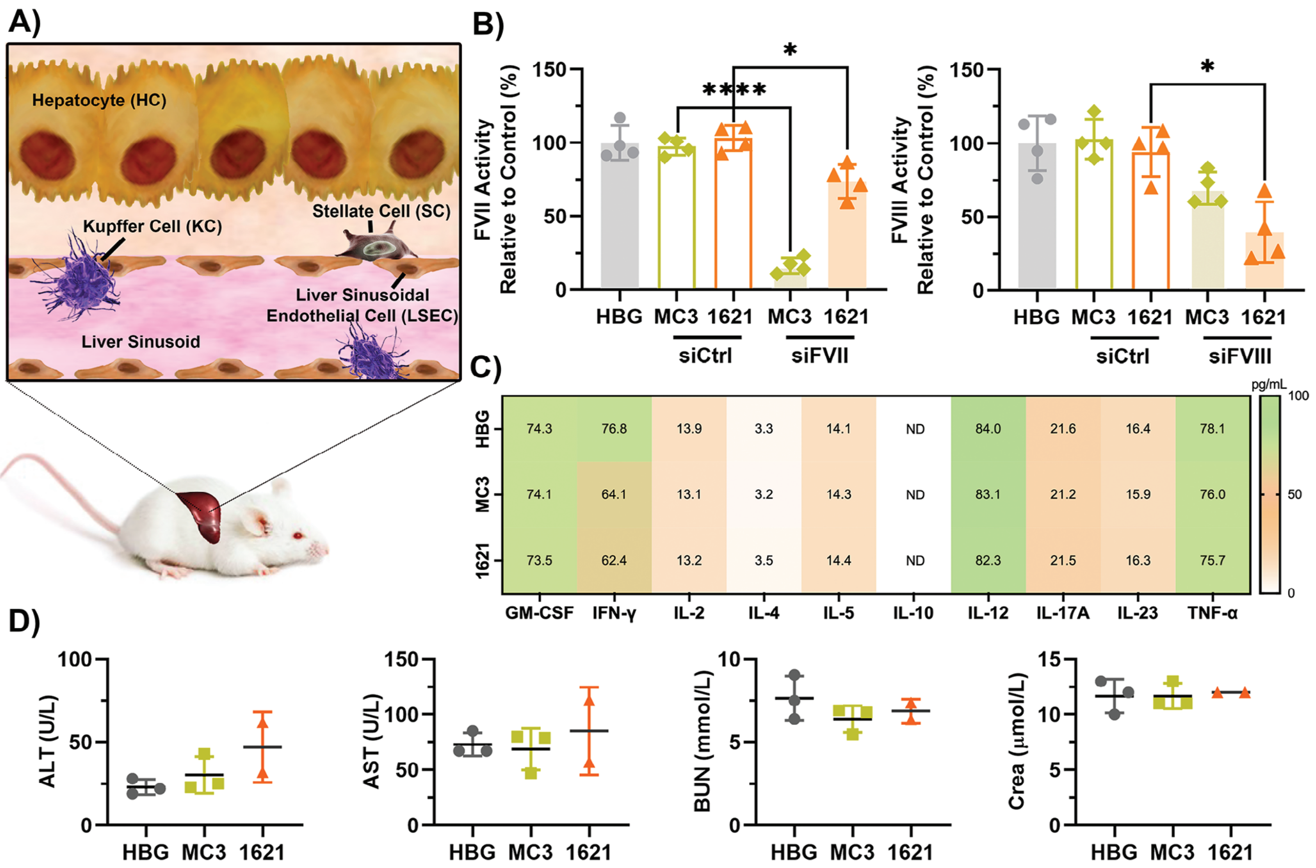

Figure 6. Effective siRNA gene silencing in liver sinusoidal endothelial cells (LSECs) by 1621-LNP. A) Scheme of liver sinusoid structure. The liver sinusoid is a specific capillary made of highly specialized cells such as hepatocytes (HCs), LSECs, Kupffer cells (KCs), and stellate cells (SCs). HCs and LSECs are separated by the space of Disse and produce respective coagulation factors VII (FVII) and FVIII, suggesting two distinct potential cell-specific targets. B) FVII and FVIII activity in mouse plasma evaluated by chromogenic assay following single intravenous (i.v.) administration of siRNA-LNPs. Each LNP (MC3 and 1621) was formulated either with siRNA against FVII (siFVII) or FVIII (siFVIII) and injected into BALB/c mice (6-8 weeks) via the tail vein (5 µg siRNA in 150 µL HBG/mouse). The identical formulations with siCtrl were used as negative controls. After 48 h, the blood was collected via heart puncture under anesthesia. FVII and FVIII activities were measured in their citrated plasma. The data are presented as percentage of the value obtained from HBG-injected mice (mean ± SD, $n = 4$). Statistical significance was determined as $*p \leq 0.05$, and $****p \leq 0.0001$. C) Cytokine profile quantified in the plasma of mice after a 48-h treatment with 1621-LNP in comparison to MC3-LNP and HBG-treated groups using MACSPlex Assays (mean of duplicate ± SD, $n = 3$). ND, not detectable. D) Hepatic (ALT and AST) and renal (BUN and Crea) functions tested in the plasma of mice after a 48-h treatment with 1621-LNP ($n = 2$) in comparison to MC3-LNP ($n = 3$) and HBG-treated ($n = 3$) groups (mean ± SD). ALT, alanine aminotransferase; AST, aspartate aminotransferase; BUN, blood urea nitrogen; Crea, creatinine.

The HeLa-Gal8-mRuby3 cells treated with our panel of the best-performing XP-LNPs (1621, 1755, 1612, and 1716) were also analyzed by the ImageStream cytometer to determine if there is a correlation between the performance rankings derived from gene silencing analysis and the Gal8 recruitment assay (Figure 5B). This advanced technique enables the quantification of endosomal disruption frequencies by taking images from each cell and automatically detecting and counting spots with higher fluorescence intensity. The distribution of spot counts by our endosome-disruptive XP carriers was highly pronounced compared with MC3 (Figure 5B). Upon ranking the XP-LNPs according to the mean spot count per cell (1621 > 1755 > 1612 > 1716), we found an apparent relationship between the endosomal disruption events and the siRNA-mediated eGFPLuc gene knockdown efficiency. Figure 5C shows representative images of high and low Gal8-mRuby3 spot counts in cells treated with 1621-LNPs derived from ImageStream data. Overall, XP-LNPs are pH-responsive, endosomolytic, and capable of robustly delivering siRNA into the cytosol of target cells, albeit to different degrees.

2.6. In Vivo Liver Targeting by XP-LNP with Preferential Affinity toward Liver Sinusoidal Endothelial Cells (LSECs)

Potential targeted therapy for liver diseases demands selective and efficient delivery of therapeutics into the cell type of interest to enhance treatment outcome with minimum off-target effects, as already achieved by Onpattro for hepatocyte gene silencing.[9] Liver is a complex organ of several major cell types, consisting of hepatocytes and non-parenchymal cells such as LSECs and Kupffer cells (KCs) (**Figure 6A**). Hepatocytes, accounting for approximately 80% of the liver cell population, have been the primary targets for LNP-delivered therapeutics because of their central role in various hepatic complications.[54] The highly specialized LSECs contain fenestrations without a diaphragm to form a permeable endothelium within sinusoid capillaries, allowing LNPs to enter the space of Disse and interact with hepatocytes (Figure 6A). The endolysosomal compartment is an essential part of the cellular machinery in LSECs, providing them with a unique endocytic capacity for LNP uptake. LNPs can also be phagocytized by KCs, the resident macrophages in the liver. Therefore, LSECs and KCs provide a powerful scavenger system, referred to as "the dual cell principle of waste clearance", for removing small and large macromolecules from the blood, respectively.[54] Despite the commonality of apoE-mediated LNP specificity to hepatocytes, as demonstrated by Onpattro, it has been so far more challenging to deliver RNAs into non-hepatic cells. Due to the unique anatomical location and provital role of LSECs in numerous pathophysiological conditions,[55] a growing interest has been raised in developing strategies for LNP-mediated RNA delivery into LSECs. Progress has already been achieved either by modulating the physicochemical properties such as size and pK_a,[56] surface charge,[31] lipid structure,[57] or by applying specific targeting ligands.[43] Our previous publication by Haase et al. (2023) indicated that 1621-LNP could efficiently deliver mRNA into LSECs and KCs.[45] Building upon this finding, and considering the lower total protein expression obtained in the livers of mice injected with 1621-LNP/mRNA compared to MC3-LNP, we hypothesized that this difference might be due to the limited ability of 1612-LNP to transfect hepatocytes. To explore this hypothesis in the context of siRNA delivery, we compared the efficacy of 1621-LNP in delivering siRNA to both hepatocytes and LSECs. Initially, the biodistribution of 1621-LNP encapsulating Cy7-siRNA was validated in the liver of BALB/c mice at 1h following intravenous (i.v.) injection (5 µg siRNA per mouse) using an IVIS imaging system (Figure S3, Supporting Information). Based on the *ex vivo* data, the 1621-LNP exhibited a comparable accumulation pattern in imaged organs to that of MC3-LNP, with high fluorescence efficiency in the liver. Next, the 1621-LNP uptake by different hepatic cell-types (e.g., hepatocytes, LSECs, and KCs) was examined at 1 h-post injection of 1621-LNP encapsulating Cy5-siRNA using ImageStream cytometer (Figure S4, Supporting Information). The data demonstrated 1621-LNP accumulation in all three tested cell types, with ≈tenfold higher distribution in LSECs in comparison to hepatocytes and ≈fivefold higher level than in KCs (Figure S4A, Supporting Information). The LSECs were identified through specific antibody (Ab) staining, and the intracellular localization of siRNA-LNP was determined by imaging the fluorescence emitted from Cy5 (Figure S4B, Supporting Information). In contrast, for MC3-LNP, a lower distribution level in LSECs has been reported as compared to hepatocytes and KCs.[58]

Since biodistribution data alone is not sufficient to predict the functionality of RNA delivered by LNPs into specific cells,[58] we evaluated the in vivo performance of 1621-LNP for siRNA delivery against either coagulation factor VII (FVII) or FVIII (Figure 6B). FVII is specifically produced by the hepatocytes and secreted into the circulation, whereas LSECs are the sites for FVIII production. The 1621-LNP was loaded with either siFVII or siFVIII and injected i.v. into BALB/c mice (5 µg siRNA per mouse). MC3-LNPs encapsulating siFVII or siFVIII were also tested for comparison. At 48 h post-injection, FVII and FVIII activities can be measured in plasma, reflecting the siRNA effect in the hepatocytes and LSECs, respectively. As also proven previously,[9] MC3-based LNP efficiently triggered the silencing of FVII (≈90%) relative to the baseline level in hepatocytes, whereas our 1621-LNPs achieved only 30% silencing under comparable conditions (Figure 6B). In contrast to MC3-LNP, 1621-LNP elicited a distinct functional targeting, resulting in optimal FVIII gene silencing in the LSECs (≈80%) (Figure 6B). The specificity of gene silencing was verified by using similar formulations containing siCtrl. Based on the results, it can be concluded that 1621-LNP has an efficient functional siRNA targeting to LSECs rather than hepatocytes. The interpretation of such results can be undertaken with consideration of our novel ionizable component and the differing chemistry of 1621-LNP from MC3-LNP. According to the work of others, the composition profile of LNPs plays a key role in both efficiency and liver cell specificity of gene delivery by influencing LNP physicochemical properties and their biological interaction with blood proteins.[56] In our study, we therefore compared 1621-LNP and MC3-LNP with the most similar composition profiles and physicochemical properties. MC3-LNP has been validated as a very well-established reference for chemical targeting of hepatocytes and a reliable benchmark for comparison due to its known mechanism and consistent performance across different experimental conditions.[29] When considering the similar LNP composition and physicochemical properties (especially regarding the size, zeta potential, and pK_a) between 1621-LNP and MC3-LNP, the functional silencing activity of 1621-LNP in LSECs can be attributed to the chemistry of 1621, enabling efficient endogenous targeting of LSECs, as opposed to hepatocyte targeting observed with MC3-LNP. In line with our observations, Johnson et al. reported that two LNPs sharing similarities in formulation and physical properties, except for the type of ionizable lipid, displayed different abilities to deliver RNA to various types of liver cells. This discrepancy was attributed to differences in protein corona formation, which in turn can impact various aspects of in vivo LNP behavior.[59] Interestingly, internal cellular signaling can also alter the fate of RNAs once they reach their targets.[58] The data of intrahepatic biodistribution and gene silencing efficacy suggest that MC3-LNPs traverse the barrier of KCs and LSECs to internalize into hepatocytes, while 1621-LNPs may predominantly become entrapped within LSECs and KCs. To note, the fast kinetic and ionizable lipid-assisted robust endosomal escape may contribute to the efficient gene silencing in these cells. The development of carriers to interact with and to be taken up by a specific cell type represents a major advance in medical research. In the current paper, we proposed an ionizable carrier-dependent cell tropism for efficient and functional siRNA delivery into LSECs via 1621-LNP, providing a foundation for future studies.[55] Although our experiment gives well-reasoned predictions of 1621-LNP ability for LSEC targeting, pharmacokinetic studies are needed to elucidate the structural-related activities.

Attention has always been paid to the safety aspect of delivery carriers in the drug development field, which has often limited the translation of discoveries into clinical practice. It has been reported that hepatotropic LNPs can induce liver and systemic toxicity via accumulation in the LSECs.[60] These concerns urged us to check the biocompatibility of 1621-LNP by analyzing several well-known cytokines responsible for immune responses (Figure 6C). All measured cytokines in the plasma of 1621-treated mice were found to be within the normal range and not significantly different from those in control groups. Moreover, the indicators for liver damage (e.g., aspartate transaminase, AST, and alanine transaminase, ALT) and kidney function (blood urea nitrogen, BUN, and creatinine, Crea) in 1621-treated mice were compared with those in HBG and MC3-treated mice (Figure 6D). No abnormal alterations were found in these biochemical parameters following 1621-LNP administration. The immunogenicity and biochemical studies revealed a favorable safety profile of 1621-LNP at the administered dose of 5 µg per mouse (≈0.25 mg kg^{-1}).

2.7. In Vivo Targeting of Tumor Endothelial Cells (TECs) Enabled by Surface Modification of XP-LNP

Angiogenesis refers to the process of forming new blood vessels from pre-existent ones to fuel the metabolic demands of fast-growing cancer cells. Therapeutic gene delivery into TECs is a valuable strategy in targeted cancer treatment. This importance comes from the essential role of TECs during angiogenesis, as well as their distinct phenotype compared to the normal endothelial cells, ensuring safe and selective therapy.[61] A panel of potential targets can be found in TECs, which are among the appropriate candidates for antiangiogenic interventions. For instance, the vascular endothelial growth factor receptor-2 (VEGFR-2) is a key transducer of the signals from pro-angiogenic factors (e.g., vascular endothelial growth factor, VEGF) to TECs. Any interventions in the VEGF/VEGFR-2 signaling pathway can impair angiogenesis and tumor growth.[61,62] Another excellent target within the tumor vasculature is the integrin $\alpha_v\beta_3$ receptor, which is predominantly expressed on TECs but poorly on normal endothelium. Moreover, integrin $\alpha_v\beta_3$ promotes the migration and invasion of TECs as a critical step in vasculogenesis.[61] Of particular interest is the synergistic crosstalk between $\alpha_v\beta_3$ and VEGF/VEGFR2 axis during pathological angiogenesis.[63] These significances have qualified integrin $\alpha_v\beta_3$ not only as an ideal target for pharmacological attack but also as a receptor for ligand-directed therapeutics.

Using the capability of integrin $\alpha_v\beta_3$ to be recognized by arginyl-glycyl-aspartic acid (RGD) sequence,[64,65] various RGD-containing peptides have been extensively synthesized, with a preference for cyclic conformation (cRGD), for integrin-targeting applications.[66–68] Modifying siRNA-loaded nanoparticles with RGD-containing peptides (e.g., c(RGDfK)) has been identified as an effective strategy for targeting both tumor cells and tumor vasculature.[69–72]

By bringing these attractive concepts together, we aimed to optimize the effectiveness of our 1621-LNP for targeting integrin-positive cells by changing the lipid composition and cRGD surface modification. In doing so, 2% of non-sheddable DSPE-PEG2000-N_3 in addition to 0.5% DMG-PEG2000 were incorporated in the formulation with proper adjustment of their ratio to the other components (**Figure** 7A). This newly formulated azido-PEG containing 1621-LNP was termed "Azido-LNP" (Az-LNP). Moreover, c(RGDfK) peptide conjugated with a monodisperse PEG_{24} spacer via one N-terminally attached dibenzyl cyclooctene (DBCO) moiety (DBCO-PEG_{24}-c(RGDfK)), as well as DBCO-PEG_{24} as a ligand-free negative control were synthesized (Figure 7B; Figures S5 and S6, Supporting Information). The Az-LNP were subsequently post-modified with DBCO-PEG_{24}-c(RGDfK) or DBCO-PEG_{24} via click chemistry over a 4-h reaction time, thereby increasing the PEG chain length by a further ≈1 kDa (Figure 7C). This reaction was optimized by applying 2 molar equivalents (eq) of DBCO-PEG-ligand per DSPE-PEG-N_3. The 100% conjugation efficiency between DSPE-PEG-N_3 and DBCO-PEG_{24}-c(RGDfK) was confirmed via UV/vis spectroscopy, achieving this within our standard incubation time (4 h) for post-click functionalization (Figure S7, Supporting Information). The Az-LNP, without any modification, were well-dispersed (PDI 0.1) and possessed a uniform size of ≈115 nm in diameter. Neither PEGylation nor cRGD modification induced apparent changes in the particle size or zeta potential. Only PEGylation slightly decreased the surface charge from around −4 to −8 (Figure 7D). To determine the transfection capacity of the formulations, we employed siRNA to silence VEGFR-2 expression (siVEGFR-2) in bEnd.3 cell line and the knockdown effectiveness was verified at the translation level by flow cytometry (Figure 7E). The bEnd.3 cells served as a suitable cell line for analyzing the targeting effect of RGD-modified LNPs due to the expression of integrin $\alpha_v\beta_3$ receptor and VEGFR-2 (Figures S8 and S9A-D, Supporting Information). To evaluate the changes of VEGFR-2 expression upon various treatment groups, the cells treated with a control isotype-matched monoclonal Ab (mAb) were used to set the threshold for VEGFR-2 expression (Figure S9E, Supporting Information). Since HBG-treated cells show the baseline expression of VEGFR-2 compared to isotype control, the percentages and MFI fold change of VEGFR-2 positive cells in the formulation-treated groups were presented relative to the HBG group (Figure 7E). The results indicated that the formulations of Az, PEGylated, and cRGD-modified LNPs decreased the percentage positivity and expression intensities, implying VEGFR-2 gene silencing with higher efficiency for the ligand-targeted LNPs (Figure 7E). The lower total in vitro potency of the targeted LNP (arising from the presence of DSPE-PEG) versus original 1621-LNP (containing only sheddable DMG-PEG) aligns with previous research on DSPE-PEG effect on reducing the cellular uptake and endosomal escape.[73,74] However, this negative effect of PEGylation on transfection efficiency can be restored either by increasing the amount of ionizable lipid in LNP formulation[75] or by employing active targeting using ligands.[73] On the positive side, increasing PEGylation, as in the current case by adding stable DSPE-PEG (C18 acyl chains), plus subsequent further click-PEGylation, has been postulated to increase blood circulation in vivo by minimizing the interaction of stealth carriers with serum proteins, ensuring accumulation in extrahepatic organs such as tumor with favorable transfection efficiency, without necessarily correlating with in vitro data.[73,74,76,77] Accordingly, we examined VEGFR-2 gene silencing in tumor endothelium following i.v. administration of cRGD-modified 1621-LNP in a nude mouse tumor xenograft model (Figure 7F). Since integrin $\alpha_v\beta_3$ can also be found in several tumors, such as neuroblastomas, a subcutaneous Huh7 tumor (with no expression of integrin $\alpha_v\beta_3$) was modeled to validate the efficiency of the system to target integrin $\alpha_v\beta_3$-expressing TECs. When the tumor size reached 400–500 mm^3, the biocompatible dose of 1621-LNPs (5 µg per mouse) was applied based on the previous animal experiment. The

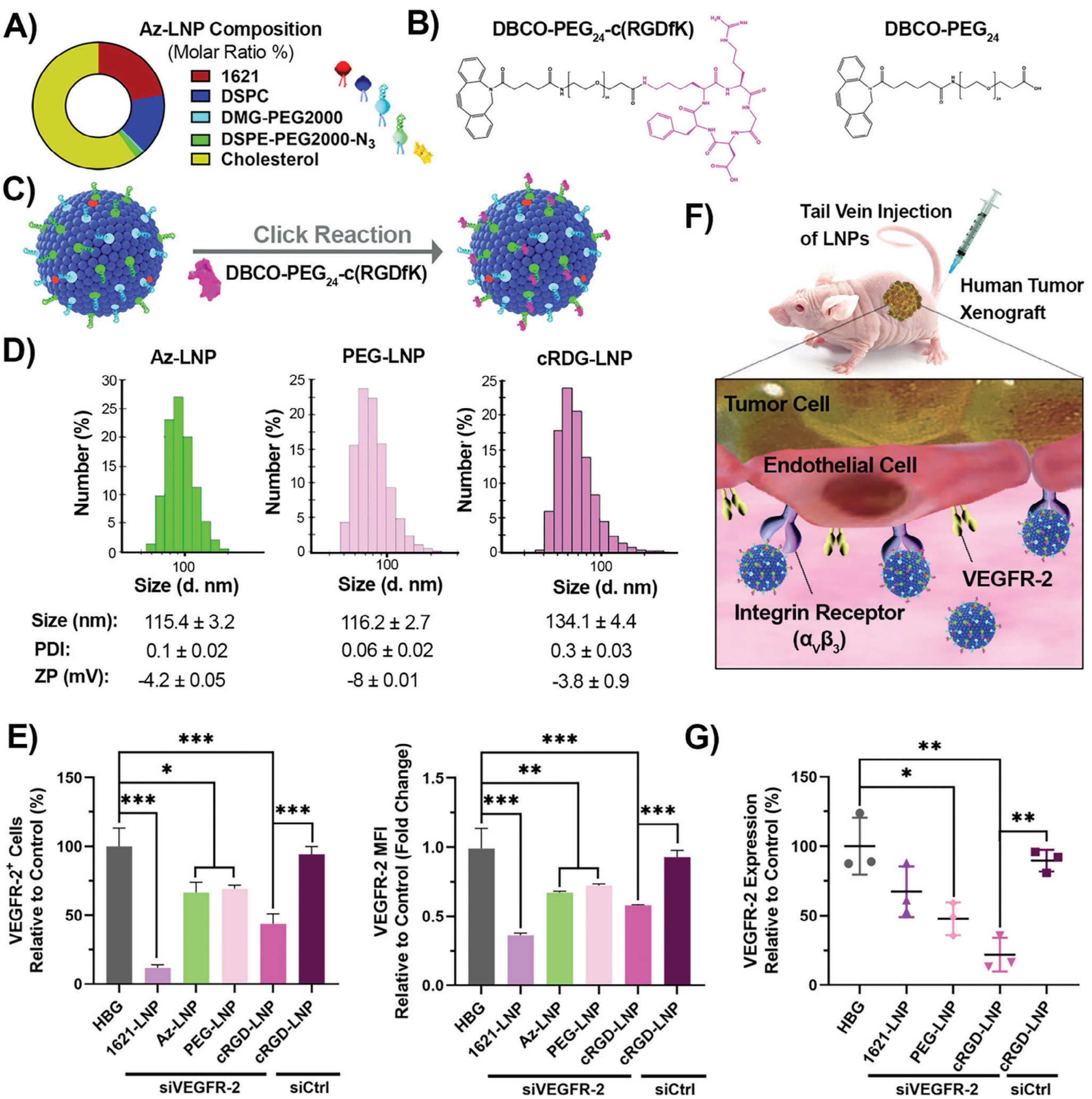

Figure 7. Targeting tumor endothelial cells (TECs) by cRGD-modified 1621-LNP. A) zido-PEG containing 1621-LNP (Az-LNP) formulated with 1621/DSPC/DMG-PEG/DSPE-PEG-N$_3$/cholesterol at a molar ratio (%) of 22.2/15.6/0.5/2/59.7 (N/P 9). B) DBCO-PEG$_{24}$-c(RGDfK) and DBCO-PEG$_{24}$ synthesized via SPPS. C) The azide groups on the surface of LNPs clicked with DBCO-PEG$_{24}$-c(RGDfK) or DBCO-PEG$_{24}$ conjugates at 1:2 molar equivalents (eq). D) Size distribution (number), intensity-averaged diameter, PDI, and zeta potential (ZP) of Az-LNP and modified-LNPs (PEG-LNP, cRGD-LNP) detected by DLS and ELS. E) Expression of VEGFR-2 on bEnd.3 cells quantified by flow cytometry after a 48-h exposure to different siVEGFR-2-LNP formulations at an siRNA dose of 30 ng siRNA (per 5000 cells). The cRGD-LNP (encapsulating siCtrl) was used as a negative control. The obtained data were calculated as percentage (%) and MFI fold changes of positive cells (over isotype control) and are presented relative to the respective values found in HBG group (mean ± SD, *n* = 3). F) Principles for in vivo experiment-based siRNA delivery into a tumor xenograft model by modified-LNPs. The formulations (5 µg siVEGFR-2 in 200 µL HBG/mouse) were injected once into nude mice (6-8 weeks)-bearing Huh7 tumor xenografts (400-500 mm^3) via the tail vein. The strategy for TEC targeting was based on the recognition of integrin ($\alpha_v\beta_3$) by cRGD-modified LNP for efficient functional siVEGFR-2 delivery. G) Expression of VEGFR-2 on TECs quantified by flow cytometry following single i.v. administration of different siRNA-LNP formulations. At 48 h after injection, the tumors were harvested and the TEC-expressing VEGFR-2 in each tumor cell suspension was determined as MFI and is presented as percentage of the value obtained from HBG-injected mice (mean ± SD, *n* = 3). Unstained and isotype controls were employed to eliminate background fluorescence and non-specific binding for each sample. Statistical significance was determined as $^*p \leq 0.05$, $^{**}p \leq 0.01$ and $^{***}p \leq 0.001$.

tumors were dissected at 48 h after treatment with the LNP formulations, and the VEGFR-2 expression was quantified in TEC population of single-tumor cell suspension using flow cytometry. The gating strategy is provided in Figure S10 (Supporting Information). Compared to HBG-treated mice, the VEGFR-2 downregulation was more significant in the mice treated with cRGD-modified LNPs ($p \leq 0.01$) than in those treated with PEG-clicked LNPs ($p \leq 0.05$) (Figure 7G). The stringent specificity of VEGFR-2 silencing was confirmed using siCtrl ($p \leq 0.01$). No difference was found between the PEG-clicked LNP and the initial 1621-LNP formulation (without DSPE-PEG). In contrast to the in vitro results, cRGD-modified LNPs outperformed 1621-LNP in gene silencing in TECs. The results emphasize the role of DSPE-PEG in vivo, by which the DSPE-PEG-decreased transfection efficacy could be rescued. Remarkably, the synergistic effect of PEGylation with cRGD-targeting strategy could promote 1621-LNP efficiency in targeting TECs. It is worth mentioning that the modified Az-LNPs (with PEG and cRGD) were well-tolerated by the mice, as confirmed by no considerable changes in the blood levels of AST, ALT, BUN, and Crea parameters (Figure S11, Supporting Information).

3. Conclusion

Based on the encouraging therapeutic potential of RNA medicines, novel synthetic carriers have been developed for delivery.[78–80] In summary, our research endeavors have led to the development of LNPs with an enhanced capability for siRNA delivery in vitro and in vivo. The innovation lies in using double pH-responsive XP carriers with four units of lipophilic cationizable LAF domains and one unit of hydrophilic cationizable Stp (LAF_4-Stp_1). When incorporated into siRNA-LNPs, the in vitro screening exhibited considerable improvement in cellular uptake, fast and strong endosomal escape, and functional cargo release in comparison with LNPs formulated with the gold standard MC3 lipid. Given the differences between XP-LNP activities in various cell lines, LAF_4-Stp_1 carriers with bundle topology outperformed U-shape topology, and 1621 attained the first rank of efficiency among all tested bundles. The excellent performance of 1621-LNP was well illustrated by >60% gene silencing at a very low siRNA dose of 150 pg in the neuroblastoma cell line. Following systemic administration into mice, 1621 integration in siRNA-LNP resulted in a higher chemical structure-dependent functional targeting of LSECs ("chemical targeting"). These findings were concluded from the efficient siRNA-mediated FVIII knockdown in LSECs and only moderate FVII knockdown in hepatocytes, just the opposite of what was obtained with MC3-LNP. The differential cellular specificity is not yet clarified and might be ascribed to distinct scavenger receptors on LSEC surfaces interacting with the formed protein corona on 1621-LNP, analogous to the apoE/LDRL pathway for MC3-LNP. Alternatively, the fast and potent escape from endosomes might be responsible for the differences in functional targeting.

To pave the way for a 1621-LNP application to TECs, the PEG-lipid profile in the formulation was optimized for improved shielding in blood circulation and better tumor accumulation. Moreover, incorporation of c(RGDfK) on 1621-LNP/siVEGFR-2 surface for "biological targeting" of integrin ($\alpha_v\beta_3$)-overexpressing TECs resulted in strong down-regulation of VEGFR-2 in xenografted Huh7 tumors in nude mice. In sum, our work presents highly potent siRNA-LNPs with tunable endothelial tropism achieved through chemical and active functional targeting, thereby contributing to the evolution of targeted gene silencing strategies in molecular medicine.

4. Experimental Section

Synthesis of Cationizable XP Carriers: The library of XP carriers (Table 1) was synthesized via SPPS as described in Thalmayr et al.[44]

Synthesis of DBCO-PEG-Ligand: The synthesis of DBCO-PEG_{24}-c(RGDfK) and DBCO-PEG_{24} was carried out based on the previous publications.[81–83] DBCO-PEG_{24}-c(RGDfK) was synthesized on a 2-chlorotrityl chloride resin preloaded with L-Gly-OH. The linear precursor structure H_2N-DfKRG-OH was synthesized via automated SPPS by 9-fluorenyl-methoxycarbonyl chemistry. Cleavage of the peptide from the solid phase was performed under mild conditions to keep the side chain protecting groups intact (dichloromethane (DCM)/trifluoroacetic acid (TFA)/triisopropylsilane (TIS) 92.5/5/2.5 (v/v/v), 30 min). Cyclization of the linear peptide was achieved by amide formation between the free N-terminal amino group of aspartic acid and the free C-terminal carboxylic group of glycine. Therefore, the linear peptide was dissolved in DCM to which PyBOP (benzotriazol-1-yl-oxytripyrrolidinophosphonium-hexafluorophosphate, 4 eq), HOBt (1-hydroxybenzotriazol, 4 eq), and DIPEA (diisopropylethylamine, 8 eq) were added for a 3 days incubation at RT. To remove the side chain protecting groups of the cyclic peptide, the solvent was evaporated under reduced pressure and the dried product was dissolved in a cleavage cocktail of TFA/H_2O/TIS 95/2.5/2.5 (v/v/v) for 90 min followed by precipitation of the product in a pre-cooled mixture of n-hexane and methyl tert-butyl ether (MTBE) (3:1 (v/v)). After centrifugation and removal of the supernatant, the resultant pellet was dried under nitrogen stream and purified via reverse-phase high-performance liquid chromatography (RP-HPLC, LaPrep system, VWR International GmbH, Germany) with a Symmetry C18 column (Waters, Germany). For subsequent in-solution coupling of a DBCO-PEG_{24} residue, c(RGDfK) was redissolved in HEPES buffer, and the pH was adjusted to 8.5 with 1 M sodium hydroxide (NaOH). DBCO-dPEG_{24}-TFP (1.2 eq.) was dissolved in DMF, added to the H_2N-c(RGDfK) solution, and the reaction mixture was incubated for 6 h. Finally, DBCO-PEG_{24}-c(RGDfK) was purified via RP-HPLC and analyzed by Matrix-assisted laser desorption/ionization-time of flight-mass spectrometry (MALDI-TOF-MS, Autoflex II mass spectrometer, Bruker Daltonics, Germany). Regarding DBCO-PEG_{24} synthesis, after final cleavage, the obtained product was dialyzed (1000 MWCO, Carl Roth) against 10 mM hydrochloric acid (HCl) for 48 h at 4 °C. Its characterization was performed by MALDI-TOF-MS.

siRNA-LNP Formulation: siRNA-LNPs were formed using the ethanol dilution method in a self-assembly process. First, cholesterol (Sigma-Aldrich), DSPC (Avanti Polar Lipids), DMG-PEG2000 (Avanti Polar Lipids), and either DLin-MC3-DMA (MedChemExpress) or XP carriers were dissolved in 100% ethanol at predetermined molar ratios (%). XP-LNPs and MC3-LNP were made at N/P ratios of 9 or 18 and 3, respectively. The N/P ratio defines the molar ratio of protonatable nitrogen molecules of the carrier (including all secondary amines of Stp units, tertiary amines of LAF units, and terminal amines) to the phosphorous ones in the siRNA backbone. The siRNA was diluted in citrate buffer (10 mM, pH 4). Next, the ethanolic and aqueous solutions were rapidly mixed (1:3 v/v). The resultant mixture was incubated for 10 min at RT and then dialyzed against HBG in a cassette membrane (1000 or 3500 MWCO, Sigma-Aldrich) for 2 h at 4 °C. For empty LNP formulation, all procedures were followed as described above, except for no siRNA being added to the citrate buffer before mixing with lipids. To post-modify the LNPs, DSPE-PEG2000-N_3 (Avanti Polar Lipids) was also added into the ethanolic solution at an optimized molar ratio (%) for azido/DBCO click chemistry reaction. The DBCO-PEG_{24}-c(RGDfk) or DBCO-PEG_{24} was then added to the assembled LNPs at 2 eq (defined as the molar ratio of DBCO to azide groups) for a 4-h incubation at RT. The final siRNA concentration in the transfection solution was 0.012 mg mL^{-1} for in vitro assays and 0.025 or 0.033 mg mL^{-1} for in vivo experiments.

DLS and ELS Measurements: The particle size and zeta potential were evaluated in a folded capillary cell (DTS1070) with DLS and ELS using a Zetasizer Nano ZS (Malvern Instruments, UK). Size and PDI were measured (three times with 6 sub-runs each) in 80 µL of the LNP solution after an equilibration time of 30 s at 25 °C with a refractive index of 1.330 and viscosity of 0.8872 mPa*s. After diluting each sample with HEPES to a final volume of 800 µL, the electrophoretic mobility was read three times with 15 sub-runs, and zeta potential was calculated using the Smuchowski equation. All the setting parameters were the same for surface charge measurement, except for an equilibration time of 60 s. To examine the stability of formulations in cell culture medium in the presence of serum, LNPs were incubated in Dulbecco's modified Eagle's medium (DMEM) supplemented with 10% (v/v) FBS for various time points (1, 2, and 4 h) at 37 °C before measurement. The DLS measurements of DMEM + 10% FBS and LNPs (immediately after formulation in HBG) were proposed as references to distinguish their respective peaks in intensity-size distribution plots.

Agarose Gel Shift Assay: A 2.5% (w/v) gel solution was prepared by dissolving agarose in hot 1x TBE buffer (10.8 g Tris base, 5.5 g boric acid, 0.75 g disodium ethylenediaminetetraacetic acid (EDTA) at pH 8, in 1 L of water), and then cooling down to about 50 °C. The solution was stained with GelRed, poured into a gel-forming plate with a comb, and the comb was removed after gel solidification. Each sample was mixed with loading buffer (6 mL glycerol, 1.2 mL 0.5 M EDTA, 2.8 mL H_2O, 0.02 g bromophenol blue) in a ratio of 5:1 (v/v) to a total volume of 24 µL. The samples were loaded into the gel pockets, and electrophoresis was carried out in 1x TBE buffer for 70 min at 120 V. Free siRNA in HBG at an equal concentration as in the formulations was used as a positive control and HBG as a negative control. To examine the stability of formulation in serum, LNPs were incubated in HBG in the presence of 90% (v/v) FBS for 2 h at 37 °C before running in the gel. The bands were visualized by a UV transilluminator (Biostep, Germany).

TEM Measurement: Each LNP sample (10 µL) was applied to a carbon-coated copper grid (Ted Pella, Inc. USA, 300 mesh, 3.0 mm O.D.) hydrophilized by argon plasma (420 V, 1 min) for 30 s. After removing the residual solvent with filter paper, the grid was quickly washed with 5 µL of 1% (w/v) uranyl formate, stained immediately afterward with another 5 µL droplet of uranyl formate solution for 5s, and finally air-dried at RT. The grid was imaged via a JEOL JEM-1100 (JEOL, Tokyo, Japan) electron microscope at 80 kV.

RiboGreen Assay: The encapsulation efficiency of siRNA in LNPs (siRNA-EE) was quantitated using Quant-it RiboGreen RNA Assay Kit (ThermoFisher Scientific) and analyzed on a Tecan microplate reader (Spectrafluor Plus, Switzerland). Briefly, 40 µL of LNP solution was diluted with 210 µL 1× TE (10 mM Tris-HCl, 1 mM EDTA, pH 7.5, in RNase-free water). HBG was used as a blank sample. Then, 50 µL of diluted LNP solution was added to either 50 µL 1x TE buffer (non-lysed LNPs) or 50 µL 1× TE containing 2% (v/v) TritonX-100 (lysed LNPs) into a black 96-well plate in duplicate. The plate was kept for 10 min at 37 °C under constant shaking followed by RT-cooling down for 5 min. Next, the samples were incubated with 100 µL Ribogreen solution (RiboGreen reagent diluted 200-fold in 1x TE buffer) for 15 min at 37 °C under a light protected condition before measuring the fluorescent signal (excitation/emission 485/520). The siRNA-EE was calculated by the following formula and given in percentage.

$$EE\ (\%) = 100\% - \left(\frac{mean\ emission_{untreated\ control}}{mean\ emission_{treated\ sample}} \right) * 100\% \qquad (1)$$

Cell Culture: The human cervical adenocarcinoma HeLa cells (DSMZ, German Collection of Microorganisms and Cell Cultures GmbH, Braunschweig, Germany) and HeLa-Gal8-mRuby3 cells[84] with stably expressing Galectin8-mRuby3 fusion protein were cultured in DMEM-low glucose (1 g L^{-1} glucose). The gene silencing effect of siRNA-LNPs was examined in cell lines with stable expression of eGFPLuc reporter gene, including murine neuroblastoma Neuro2A (N2A)/eGFPLuc cells,[85] human cervix carcinoma KB/eFPLuc cells,[86] and murine colon carcinoma CT26/eGFPLuc cells[87] grown in DMEM-low glucose, and human hepatocellular carcinoma Huh7/eGFPLuc cells,[88] and Huh7 WT cells (Japanese Collection of Research Bioresources Cell Bank, Osaka, Japan) grown in DMEM/Nutrient Mixture F12-Ham. The murine brain adenocarcinoma bEnd.3 cells were cultured in DMEM-high glucose (4.5 g L^{-1} glucose). For maintenance of cultures, all the media were supplemented with 10% (v/v) FBS, and antibiotics (100 U mL^{-1} of penicillin, 100 µg mL^{-1} of streptomycin). The cells were kept in an incubator set at 37 °C with 5% CO_2 and a relative humidity of 95%.

Cellular Viability by MTT Assay: The cells were seeded in 96-well plates (5×10^3 cells per well). After 24 h, cell transfection was performed with different LNPs at various doses (240, 120, 60, 30, 15, 7.5 ng siRNA per well). For this, the indicated volumes of siRNA-LNP solution were added to the corresponding wells as well as HBG to achieve a final volume of 100 µL per well. HBG was applied as a negative control. After 48 h incubation at 37 °C, 10 µL MTT (5 mg mL^{-1}, Sigma-Aldrich) was added to each well followed by incubation for a further 2 h. Afterward, the supernatant was removed and the cells were frozen at –80 °C for at least 1 h. Next, the violet crystals were dissolved in DMSO (100 µL per well), and the plates were kept for 30 min at 37 °C under gentle shaking. Absorbance was measured at a wavelength of 590 nm with a reference wavelength of 690 nm using a microplate reader. The viability of transfected cells was calculated as a percentage of HBG-treated cells (100%) and is presented as means of triplicate wells ± SD.

Cellular Internalization by CLSM: The cells were seeded overnight on Ibidi µ-slide 8-well chamber slides (Ibidi GmbH, Germany) (2×10^4 cells per well). The LNPs containing 20% Cy5-labeled + 80% unlabeled siRNA were exposed to cells at a dose of 120 ng siRNA per well (30 ng/5000 cells) for 1 h at 37 °C. Next, the cells were washed twice with phosphate-buffered saline (PBS, pH 7.4), fixed with 4% w/v paraformaldehyde (PFA) for 30 min at RT, and re-washed before staining of actin skeletons with rhodamine-phalloidin (1 µg mL^{-1}, Invitrogen) and cell nuclei with DAPI (1 µg mL^{-1}, Sigma-Aldrich). After 1 h incubation at RT, the staining solutions were removed, and the wells were washed and then filled with PBS before imaging. The images were captured by a Leica-TCS-SP8 confocal microscope with HC PL APO 63 × 1.4 objective (Germany) using Leica LAS X software.

Cellular Uptake by Flow Cytometry: The cells were seeded in 96-well plates (1×10^4 cells per well). On the following day, the cells were treated with LNPs containing 20% Cy5-labeled + 80% unlabeled siRNA at a dose of 60 ng siRNA per well (30 ng/5000 cells) for 1 h at 37 °C, followed by PBS washing. HBG-treated cells served as a negative control. To remove non-specifically bound LNPs, the cells were incubated with heparin (1000 I.U. mL^{-1} in PBS) for 15 min at RT, washed twice with PBS, and collected in flow cytometry buffer (PBS with 10% v/v FBS) containing DAPI viability dye. The read-out was conducted in viable cells using CytoFLEX S flow cytometry (Beckman, USA). Data were analyzed using FlowJo software (version 10.10). The cellular uptake was quantified as the percentage of positive cells and MFI, and is presented as means of triplicate wells ± SD.

Reporter Gene Silencing Study by Luciferase Assay: The cells expressing eGFPLuc reporter gene were seeded in 96-well plates (5×10^3 cells/well) one day prior to the experiment. On the day of experiment, the medium was refreshed, and the cells were transfected with different LNPs at various doses (30, 15, 7.5 ng siRNA per well). The LNPs were formulated with control siRNA (siCtrl, sense strand: 5′-AuGuAuuGGccuGuAuuAGdTsdT-3′; antisense strand: 5′-CuAAuAcAGGCcAAuAcAUdTsdT-3′) or eGFP-targeting siRNA (siGFP, sense strand: 5′-AuAucAuGGccGAcAAGcAdTsdT-3′; antisense strand: 5′-UGCUUGUCGGCcAUGAuAUdTsdT-3′) from Axolabs GmbH (Kulmbach, Germany) with 2′methoxy modifications (indicated by small letters) and phosphorothioate linkages (indicated by "s"). After 48 h incubation at 37 °C, the medium was exchanged by 100 µL of cell culture 0.5x lysis buffer (Promega), followed by 45 min incubation at RT. Luciferase activity was measured in 35 µL cell lysate by Centro LB 960 plate reader luminometer (Berthold Technologies, Germany) using LAR buffer (20 mM glycylglycine, 1 mM $MgCl_2$, 0.1 mM EDTA, 3.3 mM dithiothreitol (DTT), 0.55 mM adenosine 5′-triphosphate (ATP), 0.27 mM coenzyme A, pH 8-8.5) supplemented with 5% (v/v) of luciferin solution (10 mM luciferin, 29.4 mM glycylglycine). The relative light units (RLUs) were calculated as a percentage of HBG-treated cells (100%), and the luciferase activity of the eGFPLuc fusion protein is presented as means of triplicate wells ± SD.

Reporter Gene Silencing Study by Flow Cytometry: The cells were seeded in 24-well plates (2 × 10^4 cells per well). Next day, different LNP formulations loaded with VEGFR-2-targeting siRNA (siVEGFR-2, ON-TARGETPlus SMARTpool siRNA, Dharmacon) were given to the cells at a dose of 120 ng siRNA per well (30 ng per 5000 cells). After 48 h incubation at 37 °C, the cells underwent PBS washing, harvesting, and incubation in flow cytometry buffer containing PE-Vio-conjugated VEGFR-2 mAb (REA1116, Miltenyi Biotec) for 30 min on ice (in the dark). Subsequently, the cells were washed twice and re-suspended in flow cytometry buffer with 0.1% Sytox blue viability dye (Invitrogen). The samples were acquired by flow cytometry (MACSQuant Analyzer 10, Miltenyi Biotec, Germany) and the data were analyzed using FlowJo software (version 10.1) to determine the percentage of VEGFR-2-positive cells and MFI values. An isotype-matched mAb (IgG1, REA293, Miltenyi Biotec) served as a control to set the threshold. The data is presented as means of triplicate wells ± SD (relative to HBG control group).

Receptor Gene Expression Study by Flow Cytometry: The harvested cells were suspended in the flow cytometry buffer containing primary integrin $\alpha_v\beta_3$ mAb (BS1310R, BIOSS) for 2 h on ice. Then, the cells were washed and incubated with DyLight 488-secondary Ab (Poly4064, BioLegend) for a further 2 h. After two final washing steps, the cells were re-suspended in flow cytometry buffer with 0.1% Sytox dye. The integrin expression was flow cytometrically quantified on the cell surface, and the resulting data were analyzed using FlowJo software.

Gal8 recruitment Assay: The HeLa-Gal8-mRuby cells were plated on Ibidi μ-slide 8-well chamber slides at 24 h before the experiment (2 × 10^4 cells/well). The siRNA-LNPs were then incubated with the cells at a dose of 120 ng siRNA (30 ng per 5000 cells) for 4 h, and later the cells were subjected to CLSM using the preparation steps explained in Section 4.10. For the ImageStream analysis, the cells were trypsinized at 4 h post-transfection, washed with PBS, and suspended in flow cytometry buffer containing Hoechst 33 342 dye (1 μg mL^{-1}, Invitrogen) for nuclei staining. A number of 5 × 10^3 cells per sample were acquired by the ImageStream X Mk II Imaging Flow Cytometer (MilliporeSigma, Germany) at 60X magnification, and the data were analyzed by AMNIS IDEAS Software. In this experiment, brightfield was detected in channel 1, Gal8-mRuby in channel 4, and Hoechst in channel 7. The numbers of Gal8-mRuby3 spots resulting from endosomal rapture were quantified using the Spot Count feature, and the normalized results were plotted in frequency histograms for each sample.

Animal Experiments: All animal experiments were carried out according to the guidelines of the German Animal Welfare Act and were approved by the animal experiments ethical committee of the Government of Upper Bavaria (accreditation numbers Gz. ROB-55.2–2532.Vet_02-19–19 and ROB-55.2–2532.Vet_02-19–20). For in vivo liver cell and TEC targeting studies, female BALB/c mice (Janvier, Le Genest-Saint-Isle, France) and female NMRI-nu (nu/nu) mice (Janvier, Le Genest-Saint-Isle, France) were used, respectively. The mice were housed in isolated ventilated cages under pathogen-free conditions with a 12-h light/dark cycle and free access to water and food ad libitum, and underwent at least a seven-day acclimation period before initiating the experiments.

Ex Vivo Biodistribution Study: The LNPs encapsulating Cy7-siRNA in 150 μL HBG were administered i.v. (via tail vein) to BALB/c mice (6-8 weeks of age, n = 3 per group) at a siRNA dose of 5 μg per mouse. After 1 h, the mice were euthanized by cervical dislocation, and the main organs were harvested for near infrared (NIR) *ex vivo* imaging using an in vivo optical imaging system (IVIS 100; Xenogen, USA). The fluorescence signal efficiency was analyzed following equalization of color bar scales using the IVIS Lumina system equipped with Living Image software 3.2 (Caliper Life Sciences, Hopkinton, MA, USA).

Intrahepatic Distribution Study at Cellular Level: The LNPs encapsulating Cy5-siRNA in 150 μL HBG were administered i.v. (via tail vein) to BALB/c mice (6-8 weeks of age, $n = 2$ per group) at a siRNA dose of 5 μg per mouse. After 1 h, the mice were euthanized by cervical dislocation, and the liver tissue was harvested to prepare single-cell suspension. The process involved washing the harvested tissues with PBS, gently mincing them using a gentleMACS dissociator (Miltenyi, Germany, Bergisch Gladbach), and incubating them in a digestion buffer containing collagenase IV (200 U mL-1, Merck) and DNase I (100 μg mL-1, Roche) for at least 30 min at 37 °C. Next, the cells were stained with antibodies of FITC-conjugated CD45 (REA737, Miltenyi Biotec), PE-Vio770-conjugated CD31 (REA784, Miltenyi Biotec), PE-Vio770-conjugated F4/80 (REA126, Miltenyi Biotec), and PE-conjugated CD32b (AT130-2, Invitrogen) for 30 min at 4 °C. Following centrifugation, the supernatant was discarded, and the remaining cell pellet was resuspended in flow cytometry buffer with Hoechst 33 342 dye. The uptake of Cy5-siRNA-LNP by hepatocytes, LSECs, and KCs was acquired on an Imaging Flow Cytometer, and the data were analyzed using AMNIS IDEAS Software. The liver cells of HBG-treated mice were applied to exclude background autofluorescence. The siRNA-LNP delivery was assessed by quantifying the Cy5-positive cells, using histograms derived from gated cell populations.

Determination of FVII and FVIII Activities in Mice Plasma by Chromogenic Assay: The LNPs were formulated either with siFVII (Ambion In Vivo Factor VII siRNA, ThermoFischer Scientific) or siFVIII (ON-TARGETPlus SMARTpool siRNA, Dharmacon). siRNA-loaded LNPs in 150 μL HBG were administered i.v. (via tail vein) to BALB/c mice (6-8 weeks of age, $n = 4$ per group) at a siRNA dose of 5 μg per mouse. After 48 h, the mice were placed under anesthesia by isoflurane inhalation, and their blood was collected by heart puncture in citrate-treated tubes (Sarstedt AG & Co) to separate plasma. The activity levels of FVII and FVIII were determined in the plasma by chromogenic assay. The plasma of HBG-treated mice represented the baseline control level of FVII/FVIII activity, and FVII and FVIII activity in LNP-treated groups were calculated as a percentage relative to the control group ($n = 4$ per group).

Determination of Gene Knockdown in Mice TECs by Flow Cytometry: The tumor inoculation was performed in nude mice by subcutaneous injection of 5 × 10^6 Huh7 cells (in 150 μL) into the left flank. The tumor volume was measured using a caliper and calculated as [0.5 × (longest diameter) × (shortest diameter)^2], and daily body weights were monitored. Once tumors reached 400–500 mm^3 in size, different LNP formulations encapsulating siVEGFR-2 (ON-TARGETPlus SMARTpool siRNA, Dharmacon) or siCtrl in 200 μL HBG were administered i.v. (via tail vein) to tumor-bearing nude mice (6-8 weeks of age, $n = 3$ per group) at a siRNA dose of 5 μg per mouse. After 48 h, mice were euthanized by cervical dislocation, and the tumor tissues were harvested. The tumor cell suspension was prepared as detailed in Section 4.18, and the cells were then stained with antibodies including FITC-conjugated CD45 (REA737, Miltenyi Biotec), PE-conjugated CD31 (REA784, Miltenyi Biotec), and PE-Vio770-conjugated VEGFR-2 (REA1116, Miltenyi Biotec) for 30 min at 4 °C. After centrifugation, the supernatant was removed, and the remaining cell pellet was resuspended in flow cytometry buffer with Sytox Blue dye. Flow cytometry (MACSQuant Analyzer 10, Miltenyi Biotec, Germany) was then employed to measure VEGFR-2 expression in TECs of viable tumor cell suspension. Unstained and isotype controls were implemented to eliminate background fluorescence and non-specific binding from the analysis, respectively. Data were analyzed using FlowJo software (version 10.10).

Blood Biochemistry Analysis: The blood samples of mice were collected using EDTA-coated tubes (Sarstedt AG & Co), and plasma was separated after centrifugation at 3000 rpm for 7 minutes. The plasma levels of ALT, AST, BUN), and Crea were analyzed in the Clinic of Small Animal Medicine of the faculty of Veterinary Medicine at the Ludwig-Maximilians-Universität (LMU), Munich, Germany.

Multiplex Cytokine Analysis: The concentrations of inflammatory cytokines (e.g., GM-CSF, IFN-γ, IL-2, IL-4, IL-5, IL-10, IL-12, IL-17A, IL-23, and TNF-α) in mouse plasma samples were quantitatively measured based on a fluorescent bead-based system using MACSPlex Cytokine Kits (Miltenyi Biotec) according to the manufacturer's protocol.

Ultraviolet/Visible Light (UV-VIS) Spectrometer Study: The DBCO-PEG24-c(RGDfK) conjugate and DSPE-PEG2000-N3 lipid were mixed at 2:1 molar eq and then transferred into a micro UV-cuvettes (Brand GmbH & Co. KG, Germany). The absorbance of DBCO was recorded at 308 nm at 1-minute intervals over a period of 12 h using a UV-VIS spectrometer (Agilent Cary 3500, USA). The progress/completion of the click chemistry reaction was verified by observing the decrease in DBCO signal over time.

Statistical Analysis: Statistical analyses were performed using the unpaired Student's t-test, one-way analysis of variance in GraphPad Prism (Version 9.5.1, GraphPad, San Diego, CA, USA). p values were considered statistically significant as follows: ns: not significant, $^{*}p \leq 0.05$, $^{**}p \leq 0.01$, $^{***}p \leq 0.001$, and $^{****}p \leq 0.0001$.

Supporting Information

Supporting Information is available from the Wiley Online Library or from the author.

Acknowledgements

The authors acknowledge support by the German Research Foundation (DFG) SFB1032 (project-ID 201269156) sub-project B4 (to E.W.), and BMBF Cluster for Future "CNATM – Cluster for Nucleic Acid Therapeutics Munich" (to E.W.). The authors thank i) Dr. Yi Lin and Prof. Ulrich Lächelt for providing the HeLa-Gal8-mRuby3 cells, ii) Dr. Benli-Hoppe for ligand synthesis, iii) Susanne Kempter for performing TEM measurement, iv) Iana Gadjalova and Cell Analysis Core Facility TranslaTUM for their kind help with imaging, v) Profs. Biel and Fürst for providing the IVIS imaging system, and vi) Wolfgang Rödl and Olga Brück for practical support.

Open access funding enabled and organized by Projekt DEAL.

Conflict of Interest

The authors declare no conflict of interest.

Author Contributions

M.Y. performed conceptualization, methodology, validation, investigation, and writing of original draft. J.P. performed methodology, validation, and investigation. M.H.K. performed methodology, validation, and investigation. J.S. performed methodology, validation, and investigation. M.G. performed methodology, validation, and investigation. M.H. performed methodology, validation, and investigation. V.V. performed methodology, validation, and investigation. C.C.H. performed methodology, validation, and investigation. B.W. performed review and editing. G.M. performed review and editing. A.B.D. performed conceptualization, methodology, validation, investigation, review, and editing. E.W. performed conceptualization, supervision, review, editing, and funding acquisition. All authors have read and agreed to the published version of the manuscript.

Data Availability Statement

The data that support the findings of this study are available from the corresponding author upon reasonable request.

Keywords

cRGD, endothelial cells, lipid nanoparticles, lipoamino fatty acid, liver, siRNA delivery, targeting, tumor

Received: January 26, 2024
Revised: June 7, 2024
Published online:

---

[1] M. M. Zhang, R. Bahal, T. P. Rasmussen, J. E. Manautou, X.-b. Zhong, *Biochem. Pharmacol.* **2021**, *189*, 114432.
[2] M. Egli, M. Manoharan, *Nucleic Acids Res.* **2023**, *51*, 2529.
[3] Y. N. Lamb, *Drugs* **2021**, *81*, 389.
[4] M. Moazzam, M. Zhang, A. Hussain, X. Yu, J. Huang, Y. Huang, *Mol. Ther.* **2024**, *32*, 284.
[5] K. A. Whitehead, R. Langer, D. G. Anderson, *Nat. Rev. Drug Discovery* **2009**, *8*, 129.
[6] I. A. Khalil, Y. Yamada, H. Harashima, *Expert opinion on drug delivery* **2018**, *15*, 1053.
[7] M. A. Subhan, V. P. Torchilin, *Nanomedicine* **2020**, *29*, 102239.
[8] M. Friedrich, A. Aigner, *BioDrugs* **2022**, *36*, 549.
[9] M. Jayaraman, S. M. Ansell, B. L. Mui, Y. K. Tam, J. Chen, X. Du, D. Butler, L. Eltepu, S. Matsuda, J. K. Narayanannair, *Angew. Chem.* **2012**, *124*, 8657.
[10] J. A. Kulkarni, D. Witzigmann, S. B. Thomson, S. Chen, B. R. Leavitt, P. R. Cullis, R. van der Meel, *Nat. Nanotechnol.* **2021**, *16*, 630.
[11] F. Freitag, E. Wagner, *Adv. Drug Delivery Rev.* **2021**, *168*, 30.
[12] D. Adams, A. Gonzalez-Duarte, W. D. O'Riordan, C.-C. Yang, M. Ueda, A. V. Kristen, I. Tournev, H. H. Schmidt, T. Coelho, J. L. Berk, *N. Engl. J. Med.* **2018**, *379*, 11.
[13] L. Schoenmaker, D. Witzigmann, J. A. Kulkarni, R. Verbeke, G. Kersten, W. Jiskoot, D. J. Crommelin, *Int. J. Pharm.* **2021**, *601*, 120586.
[14] P. R. Cullis, M. J. Hope, *Mol. Ther.* **2017**, *25*, 1467.
[15] C. H. Albertsen, J. A. Kulkarni, D. Witzigmann, M. Lind, K. Petersson, J. B. Simonsen, *Adv. Drug Delivery Rev.* **2022**, *188*, 114416.
[16] D. Sun, Z.-R. Lu, *Pharm. Res.* **2023**, *40*, 27.
[17] M. Schlich, R. Palomba, G. Costabile, S. Mizrahy, M. Pannuzzo, D. Peer, P. Decuzzi, *Bioeng. Transl. Med.* **2021**, *6*, e10213.
[18] A. Spadea, M. Jackman, L. Cui, S. Pereira, M. J. Lawrence, R. A. Campbell, M. Ashford, *ACS Appl. Mater. Interfaces* **2022**, *14*, 30371.
[19] C. Qiu, F. Xia, J. Zhang, Q. Shi, Y. Meng, C. Wang, H. Pang, L. Gu, C. Xu, Q. Guo, *Research* **2023**, *6*, 0148.
[20] J. Gilleron, W. Querbes, A. Zeigerer, A. Borodovsky, G. Marsico, U. Schubert, K. Manygoats, S. Seifert, C. Andree, M. Stöter, *Nat. Biotechnol.* **2013**, *31*, 638.
[21] X. Han, H. Zhang, K. Butowska, K. L. Swingle, M.-G. Alameh, D. Weissman, M. J. Mitchell, *Nat. Commun.* **2021**, *12*, 7233.
[22] K. Lam, A. Leung, A. Martin, M. Wood, P. Schreiner, L. Palmer, O. Daly, W. Zhao, K. McClintock, J. Heyes, *Adv. Mater.* **2023**, *35*, 2209624.
[23] S. Sabnis, E. S. Kumarasinghe, T. Salerno, C. Mihai, T. Ketova, J. J. Senn, A. Lynn, A. Bulychev, I. McFadyen, J. Chan, *Mol. Ther.* **2018**, *26*, 1509.
[24] S. Liu, J. Liu, H. Li, K. Mao, H. Wang, X. Meng, J. Wang, C. Wu, H. Chen, X. Wang, *Biomaterials* **2022**, *287*, 121645.
[25] A. M. Manning, G. Tilstra, A. B. Khan, J. Couture-Senécal, Y. M. A. Lau, J. Pang, A. A. Abow, C. S. Robbins, O. F. Khan, *Small* **2023**, *19*, 2302917.
[26] K. Hashiba, Y. Sato, M. Taguchi, S. Sakamoto, A. Otsu, Y. Maeda, T. Shishido, M. Murakawa, A. Okazaki, H. Harashima, *Small Science* **2023**, *3*, 2200071.
[27] Y. Yan, X. Liu, L. Wang, C. Wu, Q. Shuai, Y. Zhang, S. Liu, *Biomaterials* **2023**, *301*, 122279.
[28] O. Escalona-Rayo, P. Papadopoulou, B. Slütter, A. Kros, *Curr. Opin. Biotechnol.* **2024**, *85*, 103041.
[29] A. Akinc, M. A. Maier, M. Manoharan, K. Fitzgerald, M. Jayaraman, S. Barros, S. Ansell, X. Du, M. J. Hope, T. D. Madden, *Nat. Nanotechnol.* **2019**, *14*, 1084.
[30] K. J. Kauffman, J. R. Dorkin, J. H. Yang, M. W. Heartlein, F. DeRosa, F. F. Mir, O. S. Fenton, D. G. Anderson, *Nano Lett.* **2015**, *15*, 7300.

[31] R. Pattipeiluhu, G. Arias-Alpizar, G. Basha, K. Y. Chan, J. Bussmann, T. H. Sharp, M. A. Moradi, N. Sommerdijk, E. N. Harris, P. R. Cullis, *Adv. Mater.* **2022**, *34*, 2201095.
[32] A. Akinc, W. Querbes, S. De, J. Qin, M. Frank-Kamenetsky, K. N. Jayaprakash, M. Jayaraman, K. G. Rajeev, W. L. Cantley, J. R. Dorkin, *Mol. Ther.* **2010**, *18*, 1357.
[33] Q. Cheng, T. Wei, L. Farbiak, L. T. Johnson, S. A. Dilliard, D. J. Siegwart, *Nat. Nanotechnol.* **2020**, *15*, 313.
[34] S. A. Dilliard, Q. Cheng, D. J. Siegwart, *Proc. Natl. Acad. Sci. USA* **2021**, *118*, e2109256118.
[35] S. T. LoPresti, M. L. Arral, N. Chaudhary, K. A. Whitehead, *J. Controlled Release* **2022**, *345*, 819.
[36] A. Algarni, E. H. Pilkington, E. J. Suys, H. Al-Wassiti, C. W. Pouton, N. P. Truong, *Biomater. Sci.* **2022**, *10*, 2940.
[37] J. Chen, Y. Xu, M. Zhou, S. Xu, A. J. Varley, A. Golubovic, R. X. Z. Lu, K. C. Wang, M. Yeganeh, D. Vosoughi, *Proc. Natl. Acad. Sci. USA* **2023**, *120*, e2309472120.
[38] N. Shobaki, Y. Sato, H. Harashima, *Int. J. Nanomed.* **2018**, *2018*, 8395.
[39] B. L. Mui, Y. K. Tam, M. Jayaraman, S. M. Ansell, X. Du, Y. Y. C. Tam, P. J. Lin, S. Chen, J. K. Narayanannair, K. G. Rajeev, *Molecular Therapy-Nucleic Acids* **2013**, *2*, 139.
[40] C. D. Sago, M. P. Lokugamage, F. Z. Islam, B. R. Krupczak, M. Sato, J. E. Dahlman, *J. Am. Chem. Soc.* **2018**, *140*, 17095.
[41] T. Suzuki, Y. Suzuki, T. Hihara, K. Kubara, K. Kondo, K. Hyodo, K. Yamazaki, T. Ishida, H. Ishihara, *Int. J. Pharm.* **2020**, *588*, 119792.
[42] D. Zukancic, E. J. Suys, E. H. Pilkington, A. Algarni, H. Al-Wassiti, N. P. Truong, *Pharmaceutics* **2020**, *12*, 1068.
[43] M. Kim, M. Jeong, S. Hur, Y. Cho, J. Park, H. Jung, Y. Seo, H. Woo, K. Nam, K. Lee, *Sci. Adv.* **2021**, *7*, eabf4398.
[44] S. Thalmayr, M. Grau, L. Peng, J. Pöhmerer, U. Wilk, P. Folda, M. Yazdi, E. Weidinger, T. Burghardt, M. Höhn, E. Wagner, S. Berger, *Adv. Mater.* **2023**, *35*, 2211105.
[45] F. Haase, J. Pöhmerer, M. Yazdi, M. Grau, Y. Zeyn, U. Wilk, T. Burghardt, M. Höhn, C. Hieber, M. Bros, E. Wagner, S. Berger, *Eur. J. Pharm. Biopharm.* **2024**, *194*, 95.
[46] A. K. Leung, I. M. Hafez, S. Baoukina, N. M. Belliveau, I. V. Zhigaltsev, E. Afshinmanesh, D. P. Tieleman, C. L. Hansen, M. J. Hope, P. R. Cullis, *J. Phys. Chem. C* **2012**, *116*, 18440.
[47] J. A. Kulkarni, D. Witzigmann, J. Leung, Y. Y. C. Tam, P. R. Cullis, *Nanoscale* **2019**, *11*, 21733.
[48] T. L. Moore, L. Rodriguez-Lorenzo, V. Hirsch, S. Balog, D. Urban, C. Jud, B. Rothen-Rutishauser, M. Lattuada, A. Petri-Fink, *Chem. Soc. Rev.* **2015**, *44*, 6287.
[49] S. Ndeupen, Z. Qin, S. Jacobsen, A. Bouteau, H. Estanbouli, B. Z. Igyártó, *Iscience* **2021**, *24*, 103479.
[50] M. J. Munson, G. O'Driscoll, A. M. Silva, E. Lázaro-Ibáñez, A. Gallud, J. T. Wilson, A. Collén, E. K. Esbjörner, A. Sabirsh, *Commun. biol.* **2021**, *4*, 211.
[51] C. Scholz, E. Wagner, *J. controlled release* **2012**, *161*, 554.
[52] K. V. Kilchrist, S. C. Dimobi, M. A. Jackson, B. C. Evans, T. A. Werfel, E. A. Dailing, S. K. Bedingfield, I. B. Kelly, C. L. Duvall, *ACS Nano* **2019**, *13*, 1136.
[53] J. P. Bost, M. Ojansivu, M. J. Munson, E. Wesén, A. Gallud, D. Gupta, O. Gustafsson, O. Saher, J. Rädler, S. G. Higgins, *Commun. Biol.* **2022**, *5*, 185.
[54] D. Witzigmann, J. A. Kulkarni, J. Leung, S. Chen, P. R. Cullis, R. van der Meel, *Adv. Drug Delivery Rev.* **2020**, *159*, 344.
[55] J. Gracia-Sancho, E. Caparrós, A. Fernandez-Iglesias, R. Frances, *Nat. Rev. Gastroenterol. Hepatol.* **2021**, *18*, 411.
[56] Y. Sato, H. Hatakeyama, M. Hyodo, H. Harashima, *Mol. Ther.* **2016**, *24*, 788.
[57] K. Paunovska, A. J. da Silva Sanchez, C. D. Sago, Z. Gan, M. P. Lokugamage, F. Z. Islam, S. Kalathoor, B. R. Krupczak, J. E. Dahlman, *Adv. Mater.* **2019**, *31*, 1807748.
[58] C. D. Sago, B. R. Krupczak, M. P. Lokugamage, Z. Gan, J. E. Dahlman, *Cell Mol. Bioeng.* **2019**, *12*, 389.
[59] L. T. Johnson, D. Zhang, K. Zhou, S. M. Lee, S. Liu, S. A. Dilliard, L. Farbiak, S. Chatterjee, Y.-H. Lin, D. J. Siegwart, *Mol. Pharmaceutics* **2022**, *19*, 3973.
[60] Y. Sato, H. Matsui, N. Yamamoto, R. Sato, T. Munakata, M. Kohara, H. Harashima, *J. Controlled Release* **2017**, *266*, 216.
[61] Z.-L. Liu, H.-H. Chen, L.-L. Zheng, L.-P. Sun, L. Shi, *Signal Transduction and Targeted Therapy* **2023**, *8*, 198.
[62] X. Fu, Y. Yang, X. Li, H. Lai, Y. Huang, L. He, W. Zheng, T. Chen, *Nanomed.: Nanotechnol., Biol. and Med.* **2016**, *12*, 1627.
[63] H. Bazzazi, Y. Zhang, M. Jafarnejad, A. S. Popel, *J. theoretical Biol.* **2018**, *455*, 212.
[64] E. Ruoslahti, M. D. Pierschbacher, *Science* **1987**, *238*, 491.
[65] W. Arap, R. Pasqualini, E. Ruoslahti, *Science* **1998**, *279*, 377.
[66] R. P. Harbottle, R. G. Cooper, S. L. Hart, A. Ladhoff, T. McKay, A. M. Knight, E. Wagner, A. D. Miller, C. Coutelle, *Hum. Gene Ther.* **1998**, *9*, 1037.
[67] Z. Ge, Q. Chen, K. Osada, X. Liu, T. A. Tockary, S. Uchida, A. Dirisala, T. Ishii, T. Nomoto, K. Toh, Y. Matsumoto, M. Oba, M. R. Kano, K. Itaka, K. Kataoka, *Biomater.* **2014**, *35*, 3416.
[68] S. Fu, X. Xu, Y. Ma, S. Zhang, S. Zhang, *J. Drug Targeting* **2019**, *27*, 1.
[69] R. M. Schiffelers, A. Ansari, J. Xu, Q. Zhou, Q. Tang, G. Storm, G. Molema, P. Y. Lu, P. V. Scaria, M. C. Woodle, *Nucleic Acids Res.* **2004**, *32*, e149.
[70] L. Liu, X. Liu, Q. Xu, P. Wu, X. Zuo, J. Zhang, H. Deng, Z. Wu, A. Ji, *Int. J. Nanomed.* **2014**, *9*, 3509.
[71] A. M. Vaidya, Z. Sun, N. Ayat, A. Schilb, X. Liu, H. Jiang, D. Sun, J. Scheidt, V. Qian, S. He, H. Gilmore, W. P. Schiemann, Z. R. Lu, *Bioconjugate Chem.* **2019**, *30*, 907.
[72] N. Maishi, Y. Sakurai, H. Hatakeyama, Y. Umeyama, T. Nakamura, R. Endo, M. T. Alam, C. Li, D. A. M. Annan, H. Kikuchi, *Cancer Sci.* **2022**, *113*, 1855.
[73] Y. Hattori, S. Shimizu, K.-i. Ozaki, H. Onishi, *Pharm.* **2019**, *11*, 181.
[74] Y. Hattori, K. Tamaki, S. Sakasai, K. I. Ozaki, H. Onishi, *Mol. Med. Rep.* **2020**, *22*, 4183.
[75] S. Chen, Y. Y. C. Tam, P. J. Lin, M. M. Sung, Y. K. Tam, P. R. Cullis, *J. Controlled Release* **2016**, *235*, 236.
[76] F. Song, N. Sakurai, A. Okamoto, H. Koide, N. Oku, T. Dewa, T. Asai, *Biol. and Pharm. Bulletin* **2019**, *42*, 996.
[77] S. G. Huayamares, M. P. Lokugamage, R. Rab, A. J. da Silva Sanchez, H. Kim, A. Radmand, D. Loughrey, L. Lian, Y. Hou, B. R. Achyut, A. Ehrhardt, J. S. Hong, C. D. Sago, K. Paunovska, E. S. Echeverri, D. Vanover, P. J. Santangelo, E. J. Sorscher, J. E. Dahlman, *J. controlled release* **2023**, *357*, 394.
[78] S. N. Bhatia, J. E. Dahlman, *Proc Natl Acad Sci U S A* **2024**, *121*, e2315789121.
[79] J. Witten, Y. Hu, R. Langer, D. G. Anderson, *Proc Natl Acad Sci U S A* **2024**, *121*, e2307798120.
[80] S. Berger, U. Lächelt, E. Wagner, *Proc Natl Acad Sci U S A* **2024**, *121*, e2307799120.
[81] I. Martin, C. Dohmen, C. Mas-Moruno, C. Troiber, P. Kos, D. Schaffert, U. Lächelt, M. Teixidó, M. Günther, H. Kessler, *Org. Biomol. Chem.* **2012**, *10*, 3258.
[82] P. M. Klein, S. Kern, D.-J. Lee, J. Schmaus, M. Höhn, J. Gorges, U. Kazmaier, E. Wagner, *Biomaterials* **2018**, *178*, 630.
[83] T. Benli-Hoppe, Ş. Göl Öztürk, Ö. Öztürk, S. Berger, E. Wagner, M. Yazdi, *Macromol. Rapid Commun.* **2022**, *43*, 2100602.
[84] M. Lyu, M. Yazdi, Y. Lin, M. Höhn, U. Lächelt, E. Wagner, *ACS Biomater. Sci. Eng.* **2022**, 99.

[85] D. Schaffert, N. Badgujar, E. Wagner, *Org. Lett.* **2011**, *13*, 1586.

[86] C. Dohmen, D. Edinger, T. Fröhlich, L. Schreiner, U. Lächelt, C. Troiber, J. Rädler, P. Hadwiger, H.-P. Vornlocher, E. Wagner, *ACS Nano* **2012**, *6*, 5198.

[87] Y. Lin, U. Wilk, J. Pöhmerer, E. Hörterer, M. Höhn, X. Luo, H. Mai, E. Wagner, U. Lächelt, *Small* **2023**, *19*, 2205318.

[88] K. Müller, P. M. Klein, P. Heissig, A. Roidl, E. Wagner, *Nanotechnology* **2016**, *27*, 464001.

Received: 26 May 2023 | Revised: 31 August 2023 | Accepted: 6 September 2023

DOI: 10.1002/jcb.30476

RESEARCH ARTICLE

Journal of Cellular Biochemistry WILEY

Analysis of cortical cell polarity by imaging flow cytometry

Jesper H. Jespersen[1] | **Andras Harazin**[1,2] | **Anja B. Bohn**[3] |
Anni Christensen[1] | **Esben Lorentzen**[1] | **Anna Lorentzen**[1,4]

[1]Department of Molecular Biology and Genetics, Aarhus University, Aarhus, Denmark

[2]Department of Biomedicine, Aarhus University, Aarhus, Denmark

[3]Department of Biomedicine, FACS Core Facility, Aarhus University, Aarhus, Denmark

[4]Department of Biomedicine, Health Bioimaging Core Facility, Aarhus University, Aarhus, Denmark

Correspondence
Esben Lorentzen and Anna Lorentzen, Department of Molecular Biology and Genetics, Aarhus University, Aarhus, Denmark.
Email: el@mbg.au.dk and anna@mbg.au.dk

Funding information
Riisfort Fonden; Novo Nordisk Fonden, Grant/Award Number: NNF20OC0064485

Abstract

Metastasis is the main cause of cancer-related death and therapies specifically targeting metastasis are highly needed. Cortical cell polarity (CCP) is a prometastatic property of circulating tumor cells affecting their ability to exit blood vessels and form new metastases that constitute a promising point of attack to prevent metastasis. However, conventional fluorescence microscopy on single cells and manual quantification of CCP are time-consuming and unsuitable for screening regulators. In this study, we developed an imaging flow cytometry-based method for high-throughput screening of factors affecting CCP in melanoma cells. The artificial intelligence-supported analysis method we developed is highly reproducible, accurate, and orders of magnitude faster than manual quantification. Additionally, this method is flexible and can be adapted to include additional cellular parameters. In a small-scale pilot experiment using polarity-, cytoskeleton-, or membrane-affecting drugs, we demonstrate that our workflow provides a straightforward and efficient approach for screening factors affecting CCP in cells in suspension and provide insights into the specific function of these drugs in this cellular system. The method and workflow presented here will facilitate large-scale studies to reveal novel cell-intrinsic as well as systemic factors controlling CCP during metastasis.

KEYWORDS

artificial intelligence, cortical cell polarity, high-throughput screening, image analysis, imaging flow cytometry, melanoma, metastasis

1 | INTRODUCTION

While metastasis is the major cause of cancer-related deaths, cancer treatments still largely target primary tumors and not metastatic spreading.[1] One reason for this discrepancy is that cancer treatment success has been evaluated based on primary tumor shrinkage and not inhibition of metastasis. The Food and Drug Administration has recently included metastasis-free survival as an endpoint for clinical trials, offering new prospects to advance the development of antimetastatic treatments for cancer patients.[1–3]

Esben Lorentzen and Anna Lorentzen are joint senior authors.

During distant-organ metastasis, cells can pass through a liquid phase in lymph or blood as circulating tumor cells (CTCs).[4,5] To form secondary tumors, CTCs need to survive the harsh conditions in blood circulation and extravasate from the bloodstream through the vessel wall.[4,5] In circulation, CTCs are exposed to potential drugs and can be isolated and monitored in patients by minimally invasive blood sampling (liquid biopsies). Circulation and extravasation, therefore, constitute particularly promising points of attack to interrupt metastasis.

Extravasation is an active process of cell attachment, adhesion, and migration that requires polarization and directionality.[6,7] We have previously described a type of cortical cell polarity (CCP) in CTCs that constitutes a basic polarity module restricted to the plasma membrane (PM) and the submembrane actin cytoskeleton.[8] This pole is characterized by folding of the PM and local accumulation of filamentous actin and the linker protein ezrin. CCP promotes attachment and adhesion of CTCs in vitro and metastatic seeding in animal models. CCP thus constitutes a potential target to reduce metastasis by interfering with the ability of CTCs to extravasate.[5,9]

Methodically, CCP has been assessed by widefield imaging and qualitative inspection or tedious manual quantification of the fraction of polarized cells.[8] As this microscopy-based method is impractical for medium- or large-scale screens for regulators of CCP, we here developed a methodology with comparably sensitive but faster readout combined with robust automated quantification.

Imaging flow cytometry (IFC) combines the spatial resolution of microscopy with the speed and quantitative multiparameter analysis of flow cytometry.[10] On the ImageStreamxMk II (Cytek Biosciences), used in this study, each event is identified based on an image captured by a charge-coupled device camera, on a pixel-by-pixel basis in up to 12 channels. The technique provides fluorescent and morphological parameters of up to 5000 cells/s and is therefore a powerful method for automated, high throughput analysis of cellular and subcellular features of cells in suspension.

We established an IFC-based workflow as a high-throughput method to measure CCP based on ezrin-green fluorescent protein(GFP) localization and present a reproducible artificial Intelligence (AI)-supported image analysis algorithm to quantify the fraction of cortically polarized cells. As proof of principle, we conducted a small-scale pilot screen of compounds with potential effects on CCP. Our results demonstrate robust and reliable measurement of CCP in melanoma cells and show that this workflow can be adapted to include measurements of additional cellular features.

2 | MATERIALS AND METHODS

2.1 | Cell culture

Generation and use of SkMel2 melanoma cells (ATCC: HTB68, RRID:CVCL_0069) stably expressing ezrin-GFP (SkMel2-ezrin-GFP), was described previously.[8] Cells were grown at 37°C under 5% CO_2 in high glucose Dulbecco's modified Eagle's medium with Glutamax (Thermo Fisher Scientific) supplemented with 10% fetal bovine serum (Merck), 100 U/mL penicillin, and 100 µg/mL streptomycin (Thermo Fisher Scientific) and 1 mg/mL active G418 (Merck). For maintenance, cells were detached with 0.5 g/L trypsin and 0.2 g/L ethylenediaminetetraacetic acid (EDTA) (Merck) solution, for experiments, with 0.2 g/L EDTA (Merck). Phosphate-buffered saline (PBS) (Merck) was used for washes. Cell numbers and viability were measured using a NuceloCounter NC-200 (Chemometek).

2.2 | Chemicals and drugs

Chemicals were dissolved in dimethyl sulfoxide (DMSO) (Merck) or 96% ethanol (VWR) according to the manufacturer's recommendations, further diluted in cell culture medium, and used at the following concentrations: Forchlorfenuron (FCF; Merck) at 100 µM, cholesterol sulfate (CS; Merck) at 35 µM, NSC23766 (Tocris Bioscience) at 10 µM, Dasatinib (Merck) at 0.5 µM, and Ml141 (Tocris Bioscience) at 1 µM. Control experiments contained 1:500 DMSO or 1:500 ethanol in a cell culture medium. Sixteen percent formaldehyde solution (Thermo Fisher Scientific) was added to suspension cultures to an end concentration of 4%. 4′,6-diamidino-2-phenylindole (DAPI; Thermo Fisher Scientific) was used at 0.2 µM.

2.3 | Polarity assays

SkMel2-ezrin-GFP cells grown in 10 cm diameter dishes (VWR) to 80%–90% confluency were treated with the indicated agents in the medium for 24 h, washed, detached with EDTA for 15 min at 37°C, resuspended in medium and incubated in suspension for the indicated time (15 min, 1 h, or 3 h) at room temperature for the training data sets or resuspended in a medium containing the indicated reagent for 1 h at room temperature for IFC experiments. After incubation, cells were fixed in 4% formaldehyde for at least 1 h, washed with PBS, resuspended in PBS containing 0.2 µM DAPI and maintained at 4°C until measurement by IFC or mounted in Mowiol (Merck) on a microscopy slide.

2.4 | Fluorescence microscopy

Manual polarity assays were performed on an IX83 widefield microscope (Olympus/Evident) with a halogen lamp using a 10× (Figure 1B) or 20× (Figure 3C) objective and standard fluorescein isothiocyanate filters. Exposure time was set to 200 ms, gain to three in CellSens Standard software (Olympus/Evident; RRID:SCR_014551). Manual quantification was done on three (Figure 3C) or four (Figure 1B) images containing at least 200 cells per replicate. Confocal microscopy was performed on an LSM710 microscope (Zeiss) with multialkali PMTs using a 63×, 1.4 oil immersion objective. DAPI was excited using a 405 Diode laser, GFP using the 488-laser line of an Argon laser. Images were recorded using ZEN black software (Zeiss; RRID:SCR_018163) and processed in Fiji[11] (RRID:SCR_002285).

2.5 | IFC

IFC was performed on an Amnis ImageStream ®XMkII (Cytek Biosciences; RRID:SCR_020142) at 60× magnification at slow speed (for highest quality). DAPI was excited by 405 nm laser (70 mW) and detected in channel 7, GFP was excited by a 488 nm laser at 70–90 mW and detected in channel 2. The 488 nm laser power was adjusted for each experiment to a level at which untreated control samples contained ≈4% oversaturated cells. Brightfield images were collected in channels 1 and 9. For each sample, 40 000 cells were imaged. A compensation matrix was created in AmnisIDEAS software using images of 10 000 untransfected DAPI-stained SkMel2 cells and 10 000 SkMel2-ezrin-GFP cells and applied to all samples. Images were gated in IDEAS (Supporting Information: Figure 1 and Table 1 and Supporting Information: Methods) to exclude out-of-focus cells, doublets, double-nucleated cells, oversaturated cells in the GFP channel, and GFP-negative cells. Apoptotic cells were identified as described by Henery et al.[12] and excluded. Approximately 50% of cells were included for further analysis after gating and loaded in AmnisAI software for training AI models or classification.

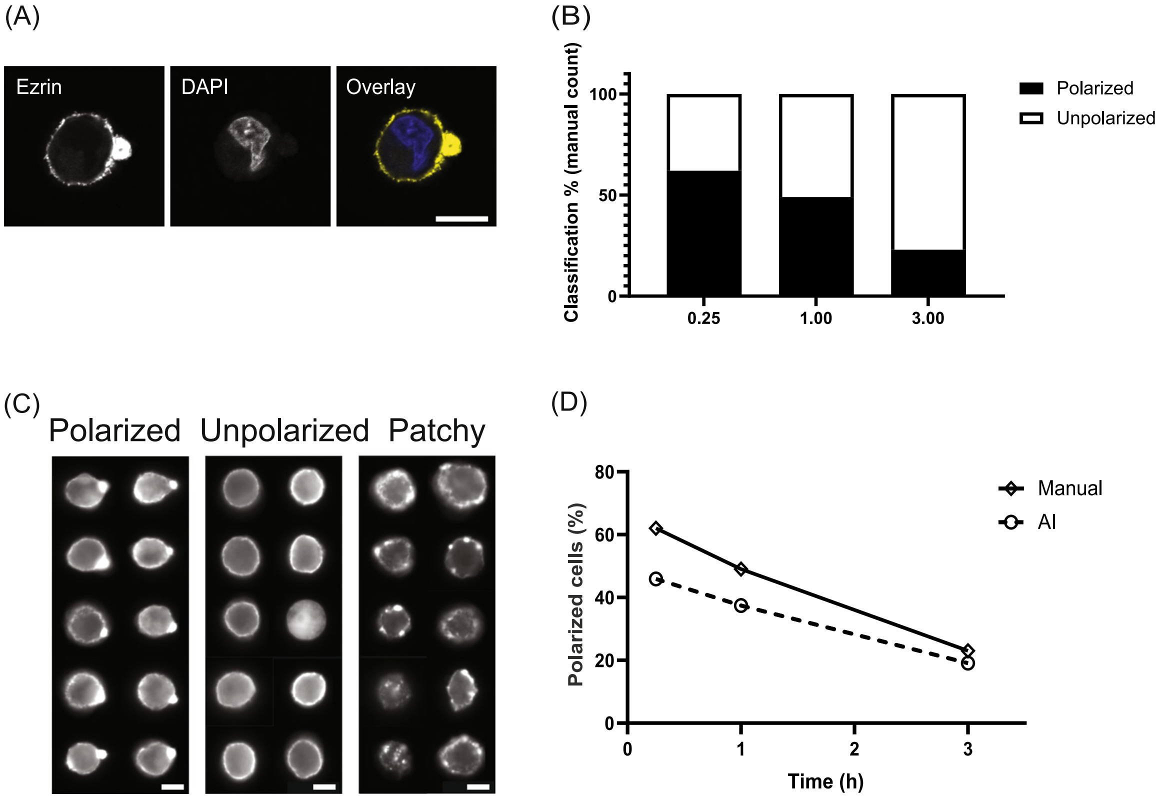

FIGURE 1 Method development. (A) Localization of ezrin-GFP in a SkMel2 cell displaying CCP imaged by confocal microscopy. Scale bar = 10 µm. (B) Quantification of the fraction of SkMel2 cells displaying CCP (black) as measured by polarized ezrin-GFP distribution using widefield microscopy and manual quantification. For the training data set, cells were maintained in suspension for 15 min (0.25), 1 h (1.00), or 3 h (3.00). Single measurements are shown. (C) Images obtained from SkMel2-ezrin-GFP cells by IFC using 60× magnification. Cells are manually classified into polarized (left), unpolarized (center) or patchy (right). (D) Comparison of the manual quantification (solid line, displaying the same data sets as in (B)) and AmnisAI-supported (dashed line) classification of the fractions of polarized cells. AI, artificial intelligence; CCP, cortical cell polarity; DAPI, 4′,6-diamidino-2-phenylindole; GFP, green fluorescent protein; IFC, imaging flow cytometry.

2.6 | AI model training

Initial base truth populations were selected in IDEAS. Only channel 2 GFP images were included for training. AmnisAI was first trained based on the truth populations made in IDEAS and the resulting algorithm used to classify the cells. Cells that were by visual inspection deemed incorrectly classified, were manually moved to the appropriate truth population, and the AI was retrained. This process was repeated until no incorrectly classified cells were detected by eye. Performance of the algorithms was tested by calculating precision, recall, and $F1$ values as

$$\text{Precision} = \frac{\text{True Positives}}{\text{True Positives} + \text{False Positives}},$$

$$\text{Recall} = \frac{\text{True Positives}}{\text{True Positives} + \text{False Negatives}},$$

$$F1 = \frac{(\text{Precision} \times \text{Recall})}{(\text{Precision} + \text{Recall})}.$$

The AmnisAI model files can be downloaded under Supporting information as Pol_vs_Unpol_vs_Patchy_model.aimdl and CP_vs_PM_model.aimdl.

2.7 | Software and statistical analysis

AmnisIDEAS 6.3 (Cytek Biosciences) was used for visualization, compensation, and gating of IFC data. Amnis®AI 2.0.7 (Cytek Biosciences) was used for training and classification of polarized, unpolarized, and patchy cells and for developing the analysis algorithm. CellSens (Olympus/Evident) and ZEN black (Zeiss) were used for acquisition and Fiji[11] for processing of fluorescence microscopy images. GraphPad Prism 9.5.0 (Dotmatics; RRID:SCR_002798) was used for visualization and statistical analyses of data. p values are based on two-tailed nonpaired t tests with assumed Gaussian distribution.

3 | RESULTS

3.1 | Establishment of an IFC-based method for measuring CCP

CCP is defined as a type of polarity adopted by cells in the liquid phase without directional stimulus and is detected by the formation of an ezrin-enriched pole.[8] We thus used ezrin-GFP localization as a marker of CCP in SkMel2 human melanoma cells in suspension (Figure 1A). To establish a new IFC-based method, a template data set was generated using a published microscopy-based method.[8] Using the observation that CCP decreases over time, polarity assays were performed with SkMel2-ezrin-GFP cells maintained in suspension for 15 min, 1 h, or 3 h after detachment. The fractions of polarized cells, as manually quantified using the microscopy-based method were 62%, 49%, and 23%, respectively (Figure 1B). It is important to note that these values do not constitute absolute values of the fractions of polarized cells, since the analyzed images were recorded in single focal planes. Out-of-focus poles were not taken into account and thus fractions of polarized cells were underscored in relation to the true numbers of polarized cells. Since IFC also records one image plane per cell, we aimed for similar values in quantification. The same cell batches used for the microscopy-based measurement were subjected to IFC, recording at least 40 000 cells for each condition. IFC provided high-quality images with clearly discernible polarized or unpolarized ezrin-GFP localization (Figure 1C). Preprocessing steps, including compensation and gating, were performed to remove out-of-focus images, cell duplets, apoptotic cells, non-GFP expressing cells, and overexposed cells from analyses (Supporting Information: Figure 1).

Attempts to classify polarized and unpolarized cells by manual adjustment of parameters and a machine learning function available in IDEAS were not successful, as they were not reflecting the results obtained by the manual quantification method, which is the standard that initially defined CCP (Supporting Information: Methods and Figure S2). We therefore employed AmnisAI software that allowed for manual corrections and training of the AI model to optimize classification. Generation of truth populations and AI training were performed on pooled data from the three time points shown in Figure 1B. Three truth populations (Figure 1C) were generated by manually classifying polarized (1912 cells with one or two poles), unpolarized (1817 cells with unpolarized ezrin at the PM and unpolarized ezrin in the cytoplasm), and a third class termed “patchy” (445 cells containing several small ezrin spots of different intensity distributed throughout the PM). The three final classes were established from the initial truth populations supported by several training rounds with manual corrections until no wrongly classified cells were observed. When this AI-supported classification was applied to our test data set (15 min, 1 h, and 3 h), the resulting fraction of polarized cells reflected the manual quantification of the microscopy-based method resulting in 45.9%, 37.4%, and 19.1% polarized cells as compared to the respective 62%, 49%, and 23% polarized cells quantified by initial manual count (Figure 1D). Precision values of 97.5%, 94.9%, and 83.3% and recall values of 92.1%, 97.7%, and 93.3% were calculated for polarized, unpolarized, and patchy classification, respectively, confirming that the

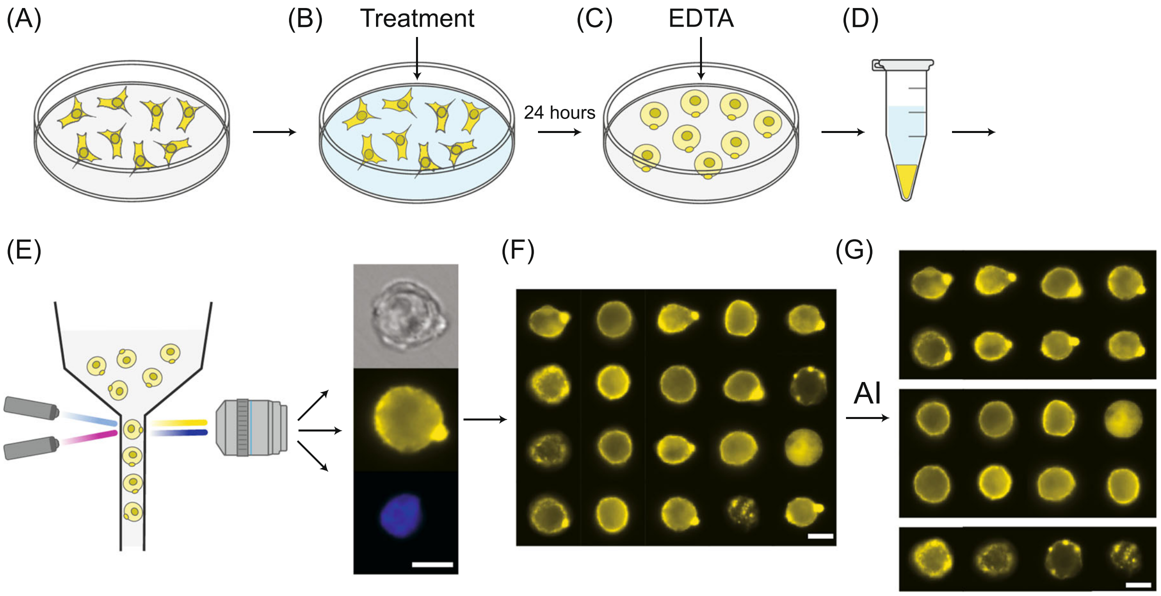

FIGURE 2 Workflow. Illustration of the IFC- and AI-based method to determine the fraction of cortically polarized cells. (A–D) Polarity assays and (E–G) IFC and image analysis (cell images from Figure 1C). SkMel2-ezrin-GFP cells are grown in adhesion cultures (A), treated with potential polarity-modulating agents (B), detached (C), and incubated and fixed in suspension (D). Images of 40 000 cells are recorded by IFC (E, F), gated in IDEAS, and classified into polarized, unpolarized, and patchy subpopulations (G) by AmnisAI. AI, artificial intelligence; EDTA, ethylenediaminetetraacetic; GFP, green fluorescent protein; IFC, imaging flow cytometry.

AI-generated algorithm can classify our data with high confidence (Supporting Information: Figure S3). In summary, a workflow has been established that allows for straightforward measurement and analysis of CCP (Figure 2).

3.2 | Experimental evaluation of the quantification algorithm

To evaluate if the quantification algorithm can be applied to biological studies of polarity regulators, we performed a small-scale pilot experiment using a collection of agents that potentially affect polarity, the PM, or the submembrane cytoskeleton (Figure 3A). For our experiments, we selected two Rho-family GTPase regulators, the Rac1 inhibitor NSC23766 (NSC)[13] and the Cdc42 inhibitor ML141,[14] the septin inhibitor FCF (1-(2-chloro-4-pyridyl)-3-phenylurea),[15] the membrane component and signaling regulator CS, and the multitarget tyrosine kinase inhibitor dasatinib.[16] To this end, SkMel2-ezrin-GFP cells were pretreated with NSC, ML141, FCF, CS, dasatinib, or the respective solvent controls for 24 h, subjected to polarity assays, imaged by IFC, and classified using our AmnisAI algorithm (Figure 2). In addition to polarization measurements, analysis of the DAPI channel in IFC allowed for the identification of apoptotic cells.[12] At the concentrations used in our experiments, none of the drugs or controls enhanced the fraction of apoptotic cells above the cutoff set at 1.0% (Supporting Information: Figure S4). We did not observe a decisive effect of NSC or ML141 on the fraction of polarized cells (Figure 3B). Both FCF and CS strongly decreased the fraction of polarized cells from 45.6 ± 3.2% in the untreated control to an average of 15.5 ± 0.8% and 13.5 ± 1.5%, respectively. Dasatinib decreased the fraction of polarized cells to an average of 33.2 ± 4.4%. In summary, this pilot screen shows that the IFC-based measurement and our AmnisAI-supported classification model are well suited to measure differences in the fractions of cortically polarized cells under different treatment conditions. To compare the IFC-based method to the microscopy-based method under treatment conditions and to assess the sensitivity of the two methods, three random samples used for the IFC experiments were additionally imaged by microscopy and counted manually (Figure 3C). A comparison of the two methods showed little difference in the fractions of polarized cells (Figure 3C), demonstrating that the IFC-based method and automated quantification is comparable in capturing changes in CCP to the microscopy-based method with manual quantification.

In addition to classifying polarized and unpolarized cells, the automated quantification includes a patchy class, which is not accounted for in the manual count. The fraction of patchy cells remained relatively low at

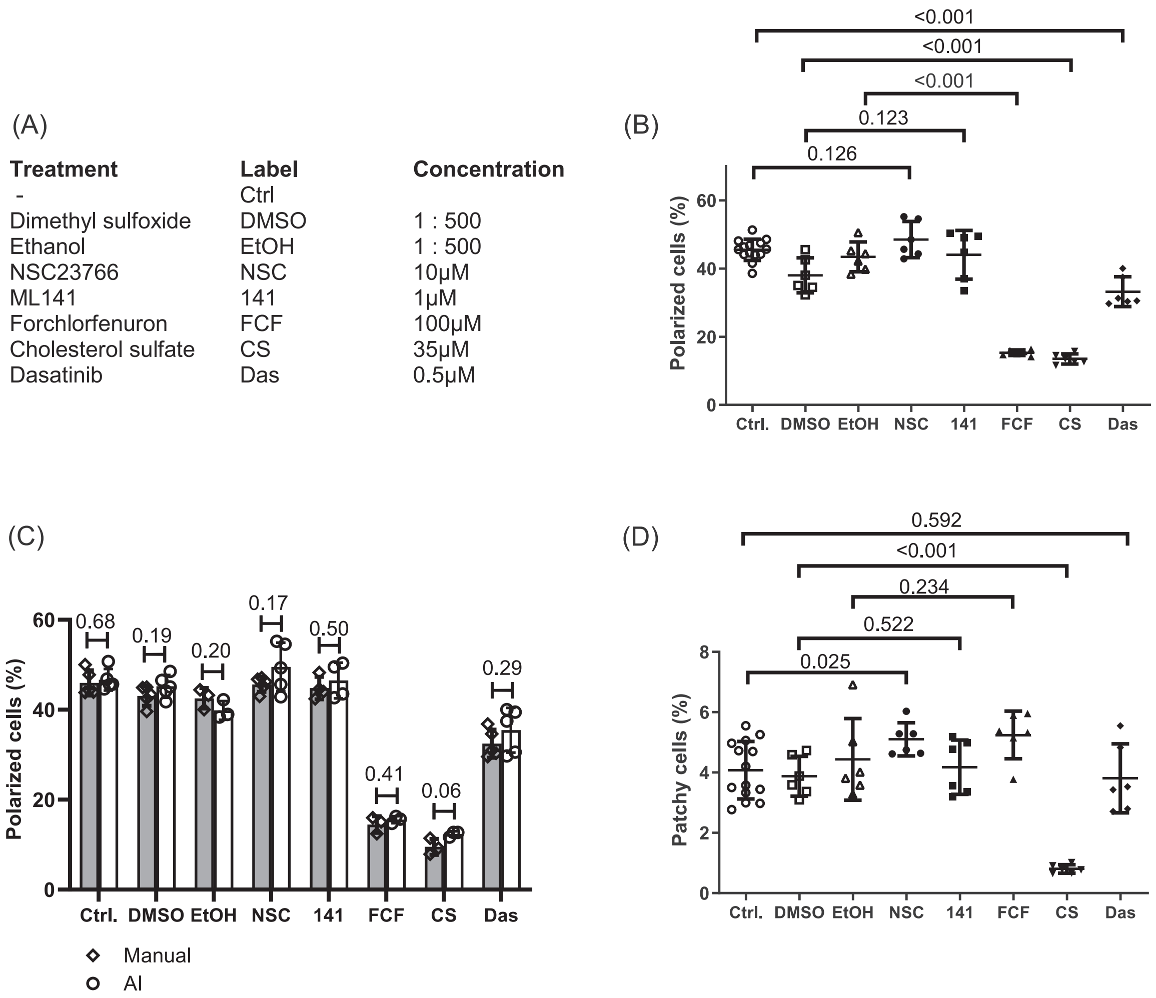

Treatment	Label	Concentration
-	Ctrl	
Dimethyl sulfoxide	DMSO	1 : 500
Ethanol	EtOH	1 : 500
NSC23766	NSC	10μM
ML141	141	1μM
Forchlorfenuron	FCF	100μM
Cholesterol sulfate	CS	35μM
Dasatinib	Das	0.5μM

FIGURE 3 Proof-of-concept experiments. Using the workflow in Figure 2, SkMel2-ezrin-GFP cells were subjected to the indicated treatments, and the effect on CCP was determined by IFC. (A) Treatments and concentrations used for this screen. (B) Fraction of cortically polarized cells as assessed by IFC method after indicated treatments. Individual measurements with mean ± SD, $n = 6$, p values from unpaired t tests. (C) Three randomly selected experiments from data shown in (B) were quantified by widefield microscopy and manual count (gray bars) and compared to AmnisAI classification (white bars). Individual measurements and bar diagrams ± SD, $n = 3$, p values from unpaired t tests. (D) Quantification of the fraction of SkMel2 cells displaying patchy ezrin-GFP distribution classified by AmnisAI in the experiments shown in (B). Individual measurements with mean ± SD, $n = 6$, p values from unpaired t tests. AI, artificial intelligence; CCP, cortical cell polarity; Ctrl, control; GFP, green fluorescent protein; IFC, imaging flow cytometry.

4.1 ± 1.0% in the untreated control and was slightly increased to 5.1 ± 0.5 upon NSC treatment (Figure 3D). In CS-treated cells, the fraction of patchy cells was reproducibly strongly reduced to 0.8 ± 0.1%, indicating that patchy cells constitute not only a fraction of nonclassifiable cells but a biological cellular phenotype.

3.3 | Introduction of PM-localized and cytoplasmic ezrin classes

Ezrin activity is regulated by phosphorylation and membrane binding[17] and active ezrin is both phosphorylated and membrane-bound. We set out to test whether it is possible to quantify the amount of membrane-bound ezrin and get a measure of ezrin activity in the images previously used to measure CCP. To this end, two new classes, PM-localized and cytoplasmic, were introduced and analyzed from our previously generated data. The new classes were generated from two new truth populations made from the previously used 15 min, 1 h, and 3 h merged data, membrane-localized (1576 cells with ezrin localized at the PM) and cytoplasmic (1994 cells with cytoplasmic ezrin) (Figure 4A). Both truth populations included polarized as well as unpolarized cells. A new AI model based on these truth populations was trained to sufficient confidence in classification (Supporting

BACK TO CONTENTS

Information: Figure S5) and applied to our full data sets (Figure 4B). FCF treatment increased the fraction of cells with membrane-bound ezrin, suggesting that FCF treatment enhances the activity of ezrin while dasatinib treatment reduced the fraction of cells with membrane-bound ezrin indicating that dasatinib reduces the activity of ezrin. Since the pole is by definition localized at the PM, we tested if polarization affects the classification of PM-localized and cytoplasmic ezrin. To this end, polarized and unpolarized classes were analyzed separately for cytoplasmic or PM-localized ezrin (Figure 4C,D). As expected, PM-localized ezrin was in general higher but differences were less pronounced in the polarized fraction. While the effect of FCF treatment enhancing membrane-bound ezrin was confirmed in both analyses, the reducing effect observed for dasatinib was not confirmed. As the pole was initially defined by localization at the cortex/PM, the biological conclusions that can be drawn from these findings are limited and this analysis should be considered a proof-of-principle experiment to test the flexibility of the method. However, our analyses indicate that inhibition of septins by FCF enhances membrane association of ezrin, reflecting its activation state. This second level of analysis demonstrates how simply new classifications and subclassifications can be added and implemented in the workflow.

Altogether, our results show that IFC-based measurement with automated analysis is comparably sensitive to microscopy-based measurement with manual counting in determining fractions of cortically polarized cells. In addition to being considerably faster and -once established- unaffected by human bias, the IFC-based analysis allows for the straightforward introduction of

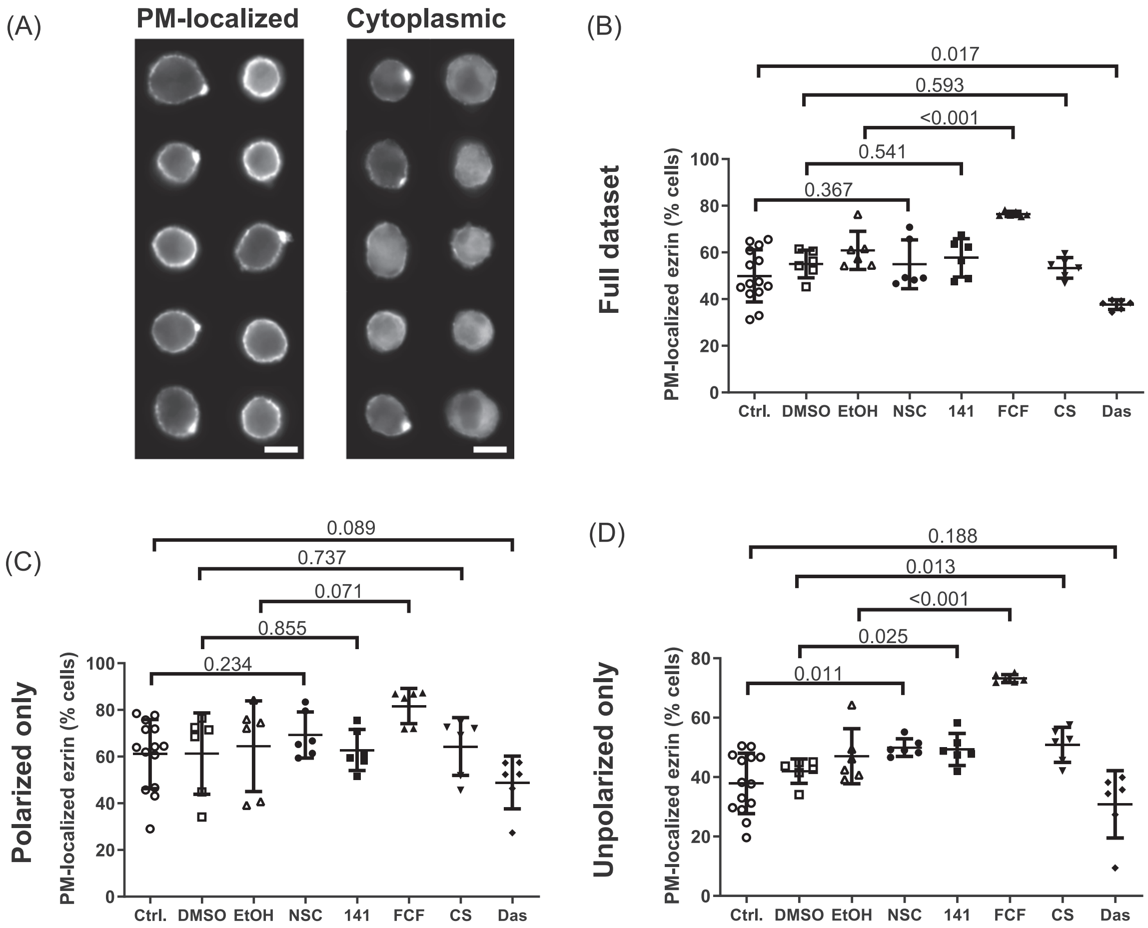

FIGURE 4 Subclassification of PM-localization. The data displayed in Figure 3 were further analyzed for PM or cytoplasmic localization of ezrin-GFP. (A) Images obtained from SkMel2-ezrin-GFP cells by IFC using 60× magnification. After gating (Supporting Information: Figure 1), cells were handpicked in IDEAS as PM-localized (left) or cytoplasmic (right). (B–D) Fractions of cells classified as displaying PM-localized ezrin-GFP. Individual measurements with mean ± SD, $n = 6$, p values from unpaired t tests. Subclassifications were performed on the full data set including polarized, unpolarized, and patchy cells (B), cells previously classified as polarized (C), and on cells previously classified as unpolarized (D). CS, cholesterol sulfate; Ctrl, control; Das, dasatinib; DMSO, dimethyl sulfoxide; EtOH, ethanol; FCF, forchlorfenuron; GFP, green fluorescent protein; IFC, imaging flow cytometry; PM, plasma membrane.

additional measurements (apoptosis) or classes (patchy, cytoplasmic vs. PM).

4 | DISCUSSION

We have established a straightforward workflow to quantify CCP. We demonstrated that this method is equally sensitive as a previously used microscopy-based method when used for biological screens of polarity regulators in tumor cells while being unbiased and automated. Importantly, this method is several orders of magnitude faster, which makes it applicable for medium- to large-scale screens allowing for an unbiased search for novel CCP regulators instead of limited directed approaches testing low numbers of suspected targets.

While imaging and analysis in this workflow are reproducible and fast, the limitations of this method are that it uses two-dimensional (2D) images and defines polarization as "focal ezrin accumulation at the cellular cortex" as observed by the eye. "Fraction of polarized cells" in this context should therefore not be considered an absolute value of polarization but as a means of comparing one visibly discernible aspect of polarity between populations of cells. Once the AI has been trained on this visibly discernible aspect, the method is highly reproducible. More in-depth characterization of the extent of polarization per cell would require fast 3D imaging such as high-speed 3D light sheet microscopy to reach statistically valuable output and automated analysis of parameters such as area of accumulated ezrin per total cell surface, or other measures of individual cell polarization. While the method presented here does not assess the absolute fraction of polarized cells or the extent of polarization per cell, it is well-suited for comparative studies assessing changes in the fraction of polarized cells upon treatment.

In this work, IFC and AI-supported image analyses were used to measure how drug treatments affect the percentage of cortically polarized cells. In addition, using a previously published method,[12] the percentage of apoptotic cells was determined in each experiment without requiring additional measurements. In the course of optimizing the classification, an additional phenotype termed "patchy" was discovered. A similar distribution of multiple F-actin polymerization spots was described at the cortex of T cells during immune synapse formation upon microtubule depolymerization.[18] The patchy fraction was affected by treatments with CS and NSC, indicating that it constitutes a *bona fide* biological phenotype to be further investigated. We demonstrated that additional parameters (such as PM or cytoplasmic localization) can be straightforwardly implemented by AI training and analyzed in the whole population or in previously generated subpopulations, to extract additional information from a single data set.

For method evaluation, a small-scale pilot screen with regulators of actin or septin cytoskeleton, PM, or cell signaling, was performed. Rho family GTPase regulators NSC[13] and ML141[14] had no decisive effect on CCP, which allows for different interpretations. First, Rac1/Cdc42 may not regulate CCP, which agrees with findings that a RhoA-specific guanine nucleotide exchange factor (GEF) GEF-H1 regulates CCP in early lymphocyte polarization during immune synapse formation.[18] Second, Rac/Cdc42 may need to act locally at the pole or outside the pole and global inhibition therefore shows no effect. This is supported by the finding that the patchy fraction of cells increased upon NSC treatment, showing that global Rac1 inhibition affects overall but not local cortical distribution of ezrin and possibly actin. Third, NSC only inhibits the interaction of Rac1 with the GEFs Trio and Tiam1,[13] and other Rac GEFs and GTPase activating proteins (GAPs) might be involved in CCP. The specific function of actin regulators in CCP needs to be tested using systems-directed approaches taking the entire GEF/GAP/guanosine diphosphate dissociation inhibitors regulatory network as well as subcellular local activities of Rho GTPases into account. The method presented here can facilitate the screening of drug libraries targeting actin-regulating networks.

A strong reduction of polarized cells was observed upon FCF treatment, indicating a contribution of septins to CCP regulation. Septins are organizers of the cell cortex and regulators of the actin cytoskeleton and are directly associated with PM structures.[19] A recent study revealed that membrane curvature at sites of PM blebbing induces cortical nucleation of septin and suggested that repeated blebbing may lead to stabilization and formation of higher-order structures.[20] According to this model, membrane blebbing and nucleation of septins could actively initiate or stabilize cortical polarization. Interestingly, septins are also involved in the loss of polarity in aging hematopoietic stem cells,[21] indicating similarities between these two types of polarization.

Treatment with the cholesterol analog CS reduced CCP, indicating regulation by either cholesterol-regulated signaling and/or the membrane lipid composition. Cholesterol affects mechanical cell properties via the actin cytoskeleton[22] and acts as a naturally occurring membrane component but is also an inhibitor of the Rac-GEF DOCK2.[23] In addition, CS could affect polarization driven by PM lipid content or distribution, a hypothesis supported by the observation that the integrity of cholesterol-dependent PM microdomains is essential for the organization of molecular cell polarity in hematopoietic stem cells.[24]

Dasatinib treatment reduced the fraction of polarized cells, implicating tyrosine kinase signaling pathways in the regulation of CCP. Dasatinib is an anti-leukemia drug that was developed as a dual Src-Abl1 kinase inhibitor but targets a wide range of tyrosine kinases.[16] The specific tyrosine kinase pathway responsible for the observed effect can therefore not be distinguished. However, inhibition of cortical polarization by dasatinib may contribute to its antitumor effects.

In summary, we developed a simple protocol for IFC-based measurement and AI-based quantification of CCP directly applicable to screening for polarity regulators in tumor cell lines. Here, we only used two fluorescence channels (ezrin-GFP and DAPI) to extract multiple layers of data using advanced image analysis. The strength of IFC, however, lies in the possible acquisition of multiple fluorescence channels simultaneously, with each additional channel adding potential for multiple layers of image analysis. Our protocols constitute a basis to build on for further analyses.

The workflow presented here can be directly used to screen for regulators of CCP in cells in suspension. In addition to assessing CCP in cancer cell lines, this method can be adapted to measure CCP and other biologically relevant phenotypes of CTCs or immune cells, for monitoring in patients as well as basic scientific research. The AI-supported analysis allows for fast and easy adaptation and limitless possibilities to combine polarity measurements with additional phenotypes. Altogether, this method opens the possibility of screening large libraries of molecules with unknown functions to identify new regulators and reveal possible pharmacologic inhibitors of CCP, and help design potential antimetastatic treatments.

ACKNOWLEDGMENTS

The authors would like to thank the FACS core facility (RRID:SCR_022323) and the Bioimaging Core facility (RRID:SCR_023876) at the Biomedicine Department at Aarhus University for providing access to instrumentation, training, and support. This work was funded partially by grants from the Novo Nordisk Foundation (Grant Number NNF20OC0064485) and Riisfort Fonden (Esben Lorentzen) as well as Harboefonden, Brødrene Hartmanns Fond, Læge Sofus Carl Emil Friis og hustru Olga Doris Friis' Legat, and Tømrermester Jørgen Holm og Hustru Elisa f. Hansens Mindelegat (Anna Lorentzen).

CONFLICT OF INTEREST STATEMENT

The authors declare no conflict of interest.

DATA AVAILABILITY STATEMENT

The data that support the findings of this study are available from the corresponding author upon reasonable request. Original data are available from the corresponding author (anna@mbg.au.dk) upon request.

ORCID

Anna Lorentzen https://orcid.org/0000-0002-4405-935X

REFERENCES

1. Ganesh K, Massagué J. Targeting metastatic cancer. *Nature Med*. 2021;27(1):34-44. doi:10.1038/s41591-020-01195-4
2. Alečković M, McAllister SS, Polyak K. Metastasis as a systemic disease: molecular insights and clinical implications. *Biochimica et Biophysica Acta Rev Cancer*. 2019;1872(1):89-102. doi:10.1016/j.bbcan.2019.06.002
3. Fernandes M, Rosel D, Brábek J. Solid cancer: the new tumour spread endpoint opens novel opportunities. *Br J Cancer*. 2019;121(7):513-514. doi:10.1038/s41416-019-0536-0
4. Massagué J, Obenauf AC. Metastatic colonization by circulating tumour cells. *Nature*. 2016;529(7586):298-306. doi:10.1038/nature17038
5. Ring A, Nguyen-Sträuli BD, Wicki A, Aceto N. Biology, vulnerabilities and clinical applications of circulating tumour cells. *Nat Rev Cancer*. 2023;23(2):95-111. doi:10.1038/s41568-022-00536-4
6. Estecha A, Sánchez-Martín L, Puig-Kröger A, et al. Moesin orchestrates cortical polarity of melanoma tumour cells to initiate 3D invasion. *J Cell Sci*. 2009;122(pt 19):3492-3501. doi:10.1242/jcs.053157
7. Strilic B, Offermanns S. Intravascular survival and extravasation of tumor cells. *Cancer Cell*. 2017;32(3):282-293. doi:10.1016/j.ccell.2017.07.001
8. Lorentzen A, Becker PF, Kosla J, et al. Single cell polarity in liquid phase facilitates tumour metastasis. *Nat Commun*. 2018;9(1):887. doi:10.1038/s41467-018-03139-6
9. Heikenwalder M, Lorentzen A. The role of polarisation of circulating tumour cells in cancer metastasis. *Cell Mol Life Sci*. 2019;76(19):3765-3781. doi:10.1007/s00018-019-03169-3
10. Rees P, Summers HD, Filby A, Carpenter AE, Doan M. Imaging flow cytometry. *Nat Rev Methods Primers*. 2022;2:86. doi:10.1038/s43586-022-00167-x
11. Schindelin J, Arganda-Carreras I, Frise E, et al. Fiji: an open-source platform for biological-image analysis. *Nature Methods*. 2012;9(7):676-682. doi:10.1038/nmeth.2019
12. Henery S, George T, Hall B, Basiji D, Ortyn W, Morrissey P. Quantitative image based apoptotic index measurement using multispectral imaging flow cytometry: A comparison with standard photometric methods. *Apoptosis*. 2008;13(8):1054-1063. doi:10.1007/s10495-008-0227-4
13. Gao Y, Dickerson JB, Guo F, Zheng J, Zheng Y. Rational design and characterization of a Rac GTPase-specific small molecule inhibitor. *Proc Natl Acad Sci USA*. 2004;101(20):7618-7623. doi:10.1073/pnas.0307512101
14. Hong L, Kenney SR, Phillips GK, et al. Characterization of a Cdc42 protein inhibitor and its use as a molecular probe. *J Biol Chem*. 2013;288(12):8531-8543. doi:10.1074/jbc.M112.435941
15. Hu Q, Nelson WJ, Spiliotis ET. Forchlorfenuron alters mammalian septin assembly, organization, and dynamics. *J Biol Chem*. 2008;283(43):29563-29571. doi:10.1074/jbc.M804962200

16. Lindauer M, Hochhaus A. Dasatinib. *Recent Results Cancer Res*. 2018;212:29-68. doi:10.1007/978-3-319-91439-8_2
17. Pelaseyed T, Viswanatha R, Sauvanet C, Filter JJ, Goldberg ML, Bretscher A. Ezrin activation by LOK phosphorylation involves a PIP2-dependent wedge mechanism. *eLife*. 2017;6:e22759. doi:10.7554/eLife.22759
18. Pineau J, Pinon L, Mesdjian O, Fattaccioli J, Lennon Duménil A-M, Pierobon P. Microtubules restrict F-actin polymerization to the immune synapse via GEF-H1 to maintain polarity in lymphocytes. *eLife*. 2022;11:e78330. doi:10.7554/eLife.78330
19. Bridges AA, Gladfelter AS. Septin form and function at the cell cortex. *J Biol Chem*. 2015;290(28):17173-17180. doi:10.1074/jbc.R114.634444
20. Weems AD, Welf ES, Driscoll MK, et al. Blebs promote cell survival by assembling oncogenic signalling hubs. *Nature*. 2023;615:517-525. doi:10.1038/s41586-023-05758-6
21. Kandi R, Senger K, Grigoryan A, et al. Cdc42-Borg4-Septin7 axis regulates HSC polarity and function. *EMBO Rep*. 2021;22(12):e52931. doi:10.15252/embr.202152931
22. Sun M, Northup N, Marga F, et al. The effect of cellular cholesterol on membrane-cytoskeleton adhesion. *J Cell Sci*. 2007;120(13):2223-2231. doi:10.1242/jcs.001370
23. Sakurai T, Uruno T, Sugiura Y, et al. Cholesterol sulfate is a DOCK2 inhibitor that mediates tissue-specific immune evasion in the eye. *Sci Signal*. 2018;11(541):eaao4874. doi:10.1126/scisignal.aao4874
24. Görgens A, Beckmann J, Ludwig A-K, et al. Lipid raft redistribution and morphological cell polarization are separable processes providing a basis for hematopoietic stem and progenitor cell migration. *Int J Biochem Cell Biol*. 2012;44(7):1121-1132. doi:10.1016/j.biocel.2012.03.020

SUPPORTING INFORMATION

Additional supporting information can be found online in the Supporting Information section at the end of this article.

Received: 19 June 2020 | Revised: 19 October 2020 | Accepted: 19 November 2020

DOI: 10.1002/cyto.b.21975

ORIGINAL ARTICLE

CLINICAL CYTOMETRY WILEY

Exploring dyserythropoiesis in patients with myelodysplastic syndrome by imaging flow cytometry and machine-learning assisted morphometrics

Carina A. Rosenberg[1] | Marie Bill[1] | Matthew A. Rodrigues[2] | Mathias Hauerslev[1] | Gitte B. Kerndrup[3] | Peter Hokland[4] | Maja Ludvigsen[1,4]

[1]Department of Hematology, Aarhus University Hospital, Aarhus, Denmark

[2]Amnis Flow Cytometry, Luminex Corporation, Seattle, Washington

[3]Department of Pathology, Aarhus University Hospital, Aarhus, Denmark

[4]Department of Clinical Medicine, Aarhus University, Aarhus, Denmark

Correspondence

Carina A. Rosenberg, Department of Hematology, Aarhus University Hospital, Palle Juul-Jensens Boulevard 99, Plan 1, C115, DK-8200 Aarhus C, Denmark.

Email: carose@rm.dk

Funding information

Danish Cancer Society, Max Wørzner and wife Inger Wørzner's Foundation

Abstract

Background: The hallmark of myelodysplastic syndrome (MDS) remains dysplasia in the bone marrow (BM). However, diagnosing MDS may be challenging and subject to inter-observer variability. Thus, there is an unmet need for novel objective, standardized and reproducible methods for evaluating dysplasia. Imaging flow cytometry (IFC) offers combined analyses of phenotypic and image-based morphometric parameters, for example, cell size and nuclearity. Hence, we hypothesized IFC to be a useful tool in MDS diagnostics.

Methods: Using a different-from-normal approach, we investigated dyserythropoiesis by quantifying morphometric features in a median of 5953 erythroblasts (range: 489–68,503) from 14 MDS patients, 11 healthy donors, 6 non-MDS controls with increased erythropoiesis, and 6 patients with cytopenia.

Results: First, we morphometrically confirmed normal erythroid maturation, as immunophenotypically defined erythroid precursors could be sequenced by significantly decreasing cell-, nuclear- and cytoplasm area. In MDS samples, we demonstrated cell size enlargement and increased fractions of macronormoblasts in late-stage erythroblasts (both $p < .0001$). Interestingly, cytopenic controls with high-risk mutational patterns displayed highly aberrant cell size morphometrics. Furthermore, assisted by machine learning algorithms, we reliably identified and enumerated true binucleated erythroblasts at a significantly higher frequency in two out of three erythroblast maturation stages in MDS patients compared to normal BM (both $p = .0001$).

Conclusion: We demonstrate proof-of-concept results of the applicability of automated IFC-based techniques to study and quantify morphometric changes in dyserythropoietic BM cells. We propose that IFC holds great promise as a powerful and objective tool in the complex setting of MDS diagnostics with the potential for minimizing inter-observer variability.

KEYWORDS

dyserythropoiesis, high-throughput morphometric quantification, imaging flow cytometry, myelodysplastic syndrome

1 | INTRODUCTION

Myelodysplastic syndrome (MDS) is a heterogeneous group of clonal diseases marked by dysplasia in one or more of the myeloid cell lineages in the bone marrow (BM) resulting in ineffective hematopoiesis and varying degrees of cytopenias (Arber et al., 2016; Garcia-Manero et al., 2020; Swerdlow et al., 2017). In the diagnostic setting, cytologic/histologic evaluation of BM is a key component in the assessment of dysplasia. However, diagnosing cases with mild cytopenia and sparse dysplastic changes may be challenging and subject to inter-observer variabilities even when specimens are reviewed by experienced hematopathologists (Arber et al., 2016; Goasguen et al., 2018; Malcovati et al., 2013). In general, the BM is considered dysplastic if two or more dysplastic features are found in more than 10% of a given cell lineage (Swerdlow et al., 2017). However, in a substantial number of patients the degree of dysplastic abnormalities may be inconclusive for a definitive MDS diagnosis despite persistent cytopenia(s). At present, these patients are categorized as having idiopathic cytopenia of undetermined significance (ICUS) (Valent et al., 2012) or—when evidence of clonality is present—clonal cytopenia of undetermined significance (CCUS) (Kwok et al., 2015). Adding to the diagnostic complexity, MDS must always be distinguished from non-clonal reactive causes of cytopenia and dysplasia (Steensma, 2012). As such, novel methods for objective, standardized and reproducible evaluation of dysplasia are highly sought after.

In this regard, multiparameter flow cytometry (MFC) may offer a supplement in the diagnostic work-up of MDS (Kern et al., 2010; M. G. D. Porta et al., 2006; Stetler-Stevenson et al., 2001; Matarraz et al., 2010; Cremers et al., 2017; Westers et al., 2017; Malcovati et al., 2013), and flow cytometric scoring systems have demonstrated diagnostic potential (Malcovati et al., 2013; Ogata et al., 2009; Wells et al., 2003; Kern et al., 2010; M. G. D. Porta et al., 2012; Cremers et al., 2017). In MFC dysplastic changes manifests as phenotypic abnormalities (Duetz et al., 2019; Mathis et al., 2013; Porwit, 2011). However, even though MFC-based evaluation of the erythroid cell lineage is gaining attention in MDS (Cremers et al., 2017; Mathis et al., 2013; Raimbault et al., 2019; Westers et al., 2017), it is important to emphasize that while aberrant antigenic expression is well established in the granulocytic and monocytic cell lineages, the erythroid and megakaryocytic cell lineages are less well characterized by MFC, in part due to a relative lack of relevant surface markers (Duetz et al., 2019). Furthermore, MFC data lack visual morphological information, and at present, aberrant immunophenotypic features per se are not diagnostic of MDS (Arber et al., 2016; Swerdlow et al., 2017). The ImageStream$^{®X}$ MKII (ISX) is a novel imaging flow cytometry (IFC) platform that integrates the high-throughput capacity of conventional MFC with visual information obtainable by microscopy. The detection system simultaneously generates up to 12 digital images (2 bright field (BF), 10 fluorescent) for every individual cell that passes through the system, and the collected image data may be analyzed using algorithms for morphometric quantification of cellular structures. Thus, the IFC technology permits acquisition of thousands of cells from BM aspirates, flow cytometric gating of immunophenotypically defined subpopulations, and subsequent quantification of image-based parameters including the size and shape of every single cell and cellular compartments such as the nucleus. Hence, user subjectivity and inter-observer variability may be minimized by automation and standardization of IFC data analysis.

Based on the above, we hypothesized that IFC could act as a supplement to visual morphological evaluation of dysplasia in MDS. At the time of diagnosis as many as 90% of all MDS-patients present with anemia as a result of ineffective erythropoiesis (Duetz et al., 2019; Nguyen & Hasserjian, 2017; Santini, 2015). In a cohort of 314 MDS patients, dyserythropoiesis was detected in 99% of the investigated MDS samples and this finding was closely related to the presence of anemia (M. G. D. Porta et al., 2015), underscoring the need for a clinically relevant and robust methodology to detect and quantify morphological abnormalities associated with erythroid dysplasia in an objective manner. Of note, McGrath et al. previously demonstrated that IFC is well-suited for identification and quantification of murine erythroid maturation stages through simultaneous investigation of cell surface markers, DNA/RNA content, and morphometric features (McGrath, Bushnell, & Palis, 2008a; McGrath, Kingsley, et al., 2008b). Additionally, morphometric characterization of abnormal mature red blood cells by IFC has proven useful in the context of red cell membrane disorders, such as sickle cell disease and hereditary spherocytosis (More et al., 2020; Van Beers et al., 2014). Recently, it has also been demonstrated that deleterious changes in red blood cells resulting from storage can be identified using conventional and deep learning IFC image analysis approaches (Doan et al., 2020; Pinto et al., 2019).

In the present study, given the high frequency of dyserythropoiesis in MDS together with evidence of the usefulness of IFC in the study of erythroid cells, we applied the IFC technology to identify and quantify dysmorphometric changes in the erythroid cell lineage in MDS BM samples with known dyserythropoiesis. Applying a different-from-normal approach, in this paper, we demonstrate proof-of-concept results of automated quantification of morphometric aberrancies in MDS by IFC. Moreover, by employing machine learning algorithms, we show that subtle morphological variations can be identified in a more robust manner than with standard IFC algorithms. Collectively, our work establishes IFC as a promising novel technique with exciting future applications in the challenging setting of MDS diagnostics.

2 | METHODS

2.1 | Bone marrow samples

Cryopreserved BM mononuclear cells (MNCs) from 14 MDS patients were included in the study (Table 1). As controls, cryopreserved BM MNCs from 11 healthy volunteers (normal BM (NBM)), 6 non-MDS patients with increased erythropoiesis on a non-malignant background (1 patient with B-12 deficiency, 2 patients with hemolytic anemia, 1 patient affected by bleeding, 1 patient with myeloproliferative

TABLE 1 Patient characteristics

					Morphology				
Patient ID	Age	Gender	WHO subtype	Karyotype[a]	Nuclear bridging	Nuclear fragments	Nuclear irregularity	Bi- and/or multinucleation	Megaloblastic changes
1	66	M	tMDS	46,XY [25]	n.d.	Yes	Yes	Yes	Yes
2	74	M	MDS-RS-MLD	Complex	n.d.	No	Yes	No	No
3	71	F	MDS-EB2	Complex	No	Yes	Yes	No	No
4	26	F	MDS-MLD	46,XX[25]	n.d.	No	No	No	Yes
5	64	F	MDS-EB1	46,XX,add(7)(p22), add(22)(q13) [13]/46,XX [12]	No	Yes	Yes	Yes	No
6	65	F	MDS-EB2	46,XX [25]	n.d.	No	Yes	Yes	Yes
7	67	M	MDS-RS-SLD	46,XY [25]	No	Yes	Yes	Yes	No
8	78	M	MDS-EB1	n.d.	n.d.	No	No	No	No
9	70	M	MDS-EB2	45,XY,-7 [6]/46,XY,del (20)(q11) [6]/46,XY [13]	No	Yes	Yes	Yes	No
10	68	F	MDS-EB2	46,XX [25]	No	No	Yes	Yes	No
11	62	M	MDS-EB2	Complex	No	Yes	Yes	Yes	No
12	77	M	MDS-U	45,XY,-7 [4]/46,XY [21]	Yes	Yes	Yes	Yes	No
13	62	F	MDS-MLD	Complex	n.d.	No	No	No	Yes
14	81	M	MDS-U	Complex	n.d.	n.d.	n.d.	n.d.	n.d.
15	64	M	ICUS	45,X,-Y [4]/46,XY [21]	No	No	No	No	No
16	75	F	CCUS	46,XX [25]	n.d.	No	No	No	No
8	78	M	CCUS	46,XY[25]	No	No	Yes	No	No
17	71	M	ICUS	46,XY [25]	No	Yes	No	Yes	No
18	84	M	CCUS	46,XY [25]	No	No	No	No	No
19	67	M	CCUS	46,XY [25]	No	Yes	Yes	Yes	No
20	54	M	Hemolytic anemia	46,XY [25]	No	No	Yes	Yes	No
21	74	M	Hemolytic anemia	n.d.	No	Yes	Yes	Yes	No
22	46	F	B12 deficiency	46,XX [25]	No	Yes	Yes	Yes	Yes
23	65	M	PV/ET	n.d.	No	Yes	Yes	Yes	No
24	73	M	Non-MDS reculocytosis	n.d.	n.d.	No	No	No	No
25	60	M	Abnormal Rh-type	45,X,-Y[4]/46,XY [21]	Yes	Yes	Yes	No	No

Abbreviations: CCUS, Clonal cytopenia of undetermined significance; ET, Essential Thrombocythemia; ICUS, Idiopathic cytopenia of undetermined significance; MDS-EB1, MDS with excess blasts 1; MDS-EB2, MDS with excess blasts 2; MDS-MLD, MDS with multilineage dysplasia; MDS-RS, MDS with ring sideroblasts, MDS-RS-MLD, MDS with ring sideroblasts and multi lineage dysplasia; MDS-RS-SLD, MDS with ring sideroblasts and single lineage dysplasia; MDS-U, MDS unclassifiabel; n.a., not available; n.d., not determined; PV, Polycythemia Vera; tMDS, therapy related MDS.

[a] Complex karyotype: ≥ 3 aberrations.

disorder, and 1 patient who had a BM aspiration performed based on the finding of spontaneous Rhesus type D alteration (Körmöczi et al., 2007)) were included (Table 1). Furthermore, we included 2 patients diagnosed with ICUS and 4 patients with CCUS to assess possible subtle dysmorphometric changes (Table 1). One CCUS patient (ID-8) was diagnosed with MDS 1 month after the CCUS diagnosis, and was therefore included in both disease entities. Inclusion criteria for both MDS patients and controls was more than 10% erythroblasts ($CD45^{neg}CD235a^{+}CD71^{+}$) out of all leukocytes in the routine diagnostic flow cytometric analysis or a confirmed MDS associated dyserythropoiesis (Supporting Information). The study was conducted in accordance with the Declaration of Helsinki and approved by The Central Denmark Region Committee on Health Research Ethics (record no.: 1-10-72-125-17) and the Danish Data Protection Agency (record no.: 1-16-02-849-17).

2.2 | Sample preparation, IFC acquisition, and gating of erythroid maturation stages

Cryopreserved MNCs were thawed in a 37°C water bath and resuspended in stain buffer containing 10% heat-inactivated fetal calf serum (Biowest, Nuaillé, France). Thawed cells were incubated for 10 minutes at 37°C with DNase (Sigma-Aldrich/Merck, MO) and $MgCl_2$ in final concentrations of 80 U/mL and 5.5 mM, respectively. Afterwards, cells were stained with Zombie Violet™ Fixable Viability dye (Biolegend, CA), washed and stained with the following pre-titrated monoclonal antibodies (MoAb): CD235a PE (clone JC159, Agilent), CD105 PE-CF594 (clone 166, BD Biosciences, CA), CD71 PerCP-Cy5.5 (clone CY14G, BioLegend), CD117 PE-Cy7 (clone 104D2, BD Biosciences), and CD45 KrO (clone J.33, Beckman Coulter, CA). Additionally, DRAQ5 (ThermoFisher Scientific, MA) and Thiazole Orange (TO; Sigma-Aldrich) was included for DNA and RNA staining in final concentrations of 1.25 μM and 0.25 μg/ml, respectively. Data acquisition was performed on an ImageStream$^{®X}$ Mark II imaging flow cytometer dual camera system (Luminex, Seattle, WA) equipped with four lasers; 405 nm (set to 120 mW), 488 nm (set to 200 mW), 561 nm (turned off) and 642 nm (set to 150 mW). Channels 1 and 9 were used to capture cellular brightfield (BF) images. Stains were detected in the following channels: Thiazole Orange (TO), channel 2; PE, channel 3; PE-CF594, channel 4; PerCP-Cy5.5, channel 5; PE-Cy7, channel 6; Zombie Violet channel, 7; KrO, channel 8; DRAQ5, channel 11. Side scatter (SSC) was detected in channel 12. Consecutive raw image files (.rif) containing 20,000 single cells, were collected at 60x magnification using a data acquisition template created in the INSPIRE® software (version 200.1.620.0, Luminex). A median of 13 (range: 4–37) replicates were acquired depending on available archival sample material. Compensation was set daily using UltraComp eBeads™ (ThermoFisher) stained with fluorochrome-conjugated moAbs in addition to single-color-stained cells (DRAQ5, TO and Zombie Violet). Compensation controls were acquired using the INSPIRE® compensation wizard and subsequent fluorescence compensation matrix calculations and data analysis was performed in the IDEAS® software (version 6.2.187.0, Luminex). Subsequent gating of erythroid maturation stages was performed in the IDEAS® software (version 6.2.187.0, Luminex). In human erythropoiesis, five morphologically distinct erythroblast intermediates can be identified; proerythroblasts (ProE), early basophilic erythroblasts (BasoE), late BasoE, polychromatic erythroblasts and orthochromatic erythroblasts (J. Hu et al., 2013; Gautier et al., 2016). Here, we refer to the terminology applied by the clinical IMDS Flow Working group (Westers et al., 2017) and define three erythroblast developmental stages; ProE, BasoE, and the combined population of poly- and orthochromatic erythroblasts (PolyOrthoE). The PolyOrthoE subset was evaluated as a combined population, as these cell subsets share immunophenotype and appeared as a continuum in morphometric parameters. In short, live, single, nucleated cells in focus were gated for identification of erythroid cells defined by expression of CD71 and co-expression of either CD235a and/or CD105 (Machherndl-Spandl et al., 2013; Westers et al., 2017). Next, erythroblasts were further gated by their CD117 and CD105 expression to distinguish between ProE ($CD117^+CD105^+$), BasoE ($CD117^-CD105^+$), and the combined subset of PolyOrthoE ($CD117^-CD105^-$). Mature lymphocytes ($SSC^{low}CD45^{high}$) were used as an internal negative control population (Figure S1; full gating strategy is provided in Supporting Information).

2.3 | Masking and gating strategy for single and binucleated erythroblasts (BNEs) using machine learning

Morphometric features were calculated using function masks that were created to highlight the cellular, nuclear and cytoplasmic areas of single nucleated erythroblasts (Figure S2; Supporting Information). By applying the specific masks to populations of interest (i.e. ProE, BasoE, and PolyOrthoE), relevant morphometric features were calculated and were used to quantify dysmorphometric erythropoiesis. Moreover, an advanced nuclear function mask was constructed to identify BNEs (Figure S2d; Supporting Information), however, visual inspection of the BNE population revealed the presence of doublet events (Figure S2e). To distinguish true BNEs from doublet events, and to exclude doublets from all morphometric analysis, we took advantage of advanced combination features and machine learning (ML) classifiers generated in the IDEAS® software (Supporting Information). Full lists of relevant features are provided in Table S1 and Table S2.

2.4 | Statistical analyses

For comparison of continuous variables between NBM and MDS patients, the Mann–Whitney *U* Non-Parametric test was applied. *p*-values <.05 were considered significant. For MDS patients, correlation between erythrocyte mean corpuscular volume (MCV) and cell area was analyzed for significance by the Non-parametric Spearman's rank order correlation. All calculations were conducted in GraphPad Prism version 7 (GraphPad Software, La Jolla, CA). For continuous parameters cut-off values for morphometric aberrancies were based on the 5th and or 95th percentile of the data of healthy controls.

3 | RESULTS

3.1 | IFC enables identification of erythroblast intermediates and subsequent confirmation of morphometric changes during erythroid development in healthy BM

To ascertain the robustness of the IFC technique to morphometrically delineate erythropoietic intermediates, we initially examined the erythropoietic maturation-pattern in BM from healthy controls. We identified the three well-described nucleated erythropoietic maturation stages based on immunophenotype; ProE, BasoE, and the combined population of PolyOrthoE characterized by distinctive expression of surface markers (Figure 1a; Figure S1), and next investigated IFC related morphometric changes of these three immunophenotypically defined erythroblast stages. As erythroblasts

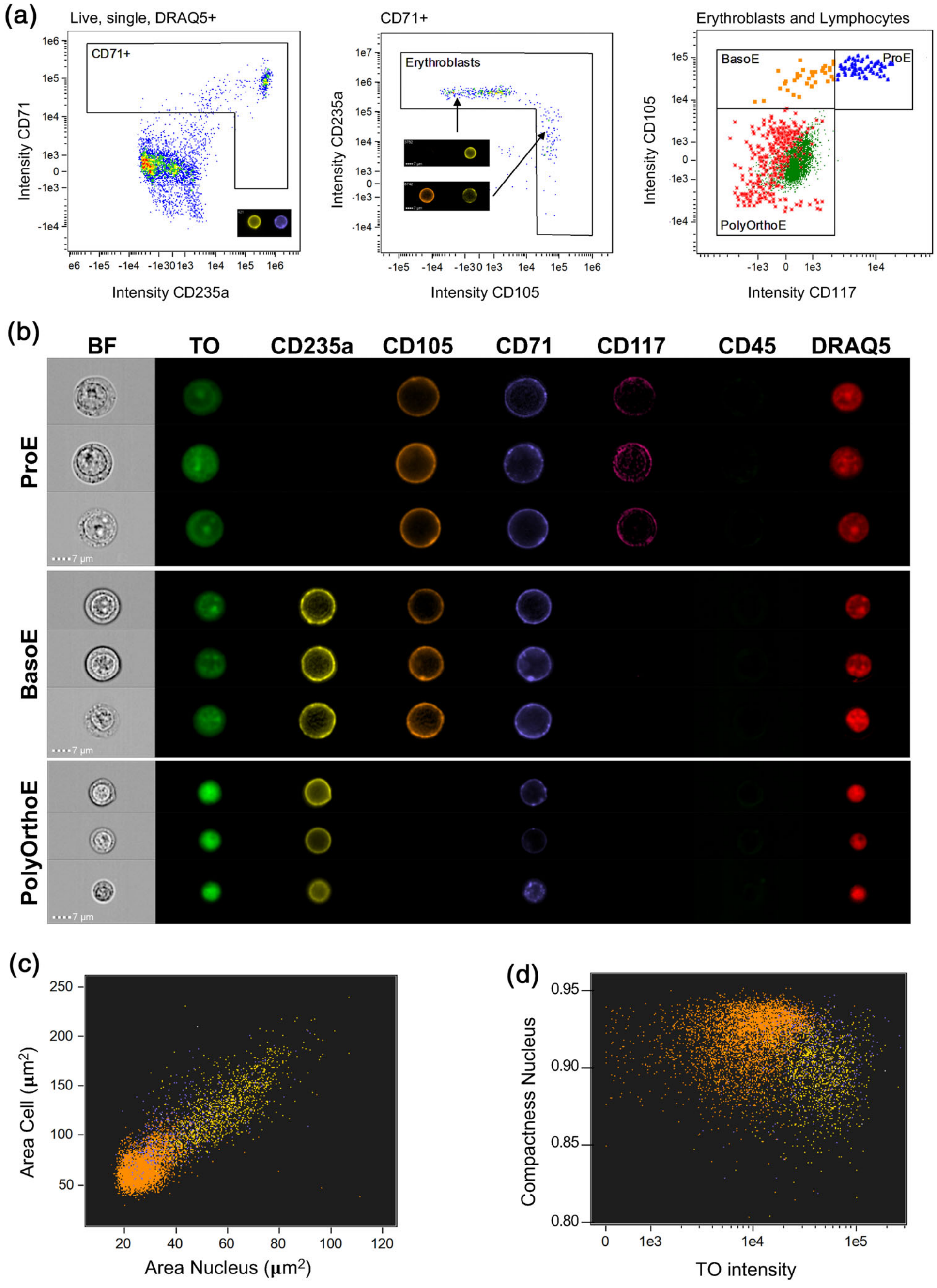

FIGURE 1 Immunophenotypic and morphometric delineation of erythroid intermediates in healthy controls. (a) Extract of the gating strategy. Live, single, nucleated cells in focus were gated for commitment to the erythroid lineage by their expression of the transferrin receptor CD71 and co-expression of either CD235a and/or CD105 (left and middle panel). Expression of CD117 and CD105 were used to distinguish between the three erythroid developmental stages; proerythroblasts (ProE, CD117$^+$CD105$^+$), basophilic erythroblasts (BasoE, CD117$^-$CD105$^+$), and the combined subset of poly- and orthochromatic erythroblasts (PolyOrthoE, CD117$^-$CD105$^-$) (right panel). This alternative nomenclature for human erythropoiesis includes an early basophilic erythroblast which, based on the immunphenotype, would fall into our proerythroblast gate (Gautier et al., 2016). The full gating strategy is depicted in Figure S1. (b) Image gallery of ProE, BasoE, and PolyOrthoE cells illustrating their surface marker expression, decreasing cell size (BF) and nuclear condensation (DRAQ5). (c) Representative bivariate plot of nuclear and cell area from one healthy control illustrating decreasing nuclear and cell area along the maturation sequence (yellow: ProE; purple: BasoE; orange: PolyOrthoE). (d) Bivariate plot of TO intensity and nuclear compactness as hallmarks of RNA degradation and nuclear condensation, illustrating synchronous nucleocytoplasmic maturation profile during healthy erythropoiesis in one representative healthy control (yellow: ProE; purple: BasoE; orange: PolyOrthoE) [Color figure can be viewed at wileyonlinelibrary.com]

differentiate, they become progressively smaller and the nucleus condenses until it is finally extruded (Porwit et al., 2011). Reassuringly, we found that immunophenotypically defined erythroid precursors demonstrated significantly decreasing cell area (ProE > BasoE: $p = .0049$ and BasoE > PolyOrthoE: $p < .0001$) nuclear area (ProE > BasoE: $p = .0002$ and BasoE > PolyOrthoE: $p < .0001$), and cytoplasm area (BasoE > PolyOrthoE: $p < .0001$) (Figure 1a–b; Figure 2a; Figure S3a–b). Thus, we could morphometrically confirm the generally described maturation process where both cellular and nuclear area, as well as the ratio between these two parameters

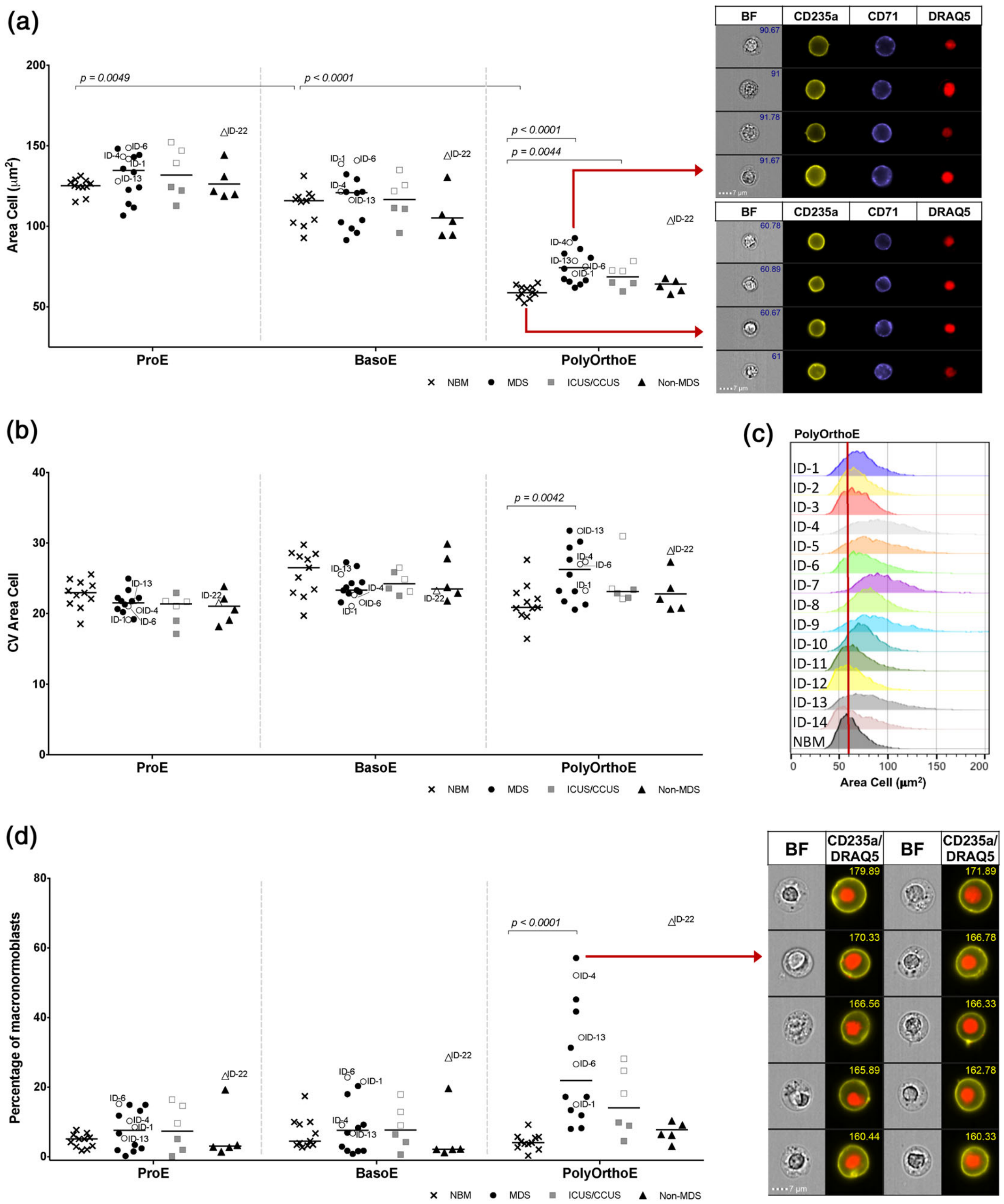

FIGURE 2 Dyserythropoietic cell size enlargement among erythroid precursor. (a) Scatter plot representation of median cell area of ProE, BasoE, and PolyOrthoE for healthy donors with normal BM function (NBM), MDS, ICUS/CCUS and non-MDS patients. Representative imagery shows the BF, CD235a, CD71 and DRAQ5 images of PolyOrthoE as well as specific cell area feature values in μm^2 for one MDS patient (ID-4) (top image gallery) and one NBM (bottom image gallery). (b) Scatter plot of the coefficient of variation (cv) within subpopulations of immunophenotypically defined ProE, BasoE, and PolyOrthoE cells. (c) Histogram visualization of cell size heterogeneity demonstrating cell size enlargement for individual MDS patients as compared to the concatenated population of PolyOrthoE in healthy controls. Red line indicates the median cell area for NBMs. (d) Scatter plot representation of macronormoblast percentages in ProE, BasoE, and PolyOrthoE BM cells including representative imagery of PolyOrthoE macroblasts from the MDS patient with the highest percentage of macronormoblasts (ID-7). Cell area values (μm^2) are shown on individual cells. MDS patients and the vitamin B12 deficiency control with morphologically confirmed megaloblastic changes are indicated with open symbols. Likewise, high-risk CCUS patients are indicated with open symbols. Patient IDs are listed in Table 1 [Color figure can be viewed at wileyonlinelibrary.com]

(Figure S3c), progressively decline during maturation. Furthermore, we demonstrated gradual decline of cytoplasmatic RNA content and concomitant nuclear condensation as tokens of cytoplasmic and nuclear maturation, respectively (Figure 1c). Of note, the nuclear fluorescence signal was significantly more compact at the transition from ProE to BasoE (Figure S3d; p = .0400) and also from BasoE to PolyOrthoE (Figure S3d; p < .0001). Collectively, these morphometric findings correlate with pathologic examination of normal erythropoiesis (Palis, 2014; Porwit et al., 2011).

3.2 | Morphometric quantification using IFC demonstrates cell size enlargement associated with MDS

Cell size enlargement among erythroid precursors can represent a dysplastic feature in MDS and is associated with megaloblastic changes, macronormoblasts, and giant erythroblasts (Goasguen et al., 2018). While megaloblastic changes are distinguished as erythroblasts of increased size with asynchrony between cytoplasmic and nuclear maturation (Goasguen et al., 2018; Porwit et al., 2011), macronormoblasts are enlarged cells with normal cytoplasmic/nuclear maturational profile. Moreover, in some MDS cases highly abnormal giant erythroblasts can be seen (Goasguen et al., 2018). However, while the latter two morphological characteristics are considered clearly dysplastic, these cells are rare and difficult to quantify by pathologists (Goasguen et al., 2018). Importantly, as MDS is often characterized by erythroid maturation arrest, that can lead to increased fractions of the most immature erythroblasts stages (Ali et al., 2018), the value of erythroblast subpopulation analyses must be emphasized, as a shift in proportions of otherwise morphologically normal erythroblasts can lead to relative enlarged average erythroblast cell size. In the present study, cytologic examination of BM smears identified substantial megaloblastic changes in the erythroid lineage in four of the MDS patients (ID-1, 4, 13, and 16; Table 1). In accordance, evaluation of the cell size dimension by IFC showed enlarged median cell areas at one or more erythroid maturation stages for these four patients (Figure 2a). As a confirmatory control of megaloblastic erythropoiesis, we found substantially enlarged cell areas for all erythroid maturation stages in a patient with known B12 deficiency (ID-22) (Table 1; Figure 2a) (Koury et al., 1997; Wickramasinghe, 1999).

In MDS BM samples, increased cell areas were also identified in cases initially not categorized as megaloblastic by pathology, and at the PolyOrthoE stage, the median area of all MDS samples was significantly increased compared to healthy controls (p < .0001) (Figure 2a). In addition, analyses of cytoplasm and nuclear area revealed that cell enlargement was derived from increased cytoplasm area, as this was significantly increased in MDS patients when compared to healthy controls (Figure S3b; PolyOrthoE: p < .0001), while the nuclear compartment was not enlarged (Figure S3a). Interestingly, for the included ICUS/CCUS patients, the median cell area of PolyOrthoEs was also significantly increased (p = .0044) (Figure 2a). Of note, we observed that the three ICUS/CCUS patients (ID-8, 16, and 19) with the largest cell areas were high-risk CCUS patients (according to Malcovati et al. (2017)), and had high variant allele frequencies (VAFs) of myeloid-associated mutations (Table S3). Of further interest, for the MDS patients, we found a significant correlation of erythrocyte mean corpuscular volume (MCV) and cell area for all erythroid maturation stages (ProE: p = .0047; BasoE: p = .0149; PolyOrthoE: p = .0145, Figure S4).

Recognizing that not all erythroid cells are necessarily dysplastic in MDS, we sought to evaluate whether the distribution of cell area in MDS erythroblasts was different from control BMs. In fact, at the PolyOrthoE maturation stage, the median coefficient of variation (CV) of cell area proved to be significantly higher in MDS BM compared to healthy controls (p = .0042) (Figure 2b), indicating a more heterogeneous cell population. Furthermore, by plotting all cell area values on a histogram, it can be seen that the distribution skews towards larger PolyOrthoE cell areas in MDS BM (Figure 2c). Moreover, based on the 95th percentile of the healthy controls (n = 11), the CV cell area could be considered increased for 50% of the MDS patients (ID-4, 5, 6, 9, 11, 13, and 14) (data not shown). Next, we investigated if we could identify erythroblasts with very large cell areas corresponding to macronormoblasts and giant erythroblasts at higher frequencies in the MDS samples. As such, we used cut-offs of 186 μm^2, 165 μm^2, and 89 μm^2 corresponding to the 95th percentile of pooled healthy ProE (n = 10,394), BasoE (n = 6509), and PolyOrthoE (n = 25,049) subpopulations, respectively. At the PolyOrthoE stage, the percentage of cells larger than the 95th percentile was significantly increased (Figure 2d; p < .0001). Of note, we found the highest macronormoblast percentage in an MDS patient (ID-7) with no previous records of megaloblastosis (Figure 2d). Remarkably, the three high-risk CCUS patients had the highest percentages of abnormally large erythroblasts at all maturational stages (Figure 2d).

3.3 | Machine learning assisted morphometric analysis allows for robust identification and quantification of BNEs

The presence of BNEs is a WHO classified dysplastic feature in MDS, but may also be found in cases with non-neoplastic acquired anemia, and in healthy controls (Bain, 1996; Goasguen et al., 2018). Hematopathological BM examination identified erythroid bi- and multinucleairity in eight out of 14 MDS patients (Table 1; Figure 3a). Moreover, BNEs were identified in two ICUS/CCUS patients and four non-MDS controls (Table 1). For BNE identification on IFC, we designed a refined BNE masking strategy that allowed separate masking of individual nuclei. By applying the spot counting feature to the BNE mask combined with ML algorithms created in the IDEAS® software, we accurately differentiated doublets from true BNEs and enumerated the latter within each subpopulation (Figure 3b). Indeed, for MDS patients, we detected significantly increased BNEs in both the ProE and PolyOrthoE subpopulations (Figure 3c; ProE: p = .0001; PolyOrthoE: p = .0001). In agreement with pathologic examination, we confirmed the presence of BNEs at one or more maturation stages in the aforementioned MDS patients, ICUS/CCUS patients, and non-MDS controls (Figure 3c). Interestingly, we identified considerable numbers of BNE ProEs in three additional MDS patients (ID-4, 8, and 13), and also in the CCUS sample from patient ID-8 (Figure 3c). In NBM the presence of genuine BNEs was confined to the immature erythroid progenitors (ProE and BasoE) and overall the frequencies were below previously reported levels of 1–2% BNEs in BM of healthy adults (Bain, 1996).

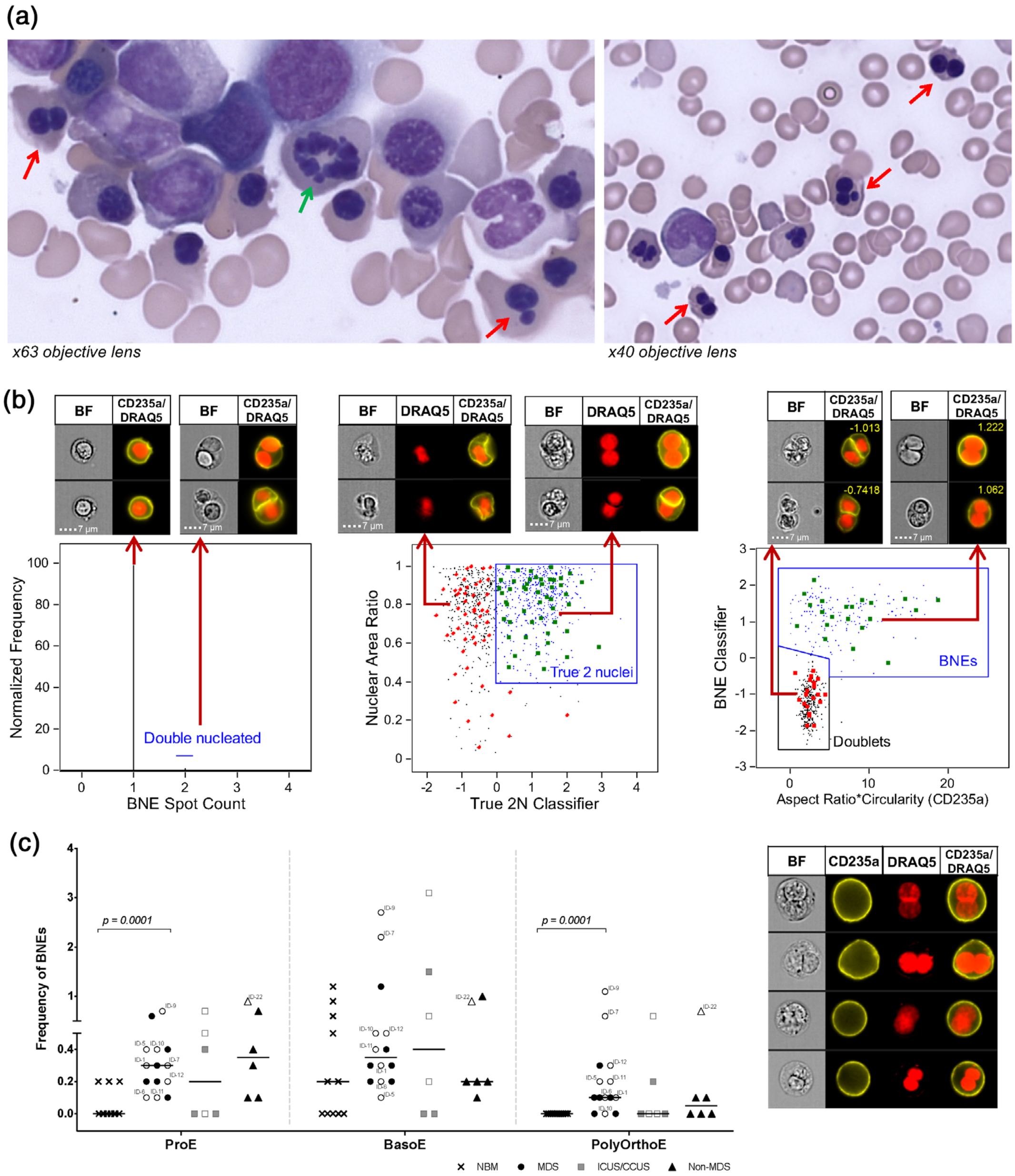

FIGURE 3 Identification and quantification of binucleated erythroblasts in dyserythropoietic and control BM. (a) Bone marrow smear from an MDS patient with dyserythropoiesis (ID-5) stained with modified Wright's stain (Hematek® stain pack) showing bi- and multinucleated erythroblasts with nuclei in close apposition (red arrow) as well as a mitotic cell (green arrow). (b) Gating strategy using machine learning (ML) to identify true binucleated erythroblasts (BNEs). Left panel: The spot count feature was applied to the BNE mask to identify all double nucleated images. Middle panel: Bivariate plot of the double nucleated ML classifier versus the nuclear area ratio feature to identify true double nucleated images. Right panel: Bivariate plot of the product of the CD235a aspect ratio and CD235a circularity features versus the BNE ML classifier. Representative imagery of single and double nucleated cells, false positive double nucleated cells and true BNEs are shown. The right column also shows BNE ML classifier values for BNE and doublet images. (c) Scatter plot representation of binucleation frequency among ProE, BasoE, and PolyOrthoE cells supported by representative imagery of binucleated ProEs in one MDS patient (ID-6). MDS patients and the vitamin B12 deficiency control with morphologically verified bi-and/or multinuclearity are indicated with open symbols. Likewise, high-risk CCUS patients are indicated with open symbols. Patient IDs are listed in Table 1 [Color figure can be viewed at wileyonlinelibrary.com]

3.4 | Examining the potential for IFC quantification of subtle dysplastic nuclear irregularities

Abnormal nuclear shape, i.e. nuclear budding and/or lobulation, internuclear bridging and nuclear fragments, is a prominent dysplastic feature in many MDS BMs. However, nuclear irregularities are infrequent and difficult to identify morphologically and furthermore, such abnormalities can be detected at low numbers in NBM as well as during non-neoplastic causes of anemia and as such are not specific of MDS (Goasguen et al., 2018). In line with this, pathologic examination identified nuclear irregularities in 10 out of 14 MDS patients, two out of six ICUS/CCUS patients, and five out of six non-MDS patients (Table 1). We investigated the possibility of applying IFC associated features for morphometric evaluation of nuclear shape. Intriguingly, when depicting histograms of nuclear *Aspect Ratio* (defined as the ratio between the minor and major axis of an object) distribution for all three maturational stages (Figure 4a), we observed that for selected MDS samples (e.g., ID-1, ID-7, and ID-9) at both the ProE and BasoE

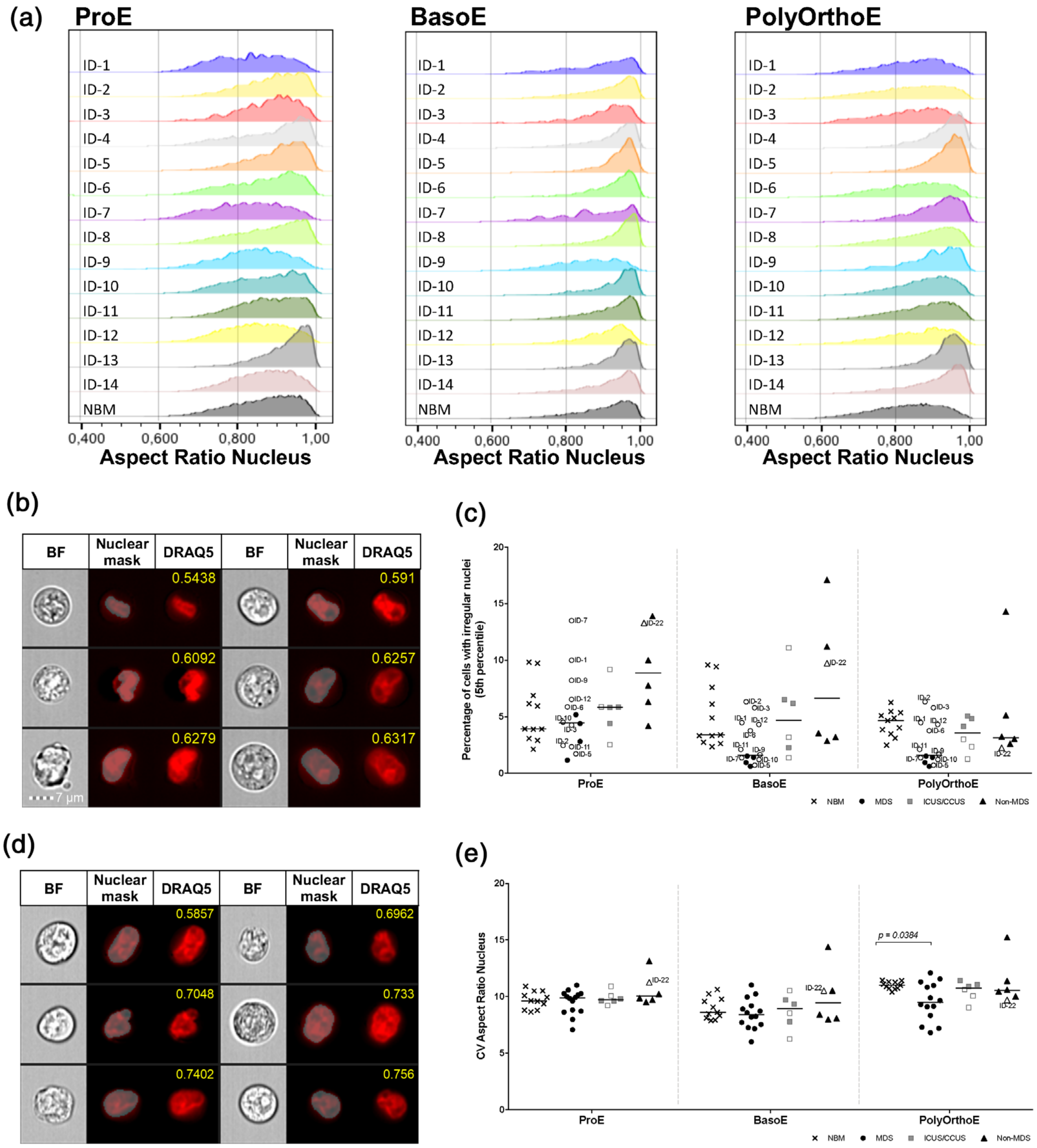

FIGURE 4 Morphometric evaluation of nuclear shape irregularities in BM samples from MDS patients and controls. (a) Histogram visualization of the distribution and heterogeneity of nuclear *Aspect Ratio* for individual MDS patients as compared to concatenated populations of ProE, BasoE, and PolyOrthoE in healthy controls. (b) Bright field and DRAQ5 imagery illustrating ProEs with low nuclear *Aspect Ratio* in a BM sample from MDS patient ID-1. In addition, the nuclear mask and *Aspect Ratio* values are indicated for individual cells. (c) Scatter plot representation of the percentage of irregularly shaped nuclei within the 5th percentile of the *Aspect Ratio*. (d) Bright field and DRAQ5 imagery illustrating ProEs with low nuclear *Aspect Ratio* in a BM sample from one healthy control. (e) Illustration of the coefficient of variation (CV) within erythroblast subpopulations. MDS patients and the vitamin B12 deficiency control with morphologically verified nuclear irregularities are indicated with open symbols. Likewise, high-risk CCUS patients are indicated with open symbols. Patient IDs are listed in Table 1 [Color figure can be viewed at wileyonlinelibrary.com]

stages, the distribution was clearly shifted towards lower *Aspect Ratio* values, indicating high numbers of cells with non-circular and/or elongated nuclei (Figure 4b). To investigate whether BM samples from MDS patients contained larger fractions of irregular nuclei, we used the 5th percentile of merged healthy ProE (*n* = 10,394), BasoE (*n* = 6509) and PolyOrthoE (*n* = 25,049) as region boundaries to demarcate subpopulations with profound nuclear irregularities. We found MDS ID-1 and ID-7 to hold the largest percentages of nuclear irregularities, but only at the ProE stage (Figure 4c). Moreover, we observed considerable fractions of irregularly nucleated ProEs, BasoEs, and PolyOrthoEs in NBM and non-MDS controls (Figure 4c–d). Of note, at the PolyOrthoE stage, in most MDS samples, there seemed to be a more homogenous distribution of cells with higher *Aspect Ratios* (Figure 4a) and correspondingly lower CV values (Figure 4e; *p* = .0384). Although, we could identify and visually confirm the presence of nuclear irregularities in all MDS patients, the applied strategy did not support distinction between dysplastic MDS BM and control samples, emphasizing the difficulties associated with quantification of nuclear irregularities.

4 | DISCUSSION

This paper demonstrates proof-of-concept applicability of IFC as a promising tool in the difficult diagnostic work-up of MDS. Currently, while morphological examination of BM remains the cornerstone in the diagnostic classification of MDS, correct evaluation of dysplastic changes requires great expertise and is prone to significant inter- and intra-observer variability (Goasguen et al., 2018; Valent et al., 2017). Typically, evaluation of MDS BM is based on approximately 500 cells, and it is generally accepted that by increasing the number of analyzed cells, the reproducibility of dysplasia assessment improves (Bennett & Orazi, 2009). To this end, we posit that IFC technology represents an exciting and novel approach as it allows for morphometric quantification of practically an unlimited number of cells combined with delineation of erythropoietic differentiation stages. Specifically, IFC offers a substantial increase in statistical robustness and sensitivity by analyzing a larger number of cells and through refined subpopulation analyses of biologically relevant cells based on immunophenotyping. In the present study, we selectively analyzed up to 68,000 erythroblasts in a single sample with an automated analysis strategy that enabled quantification and retrieval of classical dysplastic features in an objective manner.

Knowledge of morphometric changes during healthy erythropoietic maturation is mandatory in order to identify MDS associated abnormalities. Thus, by employing IFC related morphometric features such as cell and nuclear area, RNA content and nuclear compactness in combination with immunophenotypic characterization, we were able to recapitulate the normal maturation pattern of early erythropoiesis in healthy BM (Figure 1). Of note, despite abnormalities in some of these parameters, both MDS and pathological controls generally followed the same maturational pattern (Figure 2a, Figure S3a–b). In this study, an archival cohort of anonymized healthy controls with no records of clinical data was used as biological reference. As such, we were not able to account for confounding factors such as age, sex and comorbidities in the control population. Yet, we expect that our MDS patients, whose average age is 68, are significantly older than our controls. Moreover, assessment of BM morphology was not part of the protocol for healthy BM sampling, which could be of importance as morphologically dysplastic cells are common in BM from healthy individuals above 50 years of age (Bain, 1996). Collectively, age associated dysplasia and maybe even pre-malignant clonal hematopoiesis may, to some extent, explain the variation observed in the healthy controls.

Next, we studied the dyserythropoietic phenomenon of cell size enlargement in MDS samples. By combining advanced masking techniques and features in the IDEAS software, it was possible to morphometrically identify and quantify abnormally enlarged erythroblasts at the PolyOrthoE stage in MDS BM (Figure 2a). While median cell size enlargement in the compound PolyOrthoE population among MDS BM samples could be attributable to a universal enlargement of all cells in the subset, it could also represent an alternative scenario. For instance, as observed by Ali et al., impaired terminal differentiation is evident in many MDS patients, where abnormal accumulation of polychromatic erythroblasts results in a decreased level of orthochromatic cells, which in our analysis would skew the distribution towards the larger polychromatic cells (Ali et al., 2018). In addition, when we quantified abnormally large cells based on a numeric cell area threshold corresponding to the 95th percentile of NBM erythroblasts, the most pronounced and statistically significant cell size aberrations were again observed among late-stage erythroblasts, i.e. PolyOrthoE (Figure 2d).

In recent years, an increasing amount of molecular data has in some ways increased the diagnostic complexity of myeloid malignancies, and distinguishing MDS from pre-MDS conditions such as ICUS and CCUS remains a major clinical challenge (Valent et al., 2017). Previous studies of ICUS/CCUS have associated the presence of two or more mutations at VAFs ≥10% with an increased risk of subsequent hematologic neoplasia (Cargo et al., 2015; Malcovati et al., 2017). In addition, Malcovati et al. demonstrated that CCUS patients with specific mutational pattern have similar overall survival and risk of disease progression as lower risk MDS, and the authors suggest that such high-risk CCUS cases should be classified as MDS in line with MDS-defining cytogenetic abnormalities (Malcovati et al., 2017). Our results show that within the group of ICUS/CCUS patients, abnormally large erythroblasts were consistently observed in CCUS cases which according to the definition by Malcovati et al. are high-risk CCUS based on their mutational status (Figure 2a,d). In spite of the small sample size among the ICUS/CCUS patients, it is probable that these correlations were observable from analyzing large numbers of cells with IFC and it is possible that such correlations may be missed through visual histological examination. Overall, a shift towards cell size enlargement coupled with the presence of significantly higher proportions of macronormoblasts could represent early dysmorphometric manifestations preceding recognizable morphological dysplasia. In support of this, the CCUS patient (ID-8), who was diagnosed with MDS 1 month after the CCUS diagnosis, had comparable IFC results at both timepoints with regard to Area Cell, CV Area Cell, percentage of macronormoblasts and frequency of BNEs (data not shown).

Given the fact that binucleation is a prominent but sometimes infrequent erythroid dysplastic feature in MDS, IFC could prove advantageous over slide-based scoring as it allows for evaluation of a far larger number of cells. Thus, by creating a nuclear masking strategy to identify binucleated erythroblasts and using the ML module in the IDEAS software, we were able to robustly quantitate true BNEs (Figure 3b–c). Here, the ability to examine three component images of each cell (e.g., BF, CD235a and DRAQ5) proved highly useful in the discrimination of doublets from true BNEs. We observed that by examining only the BF and DRAQ5 images, all double nucleated events could be mistaken for BNEs, but the observable boundary in the CD235a image permitted doublet identification. As such, the advanced features created by the ML module in IDEAS® provided a significant advantage over the standard features, permitting the detection of false positive BNEs. By combining the ML classifiers with advanced features in IDEAS, we were able to remove i) doublets with near-circular nuclear shape and with nuclear areas comparable to singlets in a heterogeneous population where all cells are unequal in size and ii) cells in which the nuclear mask erroneously captured a single nucleus as binucleated due to imperfect differentiation of DRAQ5 intensity leading to a false segmentation point in the nuclear image. Significantly increased frequencies of BNEs at the ProE and PolyOrthoE stages in MDS BM were observed and interestingly, we could practically not detect any BNEs at the PolyOrthoE stage in NBM, which should be regarded as highly aberrant (Figure 3c).

As expected, we observed a pronounced morphometric heterogeneity in the group of MDS patients. This inter-donor variability was most noticeable within ProE and BasoE subpopulations while late-stage erythroblasts appeared more homogenous. Of note, both the presence and the degree of morphometric dysplasia (i.e. the extent of area enlargement and level of BNE frequency) varied between MDS patients, and for individual patients also between the different erythroblast maturation stages. Exemplified by patient ID-6, median cell area enlargements were clearly evident for both ProE and BasoE, while late-stage erythroblasts were affected to a lesser extent. However, as late-stage erythroblasts comprised 73% of all NECs, examination of the compound NEC population revealed that the median cell area for this patient was comparable to healthy controls (data not shown). This marked inter-donor and intra-patient variability of dysmorphometric features reflects the extreme biological heterogeneity in MDS, and our data emphasize the importance of refined subpopulation analysis facilitated by IFC.

The pronounced heterogeneity at different maturational stages presented difficulties in studying nuclear irregularities. In MDS, subtle morphometric changes, for example, nuclear irregularities might only be evident in a small fraction of cells in a given subpopulation. We were only able to observe an increased fraction of such cells in two MDS patients at the ProE stage (Figure 4a–c), but precise detection of the nuclear boundary is dependent on how well the IDEAS software can mask the nucleus. As such, accurate masking of small nuclei (i.e. PolyOrthoEs) is more difficult than for larger nuclei given the smaller number of pixels in the image. Therefore, in future studies it might be relevant to include a nuclear skeleton lamin stain to better demarcate the nuclear boundary to enhance masking accuracy (Tsai et al., 2020). Additionally, identification of subtle nuclear irregularities, such as nuclear budding and nuclear bridges, may be enhanced with more advanced machine learning techniques (e.g., convolutional neural networks) that do not rely on image masking (Rodrigues et al., 2018).

The results presented here add to the growing evidence supporting the applicability of IFC in hematological diagnostics (Grimwade et al., 2012; Mirabelli et al., 2012; Sundaravel et al., 2015; H. Hui et al., 2018; H. Y. L. Hui et al., 2019). However, IFC requires cells to be in suspension and morphological architecture, for example, abnormal localization of immature precursors, cannot be captured by IFC. Thus, as no single biological or genetic reliable diagnostic parameter has yet been discovered for MDS, IFC should be viewed as a promising supplement to established diagnostics in line with MFC, and we envisage that integration of IFC technology into existing diagnostic MFC scoring models complemented by routinely documented clinical parameters (Abelson et al., 2018; L. Hu et al., 2017), cytogenetics and molecular genetics may assist in identifying dyserythropoiesis in MDS (Van De Loosdrecht et al., 2008; Ogata et al., 2009; Cremers et al., 2017; M. G. D. Porta & Picone, 2017; Westers et al., 2017). We have presented a novel, proof-of-concept image-based flow cytometric platform to study and quantify morphometric changes in erythropoietic intermediates in BM samples from MDS patients. Using a different-from-normal approach, the ability to identify abnormalities in MDS patients with morphological dyserythropoiesis has been demonstrated. Certainly, exploration of the technique in a clinical context will need confirmation in a larger cohort of known MDS patients and respective controls performed on fresh BM samples. Importantly, the study of MDS erythropoiesis should preferably be performed on non-lysed BM samples, as the lysing procedure has been shown to alter the distribution of erythroblast stages (Violidaki et al., 2020; Westers et al., 2017). Ideally, validation should be designed as a prospective study with blinded examination of samples by both morphology, MFC, cytogenetic analyses and IFC including longitudinal samples from patients with unexplained cytopenia that might turn out to be diagnosed with MDS at a later timepoint. Moreover, such a study should include definitions of IFC related cut-off values and assessment of intra- and inter-observer variability/consistency. Taken as a whole, we propose that IFC holds great promise as a powerful supplemental tool in the challenging and complex setting of MDS diagnostics.

ACKNOWLEDGMENTS

The authors gratefully acknowledge the FACS Core Facility at Aarhus University, Denmark for access to the ImageStream®X Mark II and for technical assistance. We thank Lene Hyldahl Ebbesen at Department of Hematology, Aarhus University Hospital, Denmark for access to BM material from healthy controls. The study was supported by a grant from the Danish Cancer Society to P.H., and by a grant from Max Wørzner and wife Inger Wørzner's Foundation to C.A.R.

CONFLICT OF INTEREST

M.A.R. is employed by Luminex Corporation, the developer of the Amnis ImageStream technology and instruments as well as the data analysis software used in this study. No other competing interests were declared by the authors.

AUTHOR CONTRIBUTIONS

Carina A. Rosenberg, Marie Bill, and Maja Ludvigsen designed the research project; Carina A. Rosenberg and Mathias Hauerslev performed the IFC experiments; Gitte B. Kerndrup reviewed BM smears; Carina A. Rosenberg, Marie Bill, Matthew A. Rodrigues, Maja Ludvigsen and Mathias Hauerslev conducted the data analyses; Carina A. Rosenberg, Marie Bill, and Matthew A. Rodrigues wrote the first draft and made the figures; and all authors revised, read, and approved the final manuscript.

ORCID

Carina A. Rosenberg https://orcid.org/0000-0002-9609-8991

REFERENCES

Abelson, S., Collord, G., Ng, S. W. K., Weissbrod, O., Cohen, N. M., Niemeyer, E., Barda, N., et al. (2018). Prediction of acute myeloid Leukaemia risk in healthy individuals. *Nature*, *559*, 400–404. https://doi.org/10.1038/s41586-018-0317-6.

Ali, A. M., Huang, Y., Pinheiro, R. F., Xue, F., Hu, J., Iverson, N., Hoehn, D., et al. (2018). Severely impaired terminal erythroid differentiation as an independent prognostic marker in myelodysplastic syndromes. *Blood Advances*, *2*(12), 1393–1402. https://doi.org/10.1182/bloodadvances.2018018440.

Arber, D. A., Orazi, A., Hasserjian, R., Thiele, J., Borowitz, M. J., Le Beau, M. M., Bloomfield, C. D., Cazzola, M., & Vardiman, J. W. (2016). The 2016 revision to the World Health Organization classification of myeloid neoplasms and acute leukemia. *Blood*, *127*(20), 2391–2405. https://doi.org/10.1182/blood-2016-03-643544.

Bain, B. J. (1996). The bone marrow aspirate of healthy subjects. *British Journal of Haematology*, *94*(1), 206–209. https://doi.org/10.1046/j.1365-2141.1996.d01-1786.x.

Bennett, J. M., & Orazi, A. (2009). Diagnostic criteria to distinguish Hypocellular acute myeloid leukemia from Hypocellular myelodysplastic syndromes and aplastic anemia: Recommendations for a standardized approach. *Haematologica*, *94*(2), 264–268. https://doi.org/10.3324/haematol.13755.

Cargo, C. A., Rowbotham, N., Evans, P. A., Barrans, S. L., Bowen, D. T., Crouch, S., & Jack, A. S. (2015). Targeted sequencing identifies patients with preclinical MDS at high risk of disease progression. *Blood*, *126*(21), 2362–2365. https://doi.org/10.1182/blood-2015-08-663237.

Cremers, E. M. P., Westers, T. M., Alhan, C., Cali, C., Visser-Wisselaar, H. A., Chitu, D. A., van der Velden, V. H. J., et al. (2017). Implementation of erythroid lineage analysis by flow cytometry in diagnostic models for myelodysplastic syndromes. *Haematologica*, *102*(2), 320–326. https://doi.org/10.3324/haematol.2016.147843.

Doan, M., Sebastian, J. A., Caicedo, J. C., Siegert, S., Roch, A., Turner, T. R., Mykhailova, O., Pinto, R. N., McQuin, C., Goodman, A., Parsons, M. J., Wolkenhauer, O., Hennig, H., Singh, S., Wilson, A., Acker, J. P., Rees, P., Kolios, M. C., & Carpenter, A. E. (2020). Objective assessment of stored blood quality by deep learning. *Proceedings of the National Academy of Sciences*, *117*(35), 21381–21390. https://doi.org/10.1073/pnas.2001227117.

Duetz, C., Westers, T. M., & Van De Loosdrecht, A. A. (2019). Clinical implication of multi-parameter flow cytometry in myelodysplastic syndromes. *Pathobiology*, *86*(1), 14–23. https://doi.org/10.1159/000490727.

Garcia-Manero, G., Chien, K., & Montalban-Bravo, G. (2020). Myelodysplastic syndromes: 2021 update on diagnosis, risk-stratification and management. *American Journal of Hematology.*, *95*, 1399–1420. https://doi.org/10.1002/ajh.25950.

Gautier, E. F., Ducamp, S., Leduc, M., Salnot, V., Guillonneau, F., Dussiot, M., Hale, J., Giarratana, M.-C., Raimbault, A., Douay, L., Lacombe, C., Mohandas, N., Verdier, F., Zermati, Y., & Mayeux, P. (2016). Comprehensive proteomic analysis of human erythropoiesis. *Cell Reports*, *16*(5), 1470–1484. https://doi.org/10.1016/j.celrep.2016.06.085.

Goasguen, J. E., Bennett, J. M., Bain, B. J., Brunning, R., Vallespi, M. T., Tomonaga, M., Zini, G., & Renault, A. (2018). Dyserythropoiesis in the diagnosis of the myelodysplastic syndromes and other myeloid neoplasms: Problem areas. *British Journal of Haematology*, *182*(4), 526–533. https://doi.org/10.1111/bjh.15435.

Grimwade, L., Gudgin, E., Bloxham, D., Bottley, G., Vassiliou, G., Huntly, B., Scott, M. A., & Erber, W. N. (2012). Detection of cytoplasmic Nucleophosmin expression by imaging flow cytometry. *Cytometry Part A*, *81*(10), 896–900. https://doi.org/10.1002/cyto.a.22116.

Hu, J., Liu, J., Xue, F., Halverson, G., Reid, M., Guo, A., Chen, L., Raza, A., Galili, N., Jaffray, J., Lane, J., Chasis, J. A., Taylor, N., Mohandas, N., & An, X. (2013). Isolation and functional characterization of human erythroblasts at distinct stages: Implications for understanding of Normal and disordered erythropoiesis in vivo. *Blood*, *121*(16), 3246–3253. https://doi.org/10.1182/blood-2013-01-476390.

Hu, L., Li, M., Ding, Y., Pu, L., Liu, J., Xie, J., Cabanero, M., Li, J., Xiang, R., & Xiong, S. (2017). Prognostic value of RDW in cancers: A systematic review and meta-analysis. *Oncotarget*, *8*(9), 16027–16035. https://doi.org/10.18632/oncotarget.13784.

Hui, H., Fuller, K. A., Chuah, H., Liang, J., Sidiqi, H., Radeski, D., & Erber, W. N. (2018). Imaging flow cytometry to assess chromosomal abnormalities in chronic lymphocytic Leukaemia. *Methods*, *134–135*, 32–40. https://doi.org/10.1016/j.ymeth.2017.11.003.

Hui, H. Y. L., Clarke, K. M., Fuller, K. A., Stanley, J., Chuah, H. H., Ng, T. F., Cheah, C., McQuillan, A., & Erber, W. N. (2019). 'Immuno-FlowFISH' for the assessment of cytogenetic abnormalities in chronic lymphocytic leukemia. *Cytometry Part A*, *95*(5), 521–533. https://doi.org/10.1002/cyto.a.23769.

Kern, W., Haferlach, C., Schnittger, S., & Haferlach, T. (2010). Clinical utility of multiparameter flow cytometry in the diagnosis of 1013 patients with suspected myelodysplastic syndrome: Correlation to Cytomorphology, cytogenetics, and clinical data. *Cancer*, *116*(19), 4549–4563. https://doi.org/10.1002/cncr.25353.

Körmöczi, G. F., Dauber, E. M., Haas, O. A., Legler, T. J., Clausen, F. B., Fritsch, G., Raderer, M., Buchta, C., Petzer, A. L., Schönitzer, D., Mayr, W. R., & Gassner, C. (2007). Mosaicism due to myeloid lineage-restricted loss of heterozygosity as cause of spontaneous Rh phenotype splitting. *Blood*, *110*(6), 2148–2157. https://doi.org/10.1182/blood-2007-01-068106.

Koury, M. J., Horne, D. W., Brown, Z. A., Pietenpol, J. A., Blount, B. C., Ames, B. N., Hard, R., & Koury, S. T. (1997). Apoptosis of late-stage erythroblasts in megaloblastic anemia: Association with DNA damage and Macrocyte production. *Blood*, *89*(12), 4617–4623.

Kwok, B., Hall, J. M., Witte, J. S., Yin, X., Reddy, P., Lin, K., Flamholz, R., et al. (2015). MDS-associated somatic mutations and clonal hematopoiesis are common in idiopathic Cytopenias of undetermined significance. *Blood*, *126*(21), 2355–2361. https://doi.org/10.1182/blood-2015-08-667063.

Machherndl-Spandl, S., Suessner, S., Danzer, M., Proell, J., Gabriel, C., Lauf, J., Sylie, R., Klein, H. U., Béné, M. C., Weltermann, A., & Bettelheim, P. (2013). Molecular pathways of early CD105-positive erythroid cells as compared with CD34-positive common precursor cells by flow cytometric cell-sorting and gene expression profiling. *Blood Cancer Journal*, *3*(1), e100. https://doi.org/10.1038/bcj.2012.45.

Malcovati, L., Gallì, A., Travaglino, E., Ambaglio, I., Rizzo, E., Molteni, E., Elena, C., Ferretti, V. V., Catricalà, S., Bono, E., Todisco, G., Bianchessi, A., Rumi, E., Zibellini, S., Pietra, D., Boveri, E., Camaschella, C., Toniolo, D., Papaemmanuil, E., … Cazzola, M. (2017). Clinical significance of somatic mutation in unexplained blood Cytopenia. *Blood*, *129*(25), 3371–3378. https://doi.org/10.1182/blood-2017-01-763425.

Malcovati, L., Malcovati, L., Hellstrom-Lindberg, E., Hellström-Lindberg, E., Bowen, D., Adès, L., Cermak, J., et al. (2013). Diagnosis and treatment of primary myelodysplastic syndromes in adults: Recommendations from the European LeukemiaNet. *Blood*, *122*(17), 2943–2964. https://doi.org/10.1182/blood-2013-03-492884.

Matarraz, S., López, A., Barrena, S., Fernandez, C., Jensen, E., Flores-Montero, J., Rasillo, A., et al. (2010). Bone marrow cells from myelodysplastic syndromes show altered Immunophenotypic profiles that may contribute to the diagnosis and prognostic stratification of the disease: A pilot study on a series of 56 patients. *Cytometry Part B—Clinical Cytometry*, *78*(3), 154–168. https://doi.org/10.1002/cyto.b.20513.

Mathis, S., Chapuis, N., Debord, C., Rouquette, A., Radford-Weiss, I., Park, S., Dreyfus, F., Lacombe, C., Béné, M. C., Kosmider, O., Fontenay, M., & Bardet, V. (2013). Flow cytometric detection of Dyserythropoiesis: A sensitive and powerful diagnostic tool for myelodysplastic syndromes. *Leukemia*, *27*(10), 1981–1987. https://doi.org/10.1038/leu.2013.178.

McGrath, K. E., Bushnell, T. P., & Palis, J. (2008a). Multispectral imaging of hematopoietic cells: Where flow meets morphology. *Journal of Immunological Methods*, *336*(2), 91–97. https://doi.org/10.1016/j.jim.2008.04.012.

McGrath, K. E., Kingsley, P. D., Koniski, A. D., Porter, R. L., Bushnell, T. P., & Palis, J. (2008b). Enucleation of primitive erythroid cells generates a transient population of 'Pyrenocytes' in the mammalian fetus. *Blood*, *111*(4), 2409–2417. https://doi.org/10.1182/blood-2007-08-107581.

Mirabelli, P., Scalia, G., Pascariello, C., D'Alessio, F., Mariotti, E., Di Noto, R., George, T. C., et al. (2012). ImageStream Promyelocytic leukemia protein Immunolocalization: In search of Promyelocytic leukemia cells. *Cytometry Part A*, *81 A*(3), 232–237. https://doi.org/10.1002/cyto.a.22013.

More, T. A., Dalal, B., Devendra, R., Warang, P., Shankarkumar, A., & Kedar, P. (2020). Applications of imaging flow cytometry in the diagnostic assessment of red cell membrane disorders. *Cytometry Part B—Clinical Cytometry*, *98*(3), 238–249. https://doi.org/10.1002/cyto.b.21857.

Nguyen, P. L., & Hasserjian, R. P. (2017). *Myelodysplastic syndromes. Hematopathology, A Volume in the Series: Foundations in Diagnostic Pathology*, Philadelphia, PA: Elsevier Inc. Vol. 3, 539–563.e2. https://doi.org/10.1016/B978-0-323-47913-4.00018-5.

Ogata, K., Porta, M. G. D., Malcovati, L., Picone, C., Yokose, N., Matsuda, A., Yamashita, T., Tamura, H., Tsukada, J., & Dan, K. (2009). Diagnostic utility of flow cytometry in low-grade myelodysplastic syndromes: A prospective validation study. *Haematologica*, *94*(8), 1066–1074. https://doi.org/10.3324/haematol.2009.008532.

Palis, J. (2014). Primitive and definitive erythropoiesis in mammals. *Frontiers in Physiology*, *5*(3), 1–9. https://doi.org/10.3389/fphys.2014.00003.

Pinto, R. N., Sebastian, J. A., Parsons, M. J., Chang, T. C., Turner, T. R., Acker, J. P., & Kolios, M. C. (2019). Label-free analysis of red blood cell storage lesions using imaging flow cytometry. *Cytometry Part A*, *95A*(9), 976–984. https://doi.org/10.1002/cyto.a.23846.

Porta, M. G. D., Malcovati, L., Invernizzi, R., Travaglino, E., Pascutto, C., Maffioli, M., Gallí, A., et al. (2006). Flow cytometry evaluation of erythroid dysplasia in patients with myelodysplastic syndrome. *Leukemia*, *20*(4), 549–555. https://doi.org/10.1038/sj.leu.2404142.

Porta, M. G. D., & Picone, C. (2017). Diagnostic utility of flow cytometry in myelodysplastic syndromes. *Mediterranean Journal of Hematology and Infectious Diseases*, *9*(1), 1–9. https://doi.org/10.4084/mjhid.2017.017.

Porta, M. G. D., Picone, C., Pascutto, C., Malcovati, L., Tamura, H., Handa, H., Czader, M., et al. (2012). Multicenter validation of a reproducible flow cytometric score for the diagnosis of low-grade myelodysplastic syndromes: Results of a European LeukemiaNET study. *Haematologica*, *97*(8), 1209–1217. https://doi.org/10.3324/haematol.2011.048421.

Porta, M. G. D., Travaglino, E., Boveri, M., Ponzoni, L., Malcovati, E., Papaemmanuil, G. M. R., et al. (2015). Minimal morphological criteria for defining bone marrow dysplasia: A basis for clinical implementation of WHO classification of myelodysplastic syndromes. *Leukemia*, *29*, 66–75. https://doi.org/10.1038/leu.2014.161.

Porwit, A. (2011). Role of flow cytometry in diagnostics of myelodysplastic syndromes-beyond the WHO 2008 classification. *Seminars in Diagnostic Pathology*, *28*(4), 273–282. https://doi.org/10.1053/j.semdp.2011.06.003.

Porwit, A., McCullough, J., & Erber, W. N. (2011). *Blood and Bone Marrow Pathology*. Vol. 2, Amsterdam, Netherlands: Elsevier Ltd. https://doi.org/10.1016/C2009-0-52942-X.

Raimbault, A., Itzykson, R., Willems, L., Rousseau, A., Chapuis, N., Mathis, S., Clauser, S., et al. (2019). The fraction of CD117/c-KIT-expressing erythroid precursors predicts ESA response in low-risk myelodysplastic syndromes. *Cytometry Part B—Clinical Cytometry*, *96B*, 215–222. https://doi.org/10.1002/cyto.b.21781.

Rodrigues, M. A., Beaton-Green, L. A., Wilkins, R. C., & Fenech, M. F. (2018). The potential for complete automated scoring of the cytokinesis block micronucleus Cytome assay using imaging flow cytometry. *Mutation Research—Genetic Toxicology and Environmental Mutagenesis*, *836*(Part A), 53–64. https://doi.org/10.1016/j.mrgentox.2018.05.003.

Santini, V. (2015). Anemia as the Main manifestation of myelodysplastic syndromes. *Seminars in Hematology*, *52*(4), 348–356. https://doi.org/10.1053/j.seminhematol.2015.06.002.

Steensma, D. P. (2012). Dysplasia has a differential diagnosis: Distinguishing genuine myelodysplastic syndromes (MDS) from mimics, imitators, copycats and impostors. *Current Hematologic Malignancy Reports*, *7*(4), 310–320. https://doi.org/10.1007/s11899-012-0140-3.

Stetler-Stevenson, M., Arthur, D. C., Jabbour, N., Xie, X. Y., Molldrem, J., Barrett, A. J., Venzon, D., & Rick, M. E. (2001). Diagnostic utility of flow cytometric Immunophenotyping in myelodysplastic syndrome. *Blood*, *98*(4), 979–987. https://doi.org/10.1182/blood.V98.4.979.

Sundaravel, S., Duggan, R., Bhagat, T., Ebenezer, D. L., Liu, H., Yiting, Y., Bartenstein, M., et al. (2015). Reduced DOCK4 expression leads to erythroid dysplasia in myelodysplastic syndromes. *Proceedings of the National Academy of Sciences of the United States of America*, *112*(46), E6359–E6368. https://doi.org/10.1073/pnas.1516394112.

Swerdlow, S. H., Campo, E., Harris, N. L., Jaffe, E. S., Pileri, S. A., Stein, H., Thiele, J., et al. (2017). *WHO Classification of Tumours of Haematopoietic and Lymphoid Tissues*, *4th Edition (IARC WHO Classification of Tumours*, *Volume 2)*. International Agency for Research on Cancer (IARC). http://scholar.google.com/scholar?hl=en&btnG=Search&q=intitle:WHO+Classification+of+Tumours+of+Haematopoietic+and+Lymphoid+Tissues+,+Fourth+Edition#5.

Tsai, A. G., Glass, D. R., Juntilla, M., Hartmann, F. J., Oak, J. S., Fernandez-Pol, S., Ohgami, R. S., & Bendall, S. C. (2020). Multiplexed single-cell morphometry for Hematopathology diagnostics. *Nature Medicine*, *26*, 408–417. https://doi.org/10.1038/s41591-020-0783-x.

Valent, P., Bain, B. J., Bennett, J. M., Wimazal, F., Sperr, W. R., Mufti, G., & Horny, H. P. (2012). Idiopathic Cytopenia of undetermined significance

(ICUS) and idiopathic dysplasia of uncertain significance (IDUS), and their distinction from low risk MDS. *Leukemia Research*, *36*(1), 1–5. https://doi.org/10.1016/j.leukres.2011.08.016.

Valent, P., Orazi, A., Steensma, D. P., Ebert, B. L., Haase, D., Malcovati, L., van de Loosdrecht, A. A., Haferlach, T., Westers, T. M., Wells, D. A., Giagounidis, A., Loken, M., Orfao, A., Lübbert, M., Ganser, A., Hofmann, W.-K., Ogata, K., Schanz, J., Béné, M. C., … Bennett, J. M. (2017). Proposed minimal diagnostic criteria for myelodysplastic syndromes (MDS) and potential pre-MDS conditions. *Oncotarget*, *8*(43), 73483–73500. https://doi.org/10.18632/oncotarget.19008.

Van Beers, E. J., Samsel, L., Mendelsohn, L., Saiyed, R., Fertrin, K. Y., Brantner, C. A., Daniels, M. P., Nichols, J., Philip McCoy, J., & Kato, G. J. (2014). Imaging flow cytometry for automated detection of hypoxia-induced erythrocyte shape change in sickle cell disease. *American Journal of Hematology*, *89*(6), 598–603. https://doi.org/10.1002/ajh.23699.

Van De Loosdrecht, A. A., Westers, T. M., Westra, A. H., Dräger, A. M., Van Der Velden, V. H. J., & Ossenkoppele, G. J. (2008). Identification of distinct prognostic subgroups in low- and Intermediate-1-risk myelodysplastic syndromes by flow cytometry. *Blood*, *111*(3), 1067–1077. https://doi.org/10.1182/blood-2007-07-098764.

Violidaki, D., Axler, O., Jafari, K., Bild, F., Nilsson, L., Mazur, J., Ehinger, M., & Porwit, A. (2020). Analysis of erythroid maturation in the nonlysed bone marrow with help of radar plots facilitates detection of flow cytometric aberrations in myelodysplastic syndromes. *Cytometry Part B—Clinical Cytometry*, *98*, 399–411. https://doi.org/10.1002/cyto.b.21931.

Wells, D. A., Benesch, M., Loken, M. R., Vallejo, C., Myerson, D., Leisenring, W. M., & Deeg, H. J. (2003). Myeloid and Monocytic Dyspoiesis as determined by flow cytometric scoring in myelodysplastic syndrome correlates with the IPSS and with outcome after hematopoietic stem cell transplantation. *Blood*, *102*(1), 394–403. https://doi.org/10.1182/blood-2002-09-2768.

Westers, T. M., Cremers, E. M. P., Oelschlaegel, U., Johansson, U., Bettelheim, P., Matarraz, S., Orfao, A., et al. (2017). Immunophenotypic analysis of erythroid dysplasia in myelodysplastic syndromes. A report from the IMDSFlow working group. *Haematologica*, *102*(2), 308–319. https://doi.org/10.3324/haematol.2016.147835.

Wickramasinghe, S. N. (1999). The wide Spectrum and unresolved issues of megaloblastic anemia. *Seminars in Hematology*, *36*(1), 3–18.

SUPPORTING INFORMATION

Additional supporting information may be found online in the Supporting Information section at the end of this article.

BACK TO CONTENTS